

REPORT DOCUMENTATION PAGE			Form Approved OMB No. 0704-0188	
Public reporting burden for this collection of information is estimated to average 1 hour per response, including the time for reviewing instructions, searching existing data sources, gathering and maintaining the data needed, and completing and reviewing the collection of information. Send comments regarding this burden estimate or any other aspect of this collection of information, including suggestions for reducing this burden, to Washington Headquarters Services, Directorate for Information Operations and Reports, 1215 Jefferson Davis Highway, Suite 1204, Arlington, VA 22202-4302, and to the Office of Management and Budget, Paperwork Reduction Project (0704-0188), Washington, DC 20503.				
1. AGENCY USE ONLY (Leave blank)		2. REPORT DATE <i>Dec 95</i>	3. REPORT TYPE AND DATES COVERED	
4. TITLE AND SUBTITLE <i>Unsteady Pressure Distributions Around Compressor Vanes in an Unsteady, Transonic Cascade</i>			5. FUNDING NUMBERS	
6. AUTHOR(S) <i>Michael Kenneth Fabian</i>				
7. PERFORMING ORGANIZATION NAME(S) AND ADDRESS(ES) AFIT Students Attending: <i>Notre Dame</i>			8. PERFORMING ORGANIZATION REPORT NUMBER <i>95-034D</i>	
9. SPONSORING / MONITORING AGENCY NAME(S) AND ADDRESS(ES) DEPARTMENT OF THE AIR FORCE AFIT/CI 2950 P STREET, BLDG 125 WRIGHT-PATTERSON AFB OH 45433-7765			10. SPONSORING / MONITORING AGENCY REPORT NUMBER	
11. SUPPLEMENTARY NOTES				
12a. DISTRIBUTION / AVAILABILITY STATEMENT Approved for Public Release IAW AFR 190-1 Distribution Unlimited BRIAN D. Gauthier, MSgt, USAF Chief Administration			12b. DISTRIBUTION CODE	
13. ABSTRACT (Maximum 200 words)				
<i>19960124 081</i>				
14. SUBJECT TERMS			15. NUMBER OF PAGES <i>252</i>	
			16. PRICE CODE	
17. SECURITY CLASSIFICATION OF REPORT	18. SECURITY CLASSIFICATION OF THIS PAGE	19. SECURITY CLASSIFICATION OF ABSTRACT	20. LIMITATION OF ABSTRACT	

UNSTEADY PRESSURE DISTRIBUTIONS AROUND COMPRESSOR VANES

IN AN UNSTEADY, TRANSONIC CASCADE

Michael Kenneth Fabian, Capt, USAF

1995

252 pages

Ph.D., Aerospace Engineering

University of Notre Dame

UNSTEADY PRESSURE DISTRIBUTIONS AROUND COMPRESSOR VANES
IN AN UNSTEADY, TRANSONIC CASCADE

Abstract

by

Michael Kenneth Fabian

Unsteady surface pressure measurements were made at various chord locations on the turning vanes in an unsteady, compressible-flow, linear cascade. The turning vanes were made from production stator vanes from the fan stage of a Garrett F109 engine. The cascade unsteady forcing was produced by von Karman shedding from a row of circular-cylinder rods positioned at either 80% chord upstream of the turning vanes (forward forced) or at 80% chord downstream (rearward forced). Nominal time series of many complete cycles of the unsteady pressure response required acquiring the phase-locked response from eight instrumented vanes, each having pressure transducers at two chord locations. Unsteady pressure response from rearward forcing was of the same order as

that for forward forcing. Decomposition of the ensembled, phase-locked signals into their primary and harmonic components provided insight into the amplitude decay rates and wave propagation direction within the cascade row. Although the unsteady cascade was limited to passage Mach numbers near 0.75, the rearward forcing cases indicated a suction-surface, unsteady-pressure bulge or amplification that increased with increasing Mach number. This "bulge" appears to be compatible with the *acoustic blockage* phenomenon. Forward forcing of the stator vane row showed the importance of the constructive and destructive interference between convective wakes and potential disturbances that propagate at acoustic speeds. These interactions created unexpected unsteady surface pressure profiles which could be important for analysis of stator vibration modes.

REFERENCES

- Adachi, T., and Murakami, Y., "Three Dimensional Velocity Distribution Between Stator Blades and Unsteady Force on a Blade due to Passing Wakes," Japan Society of Mechanical Engineers, August, 1979, pp. 1074-1082.
- Adamczyk, J.J., "Passage of a Swept Airfoil through an Oblique Gust," Journal of Aircraft, May, 1974, pp. 281-287.
- Anderson, J.D., Jr., Fundamentals of Aerodynamics, McGraw-Hill, New York, 1991.
- Atassi, H.M., personal communication, University of Notre Dame, 22 June, 1995.
- Atassi, H.M., "The Sears Problems for a Lifting Airfoil Revisited - New Results," Journal of Fluid Mechanics, Vol. 141, 1984, pp. 109-122.
- Atassi, H.M., "Unsteady Aerodynamics of Vortical Flows: Early and Recent Developments," Aerodynamics and Aeroacoustics, Editor K.Y. Fung, World Scientific, Chapter 4, pp. 119-169, 1994.
- Atassi, H.M., and Akai, T.J., "Aerodynamic and Aeroelastic Characteristics of Oscillating Loaded Cascades at Low Mach Number, Part I: Pressure Distribution, Forces, and Moments," Journal of Engineering for Power, Vol. 102, No. 2, 1980, pp. 344-351.
- Atassi, H.M., and Akai, T.J., "Aerodynamic and Aeroelastic Characteristics of Oscillating Loaded Cascades at Low Mach Number, Part II: Stability and Flutter Boundaries," Journal of Engineering for Power, Vol. 102, No. 2, 1980, pp. 352-356.
- Atassi, H.M., Fang, J., and Ferrand, P., "A Study of the Unsteady Pressure of a Cascade Near Transonic Flow Condition," ASME Paper 94-GT-476, International Gas Turbine and Aerospace

Congress and Exposition, The Hague, Netherlands, 1994.

Atassi, H.M., Fang, J., and Patrick, S., "Direct Calculation of Sound Radiated From Bodies in Nonuniform Flows," *Journal of Fluids Engineering*, Vol. 115, 1993, pp. 573-579.

Batill, S.M., and Nebres, J.V., "Application of Digital Filtering Techniques to Unsteady Pressure Measurements," AIAA-91-0061, 29th Aerospace Sciences Meeting, Reno, Nevada, 1991.

Bentele, M., Engine Revolutions: The Autobiography of Max Bentele, Society of Automotive Engineers, Warrendale, PA, 1991.

Bisplinghoff, R.L., and Ashley, H., Principles of Aeroelasticity, John Wiley and Sons, New York, 1962.

Blöcs, A., and Fransson, T.H., "Aeroelasticity in Turbomachines: Comparison of Theoretical and Experimental Cascade Results," Lausanne Institute of Technology, Switzerland, Communication du laboratoire de Thermique Appliquee No. 13, 1986.

Boyne, W.J., and Lopez, D.S., The Jet Age: Forty Years of Jet Aviation, Smithsonian Institution Press, Washington City, 1979.

Bratt, J.B., and Scruton, C., "Measurements of Pitching Moment Derivatives for an Aerofoil Oscillating About the Half-Chord Axis," British Aeronautical Research Council, London, R&M 1921, November, 1938.

Buffum, D.H., and Fleeter, S., "Oscillating Cascade Aerodynamics by an Experimental Influence Coefficient Technique," *Journal of Propulsion*, Vol. 6, No. 5, 1990, pp. 612-620.

Campbell, W., "Protection of Steam Turbine Disc Wheels from Axial Vibration," ASME Paper 1920, May 1924.

Carta, F.O., "Unsteady Aerodynamics and Gapwise Periodicity of Oscillating Cascaded Airfoils," *Journal of Engineering for Power*, July, 1983, pp. 565-574.

Cohen, H., Rogers, G.F.C., and Saravanamuttoo, H.I.H., Gas Turbine

Theory, Longman Scientific & Technical, Singapore, 1987.

Commerford, G.L., and Carta, F.O., "Unsteady Aerodynamic Response of a Two-Dimensional Airfoil at High Reduced Frequency," AIAA Journal, January, 1974, pp. 43-48.

Davis, E.L., "The Measurement of Unsteady Pressures in Wind Tunnels," AGARD Report 169, London, March, 1958.

Dring, R.P., Joslyn, H.D., and Hardin, L.W., "An Investigation of Axial Compressor Rotor Aerodynamics," Journal of Engineering for Power, January, 1982, pp. 84-96.

Epstein, A.H., Gertz, J.B., Owen, P.R., and Giles, M.B., "Vortex Shedding in High-Speed Compressor Blade Wakes," Journal of Propulsion, Vol. 4, No. 3, 1987, pp. 236-244.

Evans, R.L., "Boundary-Layer Development on an Axial-Flow Compressor Stator Blade," Journal for Engineering for Power, April, 1978, pp. 287-293.

Evans, R.L., "Turbulence and Unsteadiness Measurements Downstream of a Moving Blade Row," Journal of Engineering for Power, January, 1975, pp. 131-139.

Fabian, M.K., and Jumper, E.J., "Unsteady Pressure Distributions around Compressor Vanes in an Unsteady, Transonic Cascade," AIAA-95-0302, 33rd Aerospace Sciences Meeting, Reno, Nevada, 1995.

Fang, J., and Atassi, H.M., "Compressible Flows with Vortical Disturbances Around a Cascade of Loaded Airfoils," Unsteady Aerodynamics, Aeroacoustics, and Aeroelasticity of Turbomachines and Propellers, Springer-Verlag, New York, 1993.

Figliola, R.S., and Beasley, D.E., Theory and Design for Mechanical Measurements, John Wiley and Sons, New York, 1991.

Fleeter, S., "Fluctuating Lift and Moment Coefficients for Cascaded Airfoils in a Nonuniform Compressible Flow," Journal of

Aircraft, Vol. 10, No. 2., 1973, pp. 93-98.

Fleeter, S., Jay, R.L., Bennett, W.A., "Rotor Wake Generated Unsteady Aerodynamic Response of a Compressor Stator," Journal of Engineering for Power, October, 1978, pp. 664-675.

Fleeter, S., Jay, R.L., Bennett, W.A., "The Time-Variant Aerodynamic Response of a Stator Row Including the Effects of Airfoil Camber," Journal of Engineering for Power, April, 1980, pp. 334-343.

Franke, G.F., and Henderson, R.E., "Unsteady Stator Response to Upstream Rotor Wakes," Journal of Aircraft, July, 1980, pp. 500-507.

Fujita, H., and Kovasznay, L.S., "Unsteady Lift and Radiated Sound from a Wake Cutting Airfoil," AIAA Journal, Vol. 12, No. 9, 1974, pp. 1216-1221.

Fung, Y.C., An Introduction to the Theory of Aeroelasticity, Dover Publications, 1993, p. 66.

Gallus, H.E., Lambertz, J., and Wallmann, T., "Blade-Row interaction in an Axial Flow Subsonic Compressor Stage, Journal of Engineering for Power," January, 1980, pp. 169-177.

Garrick, I.E., "On the Plane Potential Flow past a Lattice of Arbitrary Aerofoils," NACA Rep. 788, 1944.

Garrick, I.E., "Perspectives in Aeroelasticity," Aeroelasticity in Turbomachines, Detroit Diesel Allison, 1972, pp. 1-75.

"GE to Test Production Design of B-1B Fan Blade Dampers," Aviation Week & Space Technology, McGraw-Hill, October 7, 1991, p. 17.

Glegg, S.A.L., personal communication, University of Notre Dame, November 8, 1995.

Goldstein, M.E., and Atassi, H., "A Complete Second-Order Theory for the Unsteady Flow about an Airfoil due to a Periodic Gust," Journal of Fluid Mechanics, Vol. 74, Part 5, 1976, pp. 741-765.

Goldstein, S., Modern Developments in Fluid Dynamics, Oxford Press, Oxford, England, 1943.

Gostelow, J.P., "A New Approach to the Experimental Study of Turbomachinery Flow Phenomena," *Journal of Engineering for Power*, January 1977, pp. 97-105.

Gostelow, J.P., Cascade Aerodynamics, Pergamon Press, Oxford, England, 1984.

Green, W., Rocket Fighter, Random House, New York, 1971.

Green, W., The World's Fighting Planes, Doubleday, Garden City, New York, 1964.

Hartog, J.P.D., Mechanical Vibrations, Dover, 1985, p. 270.

Hathaway, M.D., Gertz, J.B, Epstein, A.H., and Strazisar, A.J., "Rotor Wake Characteristics of a Transonic Axial-Flow Fan," *AIAA Journal*, Vol. 24, No. 11, 1986, pp. 1802-1810.

Hawthorne, W.R., Aerodynamic of Turbine and Compressors, Princeton University Press, Princeton, New Jersey, 1964.

Heiser, W., personal communication, U.S. Air Force Academy, January, 1992.

Henderson, R.E., and Horlock, J.H., "An Approximate Analysis of the Unsteady Lift on Airfoils in Cascade," *Journal of Engineering for Power*, October, 1972, pp. 233-240.

Horlock, J.H., "Fluctuating Lift Forces on Aerofoils Moving Through Transverse and Chordwise Gusts," *Journal of Basic Engineering*, December, pp. 494-500, 1968.

Ives, D.C., "A Modern Look at Conformal Mapping Including Multiply Connected Regions," *AIAA Journal*, Vol. 14, no. 8, pp. 1006-1011, 1976.

"Jet Engine Inspections Urged," Associated Press Release, 25 August

1995.

Johnsen, I.A., and Bullock, R.O., Aerodynamic Design of Axial-Flow Compressors, NASA SP-36, Washington, D.C., 1965.

Kemp, N.H., and Sears, W.R., "Aerodynamic Interference Between Moving Blade Rows," *Journal of the Aeronautical Sciences*, Vol. 20, No. 9, 1953, pp. 585-612.

Kemp, N.H., and Sears, W.R., "The Unsteady Forces Due to Viscous Wakes in Turbomachines," *Journal of the Aeronautical Sciences*, July, 1955, pp. 478-483.

Kerrebrock, J.L., and Mikolajczak, A.A., "Intra-Stator Transport of Rotor Wakes and Its Effect on Compressor Performance," *Journal of Engineering for Power*, October, 1970, pp. 359-368.

"Kulite Miniature IS Silicon Diaphragm Pressure Transducer Catalog," Bulletin KS-1000E, Leonia, New Jersey, 1992.

Kurosaka, M., "AA 526 Aircraft Engine Noise," Course Notes, Lesson #8, University of Washington, October, 1989.

Lefcort, M.D., "An Investigation into Unsteady Blade Forces in Turbomachines," *Journal of Engineering for Power*, October, 1965, pp. 345-354.

Lotz, M., and Raabe, J., "Blade Oscillations in One-Stage Axial Turbomachinery," *Journal of Basic Engineering*, December, 1968, pp. 485-493.

Lykins, C., and Watson K., "IHPTET: Technology Teams in Action," Aero-Propulsion and Power Directorate, Wright-Patterson AFB, Ohio, 1993.

Manwaring, S.R., and Wisler, D.C., "Unsteady Aerodynamics and Gust Response in Compressors and Turbines," ASME Paper 92-GT-422.

Meyer, R.X., "The Effect of Wakes on the Transient Pressure and Velocity Distributions in Turbomachines," *Transactions of the*

American Society of Mechanical Engineers, October, 1958, pp. 1544-1552.

Naumann, H., and Yeh, H., "Lift and Pressure Fluctuations of a Cambered Airfoil under Periodic Gusts and Applications in Turbomachinery," *Journal of Engineering for Power*, January, pp. 1-10, 1973.

Oates, G.C., Aerothermodynamics of Gas Turbine and Rocket Propulsion: Revised and Enlarged, AIAA Educational Series, Washington D.C., 1988.

Oates, G.C., Aircraft Propulsion Systems Technology and Design, AIAA Educational Series, Washington D.C., 1989.

O'Connor, L., "Taming Vibrations in Turbines," *Mechanical Engineering*, April, 1993, pp. 49-52.

Osborne, C., "Compressible Unsteady Interactions between Blade Rows," *AIAA Journal*, Vol. 11, No. 3, pp. 340-346, 1973.

Press, W.H., Teukolsky, S.A., Vetterling, W.T., Flannery, B.P., Numerical Recipes in Fortran: The Art of Scientific Computing, Cambridge University Press, Cambridge, UK, 1986.

Rainey, A.G., "Measurement of Aerodynamic Forces for Various Mean Angles of Attack on an Airfoil Oscillating in Pitch and on Two Finite-Span wings Oscillating in Bending with Emphasis on Damping in Stall," *NACA Report 1305*, 1957.

Rao, J.S., Turbomachine Blade Vibration, John Wiley and Sons, New Delhi, India, 1991.

Reynolds, W.C., and Perkins, H.C., Engineering Thermodynamics, McGraw-Hill, New York, 1977.

Schlichting, H., "Problems and Results of Investigations on Cascade Flow," *Journal of the Aeronautical Sciences*, March, 1954, pp. 163-178.

Schlichting, H., Boundary Layer Theory, McGraw-Hill, New York, 1955.

- Schmidt, D.P., and Okiishi, T.H., "Multistage Axial-Flow Turbomachine Wake Production, Transport, and Interaction," AIAA Journal, Vol. 15, No. 8, 1977, pp. 1138-1145.
- Schwarz, L., "Berechnung der Druckverteilung einer Harmonisch sich Verformenden Tragfläche in ebener Strömung," Luftfahrt-Forschung, Vol 17, 1940, p. 379.
- Sears, W.R., "Some Aspects of Non-Stationary Airfoil Theory and Its Practical Application," Journal of the Aeronautical Sciences, Vol. 8, No. 3, pp. 43-47, 1941.
- "T-46 Termination Will Force Closure of Fairchild Facility on Long Island," Aviation Week & Space Technology, McGraw-Hill, March 23, 1987, p. 27.
- Theodorsen, T., "General Theory of Aerodynamic Instability and the Mechanism of Flutter," NACA Report 496, 1935.
- Verdon, J.M., and Caspar, J.R., "Subsonic Flow Past an Oscillating Cascade with Finite Mean Flow Deflection," AIAA Journal, Vol. 18, No. 5, 1980, pp. 540-548.
- Verdon, J.M., "Unsteady Aerodynamics for Turbomachinery Aeroelastic Applications," Unsteady Transonic Aerodynamics, AIAA Progress in Astronautics and Aeronautics, Vol. 120, 1989. pp. 287-347.
- von Karman, T., and Sears, W.R., "Airfoil Theory for Non-Uniform Motion," Journal of the Aeronautical Sciences, Vol. 5, No. 10, pp. 6-17, 1938.
- Vukelich, S., "US Air Force Structural Integrity Program," University of Tennessee Space Institute, Tullahoma, Tennessee, June, 1992.
- Walker, G.J., and Oliver, A.R., "The Effect of Interaction Between Wakes from Blade Rows in an Axial Flow Compressor on the Noise Generated by Blade Interaction," Journal of Engineering for Power, October, 1972, pp. 241-248.

Whitehead, D.S., "Force and Moment Coefficients for Vibrating Aerofoils in Cascade," British Aeronautical Research Council, London, R&M 3254, 1960.

Whitfield, C.E., Kelly, J.C., Barry, B., "A Three-Dimensional Analysis of Rotor Wakes," Aeronautical Quarterly, November, 1972, pp. 285-300.

Wilson, D.G., The Design of High-Efficiency Turbomachinery and Gas Turbines, MIT Press, Cambridge, Massachusetts, 1984.

Zierke, W.C., and Okiishi, T.H., "Measurement and Analysis of Total-Pressure Unsteadiness Data from an Axial-Flow Stage," Journal of Engineering for Power, April, 1982, pp. 479-488.

UNSTEADY PRESSURE DISTRIBUTIONS AROUND COMPRESSOR VANES
IN AN UNSTEADY, TRANSONIC CASCADE

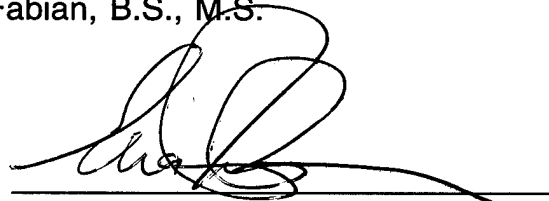
A Dissertation

Submitted to the Graduate School
of the University of Notre Dame
In Partial Fulfillment of the Requirements
of the Degree of

Doctor of Philosophy

by

Michael Kenneth Fabian, B.S., M.S.



Eric J. Jumper, Director

Department of Aerospace and Mechanical Engineering

Notre Dame, Indiana

December, 1995

UNSTEADY PRESSURE DISTRIBUTIONS AROUND COMPRESSOR VANES
IN AN UNSTEADY, TRANSONIC CASCADE

Abstract

by

Michael Kenneth Fabian

Unsteady surface pressure measurements were made at various chord locations on the turning vanes in an unsteady, compressible-flow, linear cascade. The turning vanes were made from production stator vanes from the single, axial-flow fan stage of a Garrett F109 turbofan engine. The cascade unsteady forcing was produced by von Karman shedding from a row of circular-cylinder rods positioned at either 80% chord upstream of the turning vanes (forward forced) or at 80% chord downstream of the turning vanes (rearward forced). Nominal time series of many complete cycles of unsteady pressure response (around a vane) to the unsteady forcing were acquired by phase locking the response to specific features of the forcing signal

to trigger the unsteady pressure data collection. A complete time history of the pressure response required building up the phase-locked response from eight instrumented vanes, each having pressure transducers at two chord locations. Unsteady pressure response from rearward forcing was shown to be of the same order as that for forward forcing. Decomposition of the ensembled, phase-locked signals into their primary and harmonic components provided insight into the amplitude decay rates and wave propagation direction within the cascade row. Although the unsteady cascade was limited to passage Mach numbers near 0.75, the rearward forcing cases indicated a suction-surface, unsteady-pressure bulge or amplification that increased with increasing Mach number. This "bulge" appears to be compatible with the *acoustic blockage* phenomenon. Finally, the rearward forcing data seemed to indicate a possibility of a trailing-edge singularity. Forward forcing of the stator vane row showed the importance of the constructive and destructive interference between convective wakes and aerodynamic or potential disturbances that propagate at acoustic speeds. These interactions created unexpected unsteady surface pressure profiles which could be important for analysis of stator vibration modes.

DEDICATION

I dedicate this effort to my parents, Donna and John Fabian, whose love and support allowed me to complete this dissertation and achieve my personal goals. When things were going poorly, they always helped me keep everything in the proper perspective. I am grateful for their emotional and financial help.

TABLE OF CONTENTS

LIST OF TABLES	vi
LIST OF FIGURES	vii
LIST OF SYMBOLS	x
ACKNOWLEDGEMENTS	xii
CHAPTER 1 NATURE OF PROBLEM	1
CHAPTER 2 PROJECT OBJECTIVES	5
2.1 Hardware Objectives	5
2.1.1 Vane Instrumentation	7
2.1.2 Cascade	8
2.2 Research Objectives	13
2.3 Organization Of This Dissertation	16
CHAPTER 3 CASCADE NOMENCLATURE	18
CHAPTER 4 FACILITIES, EQUIPMENT AND PROCEDURES	21
4.1 Hessert Center Transonic In-Draft Facilities ..	21
4.2 Cascade Test Section	23
4.2.1 Unsteady Flow Exciters	26
4.2.2 Trigger Signal and Conditional Sampling Technique	27
4.2.3 Location of the Excitation-Cylinder Row	29
4.2.4 Instrumented Vanes	29
4.3 Overall Experimental Set Up	35
4.4 Calibration	37
4.5 Data Acquisition	40
4.6 Data Reduction	42
CHAPTER 5 STEADY AND TIME-AVERAGED RESULTS	47

5.1	Types of Pressure Data	47
5.2	Engine-Axis-Location-1, Steady Cp Data	48
5.3	Two-Dimensional-Flow Quality and Airfoil- Geometry Sensitivity	50
5.4	Freestream Mach Number and Static Pressure .	56
5.5	Vane-Inflow Mach Number.	59
5.6	Surface Flow Visualization	61
5.6.1	Summary	67
CHAPTER 6 REARWARD FORCING OF CASCADE		69
6.1	Forcing Gust	69
6.2	Gross RMS Unsteady-Pressure Response	72
6.3	Phase-Locked Unsteady Pressure Signals	74
6.4	The Inverse Problem.	85
6.5	Chordwise Amplitude Variation with Mach Number	91
6.6	Closing Remarks	92
CHAPTER 7 FORWARD FORCING OF CASCADE		95
7.1	Forcing Gust.	95
7.2	Gross RMS Unsteady-Pressure Response	97
7.3	Phase-Locked Unsteady Pressure Signal	99
7.4	The Inverse Problem	105
7.5	Chordwise Amplitude Variation with Mach Number	114
7.6	Concluding Remarks	116
CHAPTER 8 ON THE ISSUE OF ACOUSTIC BLOCKAGE		118
8.1	Background	118
8.2	Experimental Evidence of Acoustic Blockage in the Present Study	121
8.2.1	Forward Forcing Case	122
8.2.2	Rearward Forcing Case	123
CHAPTER 9 SUMMARY OF CONCLUSIONS AND FURTHER WORK .		126
9.1	Major Results and Implications	127
9.1.1	Unsteady Pressure Data	127
9.1.2	Analysis of the Unsteady Response Data	128
9.1.2.1	Forward Forcing	128

9.1.2.2	Rearward Forcing	131
9.2	Suggestion for Future Work	133
9.2.1	Further Cascade-Related Work	133
9.2.2	Further Planned F109 Engine Work	135
9.3	Contributions of this Dissertation Research .	136
9.3.1	Cascade	136
9.3.2	Instrumentation	137
9.3.3	Rearward Forced Studies	137
9.3.4	Decomposition and Interpretation of Gust ...	138
9.3.5	Acoustic Blockage	138
9.3.6	Possible Trailing-Edge Singularity	139

APPENDICES

A	Engine Based Historical Background	140
B	F109 Turbofan Engine Background	168
C	Pressure Cavity Analysis	173
D	Steady Cascade Analysis	180
E	Stator Coordinates and Cascade Geometry ...	190
F	Surface Flow Visualization	192
G	Rearward Forcing Data	196
H	Forward Forcing Data	209
I	Cascade Duct Analysis	218
J	Uncertainty Analysis	227

REFERENCES	244
----------------------	-----

LIST OF TABLES

Table 2.1	F109 Turbofan Engine and Unsteady Cascade Parameters	13
Table 6.1	Normalizing Amplitudes for Figure 6.3 and Appendix G	78
Table 6.2	Equation (6.1) Amplitude and Phase for Mach 0.427 data	80
Table 7.1	Normalizing Amplitudes for Figure 7.3 and Appendix H	101
Table 7.2	Equation (7.1) Amplitude and Phase for Mach 0.43 data	102
Table C.1	Sample Results for an External Cavity 3 inches from the vane	178
Table C.2	Sample Results Using Internal Vane Volume as the Cavity	178
Table C.3	Sample Result, Final Design, Near Surface Mounted Transducer	179
Table E.1	Stator vane coordinates in terms of half-chord .	190
Table E.2	Cascade Geometry	191
Table I.1	Sample Results at 6700 Hz, Lowest Primary Testing Frequency	222
Table I.2	Sample Results at 9200 Hz, Highest Primary Testing Frequency	223
Table I.3	Possible Acoustic Modes for Tested Limits of Forward and Forcing Cases	226

LIST OF FIGURES

Figure 1.1	Navy Advanced Fan Compressor Technology 1st Stage Fan	2
Figure 1.2	Splittered Rotor	3
Figure 3.1	Cascade Geometry	19
Figure 4.1	Side View of Cascade Tunnel	22
Figure 4.2	Top View of Cascade Test Section	24
Figure 4.3	Sample Data Acquisition Window	28
Figure 4.4	Side View of Stator	32
Figure 4.5	Stator Instrumentation Positions	33
Figure 4.6	Experimental Equipment Schematic	36
Figure 4.7	Calibration Sequence for Transducers	39
Figure 4.8	Sample Trigger Signal shows Poor Trigger Condition for a Zero Voltage Crossing	41
Figure 4.9	Sample FFT for Stator Vane	43
Figure 5.1	Clean Tunnel Scanivalve Data	49
Figure 5.2	Engine and Cascade Axes Comparison	51
Figure 5.3	Scanivalve vs Multiple Kulites	55
Figure 5.4	Determination of Mach Number and Freestream Pressure for Rods Forward of Cascade	57
Figure 5.5	Local Mach number vs Chordwise position	60
Figure 5.6	Hub and Tip Designations of Stator Vane	62
Figure 5.7	Suction Surface Separation and Leakage Regions in Clean Tunnel Configuration	64
Figure 5.8	Suction Surface Separation and Leakage Regions in with Rods Forward, $M = 0.43$	66
Figure 6.1	Trigger Signal and Power Spectrum for Rods Rearward	71
Figure 6.2	RMS Pressures for Rods Rearward	73
Figure 6.3	Signal Averages for $M = 0.427$ with Rods Rearward ...	75
Figure 6.4	Ensembled Record vs 2 Sine Wave Representation	79
Figure 6.5	RMS Pressure Amplitude, Normalized Primary and Harmonic Pressure Amplitudes	82
Figure 6.6	Primary Time Series	86

Figure 6.7	Harmonic Time Series	87
Figure 6.8	Suction Surface Upstream Travelling Wave vs Primary and Harmonic Phase	89
Figure 6.9	Pressure Surface Upstream Travelling Wave vs Primary and Harmonic Phase	90
Figure 6.10	Normalized Pressure Amplitude at Primary Forcing Frequency for Increasing Mach Number	92
Figure 7.1	Trigger Signal and Power Spectrum for Rods Forward .	96
Figure 7.2	RMS Pressures for Rods Forward	98
Figure 7.3	Signal Averages for $M = 0.43$ with Rods Forward	100
Figure 7.4	RMS Pressure Amplitude, Normalized Primary and Harmonic Pressure Amplitudes	104
Figure 7.5	Suction Surface Downstream Travelling Wave Primary and Harmonic Phase	108
Figure 7.6	Pressure Surface Downstream Travelling Wave Primary and Harmonic Phase	108
Figure 7.7	Induced Fluctuating Velocity Normal to Wake that convects through the Vane Passage with the Mean Flow	110
Figure 7.8	Example of Interaction of Potential and Convective Disturbances	111
Figure 7.9	Experimental Data vs Interaction Model for Primary Frequency	112
Figure 7.10	Resultant Interaction Model Phase for Figure 7.9	113
Figure 7.11	Normalized Pressure Amplitude at Primary Forcing Frequency for Increasing Mach Number	115
Figure 8.1	Nozzle Geometry and Mean Flow Mach Number Contours	120
Figure 8.2	Magnitude of Unsteady Pressure for Inlet and Outlet Disturbances for $k = 0.3$	121
Figure 8.3	Normalized Pressure Amplitude at Primary Forcing Frequency for Increasing Mach Number	124
Figure 8.4	Normalized Pressure Amplitude at First Harmonic of Forcing Frequency for Increasing Mach Number	125
Figure A.1	F109 Fan Blade Campbell Diagram	145
Figure A.2	Second Mode of F109 Fan Blade	146
Figure A.3	Generic Compressor Map	149
Figure A.4	Generic Compressor Map with Flutter Boundaries	150
Figure B.1	Garrett F109 Turbofan Engine	170
Figure C.1	Pressure Cavity and Pressure Transducer	174

Figure D.1	Cascade Transformation Planes	182
Figure D.2	Momentum Balance	184
Figure F.1	Clean Tunnel, $M = 0.50$	192
Figure F.2	Rods Forward, $M = 0.43$	193
Figure F.3	Rods Forward, $M = 0.58$	194
Figure F.4	Rods Rearward, $M = 0.427$	195
Figure G.1	Engine-Axis-Two Data, $M = 0.427$	197
Figure G.2	Engine-Axis-Two Data, $M = 0.454$	198
Figure G.3	Engine-Axis-Two Data, $M = 0.475$	199
Figure G.4	Engine-Axis-Two Data, $M = 0.50$	200
Figure G.5	Harmonic Data Through Mach Number Range	201
Figure G.6	Suction Surface Phase, $M = 0.45$	202
Figure G.7	Pressure Surface Phase, $M = 0.45$	202
Figure G.8	Suction Surface Phase, $M = 0.475$	203
Figure G.9	Pressure Surface Phase, $M = 0.475$	203
Figure G.10	Suction Surface Phase, $M = 0.50$	204
Figure G.11	Pressure Surface Phase, $M = 0.50$	204
Figure G.12	Engine-Axis-One Data, $M = 0.427$	205
Figure G.13	Engine-Axis-One Data, $M = 0.454$	206
Figure G.14	Engine-Axis-One Data, $M = 0.475$	207
Figure G.15	Engine-Axis-One Data, $M = 0.50$	208
Figure H.1	Engine-Axis-Two Data, $M = 0.43$	210
Figure H.2	Engine-Axis-Two Data, $M = 0.48$	211
Figure H.3	Engine-Axis-Two Data, $M = 0.54$	212
Figure H.4	Engine-Axis-Two Data, $M = 0.585$	213
Figure H.5	Engine-Axis-One Data, $M = 0.43$	214
Figure H.6	Engine-Axis-One Data, $M = 0.48$	215
Figure H.7	Engine-Axis-One Data, $M = 0.54$	216
Figure H.8	Engine-Axis-One Data, $M = 0.585$	217
Figure I.1	Duct Coordinates	219
Figure J.1	Experimental Equipment Schematic	228
Figure J.2	Ensemble Size Comparison	233
Figure J.3	Ensemble and 2 Sine Wave Representation with Associated Error	233

List of Symbols

a	radius of cylinder
A	source in complex plane
B	sink in complex plane
c	stator chord length
C	coefficient
d	distance to source
D	diameter of cylinder
E	energy, bulk modulus of elasticity
f	frequency
F	stator force
h	height
k	reduced frequency, Boltzmann constant
L	length of tubing duct
M	Mach number
P	pressure
r	radial distance
S	stator spacing, Strouhal number
T	temperature
u	axial velocity component
v	tangential velocity component
V	velocity
x	distance along chord
z	cascade plane
α	cascade flow angle
β	stagger angle
Γ	circulation
γ	ratio of specific heats
ζ	conformal transformation plane, damping ratio
θ	angle in cylindrical coordinates
π	3.1415926...
ρ	air density
σ	cascade solidity, c/S
ϕ	angular chord position
φ	flow turning angle

ψ conformal mapping transformation parameter
 ω circular frequency

Subscripts

avg average
i throat
k Kutta condition
L local
m mean value
p pressure
s static value
x axial direction
y tangential direction
o incompressible form, stagnation quantity
1 entrance condition
2 exit condition
 ∞ freestream value

ACKNOWLEDGEMENTS

I would like to express my thanks to my advisor, Prof. Eric J. Jumper, who helped me to conduct research on a fundamental level. His assistance made a difficult problem easier to tackle and gave me new insight in research methods. Additionally, I greatly appreciate the tuition scholarship by Profs. Thomas Mueller and Eric Jumper, for otherwise the University of Notre Dame was beyond the Air Force Academy funding limit.

Thanks is also given to Profs. Hafiz Atassi, Stephen Batill, and Patrick Dunn for their time and helpful suggestions during my research.

My appreciation is also given to Joel Preston, Mike Swadener, and Marilyn Walker for their help on all too numerous occasions.

Thanks also to my fellow graduate students, the gang at the Hessay Monastery, for the fun times during lunch solving all the world's problems. Special thanks to Rich Sellar and Dr. Haun Chu for their help and experience with simulated annealing and flow visualization techniques, respectively.

I appreciate the nearly sole use of the Notre Dame transonic facilities, a superb collection of tunnels for a graduate institution,

allowing the use of production stator vanes in testing.

Thanks also to the numerous visitors including Philip Gliebe, Stewart Glegg, and Pascal Ferrand among others. Their keen insight, experience and discussion assisted this research greatly. It should be noted the such professional interaction with researchers in the field from all over the world could only take place at Notre Dame through the association with Hafiz Atassi, and other faculty in the department.

A kind thank you to my parents for partially offsetting the \$5,000.00 in lab research equipment purchases not covered by research funding.

I would like to thank my former turbomachinery instructors, Profs. Jack Mattingly, Bill Heiser, Hans von Ohain, and Mitsuru Kurosaka for sparking and expanding my interest in jet engines.

Finally, I would like to recognize the Aero-Propulsion and Power Directorate for provided the funding to conduct this F-109 research project. Without their help, this project would not have been possible.

CHAPTER ONE

NATURE OF PROBLEM

With over fifty years of jet engine development, modern engines still have problems with unanticipated and misunderstood fatigue failures. In fact, the established stationary Brayton and Rankine powerplants lose more than \$235 million annually due to vibration related failures and shut-downs (O'Connor, 1993). In aircraft applications, failures can obviously go beyond financial loss, to human loss. While this chapter gives an overview of the motivation to conduct unsteady cascade research, a much more extensive review of the development of unsteady aerodynamic theories and experiments and their application in turbomachinery design is included in Appendix A.

Although significant airfoil vibration can occur at the blade's natural frequencies, at other frequencies the material stress endurance limit can be exceeded due to the high number of operating cycles and lead to failure. Higher stage loadings, increased operating temperatures, unconventional geometries, and advanced materials

all require additional emphasis in vibration and aeroelastic analysis to maintain the current level of operational capability. In aircraft applications, where flight safety is of great importance, frequent inspections and performance/structural compromises are required to insure acceptable mean-time between failures. Unfortunately the standard practice of trying to avoid vibrational and fatigue problems has not been sufficient to eliminate turbomachinery problems. In fact new aerodynamic design approaches and advanced materials have reached beyond the known domain of experience. For instance, the Navy Advanced Fan Compressor Technology (NAFCOT) 1st stage fan, shown in Figure 1.1 and the advanced “splittered” rotor, shown

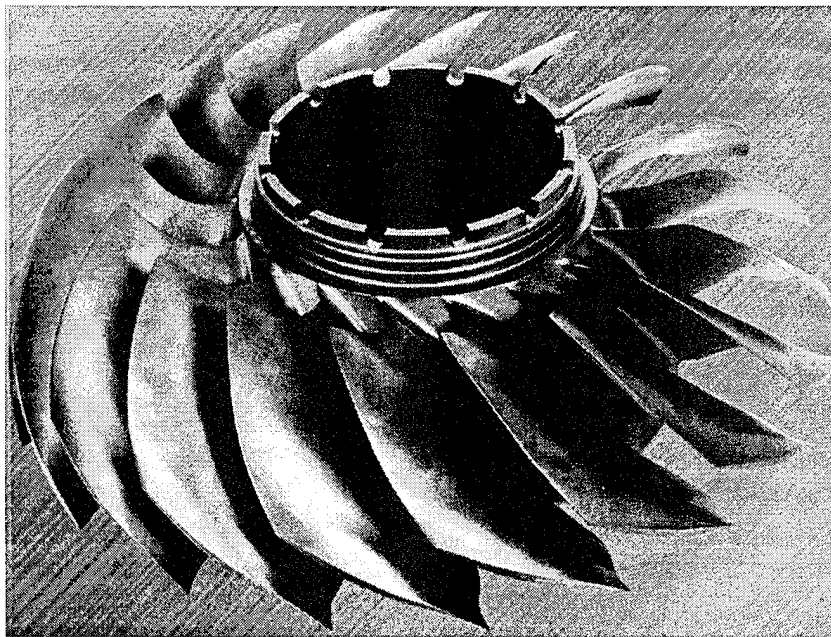


Figure 1.1 Navy Advanced Fan Compressor Technology 1st Stage Fan

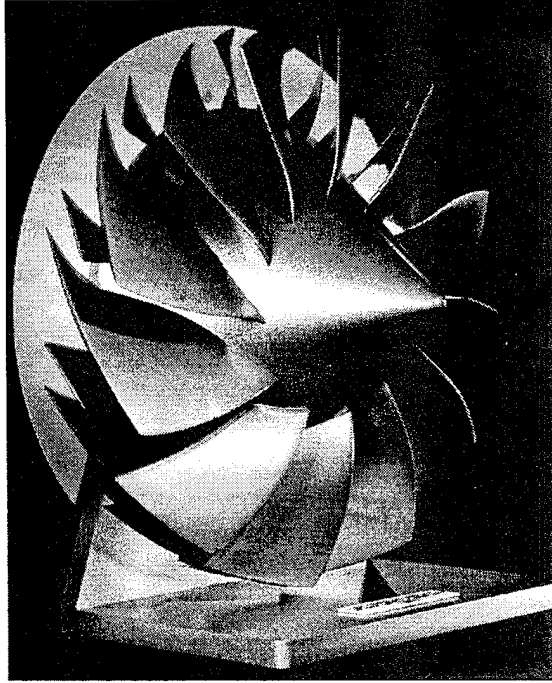


Figure 1.2 Splittered Rotor

in Figure 1.2 pass beyond the normal concepts of a compressor or fan (Lykins and Watson, 1993). The NAFCOT has an unusual leading-edge sweep from the most axially-forward position of approximately 30 percent hub-to-tip radial position to both the root and tip. This profile can be seen in the left portion of Figure 1.1. The splitted rotor has intermediate blades of shorter chord and different profile than the main rotor blades as shown in the top portion of Figure 1.2.

Unfortunately, even the aerodynamic forcing of the current simplified geometries is still not well understood. This is exemplified by the grounding of the Air Force B-1B bomber fleet in 1991 due to fan failures (Aviation Week, October 7, 1991) and the

recent requirement for additional inspections of General Electric CF6 engines following an Egypt Air Airbus rotor fatigue failure (Associated Press, 25 August 1995). Many other vibrational issues are discovered during prototype testing but are seldom referenced in the public domain. As a result, an increased understanding of the actual forcing functions and of the associated airfoil gust response is required to maintain flight safety and increase the mean time between engine shutdown.

Computational models attempt to predict the aerodynamic interactions with rigid blades and also the combined interaction through flexible finite-element blade models; however, most of the aerodynamic code validation is done using classical analytical models or low speed experiments. The lack of compressible experimental engine or cascade data to validate aerodynamic codes has limited their usefulness as design tools. Given the continued fatigue difficulties encountered with conventional compressors and turbines, further study into the nature of the aerodynamic forcing is required to insure improvement in future advanced designs. This research effort, using conventional stator airfoils, provides new data and Mach number trends in a compressible unsteady cascade.

CHAPTER TWO

OBJECTIVES AND ORGANIZATION

2.1 Hardware Objectives.

The work reported on in this dissertation is a study of unsteady pressure response on the turning vanes of a near-transonic, linear cascade, excited (forced) by unsteady flow generators located both upstream (forward) and downstream (aft) of the vane row. However, it is not possible to justify the choice of the turning-vane geometry without understanding the connection between this work and follow-on work planned for the engine test facility at the United States Air Force Academy in Colorado. It is this connection that dictated the first objective of the present work, that being to instrument production-hardware stator vanes from the single fan stage of the Garrett F109 turbofan engine. One of these engines is installed in Test Cell #3 at the Academy and is presently instrumented only with time-averaged-type measurement devices applicable to thermodynamic cycle analysis. Because of existing

instrumentation on the engine, and the relative ease of removal and reinsertion of the fan-stage stator vanes, this engine offered a unique facility for collecting actual unsteady pressure response on the vanes of an operating turbofan engine. A description of the F109 engine is contained in Appendix B.

In order to collect such data, the vanes would have to be instrumented with pressure transducers capable of faithfully measuring time-resolved unsteady pressure at up to, at least, two times the blade-passing frequency, approximately 17,000 Hz. Further, because these instrumented vanes would be exposed to the environment of the operating engine, some means of testing their structural integrity and instrumentation capabilities had to be devised. This led to the concept of constructing a linear, unsteady cascade into which the individual instrumented vanes could be placed and exposed to nearly the same flow conditions and forcing frequencies that they would be exposed to in the running F109 engine.

The F109 engine-connection, therefore, placed severe hardware and flow-environment constraints on this dissertation research. With this as a background, the hardware objectives fell

into two main categories: the instrumentation of the vanes at applicable vane locations that could facilitate the collection of meaningful unsteady pressure data for both linear cascade studies at the University of Notre Dame and follow-on F109 engine tests at the Air Force Academy; and the design of a linear cascade and concomitant unsteady-flow excitation system that could use instrumented production hardware, F109 stator vanes, as the turning vanes of the cascade.

2.1.1 Vane Instrumentation.

Initial concepts for pressure instrumenting the vanes located the unsteady pressure transducers remote from the vane-surface pressure taps a distance sufficient to keep them outside of the cascade (and ultimately the F109 engine). Work by Batill and Nebres indicated that it might be possible to derive a transfer function for a duct between the vane surface and the transducer surface so that accurate, time-resolved unsteady surface pressures could be recovered from the remotely-mounted transducer data (Batill and Nebres, 1991). Analysis in Appendix C, however, showed that for the frequencies of interest to this research, the transducers had to be

essentially surface mounted (i.e., the duct dimensions that were acceptable allowed only sufficient volume to require the transducer heads to form one surface of a small cavity directly underneath the tap (hole) in the surface of the vane at the locations where the pressure was to be sensed). As will be described in Chapter 4, the requirement to surface mount the transducers and also the presence of F-109 fan vibration dampers placed constraints on the locations on the vanes where they could be instrumented. Among other things, size constraints dictated that, at most, only two pressure taps could be accommodated on any single blade. This meant that a method of guaranteeing uniformity of the excitation scheme and ability to precisely trigger the data collection on any single blade was essential in order to build up a time-resolved representation of the overall pressure response of a "representative blade" from data collected on a set of individual blades for each passage location.

2.1.2 Cascade.

Flow Excitation. As will be discussed in the *Research Objectives*, a method of providing the unsteady flow excitation had to be devised that would provide a trigger for conditional (phase-

locked) collection of vane pressure data, and provide control over the location and frequencies of the excitation.

Methods of providing such forcing in linear cascades evolved toward attempting to simulate the translation of vortical wakes to simulate rotor blades moving past the stationary stator vanes (Gostelow, 1984). Implementation of this concept has led to, among other schemes, the development of conveyor-type, linked-rod treads that are either rapidly translated through the cascade in front of the turning vanes for a period of time determined by the translation rate and the length of the tread, or folded around and outside of the cascade and returned into the cascade to provide a continuous source of flow excitation (Heiser, 1992). Such schemes, however, because of their complexity, have only been applied to low-speed, very-low Mach number cascades. Further, these complicated schemes greatly limit the flexibility of changing the axial location of the forcing. Since the present study required nearly transonic flow speeds and flexibility in locating the excitation, schemes initially contemplated that provided flow-normal translating disturbances were discarded in favor of a less complicated scheme.

Although for a low-Mach number study, Commerford and Carta

devised an unsteady excitation scheme for a single-airfoil study that made use of von Karman shedding off a circular cylinder aligned with the airfoil span and placed upstream and above the airfoil (Commerford and Carta, 1974). They also made use of a pressure transducer placed on the excitation cylinder to serve as a trigger for conditionally sampling their pressure data on the airfoil. Such a scheme carried a number of attractive features. First, a row of such cylinders could be easily relocated both in terms of vane-row passage location and streamwise distance up or downstream from the vane row. Secondly, because the von Karman shedding has associated with it a near-constant Strouhal number over the range of Reynolds numbers used in the study, the frequency of the excitation at a specific velocity could be achieved by selecting the diameter of the cylinders. Selecting a flow-speed frequency combination that matched that in the F109 engine for a specific operating point, guaranteed that this same reduced frequency would be fixed over the entire range of cascade flow conditions used in the study. Because the fan rotor in the F109 links the flow velocity in the engine directly with the rotor RPM, and thus the blade passage frequency in front of the stator vanes, the engine too retains a near-

constant reduced frequency over its operating range.

Adaptation of the Commerford and Carta excitation scheme, however, carried some risk. First, like the Commerford and Carta experiment, there was some uncertainty of the uniformity of the excitation because of the Reynolds numbers required by the study. As described in Chapter 4, this problem, although very real, was able to be overcome by careful attention to the triggering scheme devised. Secondly, it was not clear whether it would be possible, or how difficult it would be, to synchronize the shedding from the five excited cylinders used, so that exact periodicity of the unsteady flow from one vane passage to the next be maintained. The anticipated problem led to a number of elaborate conceptual schemes for guaranteeing synchronization; as it turned out, however, the first flow tests of the cascade with excitation cylinders installed demonstrated that this anticipated problem was, in fact, not an issue. The cylinders remained perfectly synchronized over the entire range of testing up to transonic flow around the cylinders ($M = 0.585$ for forward forcing and $M = 0.50$ for rearward forcing) when periodic shedding signal ceased on all cylinders. This fortuitous development is discussed further in Chapter 4.

Flow Conditions. Although not essential to the present study, again because of the F109-engine connection, similarity of the flow conditions in the cascade to those present in the actual engine in place at the Air Force Academy was desirable. Here serendipitous circumstances made this desirable attribute to the experiment easy to provide. The F109 engine at the Academy operates at a pressure altitude of approximately 7,000 ft, the ground level altitude at the Academy. After the inlet air passes through the rotor, it is compressed before entering the stator vanes. On the other hand (as will be discussed in Chapter 4), the flow through the cascade was generated by making the cascade an integral part of one of the in-draft transonic wind tunnels in the Hessert Center at Notre Dame. Being an in-draft tunnel, this meant that the in-flowing air, initially at a pressure altitude of approximately 700 ft, was increased (i.e., pressure reduced) by its acceleration prior to entering the cascade. The compression of the flow into the F109 stator and expansion of the flow into the cascade compensated these initially disparate-density flows in such a way as to nearly match the conditions entering the vanes in both devices. In summary then, although the unsteady excitation of the cascade was from stationary sources, the

cascade nearly matched the F109 engine conditions in reduced frequency, Reynolds number, Mach number and mass flow per unit cross-sectional area, as shown in Table 2.1.

Table 2.1 F109 Turbofan Engine and Unsteady Cascade Parameters

Parameter	F109 Stator Inlet	Cascade Inlet
Reduced Frequency	5.6	5.0
Reynolds Number	145,000 - 450,000	145,000 - 360,000
Mach Number	0.3 - 0.6	0.2 - 0.585
Mass Flow per Area	16 - 51 lb _m /secft ²	16 - 40.5 lb _m /secft ²
Turning Angle	39.8° - 45.2°	42.5°

2.2 Research Objectives.

With reference to the brief Introduction in Chapter 1, it is clear that unsteady forcing in turbomachines is more complex than has been assumed by the "conventional wisdom." This dissertation research was directed toward gaining a better understanding of some aspects of the nature of unsteady forcing in turbomachines in general. In particular, a great deal of attention was paid to trying to understand the character of the unsteady pressure response on the vanes in terms of the inferred character of the excitation source. In

a sense, this part of the work tantamounted to studying the "inverse problem," which turned out to be more complex than had been initially anticipated. As will be discussed in the final chapter of this dissertation, this effort to infer the excitation source has, indeed, offered new insight into the nature of unsteady forcing in a cascade and offers new insight on interpreting data from rotating machinery. Beyond this, this research offers perhaps for the first time, experimental data on downstream forcing of a vane row. Up until now, "conventional wisdom" has assumed that downstream forcing is negligible compared to upstream excitation that subsequently convects an unsteady vortical wake through the vane row. An extensive literature search showed only one other experimental study that considered downstream forcing, and this was not only at very-low Mach number, but also in conjunction with upstream forcing (Schmidt and Okiishi, 1977). This previous study drew essentially no conclusions regarding the importance of such downstream forcing, since the upstream and downstream blade count was identical. As will be discussed in Chapter 6 and Chapter 9, such downstream forcing is, in fact, on the same order of importance as upstream forcing. Further, as confirmed by Glegg (1995),

understanding the downstream forcing problem is a crucial first step to beginning to study the stage-to-stage interaction problem.

Finally, an attempt was made to experimentally address the issue of *acoustic blockage*, raised by Atassi, Fang, and Patrick (1993) and Atassi, Fang, and Ferrand (1994).

With these general "understanding objectives" in mind, the specific procedural objectives for this research were:

1. Characterize the flow quality and conditions present in the cascade over the range of Mach numbers studied both without unsteady forcing and with unsteady forcing from upstream and downstream.

2. Collect time-resolved, conditionally-sampled unsteady pressure data on each of 16 instrumented vanes over a range of Mach numbers from approximately 0.4 up to the highest inlet Mach number that allowed von Karman shedding off the excitation cylinders, for both forward and aft forcing of the cascade.

3. Assemble a "representative blade," time resolved pressure response for each experimental condition.

4. Reduce the time-resolved composite "representative blade" data into its basis frequencies and amplitudes and attempt to infer

the character of the excitation source from the character of the pressure response for selected experimental conditions.

5. Examine the data for evidence of the *acoustic blockage* phenomenon.

2.3 Organization Of This Dissertation.

With these objectives in mind, it seems appropriate to briefly describe the organization of this Dissertation to help the reader find those sections which address each of the objectives mentioned in this chapter. Chapter 3 is a very brief chapter that is meant to simply acquaint the reader with certain cascade nomenclature that may appear routinely throughout the remainder of the Dissertation. Chapter 4 describes the facilities, equipment and procedures used to collect the data presented, analyzed, and discussed in the remaining chapters. Along with these descriptions, a number of issues associated with the hardware objectives discussed earlier in this chapter are addressed. Chapter 5 describes the steady and unsteady time-averaged flow quality and environment within the cascade. Of some importance is the presentation of the method developed for inferring the flow conditions within the cascade when upstream

forcing is used. Chapter 6 presents the results, reduction and interpretation of the rearward (downstream) forcing experiments. Chapter 7 addresses the presentation, analysis and interpretation of the forward (upstream) forcing of the cascade. Noticeably absent from Chapters 6 and 7 is interpretation of these data as evidence, or lack thereof, of the *acoustic blockage*. Since some explanation of the phenomenon is required in order to infer an acoustic-blockage interpretation, Chapter 8 is devoted entirely to this issue. Chapter 9 takes up the task of comparing forward and rearward forcing, drawing inferences from the body of work as a whole, discussing some obvious ramifications and suggesting further future work. Finally a section at the end of Chapter 9 lists the contributions of this dissertation research.

CHAPTER THREE

CASCADE NOMENCLATURE

In this section the geometry of a cascade row will be discussed including the fundamental differences between a single airfoil in a flow and an airfoil imbedded in a row of other blades. Cascade testing is frequently used in jet engine development to quantify the dominant flow physics and structural issues of rotating and stationary engine hardware. In turbomachinery applications, a linear cascade represents an unwrapping of a rotor or stator row into a row of airfoils. Typically the blade/vane row is made of blades/vanes of constant profile which is the same streamwise profile in the annular rotor or stator at one representative radial location; for reasons discussed in the last chapter, however, the vanes of the cascade in the present study vary slightly in the streamwise profile from tip to hub.

To provide some background terminology, the close proximity of airfoils in a cascade row requires the definition of additional

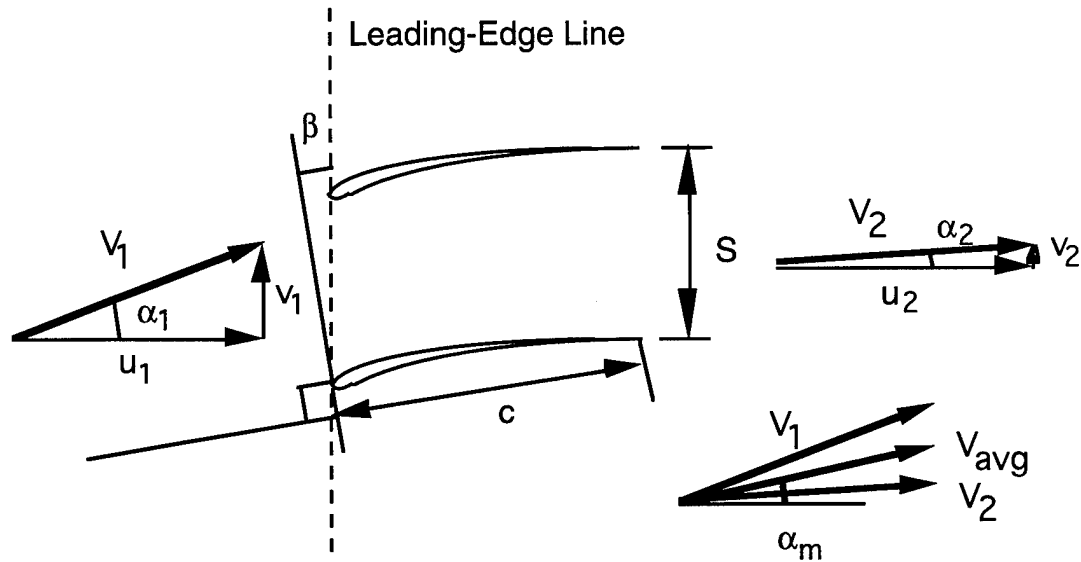


Figure 3.1 Cascade Geometry

terms beyond the single airfoil terminology. The airfoil chord has the usual definition of the distance from the leading edge to the trailing edge of an airfoil. As shown in Figure 3.1, spacing, S , is the distance from leading edge to leading edge (and also trailing edge to trailing edge) of consecutive airfoils on the row. Solidity, σ , is the ratio of chord to spacing. The leading-edge line is the line tangent to the leading edges of the cascade row. Stagger angle, β , is the angle between the leading-edge line and the perpendicular to the chord line. At high stagger angles or low solidity, the interaction of the blade pressure fields is reduced. The cascade flow angles, α_1 and α_2 , are the angles between the axial direction (perpendicular to the leading edge line) and the cascade-entrance-flow direction and exit-

flow direction, respectively. The difference between these two angles is the flow turning angle, ϕ . The turning angle represents a fundamental difference with the aerodynamics of a single-airfoil which can only turn the flow locally. In cascade flowfields, the vector average of the inlet and exit flow velocities is frequently labelled V_{avg} or V_{∞} . As shown in Appendix D, using V_{avg} helps to relate cascade aerodynamics to single-airfoil aerodynamics. The angle between V_{avg} and the perpendicular to the leading-edge line is termed the mean flow angle, α_m . The angle between the chord line and V_{avg} is the cascade angle of attack, α . A final angle to be mentioned is the deviation angle, δ , which is the difference between an extension of the trailing-edge camber line and the exit flow vector. It represents the ability of the cascade to turn the flow through the desired angle, approximately parallel to the trailing-edge-camber line. The relevant cascade parameters for this project will be discussed in Chapter 4. A simplified cascade analysis including surface pressure distributions and surface velocity ratios is included in Appendix D. More advanced solutions require multiple conformal maps or the use of a computer mean-flow solver.

CHAPTER FOUR

FACILITIES, EQUIPMENT AND PROCEDURES

The cascade used in this research was specifically designed to operate in the 4" x 4" cross-section leg of the number 2 Transonic In-Draft wind tunnel located in the Hessert Center for Aerospace Research at the University of Notre Dame. The turning vanes in the cascade are actual production vanes for the F109 turbofan engine. In this chapter, the various components making up the cascade will be described. Also included in this chapter is a description of the instrumentation and procedures for collecting the data. Along with a description of the various components of the cascade, where applicable, some of the background directly related to the component will be addressed.

4.1 Hessert Center Transonic In-Draft Facilities.

The transonic in-draft tunnels, located in the Hessert Center for Aerospace Research, are powered by three 125 horsepower Allis-Chalmers rotary vacuum pumps. In the largest tunnel, the square

cross section inlet has a contraction ratio of 150:1. A schematic of the cascade tunnel is shown in Figure 4.1. There are eleven turbulence management screens located in the largest portion of the inlet to reduce ambient laboratory disturbances. This inlet, with a matched cubic profile, provides a smooth, parallel entrance flow into the test section which has a cross sectional area of 16 square inches. The maximum flow rate for this tunnel is approximately 5 pounds per second compared to 61 pounds per second for the actual F109 engine; however, given the cascade's reduced cross-sectional area, this represents approximately the same mass flow per unit area.

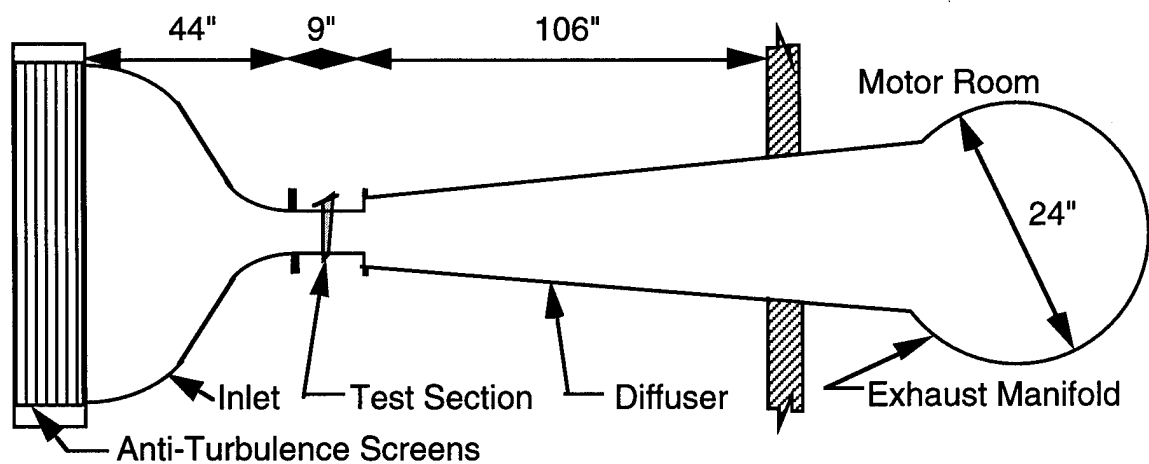


Figure 4.1 Side View of Cascade Tunnel

4.2 Cascade Test Section.

The cascade test section was designed to match with the existing facility flow areas and to incorporate F109 stators as turning vanes. A top view of the cascade test section is shown in Figure 4.2. The section was constructed from 1/4 inch and 3/8 inch aluminum plate. The turning angle of the cascade, at 42.5° , represents an average value of the engine design 39.8° and 45.2° turning of the stator tip and hub, respectively. The cascade inlet flow angle is 21.9° , while the exit flow angle is 20.6° . The stator vanes have a maximum camber and maximum thickness of 12 and 8 percent of the chord, respectively. The profile coordinates are listed in Appendix E. In the F109 engine, the stators are swept aft from the hub to the tip. The cascade height of 4 inches (required in order to mate the cascade section with the tunnel inlet and diffuser sections) prevented similar, swept positioning; the stators were instead, positioned vertically to form a nominal two-dimensional cascade. In order to alleviate flow separation concerns in the cascade, the actual engine diffusion capabilities were compromised through a relaxed cascade stagger of -9.1 degrees. Due again to tunnel geometry constraints, the cascade had constant inlet and exit

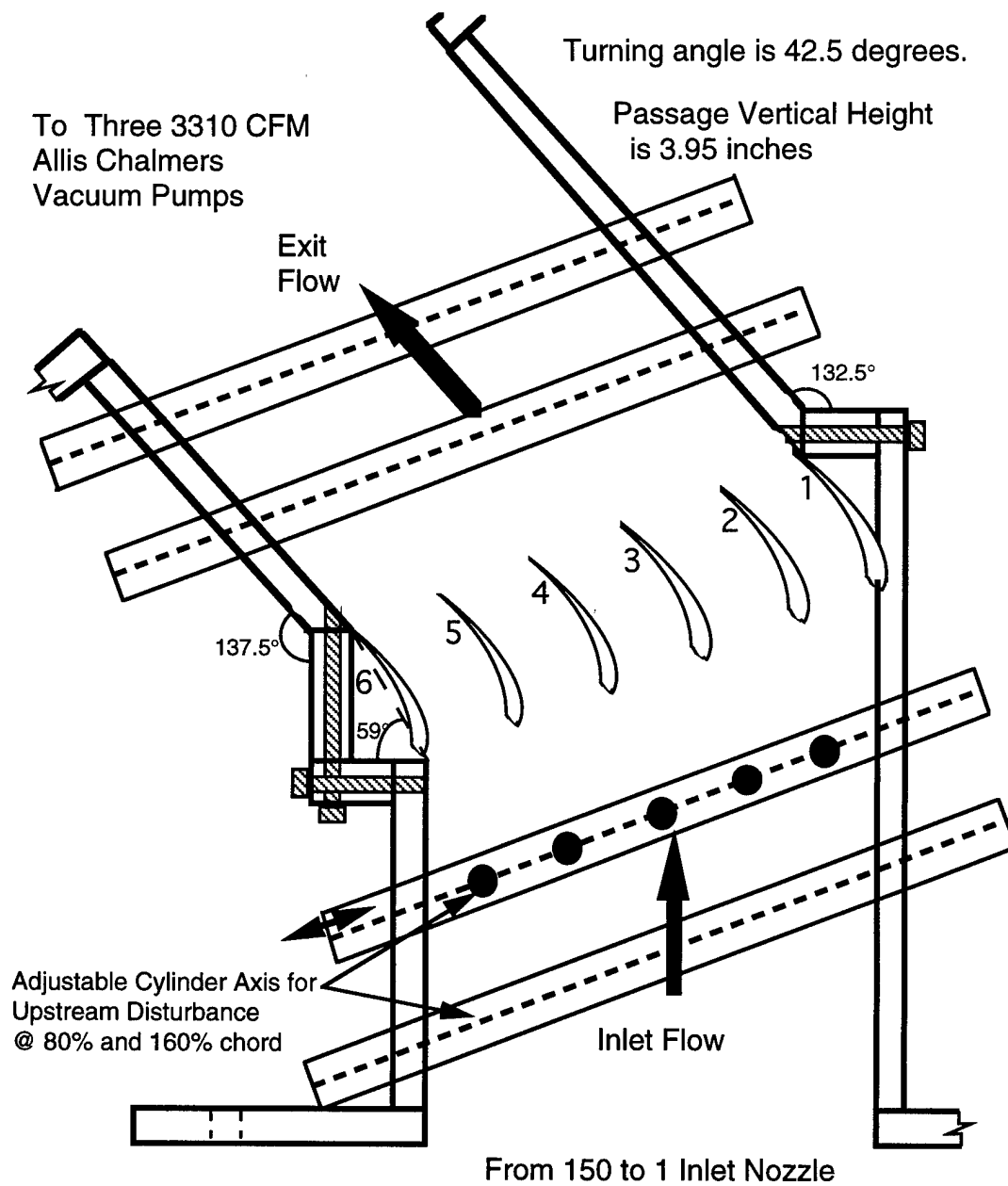


Figure 4.2 Top View of Cascade Test Section

cross-sectional areas. In order to roughly match the nominal (representative) vane spacing in the F109 engine, only 4 midstream vanes (5 resultant flow passages) were present in the cascade; two additional vanes were used to form the wall boundaries of the vane row (see Fig. 4.2). Although minimum, five passages meets the minimum condition for proper periodicity through the central passage in a subsonic cascade (Oates, 1989). The cascade solidity, chord length to stator vane spacing ratio, is 0.66 based on the chord length of the instrumented region.

The divergent exhaust region of the wind tunnel is connected to a common manifold for the two other in-draft tunnels. Since the manifold is connected to the three constant speed vacuum pumps, throttling of the cascade is controlled by the number of operating vacuum pumps and by the valves in the exhaust of the two associated smaller tunnels. Each Allis Chalmer pump has a design flow rate of 3310 cubic feet per minute. The cascade inlet velocity is determined using a pitot tube and a static port located forward of the vane row and connected to a mercury manometer bank. The flow rates of the other two tunnels are then modified with the valves to meet the required velocity in the cascade test section.

4.2.1 Unsteady Flow Exciters.

The unsteady forcing in the cascade was established through von Karman vortex shedding from a row of either upstream or downstream cylinders, positioned as shown in Figure 4.2, similar to the single airfoil approach of Commerford and Carta (1974), referred to earlier (Chapter 2). Since the choice of cylinder diameter provided the variation in shedding frequency and reduced frequency due to the Strouhal number, the cylinder row was not actively controlled by an external shaker for the purpose of selecting a forcing frequency. The Strouhal number, S , is defined as:

$$S = \frac{f D}{V} \quad (4.1)$$

where f is the number of cycles per second, D is the cylinder diameter and V is the local velocity. The Reynolds number for the present work based on cylinder diameter ranged from 20,000 to 60,000. In this Reynolds number range, the Strouhal number remains essentially constant at approximately 0.20 (Schlichting, 1955).

Reduced frequency, k , is defined as:

$$k = \frac{\omega c}{2V} \quad (4.2)$$

where ω is the forcing frequency in radians per second, so that $\omega = 2\pi f$. Thus, it is clear that fixing a single excitation-cylinder diameter, essentially guarantees that the same reduced frequency is used over the entire testing range. All unsteady results reported here are from excitation cylinders of 3/16 inch diameter which produced a nearly constant reduced frequency for the vane row of approximately 5 over the Reynold's number range.

4.2.2 Trigger Signal and Conditional Sampling Technique

The unsteady pressure measurements for all unsteady vane-pressure measurements were triggered by a pressure transducer embedded in one of the excitation cylinders with the sensing port aligned perpendicular to the flow direction; this signal was used to phase lock the sampling (Commerford and Carta, 1974). While there is a predominant shedding frequency at these Reynolds numbers, the actual magnitude or amplitude of circulation is considered "irregular" (Fung, 1993); however, as with Commerford and Carta, sufficient periodicity was present to provide ensemble results. These ensemble results were enhanced to ensure that the ensemble was representative of any single data string by conditionally

specifying an acceptable trigger pulse. All unsteady data presented was acquired using this enhanced conditional sampling based on the trigger achieving a specified minimum amplitude (near the maximum experienced at that flow condition) in the cycle following the trigger's initiation on a positive crossing of the zero voltage range. It should be noted that the data acquisition card allows the trigger initiation to be positioned anywhere within the data record. For all cases, the trigger was used at the mid-point of the sample sets with the maximum trigger amplitude occurring after the mid-point of the data set, a sample acquisition is shown in Figure 4.3.

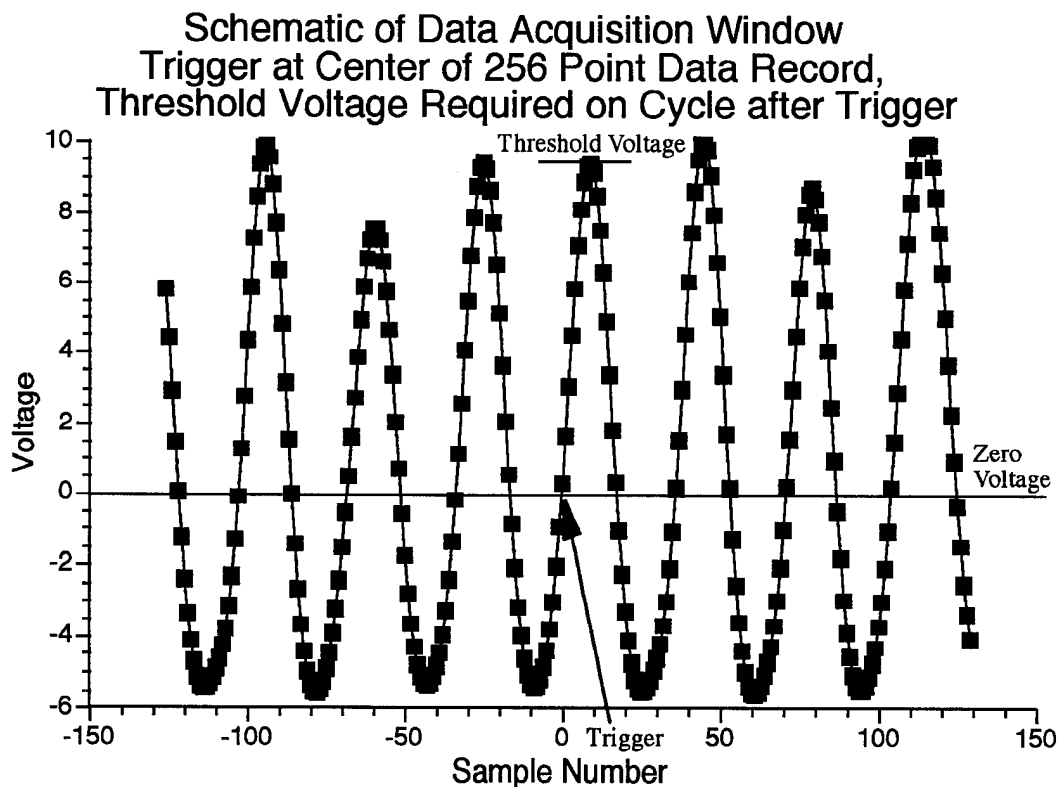


Figure 4.3 Sample Data Acquisition Window

4.2.3 Location of the Excitation-Cylinder Row

As shown in Fig. 4.2, the excitation cylinder row could be positioned 80 or 160 percent of the chord length upstream or downstream of the leading or trailing edge of the vane row, respectively; furthermore, the cylinders could be traversed laterally to produce, in the forward forcing case, wakes that convect across the stators or through various portions of each passage. Preliminary data was taken at various traversed rod positions; however, all data reported here represent the 80 percent chord upstream of the vane row or 80 percent chord downstream of the vane row positioning of the cylinders with each cylinder laterally positioned at mid-passage.

4.2.4 Instrumented Vanes

The stators used in this research are production F109 stators which have been instrumented with Kulite pressure transducers. The stators are constructed from folded 0.012 in stainless steel to form suction and pressure surfaces that are nominally double circular arc profiles, with a cusped trailing edge weld. In the instrumented region of the vanes, the chord is approximately 1.28 inches. The

production stators came filled with a dense rubber-like structural compound. While there is moderate variation in chord length from the stator engine hub to tip chord line, there is no twist along the stator. Since twisted stators would require an annular cascade, the lack of twist in this application allowed linear cascade testing. Based on reports in the literature, approximately 16 chordwise pressure taps at any given radial (span) location (eight on the suction and eight on the pressure surface) were decided upon to properly describe the unsteady pressure environment on a representative vane (Dring et al., Franke and Henderson, Fleeter et al.). Since size constraints prohibit a single stator from being instrumented with sixteen transducers, the triggering information was required to construct the unsteady flowfield around an equivalent, representative, nominal vane.

The Kulite XCS-062 ultraminiature transducers used for signal triggering and stator measurements have a maximum diameter of 0.064 inches and a length of 0.375 inches. The transducers use a fully active four arm wheatstone bridge which is "diffused" onto the silicon diaphragm (Kulite, 1992). The transducers are rated to 5 psi differential pressure with a burst pressure of 15 psi. With a rated

excitation voltage of 15 volts, the full scale output is approximately 150 millivolts. The natural frequency of the transducer is 150 KHz, thus the rated reliable frequency response is approximately 30 KHz (1/5 of the natural frequency). The transducers include a built-in temperature compensation module that has temperature insensitive trimming resistors which provide zero balance.

Since the ultimate use of the instrumented vanes is the determination of unsteady forces in the F109 engine, the instrumentation was prepared along two engine streamwise axes. The instrumented axis, nearest the engine case, was determined by the minimum mounting depth of the Kulite transducers and the associated stainless steel reference pressure line. This axis, referred to as "Engine Axis 1" is radially inward one-half an inch from the stator mounting flange as shown in Figure 4.4. The other instrumented axis, "Engine Axis 2," is halfway between Engine axis 1 and the effective wake region from the mid-span damper of the engine fan. The diameter of the Kulite transducers, the current smallest diameter transducer available in the 5 psi pressure class, exceeded the stator thickness in the area between the mid-span damper wake region and the engine hub so only the tip region was

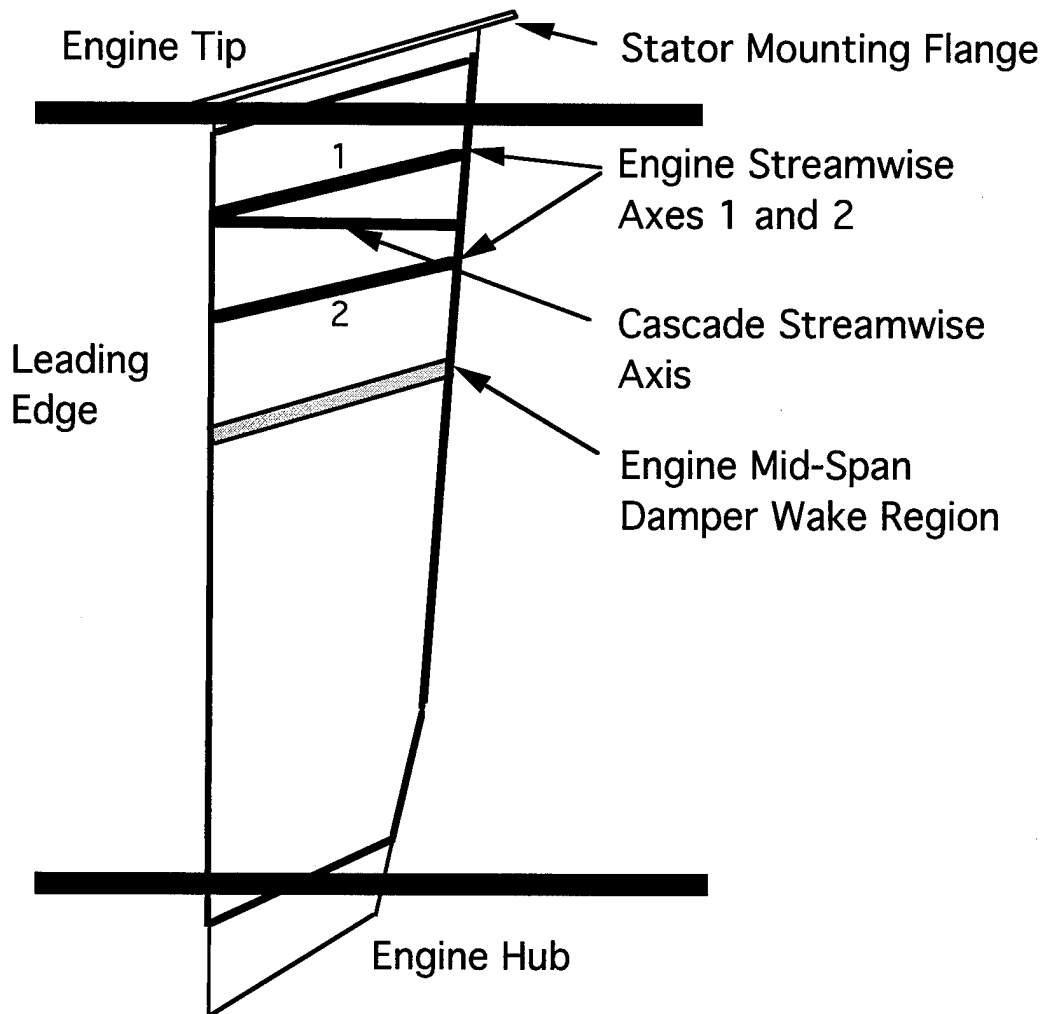


Figure 4.4 Side View of Stator

available for experimental consideration.

In addition to the two engine-related axes, a cascade reference axis was instrumented by casting an epoxy-resin stator for time-averaged measurements using a Scanivalve.

Due to the small leading edge radius and cusped nature of the stator trailing edge, surface pressure measurements were limited to the region between 7 percent and 80 percent of the chord. The

instrumented points on both the stator pressure and suction surfaces are approximately 7, 12, 20, 30, 40, 50, 65 and 80 percent of the stator chord length. The increased instrumentation resolution in the forward half of the stator was based on classical theories of higher unsteadiness near the leading edge. Relative position comparisons to other turbomachinery researchers are provided in Figure 4.5. The present research, using production F109 stators, is seen to limit the chordwise resolution on the leading and trailing edge of the vane due to size constraints of the vanes.

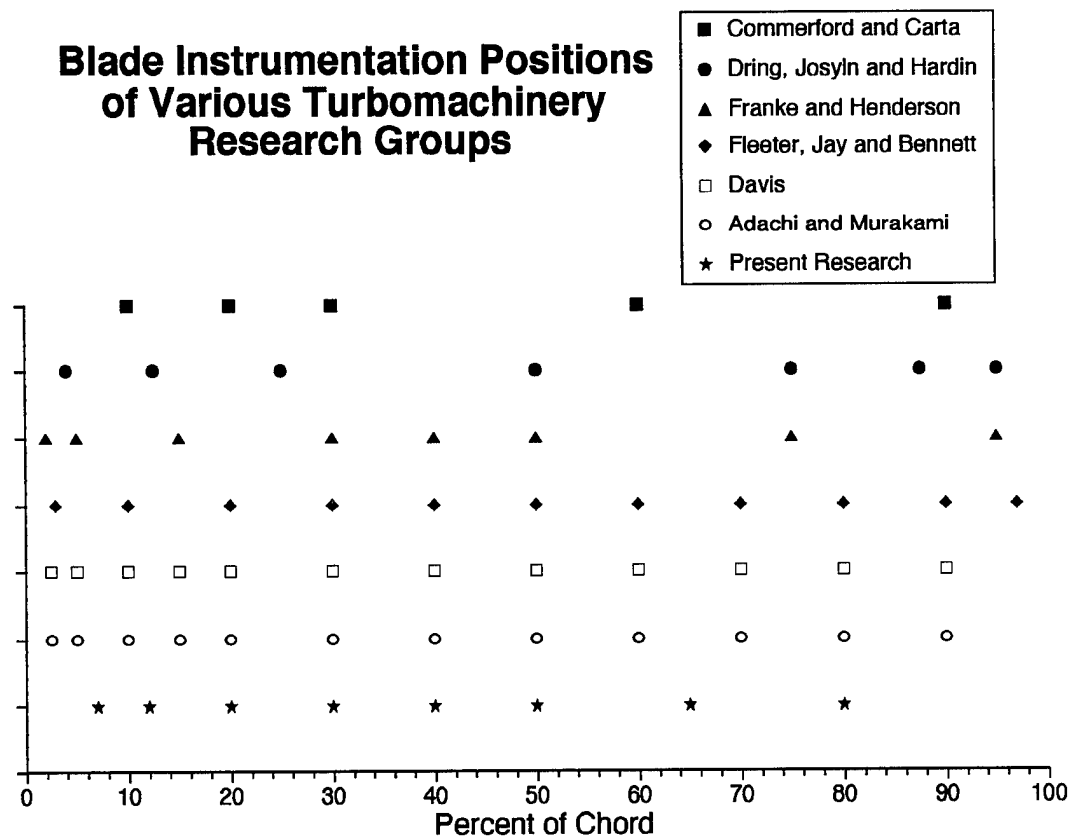


Figure 4.5 Stator Instrumentation Positions

Each stator had only one pressure surface and one suction surface instrumentation point due to the limited stator internal volume and also to prevent interference between neighboring ports on the short chord length. The 16 stators, eight for each radial profile, were instrumented by draining the rubber compound from the vane by heating it with a butane torch. The stators were then filled with a bismuth alloy to maintain proper shape, and milled in the instrumentation areas. The bismuth was then drained from the stator tip to the sensing region, and a stainless steel pressure cavity was constructed to contain the transducer sensing volume and the surface sensing port. Although nearly surface mounted, the Kulite transducer head formed one wall of a tiny cavity open to the vane surface; the internal cavity dimensions were determined using the standard practice set forth by Theory and Design for Mechanical Measurements (Figliola and Beasley, 1991) for assuming unity transfer functions at the high frequencies anticipated in the cascade and engine (see Appendix C). The stainless steel assembly was placed within the stator at the instrumentation point using a metallic epoxy. The Kulite transducer was inserted from the tip of the stator into the pressure cavity and siliconed in place. After the

transducer was siliconed in place, the remainder of the milled hole (near the sensing region and the sensing port) was covered with metallic epoxy. The rest of the stator was then refilled with bismuth alloy using a double boiler heating technique. Final surface sanding and port clearing were required to remove the remaining epoxy residue while comparing the surface contours to a contour template in an effort maintain proper epoxy surface profile.

4.3 Overall Experimental Set Up

A schematic of the overall experimental set up is shown in Figure 4.6. The major components will be discussed in terms of the signal generation path.

The excitation voltage for the Kulites was provided by Measurements Group Model 2310 signal conditioning amplifiers. Each unit operated independently with a single transducer. In addition to the 15 volt excitation, the amplifier had automatic bridge balancing and variable amplification through push button and dial adjustment. The amplifiers have a bandwidth of 100 kHz. The output range for the amplifiers is plus or minus 10 volts.

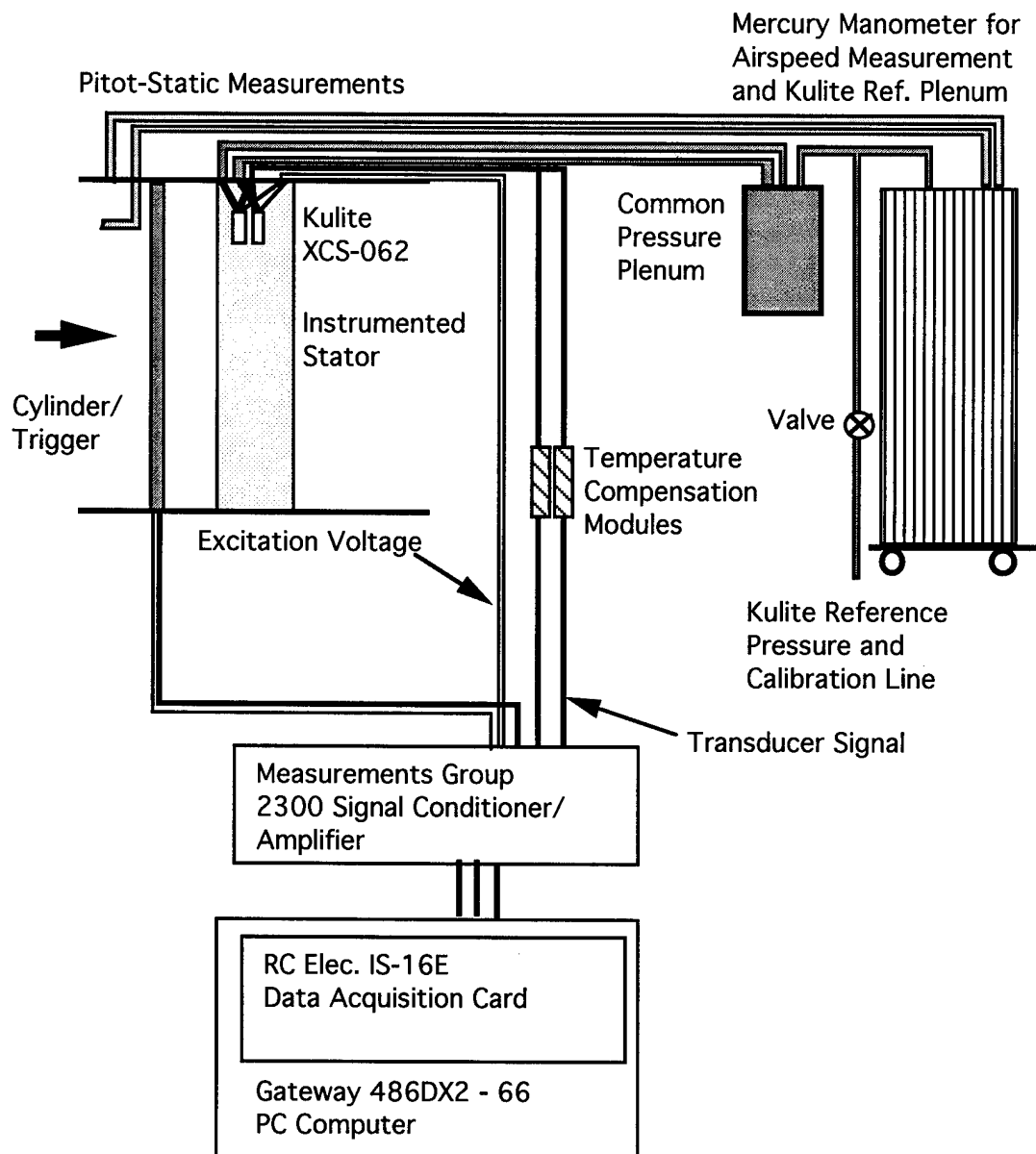


Figure 4.6 Experimental Equipment Schematic

The amplified output signal was routed to the data acquisition system based on an RC Electronics IS-16E/CR card and a Gateway 2000 486/66 personal computer. The maximum single channel acquisition rate is 1,000,000 samples per second. The card can collect additional channels in multiples of 2^n at successively lower sampling rates. It can also simultaneously sample and hold but at an even lower rate due to the increased system overhead. For example, the maximum two channel successive sampling rate is 500 kHz per channel while the two channel simultaneous rate is 350 kHz per channel. Due to its unconventional storage method, the RC Electronics Model IS-16E data acquisition card allows the collection of a programmable amount of data acquired immediately before the triggering signal and up to the buffer limit after the trigger. This capability was used in this experiment. The data acquisition card was operated in MS-DOS using a collection of RC electronic C programming language drivers and the Microsoft version of the C programming language.

4.4 Calibration.

Prior to a calibration, the wind tunnel was run at the operating

condition to set the amplifier gain for the two surface transducers within the bounds of the plus or minus 10 volts of the RC Electronics data acquisition card. During this preliminary run, the trigger and stator vane transducer traces were monitored using the card's chart recorder display mode. After the preliminary run, the instrumented stator vane was then removed from the wind tunnel to eliminate the natural convection interference through the in-draft tunnels during static pressure calibration. The differential transducers were calibrated using the transducer reference line to change the calibration pressure. At each of the 15 calibration points, 512 samples were averaged to determine the transducer voltage. The evacuation or pressurization of the transducer reference line was accomplished using a Mitivac pump and an in-line valve to hold a given pressure. The typical calibration range for the testing was ± 7 inches of mercury when the planned test case freestream Mach number was below 0.45, and ± 10 inches of mercury at higher Mach numbers. Using both positive and negative reference pressure allowed the testing of the transducer diaphragm and reference tubing for leaks prior to each run. As shown in Figure 4.7, the calibration started at the central calibration point, atmospheric

Sample Calibration Curve with order of Calibration
Data Points based on Average of 512 Samples per Station

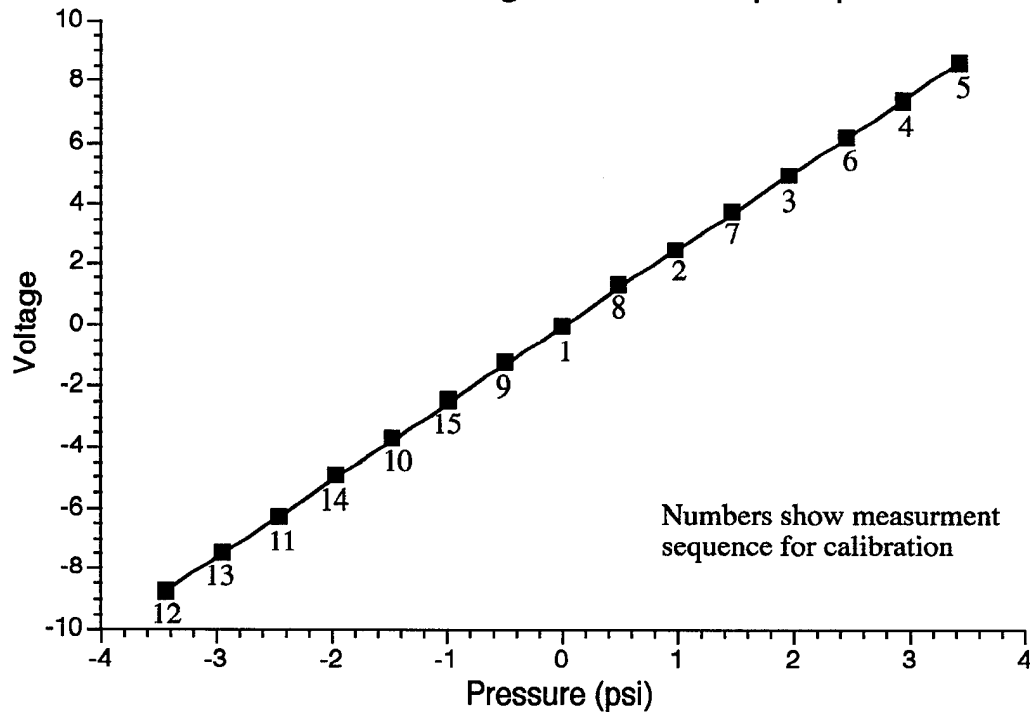


Figure 4.7 Calibration Sequence for Transducers

pressure, and went to the maximum negative reference pressure (positive pressure on the transducer measurement face) but only half of the required negative pressure points were taken. After reaching the maximum negative pressure, the remaining negative reference pressure points were acquired while returning to atmospheric conditions. The calibration continued in a similar manner to the maximum positive reference pressure (negative pressure on the transducer measurement face). The remaining test points were acquired while returning to atmospheric reference

pressure. With this method of calibration, the calibration errors due to hysteresis could be reduced without conducting an even more time consuming random test. The 512 data samples at each of the 15 calibration points were used to determine the calibration parameters using a least squares fit. Every transducer was calibrated in this manner prior to each test.

4.5 Data Acquisition.

Only one instrumented stator vane was installed in the cascade during each test run. The trigger, suction, and pressure surfaces were acquired sequentially at the maximum card sampling rate. Consequently, the single channel sampling rate was 250 KHz, which provided excellent resolution in the time domain data around the trigger initiation point. The typical spectral methods at lower sampling rates and for longer durations were not appropriate to acquire accurate phase information, due to the irregular cylinder shedding amplitude and the resulting periodic phase reversal seen on the trigger signal, Figure 4.8. Each channel was used to collect 400 records of 256 points that met the conditional sampling requirement of a threshold amplitude immediately following the zero crossing of

the AC mode triggering pressure transducer, shown previously in Fig. 4.3. The conditional threshold amplitude, typically 9.5 volts, was positioned near the center of the data acquisition window using the unique data collection capability of the card. By centering the conditional threshold, the phase reversals, seen in long duration data traces, were avoided since phase reversals tended to be associated with lower amplitude trigger peaks (Fig. 4.8). Typically, the 400 records ultimately used required over 5,000 data records to be sampled. The threshold amplitude was set near the maximum seen on

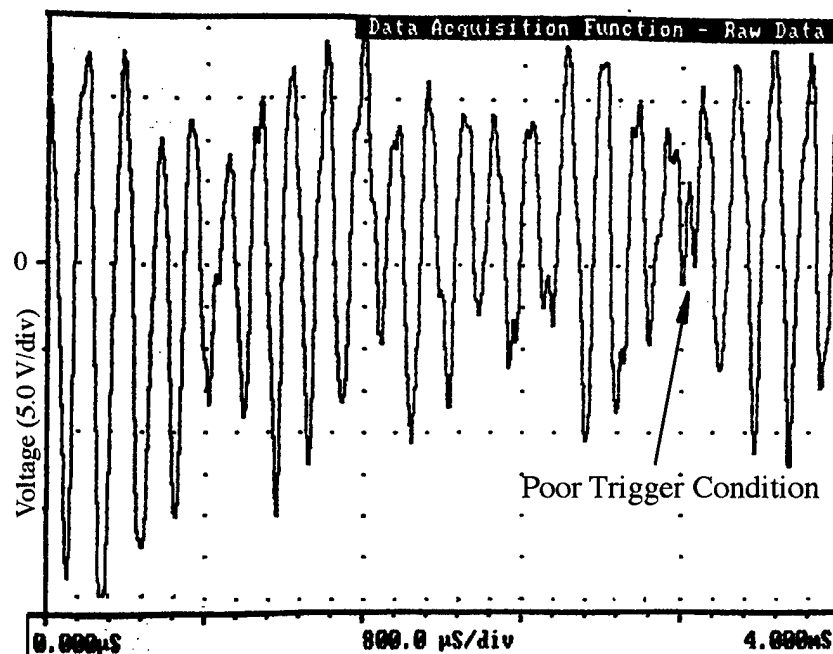


Figure 4.8 Sample Trigger Signal shows Poor Trigger Condition for a Zero Voltage Crossing

the graphic display to avoid occasional phase switching which would

have greatly biased ensembled results.

All transducer data was stored on 270 megabyte Syquest removable drive cartridges for later data reduction. Post processing was required due to the high data acquisition card sampling rate, conditional sampling routines, and the limitations of the DOS based C compiler. The PC memory within DOS could not handle the data acquisition C driver routines, the large array sizes and data reduction tasks simultaneously.

4.6 Data Reduction.

Post processing consisted of determining the mean value of each instrumented chordwise position and ensemble averaging the 400 data records. The mean value provided the average pressure value for determining the effective steady pressure coefficients. Preliminary review of the ensembled records showed what appeared to be a primary forcing frequency and a harmonic. This was confirmed by performing an FFT of the data record (Figure 4.9); however, the large frequency bin resolution of the FFT routine (approximately 1000 Hz) gave only an approximate measure of the

Sample FFT for 7% c on Pressure Surface at Mach 0.43 with rods rearward of vane row

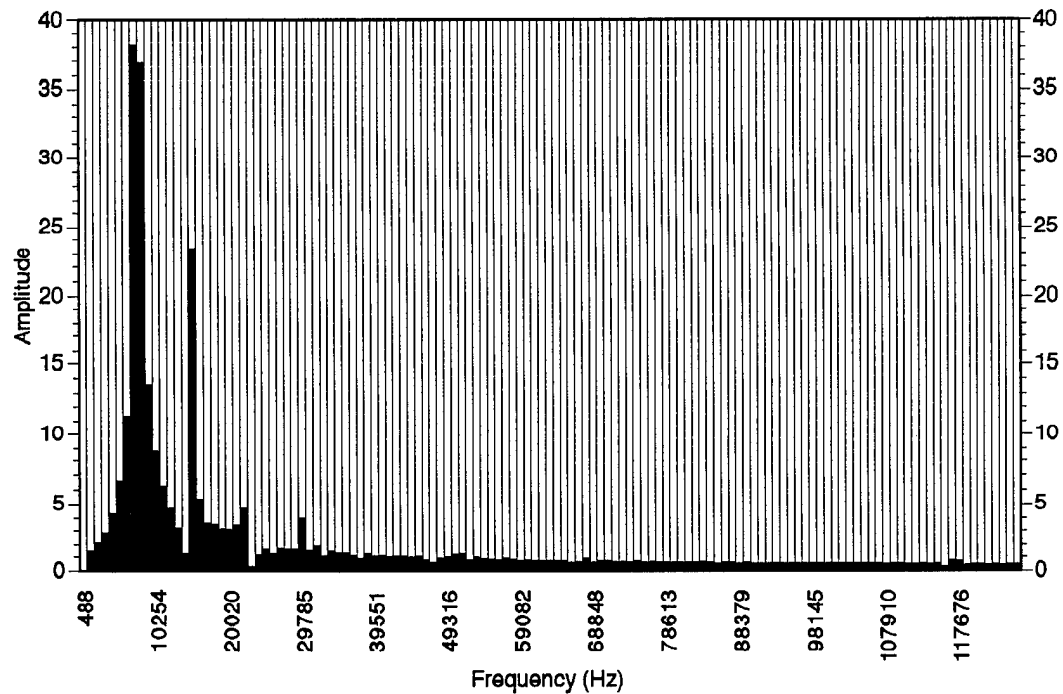


Figure 4.9 Sample FFT for Stator Vane

frequencies involved and essentially no useful phase information relative to the trigger signal.

Each ensemble record was found to be effectively represented by two sine waves, requiring the determination of 6 variables: two amplitudes, two frequencies, and two phases. The FFT routine served as a starting point by approximately identifying the primary frequency but the poor bin resolution, 1000 Hz frequency bandwidth, gave only a crude estimation of the approximate harmonic frequency. Iteration of the values of the 6 variables in an Excel spreadsheet led

to the eventual verification that a two sine wave function could represent the ensemble data records. The rms error between the two sine wave representation and the ensemble record was used as the criteria minimized for a good representation of the signal.

Since manual iteration using a spreadsheet was time consuming, a technique known as “simulated annealing” was incorporated into the data reduction to determine the signal phase, frequency, and amplitude (Press, Teukolsky, et al., 1986). Simulated annealing is an analogy to the slow cooling process that allows the formation of an ordered crystal structure in metals, like a directionally solidified turbine blade with only a few crystals, rather than the disorganized multi-crystalline structure seen from a more rapid cooled or quenched process, like the older equiax-turbine blade (Press, Teukolsky, et al., 1986). The numerical steepest descent techniques, for instance the conjugate gradient method, like quenching, are rapid processes, but may not find the best solution within the domain. A conjugate gradient method was attempted for data reduction; however, the numerous local minima meant that the final solution was overly dependent on the initial variable selections. Instead, the simulated annealing approach randomly

searches the solution domain for the global optimum and in the process attempts to avoid local minima. Using the simulated annealing technique, an objective function was minimized which in this case was the rms error between the ensembled data signal and the two sine wave representation of the signal using the primary frequency and a higher frequency. As part of the method, the Boltzmann probability distribution,

$$\text{Prob}(E) \propto e^{-(E/kT)} \quad (4.3)$$

where “k” is the Boltzmann constant relating temperature and energy and “T” is the temperature, was used to allow the search to jump beyond a local minima. In the simulated annealing model, the Boltzmann constant is included with the “temperature” and the combination decreases in finite steps following a number of solution attempts. Thus, the probability of moving beyond a minima is decreased as the “temperature” continues to fall. In the given case of six variables, a random number of the variables were changed for a given “solution.” When this solution was compared with the previous solution, if the newer solution was better, it became the new standard. If the solution was worse, there was a probability

that this new solution would be accepted as the new standard. This probability to accept a poorer solution decreased with the number of solution attempts (i.e. the decreasing temperature of the Boltzmann analogy) but, by accepting poorer solutions, the method did allow limited "uphill" excursions to avoid local minima as the final solution. Due to the random nature of the search with simulated annealing, each variable search with the program was conducted at least three times to compare final solutions and rms error, to insure that the program had not found a local minima. Although the initial frequency ranges for the program spanned 4000 Hz around the dominant frequencies indicated by the FFT, the simulated annealing approach showed that the ensembled data was in fact composed of the primary forcing frequency and its harmonic.

Further data reduction, where required, will be discussed in the later chapters.

CHAPTER FIVE

STEADY AND TIME-AVERAGED RESULTS

In this section chapter data are presented for the cascade without unsteady-flow generators, along with a single, example case for a time-averaged C_p distribution around a vane with the unsteady-flow generators (rods) upstream of the vanes. These data demonstrate the flow quality of the cascade and the method of inferring M_∞ and P_∞ for the cases where the Mach number and static pressure do not match that ahead of the unsteady-flow generators. Additionally, surface-flow visualization of the stator surfaces will be discussed.

5.1 Types of Pressure Data.

As mentioned in the experimental description in Chapter 4, Section 4.2.4, steady vane pressure data were obtained using a remotely-mounted scanivalve from four cast vanes, each with 15 pressure taps; the taps on these four vanes were located at "engine axis" 1 and 2 and at a "cascade axis" midway between locations 1

and 2 (See Figure 4.3). Two of these vanes were at engine-axis location 1 to give increased chordwise resolution. In addition, steady data for each engine axis were obtained using 8 vanes instrumented (i.e., a total of 16 vanes) with surface-mounted, pressure transducers; each blade having two sensing locations (see earlier description in Chapter 4, Section 4.2.4); these vanes provided a composite pressure distribution around a "nominal" vane. As mentioned earlier, the "freestream" Mach number and static pressure refer to the Mach number and static pressure at the inlet plane of the cascade section, just downstream of the 150-to-1 contraction-ratio inlet (Fig. 4.1).

5.2 Engine-Axis-Location-1, Steady C_p Data.

Figure 5.1 gives a composite of steady pressure data from one of the engine-axis-location-1 blades, as C_{p0} versus x/c for 12 inlet Mach numbers from 0.202 to 0.694. The data in Figure 5.1 were reduced to "equivalent" Mach-zero, incompressible C_{p0} using the Prandtl-Glauert correction, shown in Eq. (5.1).

$$C_{p0} = C_p \sqrt{1 - M_\infty^2} \quad (5.1)$$

Except for the Mach 0.694 data, Figure 5.1 shows that the C_{p0} data are "nicely behaved," and data for any Mach number through 0.6 may be obtained via an average C_p distribution made up of all the equivalent-Mach-zero data (from Mach 0.202 to 0.6), using the Prandtl-Glauert transformation. The Reynolds Number for the data presented varied from 145,000 to 400,000. As such, it can be inferred that no Reynolds-number effects are present in the static pressure data. Although not unexpected, due to the cascade being

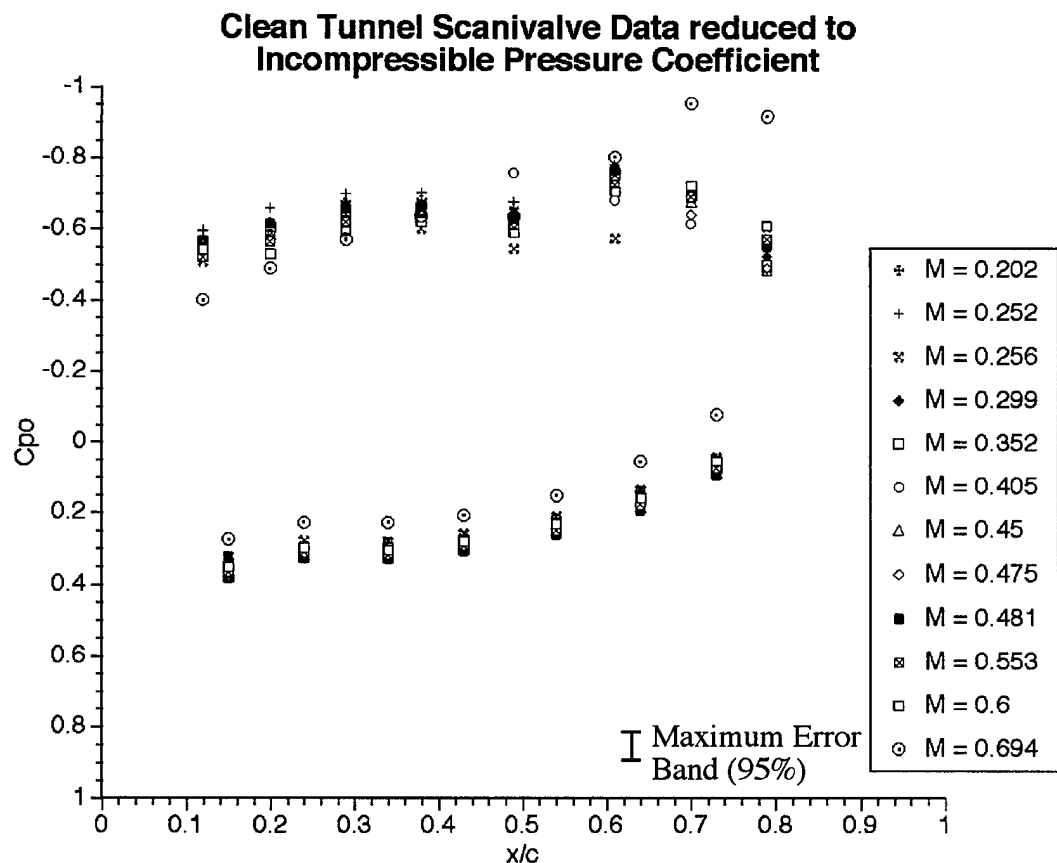


Figure 5.1 Clean Tunnel Scanivalve Data

designed for an overall favorable pressure gradient, the character of these data suggest that the cascade has attached flow over the instrumented region. This cannot be said of the Mach 0.694 flow data. These Mach 0.694 data, along with the downstream total and static pressure measurements show that the cascade becomes transonic and may experience shocks for inlet Mach numbers greater than 0.6.

5.3 Two-Dimensional-Flow Quality and Airfoil-Geometry Sensitivity.

Figure 5.2 gives a composite of C_p data at Mach 0.4 for the four 15-tap, scanivalve instrumented vanes at both engine axes and at the cascade axis. It may be generally inferred from Figure 5.2 that the flow in the cascade region including the engine-axis locations 1 and 2, and the cascade-axis location (see Figure 4.3) is two-dimensional; however, it is important to address the Figure 5.2 data scatter. Although there is uncertainty in any single data point, it is small. Specifically, each data point is the average of 512 samples; setting aside bias error, based on the standard deviation of the samples, the deviation from the expected true value is

approximately 0.03 C_p , which is approximately the size of the symbols used to represent the data points on Figure 5.2 (see Appendix J). If any bias error is present for a given blade, based on how the scanivalve was used, that bias is common to all 15 data points from that 15-tap vane. In order to minimize bias error from

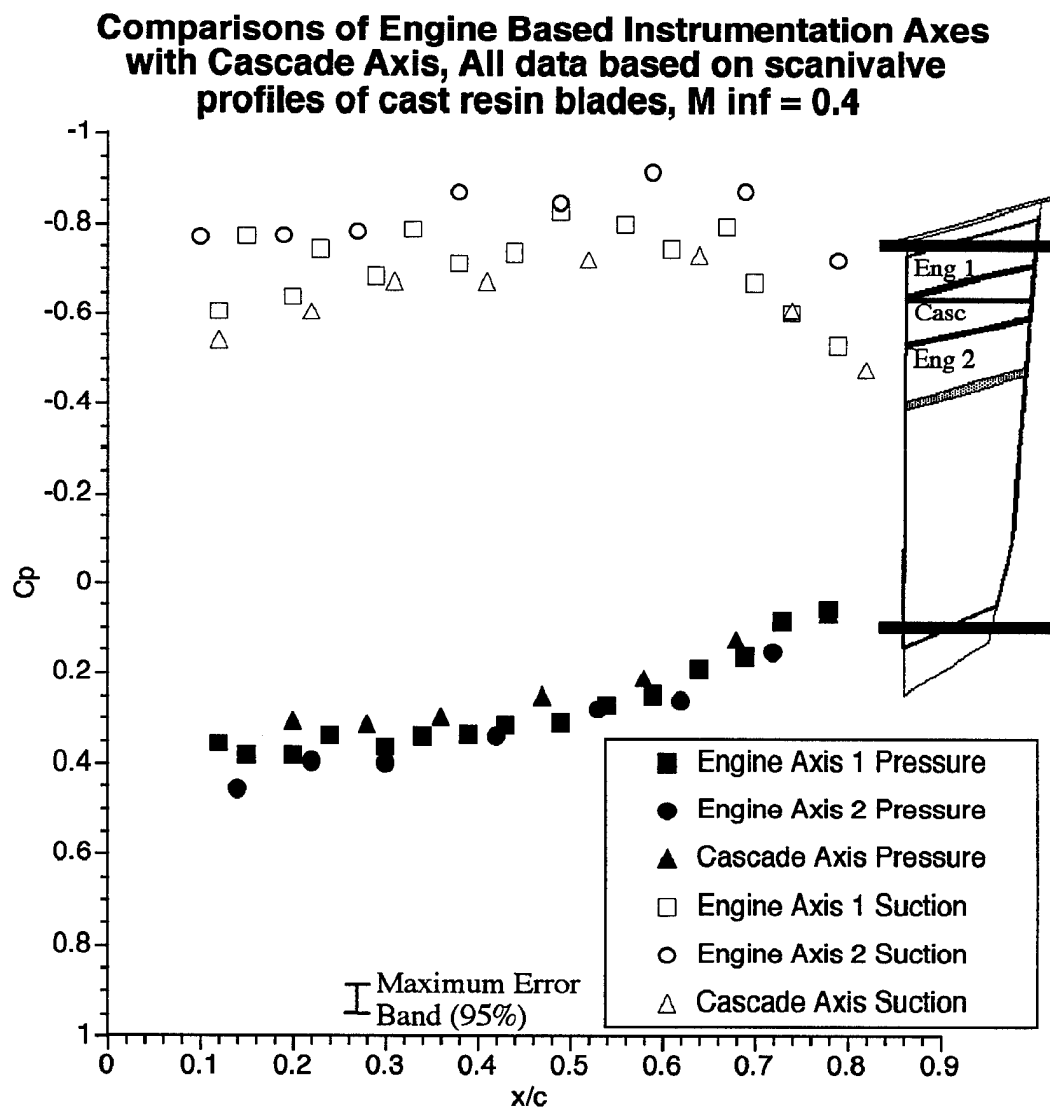


Figure 5.2 Engine and Cascade Axes Comparison

one 15-tap vane to another, calibrations were performed on the scanivalve pressure transducer prior to each run; over all data sets, including sets not reported here, the calibration coefficients varied by less than 1%. The reader's attention is directed to the engine-axis, location-1 suction-surface data (the square symbols in Fig. 5.2); for a given surface, each chordwise, alternating data point was derived by one or the other of the two location-1 vanes. The fact that the data differs by as much as 20% between vanes (appears to be a consistent trend) cannot be attributed to lack of two-dimensional-flow conditions in the cascade, first, because the vane-spanwise locations for the two 15-tap vanes lie along identical, engine-axis rays (i.e., location 1 in Figure 4.3). Further, data runs were made for each of the four 15-tap vanes and the eight composite vanes at cascade section locations 3 and 4 (see Figure 4.2); data from the same vane (both steady and unsteady) taken at cascade vane location 3 were virtually identical to those taken at vane location 4.

Because, at least for the location-1 data, non-two-dimensional effects can be discounted, it is clear that some other factor(s) must be responsible for the scatter observed in the location-1 data of Figure 5.2. It has long been known that airfoil

geometry variations have a large effect on the flow field.

Hawthorne warns against attempting to design research cascades with rotor/vane chords as small as those used in our cascade for this very reason (Hawthorne, 1964); because of the relationship of the present research with follow-on, F109 engine tests, however, there was no choice in the selection of chord length. Inspection of the four 15-tap vanes and the 16, unsteady-transducer instrumented vanes, showed relatively large camber and thickness variations between vanes. Although the largest variations were to be found in the 8 composite vanes of engine-axis location 1, small variations were also noticeable between all vanes at engine-axis location 2; the sensitivity to geometry variation is underscored by the fact that the two location-1 cast vanes are the closest geometric matches of any of the other vanes, the engine-axis location-1 geometry differences being almost imperceptible. Since the production stators are folded stainless steel with welded trailing edges, rather than cast, this may cause the majority of the vane to vane surface variations. Angle of attack variations may also be present from one vane to the next; however, these are minimized by the way in which the vanes are held in the cascade, and the fact that virtually no

difference in C_p data for a given vane is noted by placing it at cascade vane location 3 or 4 (see Fig. 4.2). It can be concluded that the variation between 15-tap, location-1 vanes is due to slight variations in their geometries. Further, since the scatter between data from the engine-axis-2 vane and one of the engine-axis-1 vanes, and the cascade-axis vane and one of the engine-axis-1 vanes is no greater than the scatter between the two engine-axis-1 vanes, the scatter between all the data in Figure 5.2 may also be attributed primarily to geometry variations between vanes.

Figure 5.3 shows the steady C_{p0} data obtained from the 8 composite vanes (with their up-to-two pressure ports lying along the engine-axis location-2 ray) overlaid on the scanivalve C_p data from the 15-tap, engine-axis-2 cast blade. The trends are similar; however, the scatter caused by the 8 instrumented vanes is apparent. The variation in geometry between the 8 instrumented vanes of engine-axis-2 were minor compared to the 8 engine-axis-1 vanes whose geometry variations were easily perceptible. Our conclusion is that the scatter in the 8-vane C_p data can be explained by these geometry variations which were less prevalent on the engine-axis-2 stator vanes but still greater than the two cascade

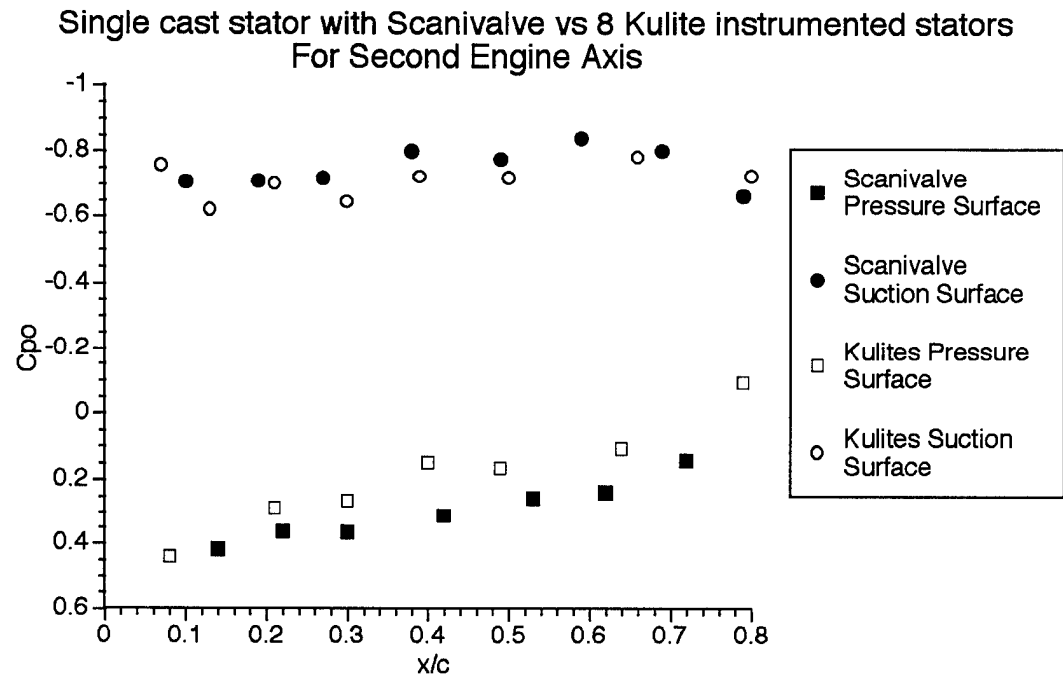


Figure 5.3 Scanivalve vs Multiple Kulites

axes scanivalve-instrumented vanes discussed in relation to Figure 5.2. With the information above taken as a caveat, Figure 5.3 indicates that composite C_p data formed from data obtained from the 8 composite vanes, should represent both the mean pressure performance of a “nominal” vane in the cascade, and the dynamic, unsteady performance of the “nominal” cascade vane to the accuracy of the dynamic response of the transducers (refer to the experimental description in Chapter 4).

5.4 Freestream Mach Number and Static Pressure.

Figure 5.1 indicates that use of the freestream Mach number and static pressure obtained from measurements made at the inlet to the cascade section properly represent the reference pressure for obtaining C_p from measured pressure data (referenced to cascade inlet total pressure, see Chapter 4); otherwise, correction back to Mach-zero, incompressible C_p using the Prandtl-Glauert rule based on the inlet Mach number would not have allowed the data sets for various Mach numbers to create a single curve (Fig. 5.1). In the case of forward unsteady forcing, with the cylinders placed upstream of the cascade vanes, both the "freestream" Mach number and the "freestream" static pressure entering the vane row change.

Numerous techniques were attempted to adequately recover the equivalent freestream Mach number and static pressure for forward forcing of the cascade row. The unsuccessful techniques included mapping the relative total pressure loss characteristic for upstream and downstream forcing of the cascade versus the clean cascade configuration and characterizing the equivalent area ratios due to the forcing rods. The best method involved using the time-averaged surface pressure profiles of the stators to determine the inlet

pressure and Mach number. Figure 5.4 demonstrates the method that was devised to recover the proper freestream conditions to use for constructing C_p data for the case of upstream (forward) unsteady forcing of the cascade. The data in Fig. 5.4.a. is for a no-cylinder, reference flow at a cascade inlet Mach number of 0.475 and the mean (time-averaged) C_p data for the same 15-tap vane at a 0.475 cascade-section-inlet Mach number, but with forward, unsteady

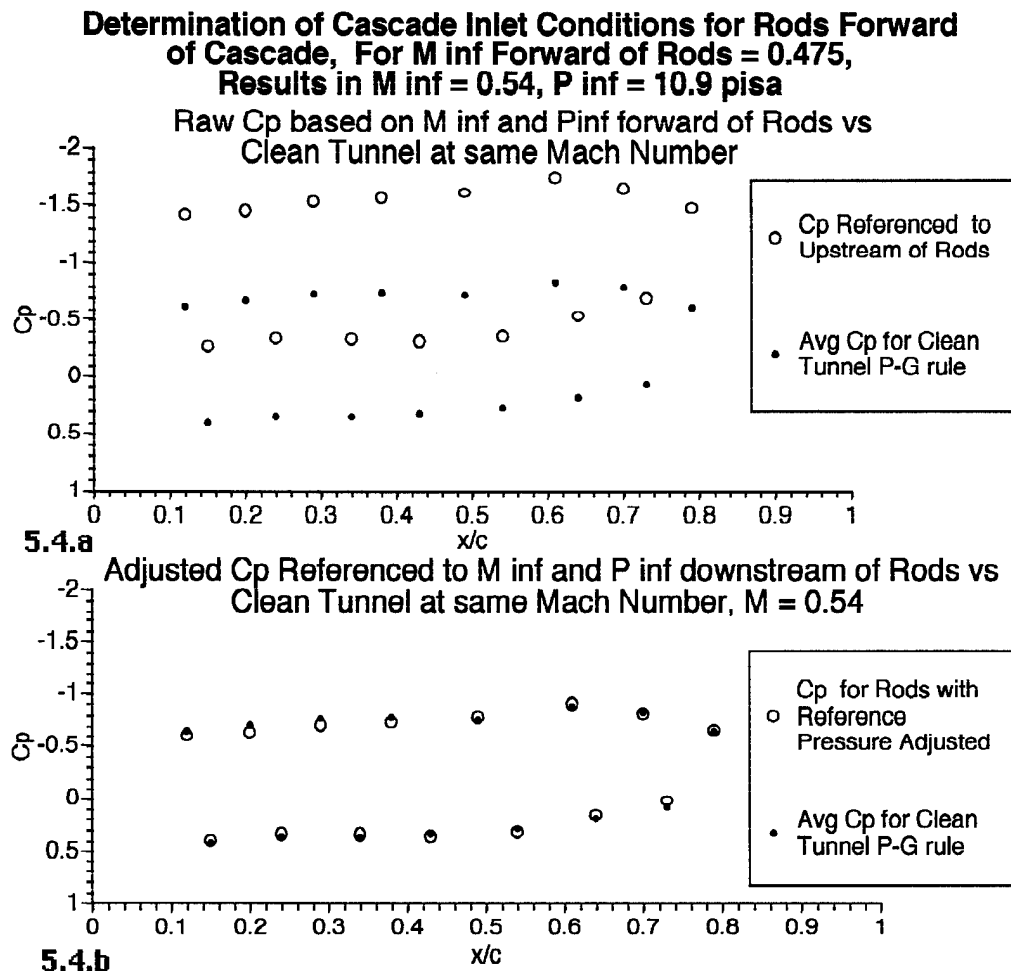


Figure 5.4 Determination of Mach Number and Freestream Pressure for Rods Forward of Cascade

flow-producing cylinders; the later C_p data were constructed assuming the inlet conditions gave the proper "freestream" conditions. It is clear that the two curves in Fig. 5.4.a. differ both in the separation between the pressure- and suction-side-curves, and in offset. The "Average C_p for the Clean Tunnel" data points in Fig. 5.4 were obtained by Prandtl-Glauert correcting the average Mach-zero C_p data, as described earlier. Note that C_p for a compressible flow is given by:

$$C_p = \frac{2}{\gamma P_\infty M_\infty^2} (P - P_\infty) \quad (5.2)$$

Manipulation of M_∞ and P_∞ in Eq. (5.2) in plotting the C_p of Fig. 5.4.a. showed what is obvious from Eq. (5.2), that, although not completely uncoupled, M_∞ primarily controls the separation between the pressure- and suction-side curves and P_∞ primarily controls the offset. Correct choice of M_∞ is further (slightly) complicated by the fact that the reference C_p data must be modified to the new "corrected" Mach number for each iteration in Mach number. Figure 5.4.b. demonstrates the result of optimizing the Mach number and

static "freestream" pressure to the correct values for entering the vane row in the cascade. Due to the dramatic total pressure loss cause by the rods forward of the cascade row, all forward-forcing data were examined in this way to obtain the correct inflow freestream Mach number and static pressure for the data set.

5.5 Vane-Inflow Mach Number.

It should be noted that with the local steady pressure values along the vane surface, the local Mach number may be inferred using the isentropic flow relations as shown in Eq. (5.3) where P_0 and P_L are the total and local pressures, respectively.

$$M_L = \sqrt{\frac{2}{\gamma - 1} \left[\left(\frac{P_0}{P_L} \right)^{\frac{\gamma - 1}{\gamma}} - 1 \right]} \quad (5.3)$$

The total pressure, P_0 , was acquired from a total pressure probe located 3 inches upstream of the vane row. Figure 5.5 shows the local Mach numbers for a inlet Mach number of 0.427 with the disturbance rods aft of the vane row. The failure of some of the Kulite transducers has reduced the pressure surface resolution. Although slightly more difficult, the forward forcing of the cascade can also provide local Mach numbers. The forward forcing case

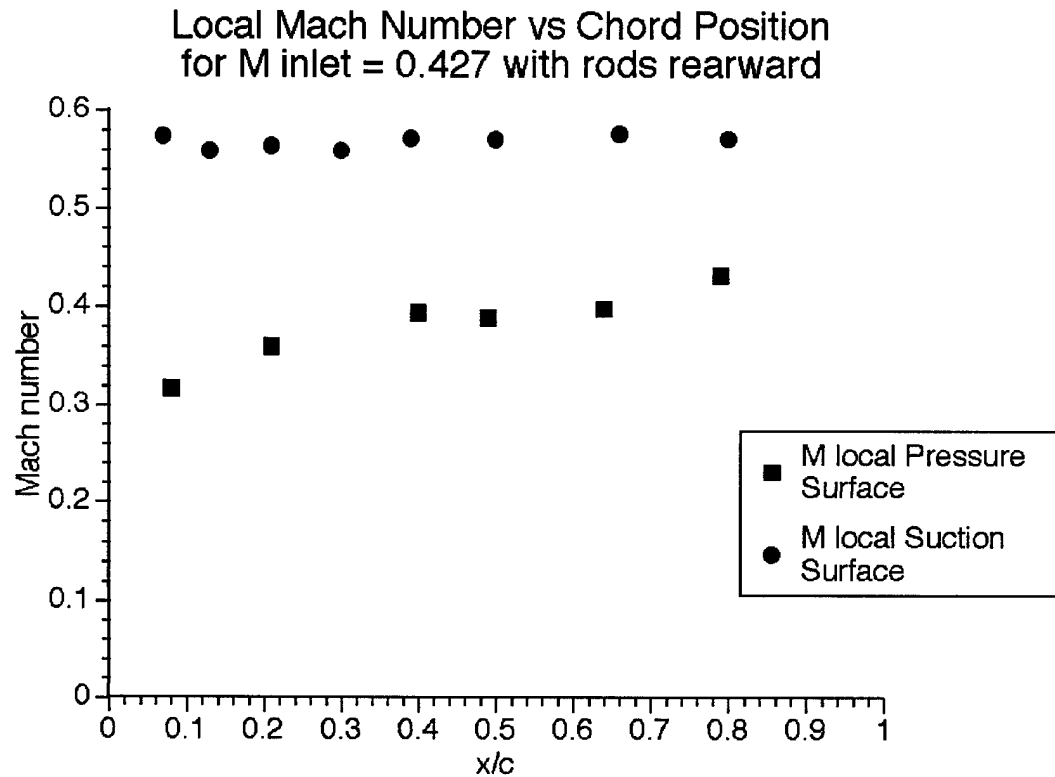


Figure 5.5 Local Mach number vs Chordwise position

requires the determination of the effective total pressure following the disturbance cylinders using the method like that shown in Figure 5.4 to determine the effective freestream Mach number and freestream pressure. As will be discussed in Chapters 6 and 8, determining the local Mach number and the associated local convection velocity is related to the associated unsteady wave propagation velocity for the unsteady forcing of the vanes by upstream or downstream cylinders.

5.6 Surface Flow Visualization.

Surface flow visualizations were conducted using titanium-dioxide. Although the surface pressure measurements indicated attached flow over the instrumented region from 7 to 80 percent of the chord length, as shown Figure 5.1, the surface flow visualization provided separation information beyond the instrumented region. Production stator vanes were painted flat black for photographic contrast purposes and coated with a solution of titanium-dioxide, acetic acid, and kerosene. Testing was conducted with and without disturbance cylinders, with the disturbance cylinders upstream, and finally with the disturbance cylinders downstream of the cascade row. References to "hub" and "tip" refer to the engine-related, short-chord region (hub) and long-chord region (tip)(with the kulite instrumentation), respectively as shown in Figure 5.6. Measurements of the percentage of chord affected by a flow phenomenon were performed using a 0.001 inch resolution caliper.

Reproductions of photographs of these flow visualization cases discussed below can be found in Appendix F. The discussion is accompanied by schematic representations of the flow visualization.

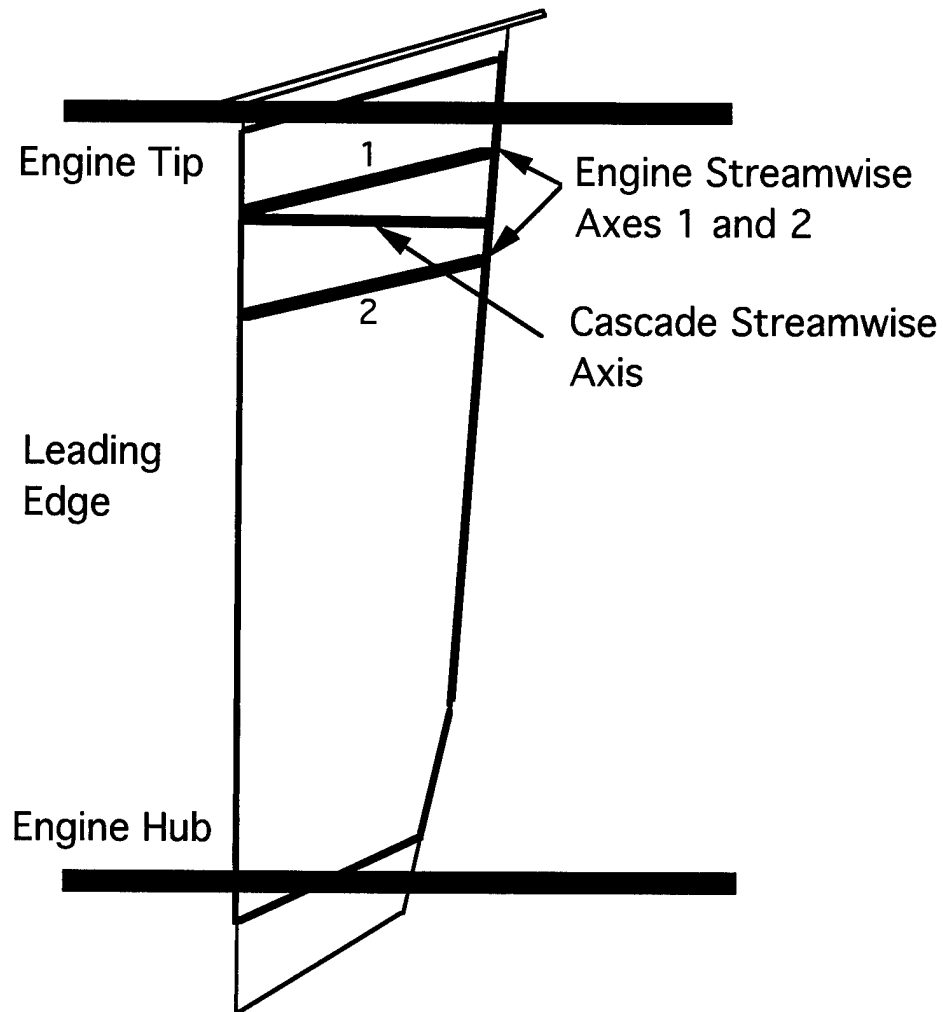


Figure 5.6 Hub and Tip Designations of Stator Vane

These schematics may be cross-referenced to the photographs in Appendix F.

In the clean-tunnel configuration at a Mach number of 0.5, the pressure surface showed no leading-edge separation and a separation at the initiation of the cusped region, at 85 percent chord. There was clear evidence of reattachment, at 90 percent chord, following the deepest portion of the cusp. Other than the

separation region, the flow appeared to be two-dimensional over the entire pressure surface. The suction surfaces showed a leading-edge separation with re-attachment at less than 5 percent chord. A trailing-edge separation was apparent at 91 percent chord. The hub region showed more prominent trailing edge separation, at 88 percent the chord, due in part to the inadequate chord length to perform the required turning in the linear two-dimensional cascade configuration. This was an expected compromise due to the increased relative stator spacing at the hub compared to an annular cascade or engine configuration. Since this hub region could not be instrumented, the increased trailing edge separation was not deemed important. At the hub and tip, a combination of wall effects, horseshoe-vortex, and tunnel leakage caused the flow to deviate from axial flow, with the strongest influence at the tip region. Although not present on the pressure surface, the suction surface, with its associated lower pressure, showed paint traces implying leakage air flow from the fixture region outside the flowfield into the cascade passage. Although the individual stators were sealed in place using tape, some leakage could not be avoided; this is a problem inherent in in-draft tunnel testing and might have been

reduced with a more complex pressure seal. The additional flow displaced the core flow in the aft portion at engine-axis location-1 instrumentation region, but did not appear to have an effect on either the instrumented engine-axis location 2 or cascade-axis location (see Figure 5.7).

With the disturbance cylinders forward of the cascade row and an inlet Mach number of 0.43, the pressure surface showed no

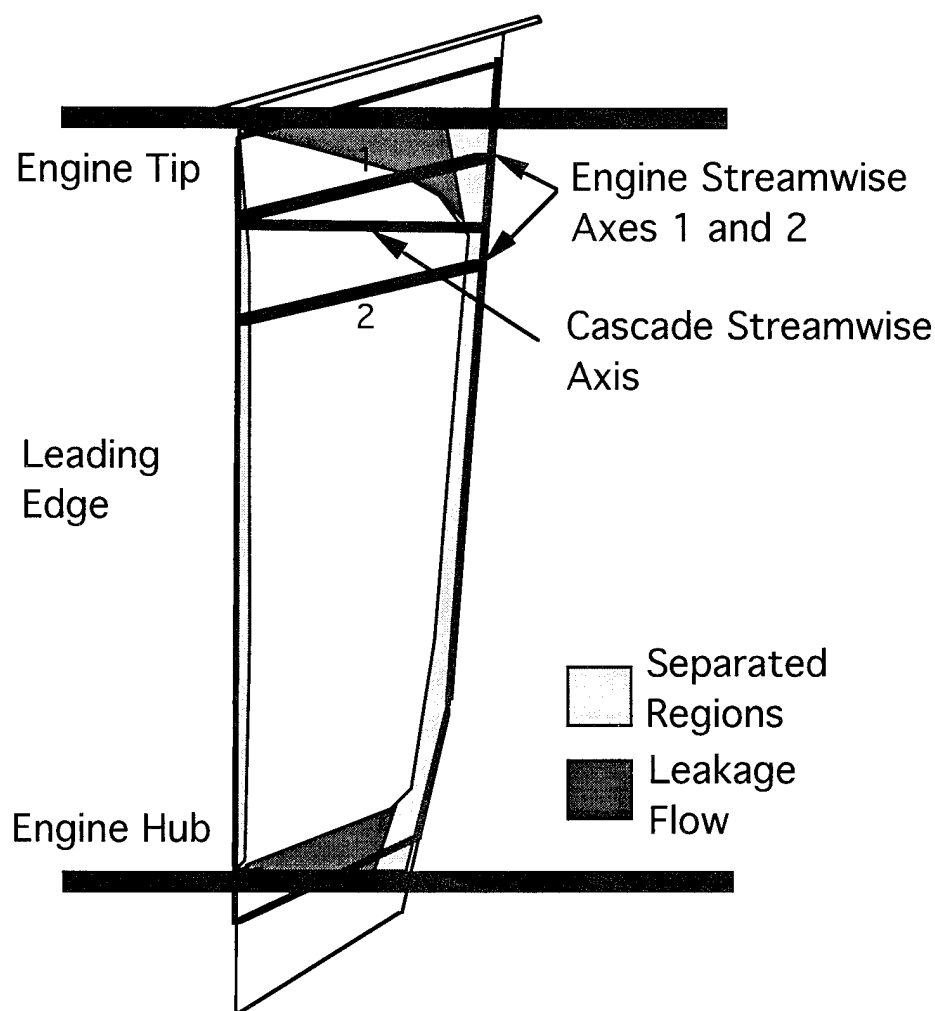


Figure 5.7 Suction Surface Separation and Leakage Regions in Clean Tunnel Configuration

leading edge separation and reduced trailing edge separation.

Although the separation occurs at the start of the cusped region, at 85 percent chord, the flow reattached more rapidly at 88 percent chord, two percent chord closer to the separation point than for steady, unforced flow. The flow appears to have remained two-dimensional over the entire pressure surface. The leading edge separation on the suction surface, was greatly reduced over that of the clean-tunnel configuration. The reattachment point occurred at less than 1.5 percent chord. Additionally, no trailing-edge separation was apparent. The hub and tip leakage problems were comparable to the clean-tunnel configuration, but with less trailing-edge extent at the tip, presumably because the flow remained attached. A recirculation zone at the stator-tip/wall-interface region started at approximately 60 percent to 80 percent chord and angled back to the trailing edge at approximately a 45° angle, as shown in Figure 5.8.

At an inlet Mach number of 0.58, with the rods forward of the cascade row, the pressure surface showed only the small separation region at the cusp which was similar in size to the previous forward forcing case. Again, the pressure surface showed two-dimensional

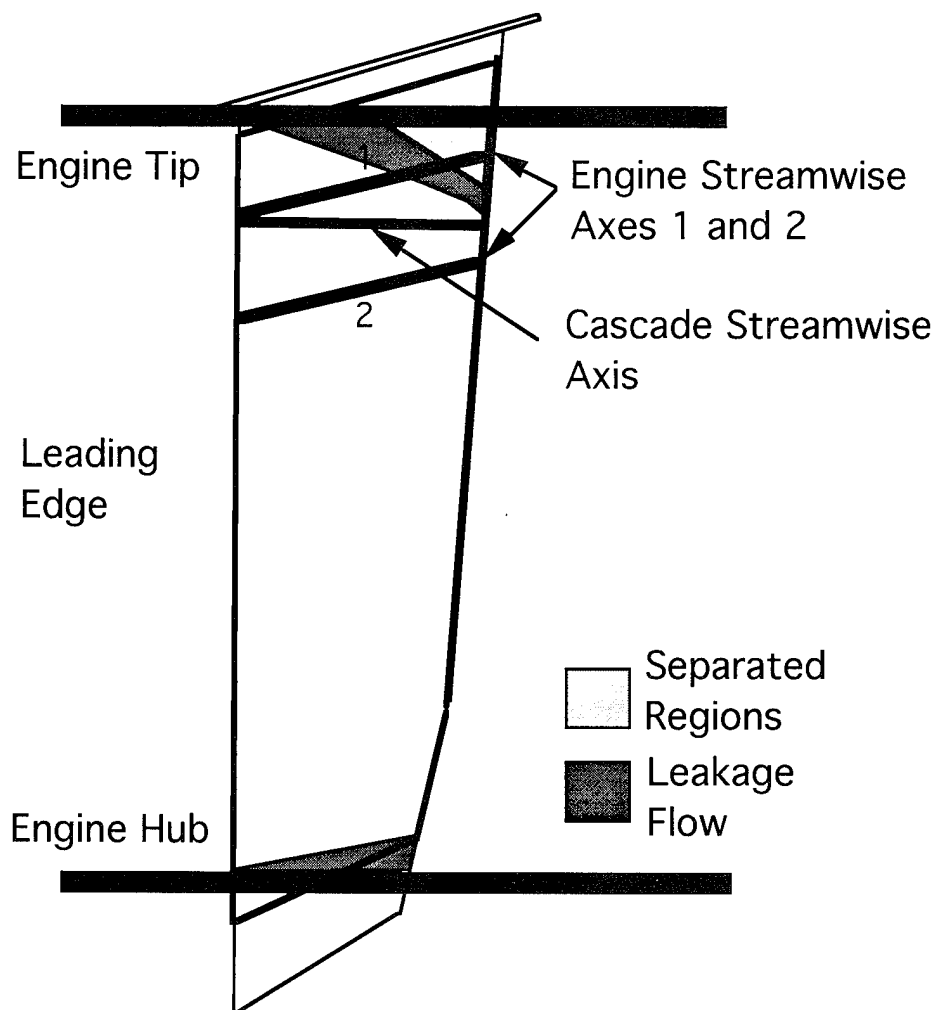


Figure 5.8 Suction Surface Separation and Leakage Regions in with Rods Forward, $M = 0.43$

flow. The suction surface had a leading-edge separation bubble of one percent of chord and no trailing-edge separation except in the hub region with its shorter chord length; however, the separation appeared to be less than 10 percent of the chord. On the suction surface, the hub and tip leakage were readily visible, with the recirculation zone near the tip wall being approximately the same

size as the previous forward forcing case.

With downstream forcing of the cascade row at Mach 0.427 (a case to be discussed extensively in Chapter 6) the pressure surface showed no leading-edge separation bubble and only the previously-mentioned separation in the cusped region. The separation started at 85 percent chord and reattached at 94 percent chord. No hub or tip leakage problems were apparent on the pressure surface. On the suction surface, the leading edge separation bubble was 2.5% of chord, while the trailing-edge separation was only visible in the hub region. The aft 25 percent of the chord next to the tip and wall, showed reversed flow; however, in this case none of the pressure taps, even at-engine-axis location 1 were affected.

5.6.1 Summary

Overall, the flow in all cases was very well behaved for this extensive flow turning, 42.5° , due in part to the circular arc geometry of the airfoils and appropriate inlet flow angle but probably due in most part to the favorable pressure gradient designed into the cascade; thus validating the cascade design. Although some hub and tip leakages were unavoidable due to the in-

draft tunnel, the separated regions are small and outside the instrumented domain for engine-axis 2 and the cascade-axis. Engine-axis 1 showed suction-surface separation at the instrumented 65% and 80% chord positions at the lower Mach numbers tested; however, the surface pressure distributions of all three axes (refer to Figure 5.2) indicate that the wall leakage had essentially no effect on the character the data, even at the engine-axis-1 location. The surface flow visualization images are included in Appendix F.

CHAPTER SIX

REARWARD FORCING OF CASCADE

6.1 Forcing Gust.

As described in Chapter 4, the unsteady "gust" was produced from von Karman vortex shedding off of five circular rods aligned normal to the incoming flow, and parallel to the vane spans, with the same spacing as the vane row. Various locations were tried and the vane unsteady-pressure response examined. In general, the response was similar regardless of the span-normal alignment location, differing primarily in magnitude but also in higher frequency content; placement of the forcing rods at the mid-passage location between vanes yielded response signals with sharper FFT peak amplitudes. All unsteady-forcing data presented in this chapter were taken for mid-passage alignment of the forcing rods. As will be clear from the discussion later in this chapter, the rearward forcing appears to be irrotational (lacking major vortical structures) in the vane passages. Regardless of the proper description of the disturbance, its "periodicity" in time can be

described by examining the trigger signal used to phase lock the data acquisition of the vane unsteady pressure response. Figure 6.1 gives the trigger signals (obtained as described in Chapter 4) and their PSD's for two Mach-number cases for aft forcing. Both traces represent 400 ensembles of conditionally-sampled trigger information. The PSD plots show that the primary forcing signal is fairly narrow band. The tailing off of the average signal from the center, trigger point, is due to a modulation of the signal amplitude at all Mach numbers. At the highest Mach numbers, this apparent low-frequency amplitude modulation of the average signal is more noticeable; this modulation is, in fact, present on all the signals as can be seen in a selected signal trace at $M_\infty = 0.50$ with the rods aft, Figure 6.1. It is not clear whether this may be a problem in "synching" the rod shedding or a synchronized modulation of the shedding; however, the low-frequency of modulation appears to be nearly the same frequency for all Mach numbers, ≈ 1700 Hz, which may indicate some mechanical vibration mode or vacuum-pump mode, characteristic of the transonic facility. It should also be noted that at these Reynold's numbers, 40,000 to 60,000, the shedding amplitude is naturally "irregular" (Fung, 1993). The

conditional sampling near the maximum amplitude seen on the trigger signal causes a portion of the apparent modulation and may contribute to the lower frequency shown in the FFT, Fig. 6.1. As the Mach number was increased, the gain for the AC coupled trigger had to be increased (as Mach number increased from 0.427 to 0.50, for example, required roughly doubling the gain) to maintain the same conditional-sampling trigger threshold. In both the highest Mach number cases reported for both aft and forward forcing (to be

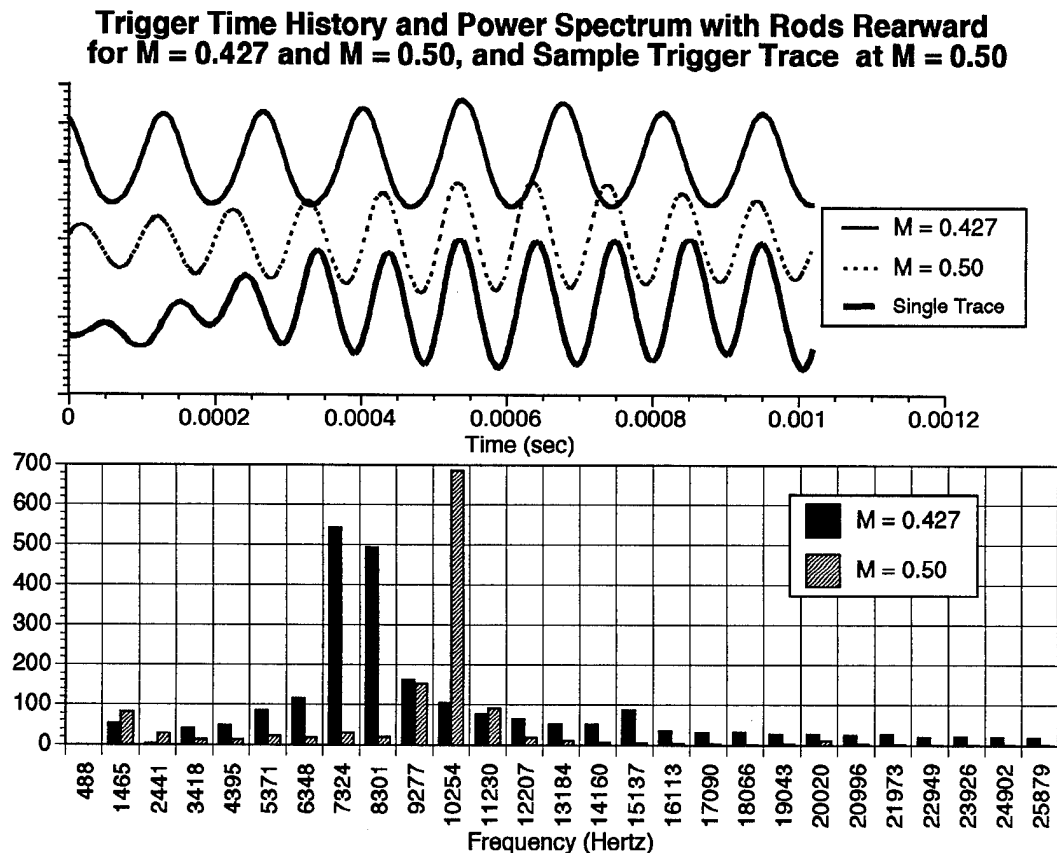


Figure 6.1 Trigger Signal and Power Spectrum for Rods Rearward

discussed in Chapter 7), any further increase in Mach number resulted in a "stabilization" of the flow around the rods and no unsteady trigger signal was generated. This stabilization of the forcing signals may be associated with near sonic flow conditions around the rods. As a result of this stabilization, the highest inlet Mach number achievable using this technique with rearward forcing was Mach 0.50 (which resulted in a passage Mach number of roughly 0.73, see technique shown in Chapter 5, Figure 5.5).

6.2 Gross RMS Unsteady-Pressure Response.

Figure 6.2 shows the rms of the fluctuating pressure as a function of span location on both the suction and pressure sides of the vanes for aft forcing. The data presented are from the more central profile, Engine Axis Two of Figure 4.3; although these data are similar to Engine-Axis-One data (Fabian and Jumper, 1995), due to possible wall effects and slight geometry effects mentioned in Chapter 5, only Engine-Axis-Two data is presented here. The Engine Axis One data gives similar trends and is included in Appendix G. It should be noted that these values represent the average rms of each of the 400 conditionally sampled signal traces and hence include all

frequencies present on the signal trace. Since the rms values were determined prior to ensemble averaging, the magnitude of the unsteady pressure data is presented without the effect of possible constructive and destructive interference in the ensemble averaging. Recall that these signals are built up from signals from eight different blades. The absolute vertical height of the data-point above and below the upper and lower airfoil surfaces, respectively, in Fig. 6.3 represent the rms pressure amplitude for each chordwise

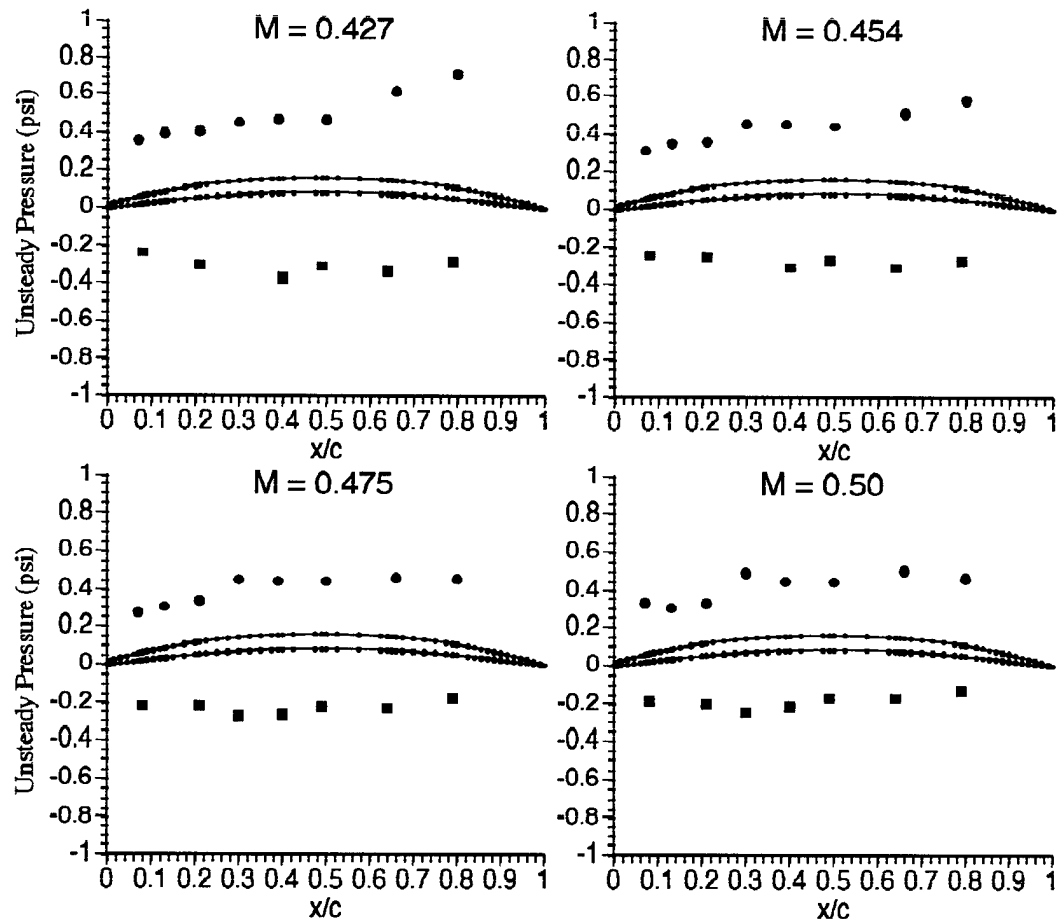


Figure 6.2 RMS Pressures for Rods Rearward

position in pounds per square inch. Apparent in the two lower-Mach-number cases, there is an increase in rms pressure with chordwise distance. Since the forcing is downstream, this indicates a decay of the rms pressure on the suction surface with increasing distance from the disturbance rods (c.f., discussion in Section 6.6). At the higher Mach numbers, this trend appears to be complicated by a slightly increased amplitude at the 30 percent chord position on the suction surface. In the rearward forcing cases, changes on the pressure surface with Mach number are more benign. In accordance with the requirement to increase the gain of the trigger signal to maintain the conditional sampling threshold with increasing Mach numbers, the amplitude of the disturbance has shown a decreased amplitude on both surfaces.

6.3 Phase-Locked Unsteady Pressure Signals.

Figure 6.3 shows phase-locked, ensemble-averaged, unsteady pressure data from 400 ensembles at a Mach number of 0.427 for the rearward forcing of the cascade. Similar data for other Mach numbers are presented in Appendix G. The three graphs of Figure 6.3 represent the normalized unsteady pressure versus nondimensional

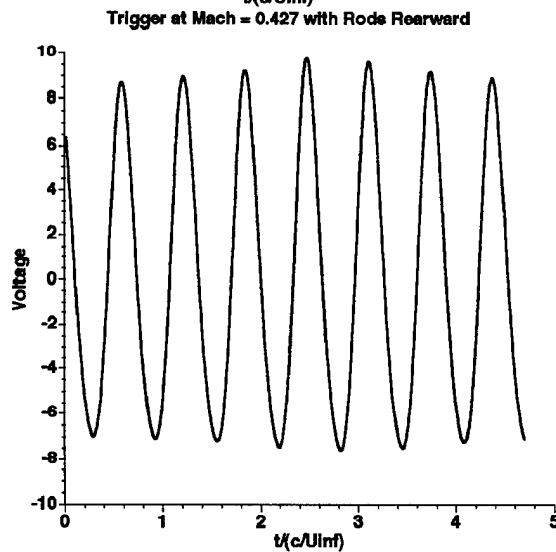
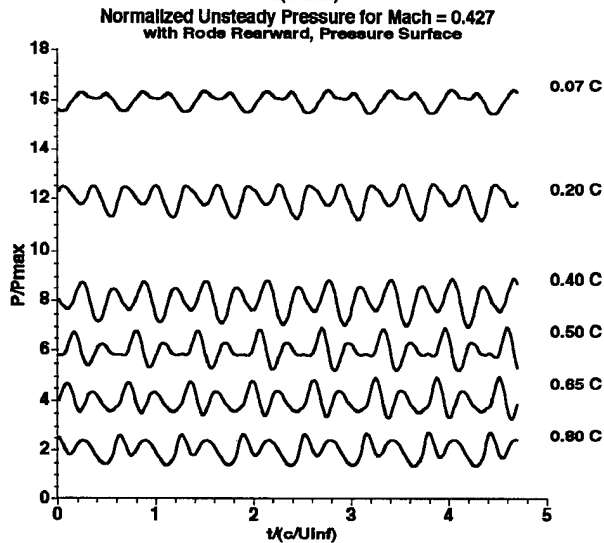
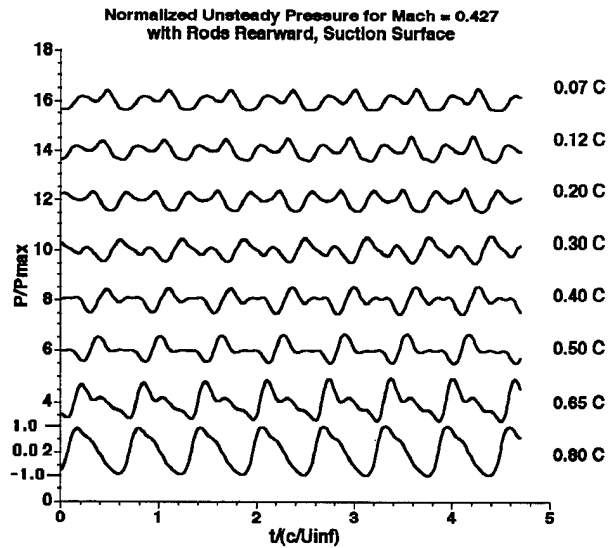


Figure 6.3 Signal Averages for $M = 0.427$ with Rods Rearward

time (i.e., tU_∞/c) for the suction surface of the vane, the normalized unsteady pressure for the pressure surface of the vane, and the ensembled trigger signal for that Mach number, respectively. The normalization for the pressure response is based on the amplitude of the largest unsteady signal, in this case, the 0.80c trace on the suction side. Each trace is displaced by two units of P/P_{\max} , so that the nominal zeros for the suction surface are at 2, 4, 6, 8, 10, 12, 14 and 16 for the 0.80c, 0.65c, 0.50c, 0.40c, 0.30c, 0.20c, 0.12c and 0.07c, respectively. The trigger signal is not normalized. The actual voltage after gain is shown with the conditional-sampling-trigger threshold set at 9.5 volts (see Chapter 4). At this Mach number (0.427), the unsteady pressure signals appear uniform over the entire nondimensional time, encompassing approximately eight cycles of unsteady forcing. This would be expected for phase-locked, ensemble averages. It is important to note that all signals are triggered at the central trigger peaks $(t/(c/U_\infty)) \approx 2.5$, and that the amplitude of the trigger decays slightly on each side of the central trigger. In fact, close examination of the pressure signals show that there are slight variations to the near uniform traces across the nondimensional time range. As can be seen in Fig. 6.1, the decay away

from the central trigger becomes more pronounced with increasing Mach number, the nonuniformity of the unsteady-pressure response with non-dimensional time noticeably increases with increasing Mach number as shown in Appendix G. Since the response curves in Figures 6.3 and the others in Appendix G represent ensemble averages and individual records show the same characteristics, these nonuniformities appear to be real. Part of the nonuniformity may be due to the decreasing magnitude of the trigger signal and the expected decrease in the associated disturbance. Cross referencing to the trigger traces with increasing Mach number, see Appendix G, the increased modulation in the forcing gust (trigger signal) can be logically linked to the nonuniformity in the unsteady-pressure response. It should be kept in mind that any such unsteady surface pressure response has an associated phase lag due to the fact that the forcing occurs $0.80c$ downstream of the vane. Table 6.1 provides the normalizing pressure values, based on the maximum unsteady pressure amplitude measured on the surface, for the pressure and suction surfaces shown in Figure 6.3 and Appendix G.

Although the primary frequency of the fluctuating pressure is at the forcing frequency, the response curves have a ubiquitous

Table 6.1 Normalizing Amplitudes for Figure 6.3 and Appendix G

Normalizing Amplitudes in psi for each plot	Suction Surface	Pressure Surface
Mach 0.427 Rods Rearward	0.843	0.662
Mach 0.454 Rods Rearward	0.351	0.250
Mach 0.475 Rods Rearward	0.217	0.212
Mach 0.50 Rods Rearward	0.329	0.211

structure. Similar structure has been noted in stator response signals from incompressible upstream rotating machines (Fleeter, Jay, and Bennett, 1978) where it was noted that the structure could be decomposed into a primary-frequency sinusoidal response plus a harmonic response. Similar decomposition was applied to the present data, and, a decomposition of the signal into a primary sinusoid at the forcing frequency and a sinusoid at the first harmonic appears to capture the character of the structure seen. Because of the consistency of the signal for the Mach 0.427 flow with rearward forcing, Figure 6.3, this data set will be discussed in the remainder of this chapter. The other Mach numbers tested produced similar trends.

Each of the fourteen response curves (8 for the suction surface and 6 for the pressure surface) was decomposed using a simulated annealing (as described in Chapter 4) into its primary and harmonic sinusoidal response. Figure 6.4 shows an example of how well two sinusoids reproduce the structure of the signals, in this case the 30 percent chord location on the suction surface. Table 6.2 gives the relevant parameters of the fourteen decompositions, primary and harmonic frequency, amplitudes, and phase referenced to zero nondimensional time. Any particular signal may be reproduced from

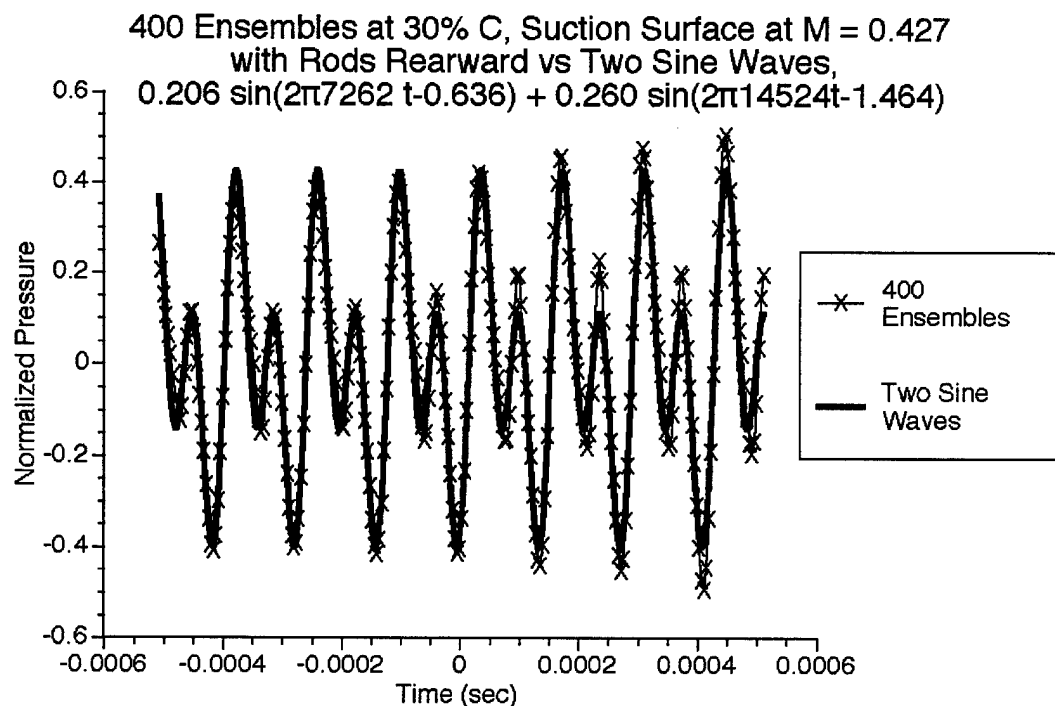


Figure 6.4 Ensembled Record vs 2 Sine Wave Representation

Table 6.2 Equation (6.1) Amplitude and Phase for Mach 0.427 data, Primary Frequency = 7280 Hz

x/c Position	Primary Amplitude, A_p psi	Primary Phase, ϕ_p radians	1st Harmonic Amplitude, A_h psi	1st Harmonic Phase, ϕ_h radians	RMS Error of Fit psi
0.07 Suction	0.183	2.415	0.189	0.659	0.054
0.12 Suction	0.179	2.874	0.217	1.699	0.056
0.20 Suction	0.158	-2.027	0.234	-2.603	0.039
0.30 Suction	0.183	-0.636	0.230	-1.464	0.043
0.40 Suction	0.180	0.413	0.243	1.372	0.064
0.50 Suction	0.200	1.638	0.237	2.964	0.075
0.65 Suction	0.412	3.158	0.257	0.067	0.014
0.80 Suction	0.751	-2.454	0.198	1.476	0.074
0.07 Pressure	0.184	2.625	0.138	0.168	0.023
0.20 Pressure	0.142	-2.257	0.331	3.038	0.050
0.40 Pressure	0.159	-1.580	0.455	-0.667	0.045
0.50 Pressure	0.115	-1.302	0.317	1.182	0.123
0.65 Pressure	0.112	-1.591	0.337	2.889	0.114
0.80 Pressure	0.184	-1.694	0.267	-1.714	0.091

these parameters as:

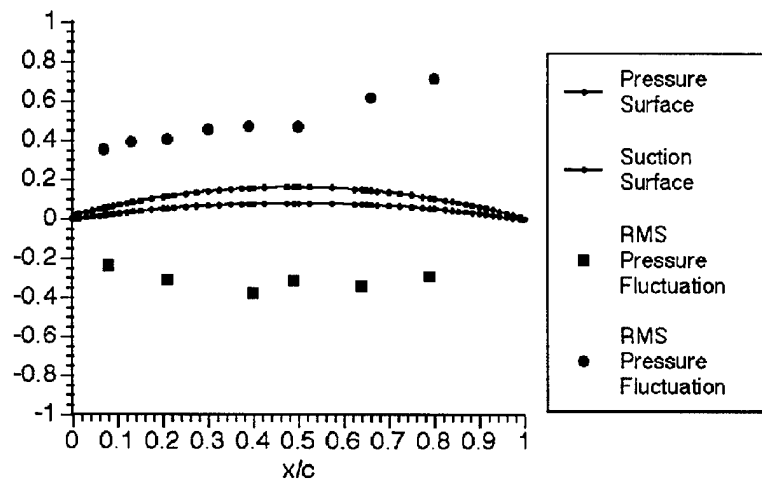
$$\tilde{P} = A_p \sin(2\pi f_p t + \phi_p) + A_h \sin(2\pi f_h t + \phi_h) \quad (6.1)$$

where A_p and A_h are the primary and harmonic amplitudes, respectively, f_p and f_h are the primary and harmonic frequencies, respectively, and ϕ_p and ϕ_h are the primary and harmonic phase lags, respectively.

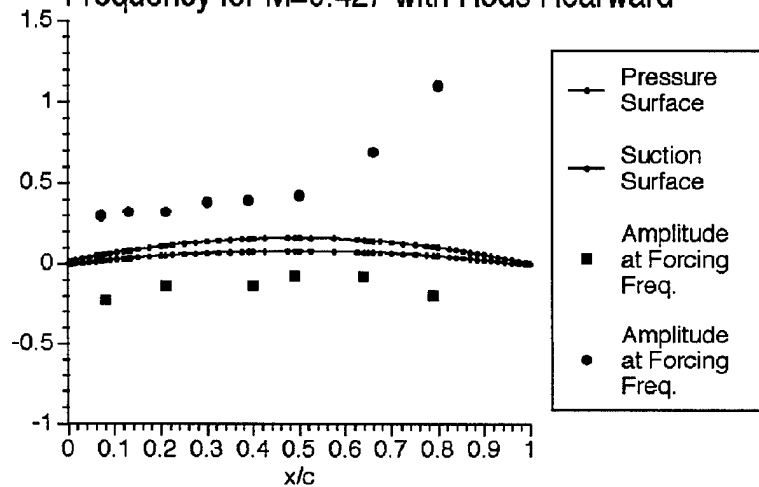
In their decomposed form, the response curves convey much more information concerning the cascade response. Consider first only the amplitudes; Figs. 6.5a,b, and c give the raw rms unsteady pressure response, the normalized primary-frequency unsteady response amplitude, and the normalized first harmonic unsteady response amplitude as a function of relative chord, respectively. From Figure 6.5.a it is not clear how the amplitude is responding to the cascade and the mean-flow distortion through the cascade; however, Figs. 6.5.b and 6.5.c provide additional information.

There are two prominent features of von-Karman shedding from a circular-cylinder that are important to the production of an unsteady field upstream from the cylinder. First, there is an oscillating circulation that manifests itself on the cylinder as a repeated oscillation of lift from positive to negative; this periodic plus/minus lift cycle constitutes the primary frequency expressed as the Strouhal number, Eq. (4.1) (Schlichting, 1955). Over this period, two spanwise, opposite-sense vortices are shed from the cylinder, the sense of each vortex being opposite of the corresponding sense of the cylinder bound circulation at the time the vortex is being shed (Goldstein, 1943). This shedding of each of the

RMS Pressure Fluctuations for $M = 0.427$
with Rods Rearward



Amplitude of Pressure Fluctuations at Forcing
Frequency for $M=0.427$ with Rods Rearward



Amplitude of Pressure Fluctuations at Twice Forcing
Frequency for $M=0.427$ with Rods Rearward

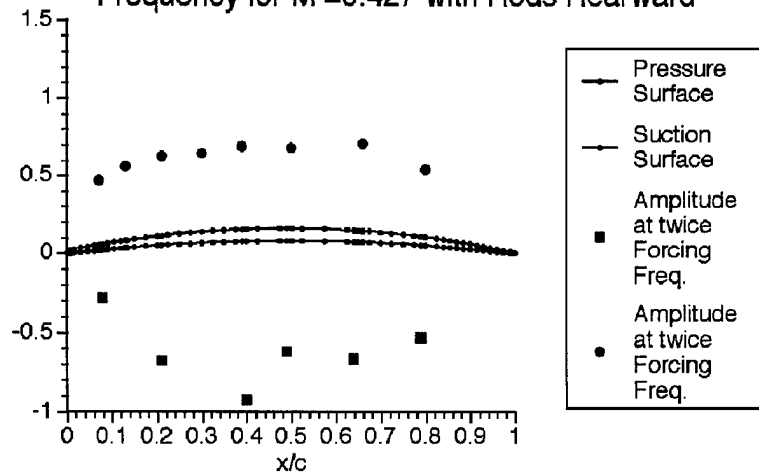


Figure 6.5 RMS Pressure Amplitude,
Normalized Primary and Harmonic Pressure
Amplitudes

opposite sense vortices causes the cylinder to experience a cycle of drag, so that the drag has a characteristic frequency twice that of the primary frequency of the lift on the cylinder.

It seems reasonable to suppose, then, that the upstream, unsteady pressure/flow field associated with the von-Karman shedding from the cylinders would be made up of two parts. The first part would have a characteristic frequency at the primary frequency, and in the absence of other sources of disturbance, would be similar to a potential flow field made up of flow around a cylinder superimposed with a sinusoidally oscillating circulation. For an incompressible flow this would have the form:

$$\bar{V}_{\text{incomp}}(r,\theta,t) = V_{\infty} \left(1 - \frac{a^2}{r^2}\right) \cos \theta \hat{r} - \left[V_{\infty} \left(1 + \frac{a^2}{r^2}\right) \sin \theta + \frac{\Gamma \sin(\omega t)}{2\pi r} \right] \hat{\theta} \quad (6.2)$$

where a is the radius of the cylinder (Anderson, 1991). Sufficiently far upstream ($r \gg a$) and along a ray directly upstream from the cylinder,

$$\bar{V}_{\text{incomp}}(r,t) \cong -V_{\infty} \hat{r} - \frac{\Gamma}{2\pi r} \sin(\omega_p t) \hat{\theta} \quad (6.3)$$

where ω_p is the frequency of the primary signal. In compressible

(subsonic) flow the pressure signals causing the unsteady velocity must propagate at the acoustic velocity upstream into the mean flow. This would have two effects: the first would be a delay time which would exhibit itself as a phase lag associated with the Mach number and the distance, r , from the source; the second would be an elongation of the apparent effect of the oscillating circulation by:

$$d_{\text{apparent}} = \frac{r}{\sqrt{1 - M_{\infty}^2}} \quad (6.4)$$

so that the signal a distance r directly upstream of the cylinder would be:

$$\bar{V}_{\text{comp}}(r,t) \cong -V_{\infty} \hat{r} - \frac{\Gamma \sqrt{1 - M^2}}{2\pi r} \sin \left[\omega_p t - \frac{r \omega_p}{a_{\infty}(1 - M)} \right] \hat{\theta} \quad (6.5)$$

The effect of the periodic drag on the unsteady velocity/pressure field is more difficult to estimate; however, it is clear that it would be associated with a characteristic frequency of two times the primary frequency, i.e., at the first harmonic. Secondly, it is clear that the effect of the drag will be time delayed due to its transmission at acoustic speed upstream into the oncoming flow. Although less clear, it is reasonable to assume that the drag will

periodically cause the tunnel speed to alternately speed up and slow down; if this is the case, unlike the potential fluctuating circulation, the effect need not decay with distance from the source. This can be approximately modelled as:

$$(\bar{V}_{\text{comp}}(r,t))_{\text{Drag}} \cong -V_{\infty} \hat{r} + V_D \sin \left[\omega_h t - \frac{r \omega_h}{a_{\infty}(1-M)} \right] \hat{r} \quad (6.6)$$

where V_D is the magnitude of the drag induced velocity fluctuation.

6.4 The Inverse Problem.

Consider now the suction-surface amplitudes of the unsteady, pressure data of Figure 6.5; it is clear that the primary response decays rapidly with increasing distance from the unsteady source, located downstream from the cascade. If each forcing rod is treated as in Eq. (6.5), then, according to Eq. (6.5), the associated

aerodynamic "gust" should demonstrate a $\sqrt{1-M_{\infty}^2}/d$ amplitude

variation, where d is now the distance from the rod (i.e., an harmonic gust of decreasing amplitude with increasing distance from the source). The decrease in amplitude with increasing d exhibited by the primary response amplitude might be interpreted as following

the variation of an aerodynamic disturbance. The harmonic response does not exhibit this decay. The harmonic response appears compatible with Eq. (6.6) (c.f., further discussion in Section 6.6).

The phase relationships of the response curves to other-location responses contains relevant phase information. Figures 6.6 and 6.7 show the primary and harmonic decomposed normalized

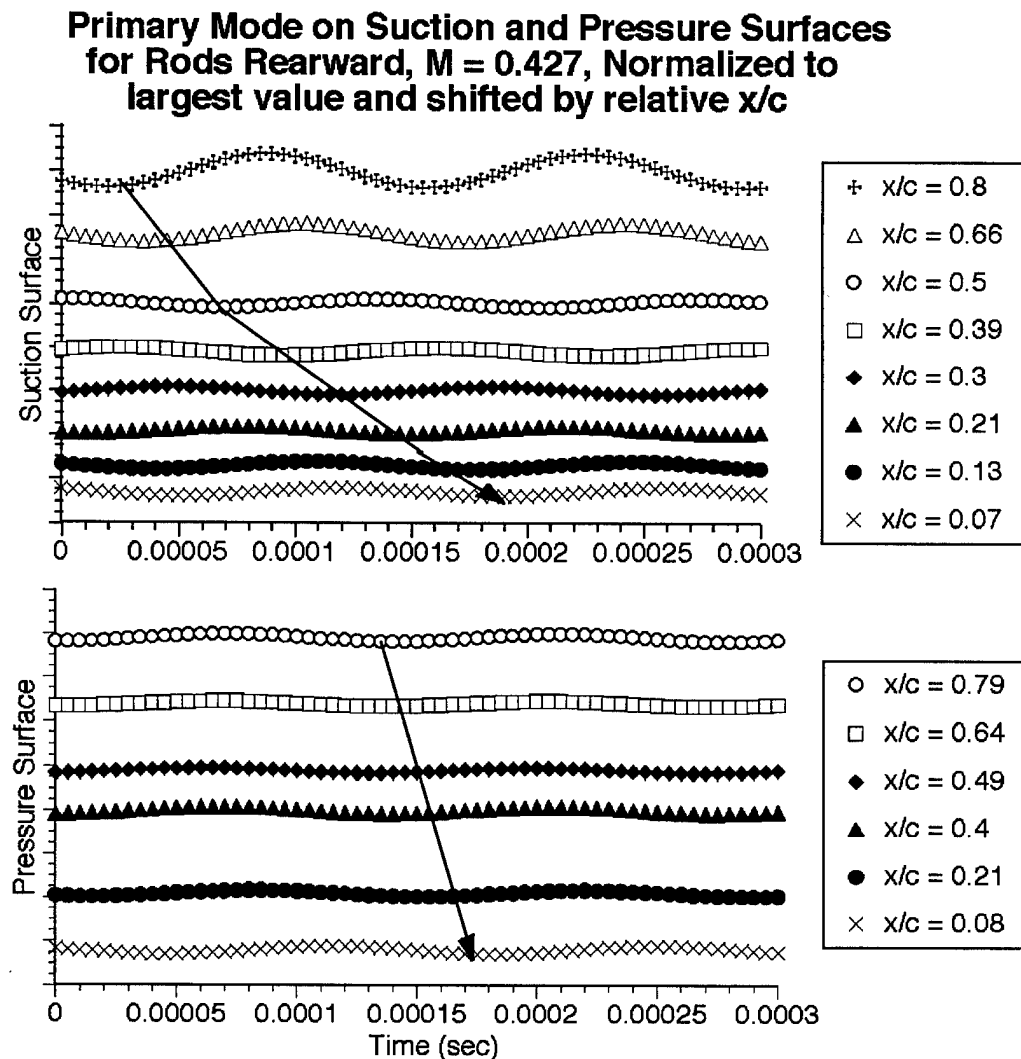


Figure 6.6 Primary Time Series

**First Harmonic on Suction and Pressure Surfaces
for Rods Rearward, $M = 0.427$, Normalized to
largest value and shifted by relative x/c**

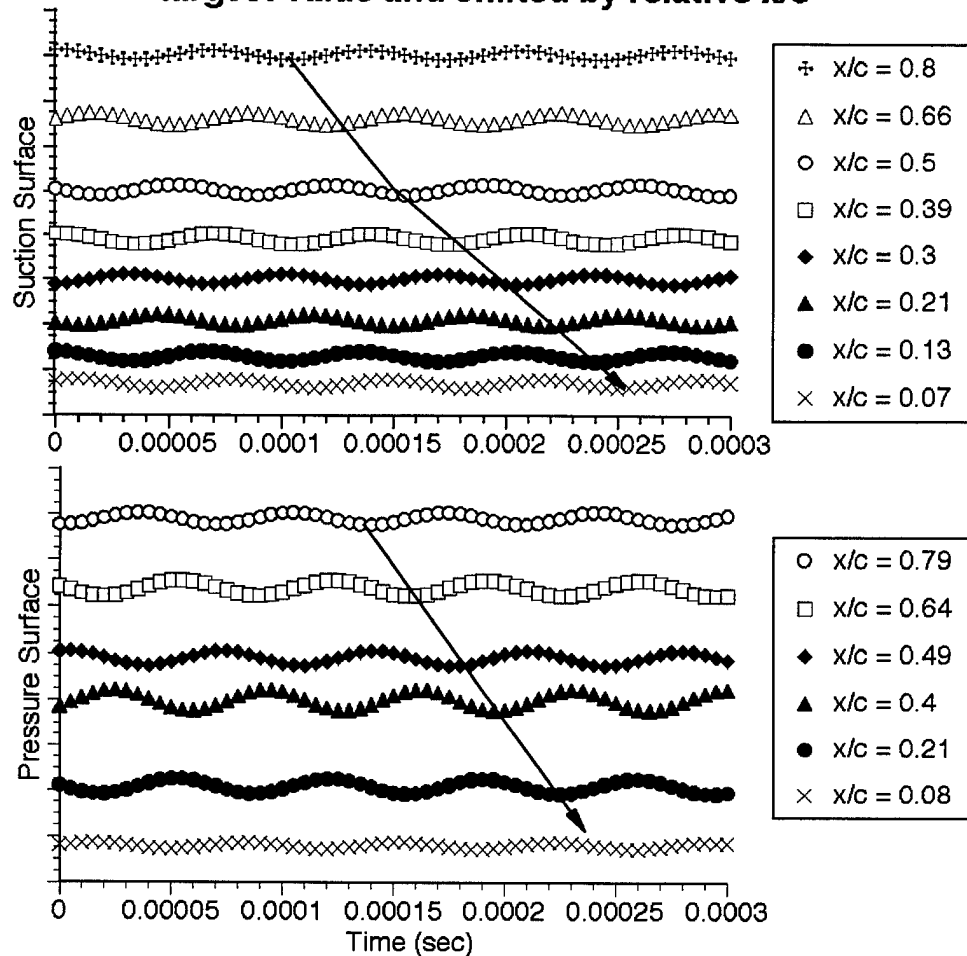


Figure 6.7 Harmonic Time Series

response as a function of time (respectively), displaced along the vertical scale to reflect each's relative-chord position to that of the other signals. It is clear from these Figures that there is a phase relationship between signals. The phase relationship of the primary and harmonic response, respectively, clearly indicates that both "waves" propagate from the trailing edge to the leading edge of the

vaness. Note that the ensembled signals of Figures 6.3, with their interaction between the primary and harmonic did not easily allow this interpretation. Using the phase lag of the emanating primary and harmonic signals as in Eqs. (6.5) and (6.6), the phase may be linearized in terms of a single freestream Mach number as:

$$\sin\left(\omega t + \phi_t - \frac{(c - x) \omega}{a_\infty(1 - M_\infty)}\right) \quad (6.7)$$

where ϕ_t is the phase delay at the vane trailing edge and a_∞ is the speed of sound. It should be noted that the phase shift is not only Mach number dependent, but also frequency dependent. Figure 6.8 shows two curves assuming a suction surface mean Mach number of 0.59 for the primary and harmonic phase shift as a function of relative vane chord predicted from the simple linearized theory of Eq. (6.7) overlaid on experimentally measured phase shift for the primary and harmonic response of the nominal cascade vane for an inlet Mach number of 0.427. Figure 6.8 shows that the primary and harmonic phase shifts may be inferred to be emanating from the same source and propagating upstream through approximately the same Mach-number flow. Further, both slopes show a phase shift

Upstream Travelling Wave for Primary Forcing Frequency of 7280 Hertz and First Harmonic with Mach 0.59 compared with data from Rods Downstream Case with $M_{inlet} = 0.427$

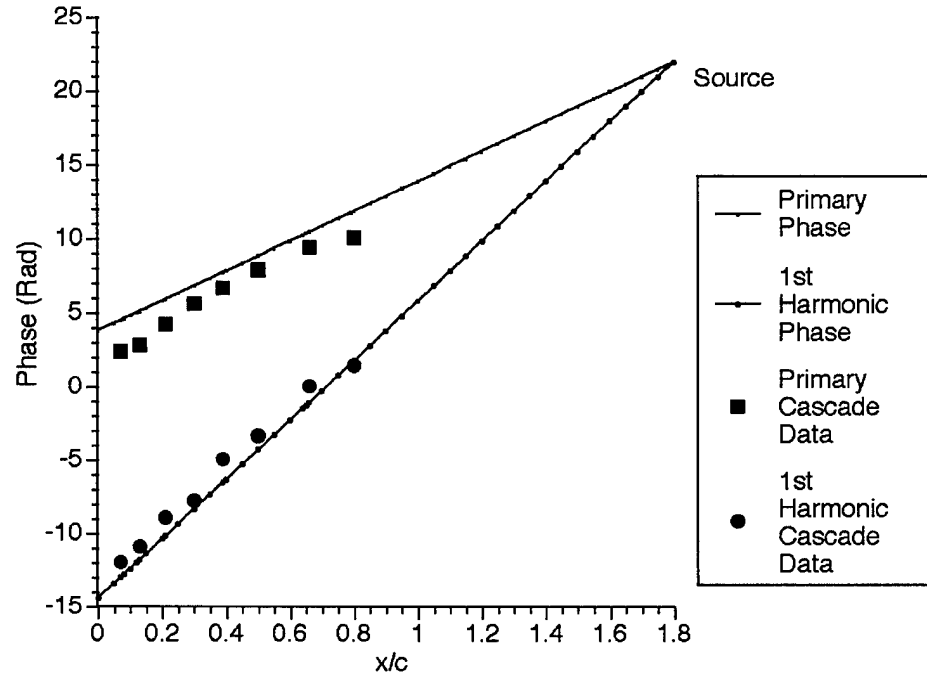


Figure 6.8 Suction Surface Upstream Travelling Wave vs Primary and Harmonic Phase

consistent with an average flow Mach number of approximately 0.59 through the cascade. This is as it should be since the flow accelerates as it passes through the cascade, its local Mach number being greater or less than the average due to the cascade aerodynamics. Additionally, the approximate average Mach number of 0.59 based on comparing propagation velocity to the measured phase of the unsteady data compares well with the local suction surface Mach number for the same flow conditions based on the steady

pressure coefficient values, as shown in Fig. 5.5 which had an average Mach number of approximately 0.57. While the pressure surface gives similar trends, the phase data is not as consistent, as shown in Figure 6.9. Similar phase information for the higher mach number cases is presented in Appendix G. The decomposition of the primary and harmonic signals using Eqs (6.5) and (6.6) constitute a reasonably compatible solution of the inverse problem (i.e. determining the input disturbance based on the surface unsteady pressure measurements) involving rearward forcing of the cascade

Upstream Travelling Wave for Primary Forcing Frequency of 7280 Hertz and First Harmonic with Mach 0.35 compared with data from Rods Downstream Case with $M_{inlet} = 0.427$

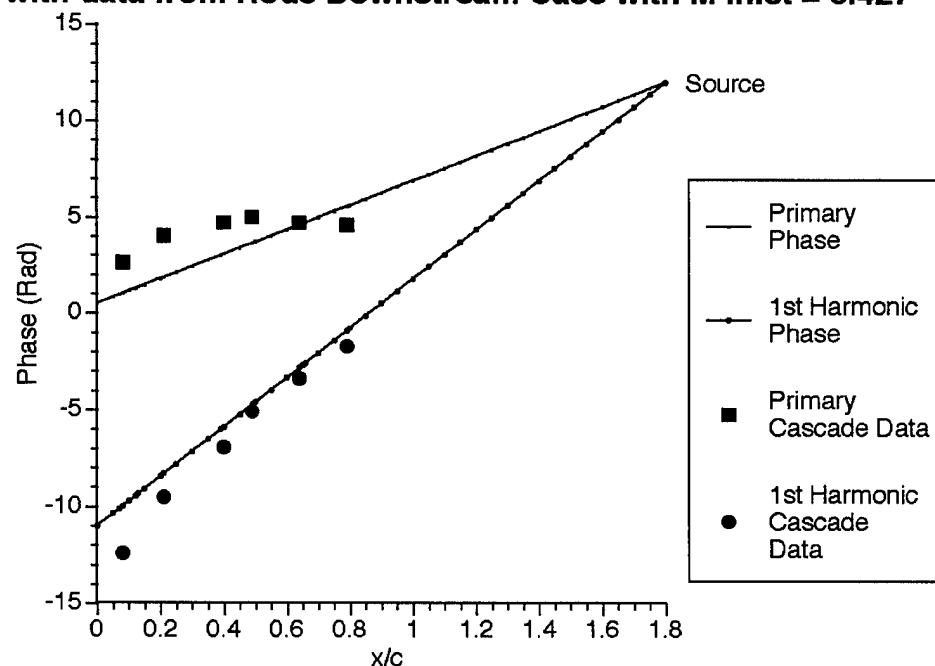


Figure 6.9 Pressure Surface Upstream Travelling Wave vs Primary and Harmonic Phase

row (c.f., discussion in Section 6.6).

6.5 Chordwise Amplitude Variation with Mach Number

The various data presentations for the range of Mach numbers tested are contained in Appendix G. Many of the same trends discussed for Mach 0.427 are also present in these other Mach-number data. There is, however, a noticeable change in the characteristic of the amplitude decay for the primary response as a function of distance from the source. It has already been noted that at Mach 0.427 these amplitude decay in a manner compatible with the notion that they are associated with a potential field of a periodic cylinder-bound circulation (c.f., Section 6.6), as shown in Fig. 6.5; this figure is repeated in Fig 6.10. As Mach number increases, this trend begins to be altered near $x/c = 0.3$. This change in character was noted for the raw rms signal in Figure 6.2; however, in Fig. 6.10, for the decomposed primary response only, the character change with Mach number is more pronounced. In fact, this "amplification" of the amplitude is so pronounced that the normalizing signal switches from the $x/c = 0.8$ pressure to the $x/c = 0.3$ signal; this shows up in Table 6.1 where the normalizing

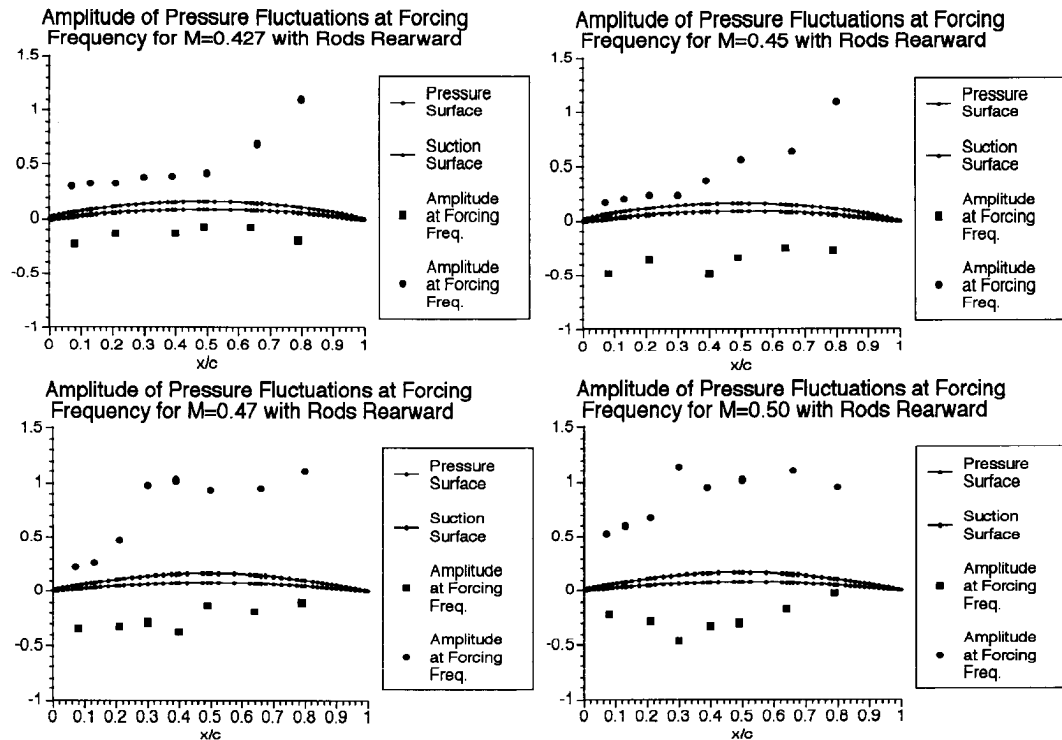


Figure 6.10 Normalized Pressure Amplitude at Primary Forcing Frequency for Increasing Mach Number

amplitude actually increases even though the source signal is decreasing as evidenced by the need to boost the gain on the trigger signal in order to maintain the post amplification voltage at over 9.0 volts. The possible significance of the unsteady pressure behavior with Mach number will be further discussed in the Chapter 8.

6.6 Closing Remarks.

The rearward forcing cases have indicated the relative amplitude of the primary and harmonic surface response and the

appropriate phase for upstream running disturbances. Furthermore, with increasing inlet Mach number, an indication of increased pressure amplitude was demonstrated at the 30 percent of chord position on the suction surface (became the new normalizing unsteady pressure). Perhaps the most significant trend is the magnitude and structure characteristics present on the rearward-forced vanes is of the same order of amplitude and as complex as the response due to forward forcing of the cascade (to be presented in Chapter 7). Although this will be discussed again in Chapter 9, it is important to mention this fact here since emphasis on rearward forcing has been historically neglected; conventional wisdom has always assumed that upstream sources with convecting and vortical disturbances dominate the response (Verdon, 1989).

Finally, a few observations about the character of the unsteady pressure (particularly on the suction surface) for the primary frequency must be noted. Although the closest pressure data to the trailing edge was only at $0.80c$, a projection of the data from Figs. 6.2 and 6.10 indicate that the rms unsteady pressure is largest at the trailing edge. Further, projection of the data from the pressure surface indicate that the unsteady pressure may be different on the

suction and pressure side at the trailing edge. Again, conventional wisdom would suggest that there is a problem (Atassi 1995, Glegg 1995). The theoretical requirement for *downstream* propagating waves that enter the vanes at their leading edge, for these cases a singularity can only exist at the leading edge, or equivalently, the Kutta condition requires that the unsteady pressure at the trailing edge be equal on pressure and suction sides. Recall from earlier discussions that the decay in the suction surface unsteady pressure of Figure 6.10.a, with an *upstream* moving disturbance, appeared to be consistent with the effect of an oscillating bound circulation at the excitation cylinder. Examination of Figure 6.10.a shows that this might be possible and still satisfy the requirement that $P'_{\text{suction}} = P'_{\text{pressure}}$; discussions with Glegg (1995), however, suggested an alternative interpretation. Apparently no one has analyzed a forward propagating disturbance with loaded, cambered airfoils; the physics of such a disturbance might actually allow a trailing-edge singularity. Unfortunately, the cusped, production stators did not allow instrumentation in the region beyond 80% chord. In any event, this rearward forcing data has raised a number of new theoretical questions.

CHAPTER SEVEN

FORWARD FORCING OF CASCADE

7.1 Forcing Gust.

Forward forcing of a stator cascade row represents the conditions within turbomachinery where convected (viscous) and potential disturbances from an upstream rotor or ingested disturbances from other sources would interact with the stator row. As described in Chapter 4, the unsteady "gust" was produced from shedding off of five circular cylinders aligned normal to the incoming flow, and parallel to the vane spans, with the same spacing as the vane row. All unsteady-forcing data presented in this chapter were taken for mid-passage alignment of the forcing rods. It is not clear whether the forward forcing "gust" produced by the cylinders is irrotational or vortical; however, its "periodicity" in time can be described by examining the trigger signal used to phase lock the vane response. Figure 7.1 gives the trigger signals (obtained as described in Chapter 4) and their PSD's for two Mach-number cases for forward forcing. Both traces represent 400 ensembles of

**Trigger Time History and Power Spectrum with Rods Forward
for $M = 0.43$ and $M = 0.585$**

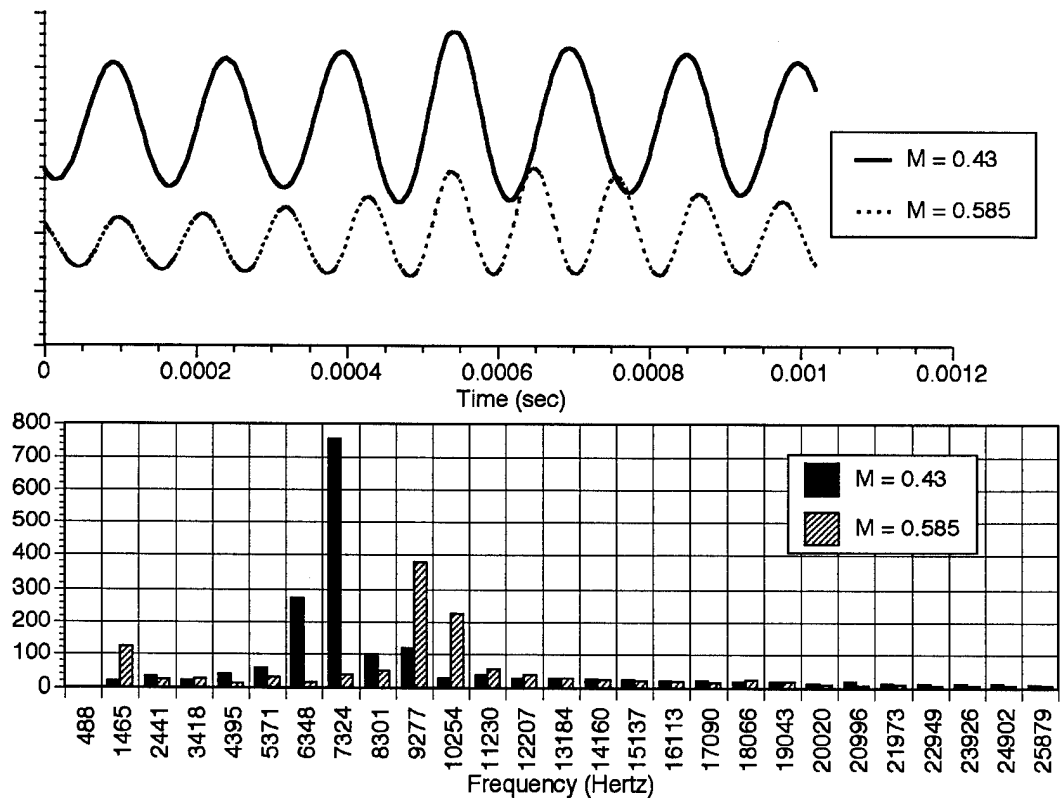


Figure 7.1 Trigger Signal and Power Spectrum for Rods Forward

conditionally-sampled trigger information. The PSD plots show that the primary forcing signal is fairly narrow band. The tailing off of the average signal from the center, locking point, is due to an amplitude modulation of the signal amplitude at all Mach numbers. The character of the modulation is similar to the rearward forcing cases described in Chapter 6. The highest cascade inlet Mach number was 0.585, limited by the loss of the cylinder-trigger signal,

probably due to near sonic conditions on the rods.

7.2 Gross RMS Unsteady-Pressure Response.

Figure 7.2 shows the rms fluctuating pressure as a function of span location on both the suction and pressure sides of the vanes for forward forcing over a range of Mach numbers. The data presented are from the more central profile, Engine Axis Two of Figure 4.3; although these data are similar to Engine-Axis-One data (Fabian and Jumper, 1995). Due to possible wall effects and slight geometry effects mentioned in Chapter 5, only Engine-Axis-Two data is presented here. The Engine Axis One data gives similar trends and is included in Appendix H. Recall that these signals are built up from phase-locked signals from eight different blades. The data is the ensemble averaging of 400 sets of conditionally sampled data. The absolute vertical height of the data-point above and below the upper and lower airfoil surfaces, respectively, in Fig. 7.2 is the rms pressure amplitude for each chordwise position in pounds per square inch. Apparent in the two lower Mach number cases is a decrease in rms pressure with increasing chordwise distance. Referring again to Figure 7.2, changes in the amplitudes of the unsteady pressures with

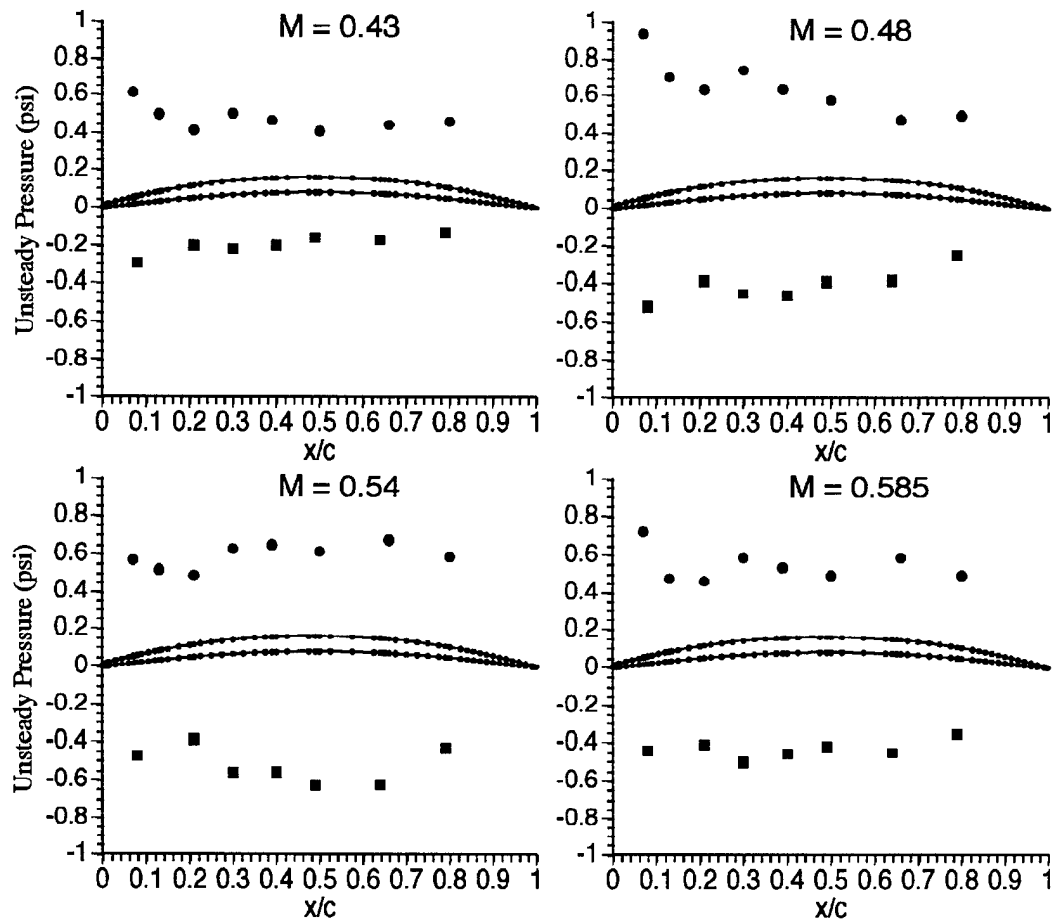


Figure 7.2 RMS Pressures for Rods Forward

Mach number are apparent, the most noticeable being the increase, decrease then increase in the near-leading-edge unsteady pressure (0.07 and 0.12% chord) with increasing Mach number in the forward forcing cases for the suction surface. On the pressure surface the increase in amplitude in the mid-chord with increasing Mach number is also evident.

7.3 Phase-Locked Unsteady Pressure Signals.

Figure 7.3 shows raw, phase-locked unsteady pressure data from 400 ensembles at a Mach number of 0.43 for the forward forcing of the cascade. Similar data for other Mach numbers are presented in Appendix H. The three graphs of Figure 7.3 represent the normalized unsteady pressure versus nondimensional time (i.e., tU_∞/c) for the suction surface of the vane, the normalized unsteady pressure for the pressure surface of the vane, and the ensembled trigger signal for that Mach number, respectively. The normalization for the pressure response is based on the amplitude of the largest unsteady signal, in this case, the 0.07c trace on the suction side. Each trace is displaced by two units of P/P_{\max} , so that the nominal zeros for the suction surface are at 2, 4, 6, 8, 10, 12, 14 and 16 for the 0.80c, 0.65c, 0.50c, 0.40c, 0.30c, 0.20c, 0.12c and 0.07c, respectively. The trigger signal is not normalized. The actual voltage after gain is shown with the conditional-sampling-trigger threshold set at 8.5 volts (see Chapter 4). At this Mach number (0.43), the unsteady pressure signals, except for the trigger signal, appear uniform over the entire nondimensional time, encompassing

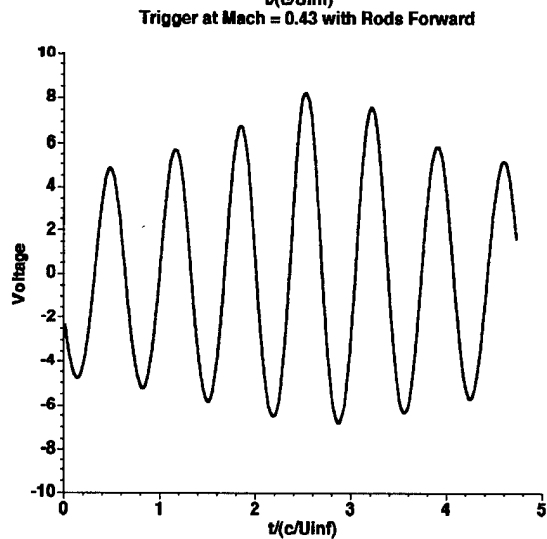
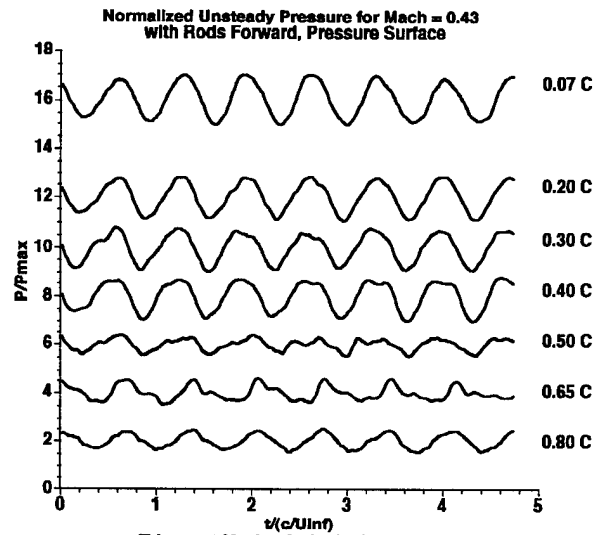
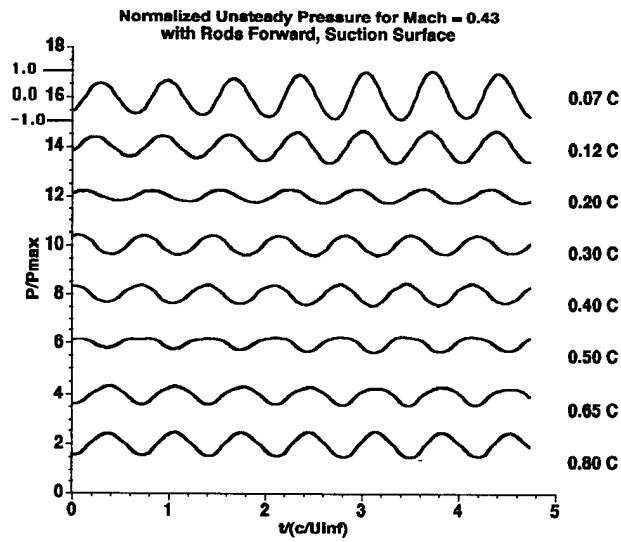


Figure 7.3 Signal Averages for $M = 0.43$ with Rods Forward

approximately seven cycles of unsteady forcing. It is important to note that all signals are triggered at the center of the data window, $(t/(c/U_\infty)) \approx 2.5$, and that the amplitude of the trigger decays slightly on each side of the central trigger. Table 7.1 provides the normalizing amplitudes for Figure 7.3 and Appendix H. These normalizing pressure represent the largest unsteady pressure measured for that Mach number. Although not appearing as complex as that shown for the rearward forcing cases (Chapter 6), it is clear that, like the rearward forcing data, there is significant structure to the forward forcing unsteady surface pressure response.

Table 7.1 Normalizing Amplitudes
for Figure 7.3 and Appendix H

Normalizing Amplitudes in psi for each plot	Suction Surface	Pressure Surface
Mach 0.43 Rods Rearward	0.714	0.157
Mach 0.48 Rods Rearward	1.04	0.367
Mach 0.54 Rods Rearward	0.334	0.539
Mach 0.585 Rods Rearward	0.390	0.258

The signals were decomposed into the primary and harmonic frequencies in manner similar to the rearward forcing cases, discussed in Chapter 6, using the simulated annealing technique described in Chapter 4. Table 7.2 gives the relevant parameters of the fifteen decompositions, primary and harmonic frequency, amplitudes, and phase referenced to zero nondimensional time. Any

Table 7.2 Equation (7.1) Amplitude and Phase for Mach 0.43 data, Primary Frequency = 6718 Hz

x/c Position	Primary Amplitude, A_p psi	Primary Phase, ϕ_p radians	1st Harmonic Amplitude, A_h psi	1st Harmonic Phase, ϕ_h radians	RMS Error of Fit psi
0.07 Suction	0.568	1.677	0.009	2.822	0.074
0.12 Suction	0.370	2.047	0.005	0.210	0.050
0.20 Suction	0.170	2.753	0.010	0.808	0.020
0.30 Suction	0.269	-2.605	0.006	0.139	0.017
0.40 Suction	0.272	-2.078	0.006	-1.881	0.021
0.50 Suction	0.170	-2.183	0.004	0.213	0.034
0.65 Suction	0.249	0.803	0.034	-2.927	0.014
0.80 Suction	0.308	0.798	0.014	2.057	0.016
0.07 Pressure	0.141	-1.015	0.011	-1.09	0.016
0.20 Pressure	0.124	-0.797	0.012	0.790	0.012
0.30 Pressure	0.118	-0.461	0.018	0.968	0.012
0.40 Pressure	0.117	-0.506	0.017	0.002	0.017
0.50 Pressure	0.043	-0.768	0.016	0.563	0.010
0.65 Pressure	0.053	-2.45	0.021	0.986	0.016
0.80 Pressure	0.059	-1.834	0.005	0.594	0.009

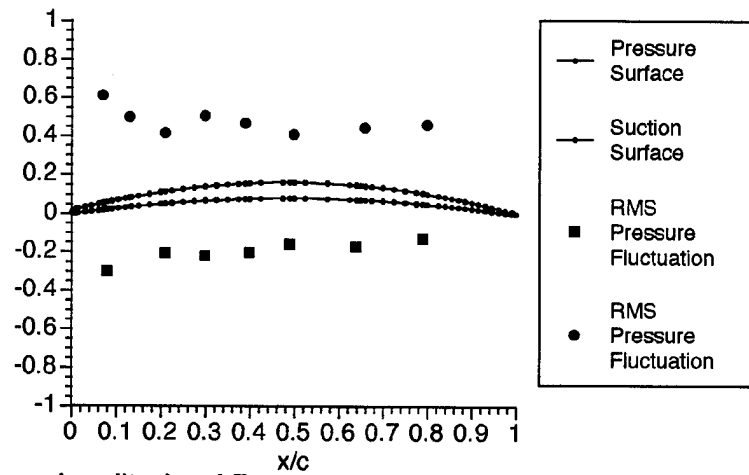
particular signal may be reproduced from these parameters as:

$$\tilde{P} = A_p \sin(2\pi f_p t + \phi_p) + A_h \sin(2\pi f_h t + \phi_h) \quad (7.1)$$

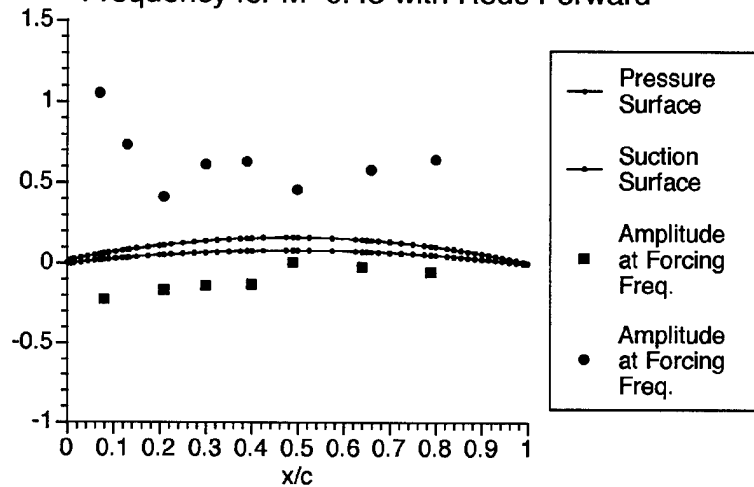
where A_p and A_h are the primary and harmonic amplitudes, respectively, f_p and f_h are the primary and harmonic frequencies, respectively, and ϕ_p and ϕ_h are the primary and harmonic phase lags, respectively.

The decomposed primary and harmonic data are presented in Figure 7.4. The primary amplitudes show an apparent nodal character along the chord, indicating possibly wave cancellation. Present are two local magnitude depressions on the suction surface and one on the pressure surface. This nodal character was not present for the rearward forcing cases discussed in Chapter 6. The harmonic data is more difficult to interpret due the relatively small magnitude of all the harmonics which are an order of magnitude smaller than the primary on the suction surface and at most half the magnitude on the pressure surface. The harmonic magnitudes are within the uncertainty bands of the measurements which are shown in Appendix J. For that reason, only the primary disturbance frequency will be discussed in the remainder of the chapter.

RMS Pressure Fluctuations for $M = 0.43$
with Rods Forward



Amplitude of Pressure Fluctuations at Forcing
Frequency for $M=0.43$ with Rods Forward



Amplitude of Pressure Fluctuations at Twice Forcing
Frequency for $M=0.43$ with Rods Forward

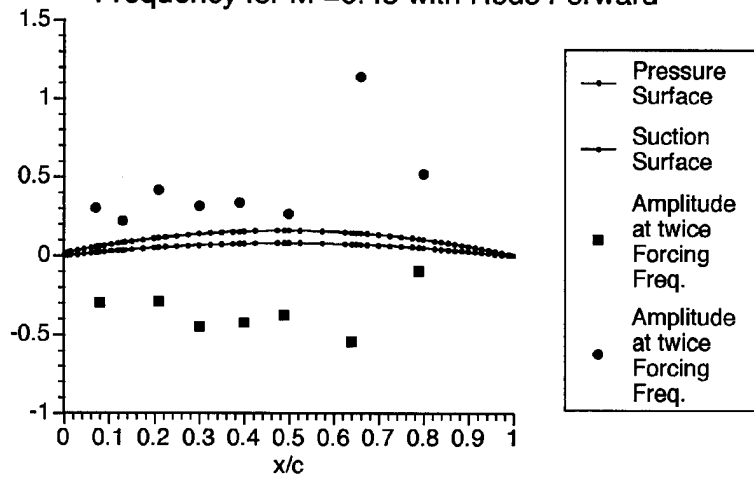


Figure 7.4 RMS Pressure Amplitude,
Normalized Primary and Harmonic Pressure
Amplitudes

7.4 The Inverse Problem

Besides the convection of a vortex street through the cascade row and its influence on the vanes, the positioning of the rods forward of the vane row could excite additional surface reflections or possible acoustic modes which might be detected by the unsteady-surface-pressure measurements. An acoustic mode analysis, which is included in Appendix I, showed no difference in possible acoustic modes between forward forcing of and rearward forcing of the vane row. Thus, the majority of the remaining analysis emphasized the more important interaction of potential and convective disturbances.

It seems reasonable to suppose that, in effect, the upstream, unsteady pressure/flow field associated with the von-Karman shedding from the cylinders would be made up of two parts. The first part would have a characteristic frequency at the primary frequency, and in the absence of other sources of disturbance (ignoring the wake for the moment), would be similar to a potential flow field made up of flow around a cylinder superimposed with a sinusoidally oscillating bound circulation. For an incompressible flow this would have the form:

$$\bar{V}_{\text{incomp}}(r, \theta, t) = V_{\infty} \left(1 - \frac{a^2}{r^2}\right) \cos \theta \hat{r} - \left[V_{\infty} \left(1 + \frac{a^2}{r^2}\right) \sin \theta + \frac{\Gamma \sin(\omega t)}{2\pi r} \right] \hat{\theta} \quad (7.2)$$

where a is the radius of the cylinder (Anderson, 1991). Sufficiently far downstream ($r \gg a$) and along a ray directly downstream from the cylinder,

$$\bar{V}_{\text{incomp}}(r, t) \cong V_{\infty} \hat{r} - \frac{\Gamma}{2\pi r} \sin(\omega_p t) \hat{\theta} \quad (7.3)$$

where ω_p is the frequency of the primary signal. In compressible (subsonic) flow the pressure signals causing the unsteady velocity must propagate at the acoustic velocity downstream with the mean flow. This would have two effects: the first would be a delay time which would exhibit itself as a phase lag associated with the Mach number and the distance, r , from the source; the second would be a foreshortening of the apparent effect of the oscillating circulation by:

$$d_{\text{apparent}} = r \sqrt{1 - M_{\infty}^2} \quad (7.4)$$

so that the signal a distance r directly downstream of the cylinder would be:

$$\bar{V}_{\text{comp}}(r,t) \cong V_{\infty} \hat{r} - \frac{\Gamma}{2\pi r \sqrt{1-M^2}} \sin \left[\omega_p t - \frac{r \omega_p}{a_{\infty}(1+M)} \right] \hat{\theta} \quad (7.5)$$

Considering the phase information from the pressure signal decompositions, the upstream disturbance could conceivably be modelled in a manner similar to the downstream disturbance (Figures 6.8 and 6.9). In the case of forward forcing of the cascade row, the unsteady lift or circulation from the cylinder would be transmitted at the local velocity plus the speed of sound. Assuming constant Mach number, a linearization similar to that discussed in Chapter 6 would result in a phase relationship of:

$$\sin \left(\omega t + \phi_L - \frac{x\omega}{a_{\infty}(1+M_{\infty})} \right) \quad (7.6)$$

where ϕ_t is the phase delay at the vane leading edge and x is the distance along the chord. Again the phase relationship is a function of the forcing frequency and the Mach number. The resulting phase lines from the source 0.8c upstream of the cascade row are plotted with the experimental phase results for the $M = 0.43$ case in Figures 7.5 and 7.6 for the suction and pressure surfaces, respectively.

Downstream Travelling Wave for Primary Forcing Frequency of 6718 Hertz and First Harmonic with Mach 0.5 compared with data from Rods Upstream Case with $M_{inlet} = 0.43$

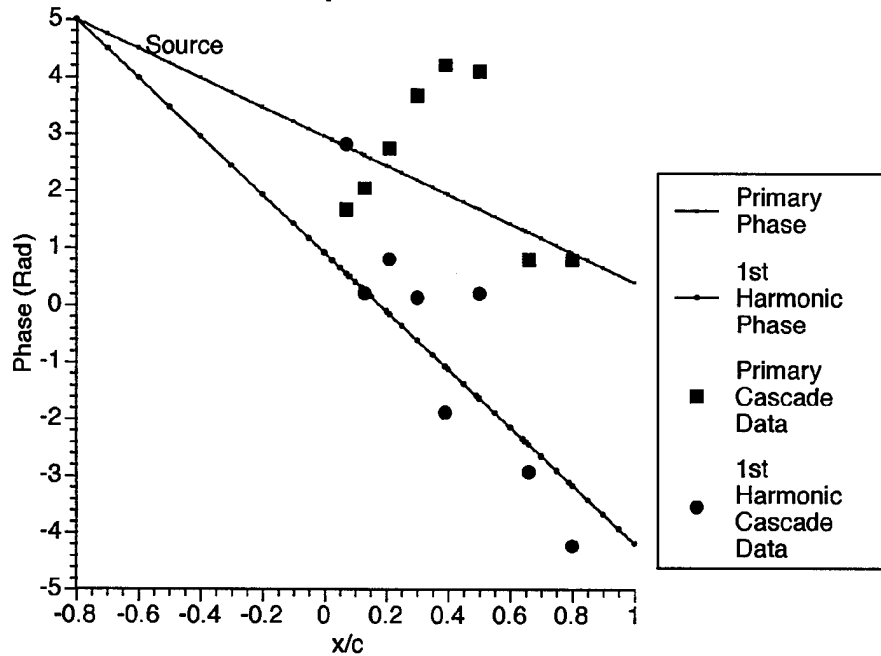


Figure 7.5 Suction Surface Downstream Travelling Wave Primary and Harmonic Phase

Downstream Travelling Wave for Primary Forcing Frequency of 6718 Hertz and First Harmonic with Mach 0.4 compared with data from Rods Upstream Case with $M_{inlet} = 0.43$

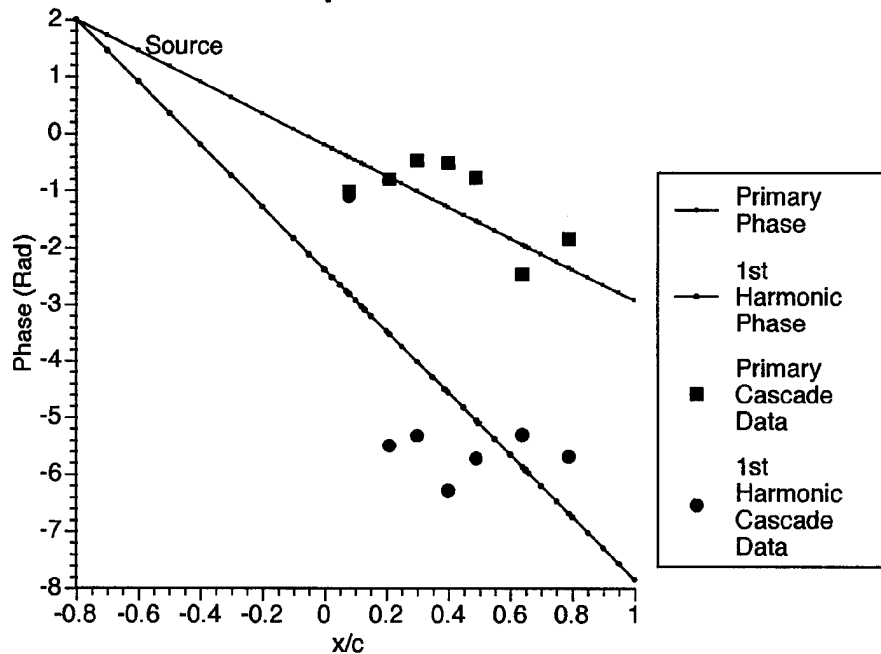


Figure 7.6 Pressure Surface Downstream Travelling Wave Primary and Harmonic Phase

Unfortunately, the agreement between the model and the data found in the rearward forcing cases of Chapter 6 was not present with the forward forcing cases. In fact, the "fits" are terrible. Again this simple model considers only the unsteady lift on the cylinder and its associated circulation. The simplified phase model derived from the rearward forcing cases did not include the influence of convected disturbances.

The second part of the current model includes the effect of disturbances convecting at the local velocity. The disturbances contain integrated vorticity (i.e., circulation) of a magnitude equal to and opposite of the periodic change in unsteady bound circulation on the cylinders. A shed vortex pair represent one cycle with a frequency matching the unsteady lift examined previously; however, the current disturbance convects at the mean flow velocity (See Figure 7.7). The magnitude of the disturbance is assumed to be constant as it is convected through the cascade passage. This train of convecting disturbance can be expected to create a near-sinusoidal oscillation on the surface due to the combination of vortex pairs inducing local acceleration of the flowfield. The convecting disturbances can be modelled as:

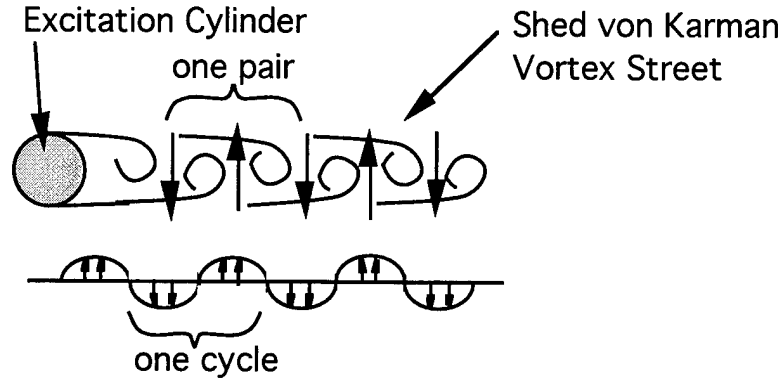


Figure 7.7. Induced Fluctuating Velocity Normal to Wake that convects through the Vane Passage with the Mean Flow

$$P_{\text{convect}}(x,t) \cong A_c \sin \left[2\pi ft + \phi_c - \frac{x2\pi f}{u_\infty} \right] \quad (7.7)$$

where A_c is the amplitude of the convected disturbance and ϕ_c is the phase of the convected component. When combined with the term due to unsteady lift on the rod, the unsteady pressure has the form:

$$P(x,t) \cong \frac{A_p}{r \sqrt{1-M^2}} \sin \left[2\pi ft + \phi_p - \frac{x2\pi f}{a_\infty + u_\infty} \right] + A_c \sin \left[2\pi ft + \phi_c - \frac{x2\pi f}{u_\infty} \right] \quad (7.8)$$

where A_p is the amplitude of the potential effect and ϕ_p is the phase of the potential disturbance. The two terms will constructively and destructively interfere due to similar frequencies and differing effective wavelengths, as shown in Figure 7.8. Note that in this simplified model, the velocity is assumed to be constant, with no

Sample Calculation at Mach 0.43 showing interaction at an Instant in Time and the resulting RMS over a Cycle

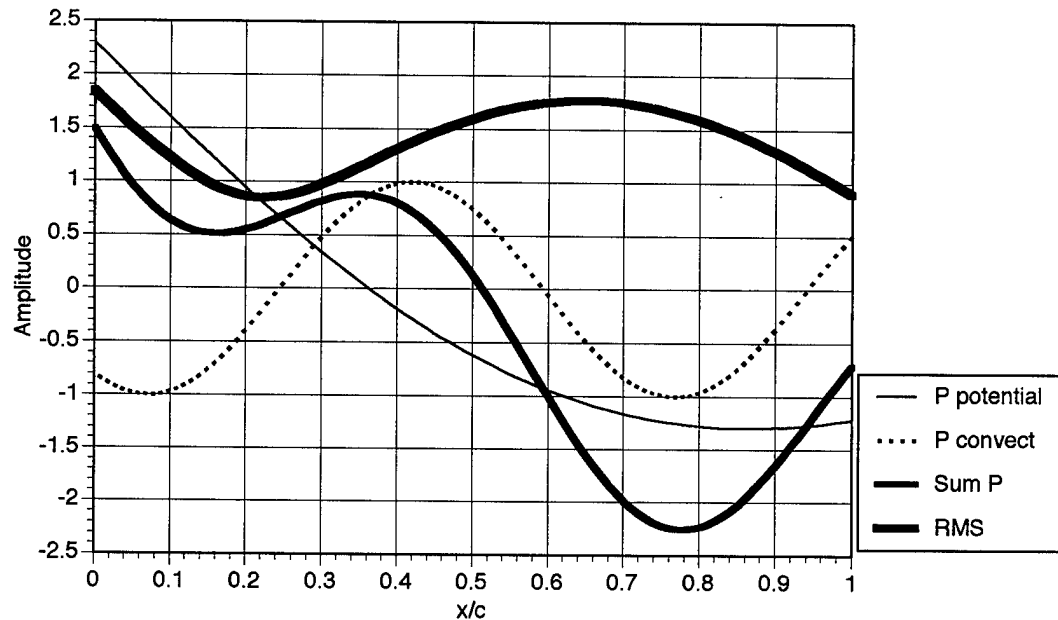


Figure 7.8 Example of Interaction of Potential and Convective Disturbances

aerodynamic distortion of the disturbance and the effect of the airfoil surface coupling back to the flow has also been neglected.

The goal of the model was to understand the key differences between the rearward forcing of the cascade row; mainly, the apparent reverse wave direction seen in the phase maps (Figures 7.5 and 7.6), and nodal nature of the pressure decompositions.

The interaction of the inferred potential and convective disturbances causes local “nodes” on the stator surface, as shown in Figure 7.9 where the experimental data was normalized to the most

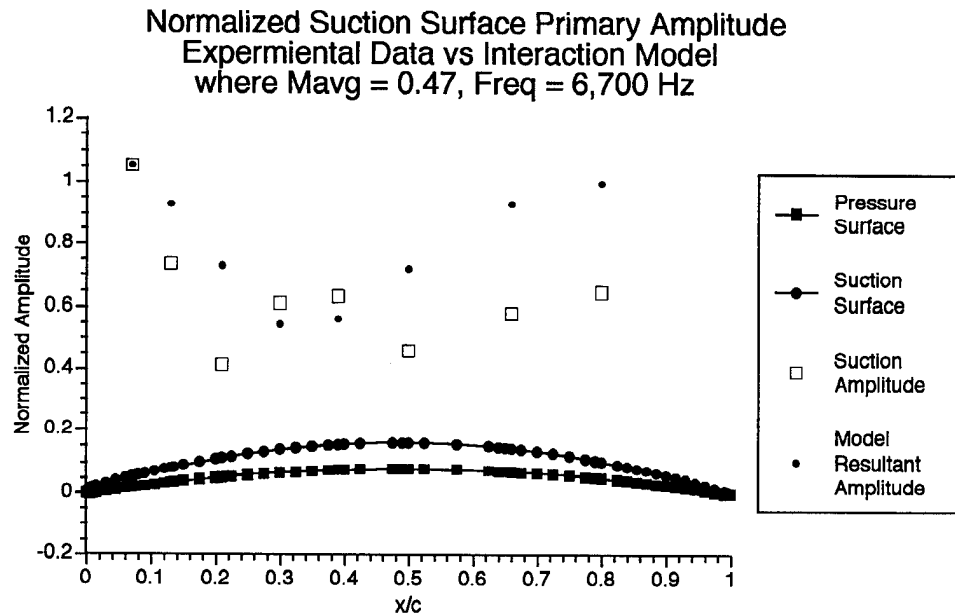


Figure 7.9 Experimental Data vs Interaction Model for Primary Frequency

forward transducer measurement. The modelled interaction was also normalized to overlay the experimental data. The modelled data shows a single node near the mid-chord but not the double node apparent in the experimental data. When considering the resultant phase, the combination of the inferred potential and convected disturbances can result in the appearance of backward running disturbances in a portion of the stator chord, as shown in Figure 7.10. In the region of 0.25% to 0.45% chord the phase indicated a disturbance moving in the opposite direction. Although not of the scale of the primary seen in Figure 7.5, this interaction appears to partially explain the unusual wave direction seen from the stator

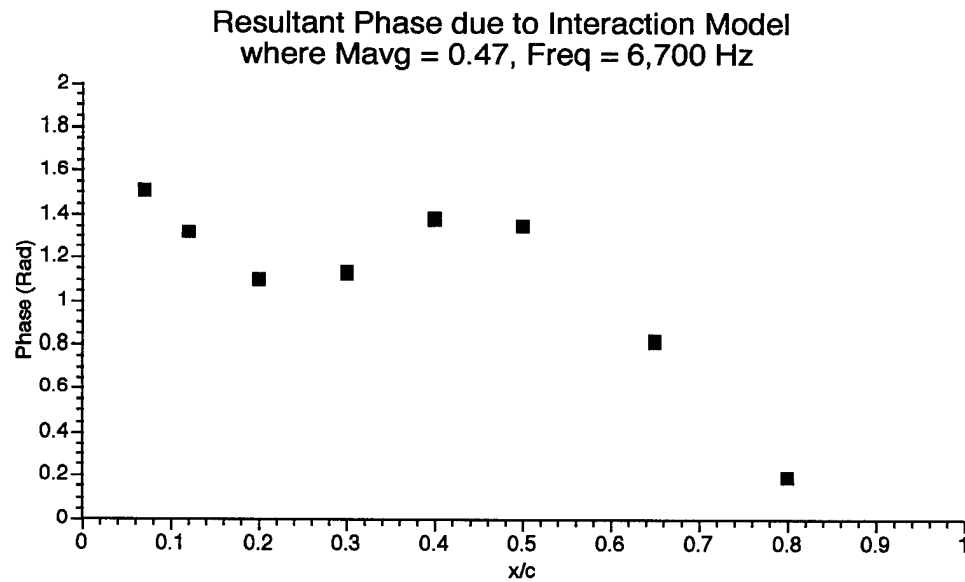


Figure 7.10 Resultant Interaction Model Phase for
Figure 7.9

surface pressure phase results (square symbols of Fig. 7.5 nearly perpendicular to phase model). Note that the current model is extremely dependent on the assumed convective speed and the relative magnitudes of the two disturbances. Furthermore, the model has not taken the effects of the stator unsteady aerodynamic effects or geometry into consideration. Unfortunately, the coupled interaction of the potential and convected disturbances at the same frequencies is difficult to properly decompose. This is further complicated since the associated unsteady airfoil interaction is also included in the surface pressure measurement. Given these caveats, the trend information from the model demonstrates a source for the

nodal nature of the surface pressure measurements and an explanation for the apparent differing wave directions on portions of the stator surface.

7.5 Chordwise Amplitude Variation with Mach Number

The various data presentations for the higher Mach number cases involving forward forcing of the cascade row are included in Appendix H; however, the trends of the primary forcing frequency on the stator surface pressure with increasing Mach number may be examined. The local depressions in unsteady pressure magnitude over the Mach range was readily apparent on both surfaces, as shown in Figure 7.11. The lower two Mach number cases showed similar characteristics on the suction surface and a trend toward increasing unsteady pressure on the mid-chord region on the pressure surface. A further increase in Mach number to 0.54 resulted in an overall decrease in the suction-surface unsteady pressure and an associated large increase in the pressure-surface unsteady pressure. In fact, the normalizing pressure moved from the leading edge on the suction surface to the 65% chord of the pressure surface. The Mach 0.54 case represented the largest unsteady pressure on the pressure

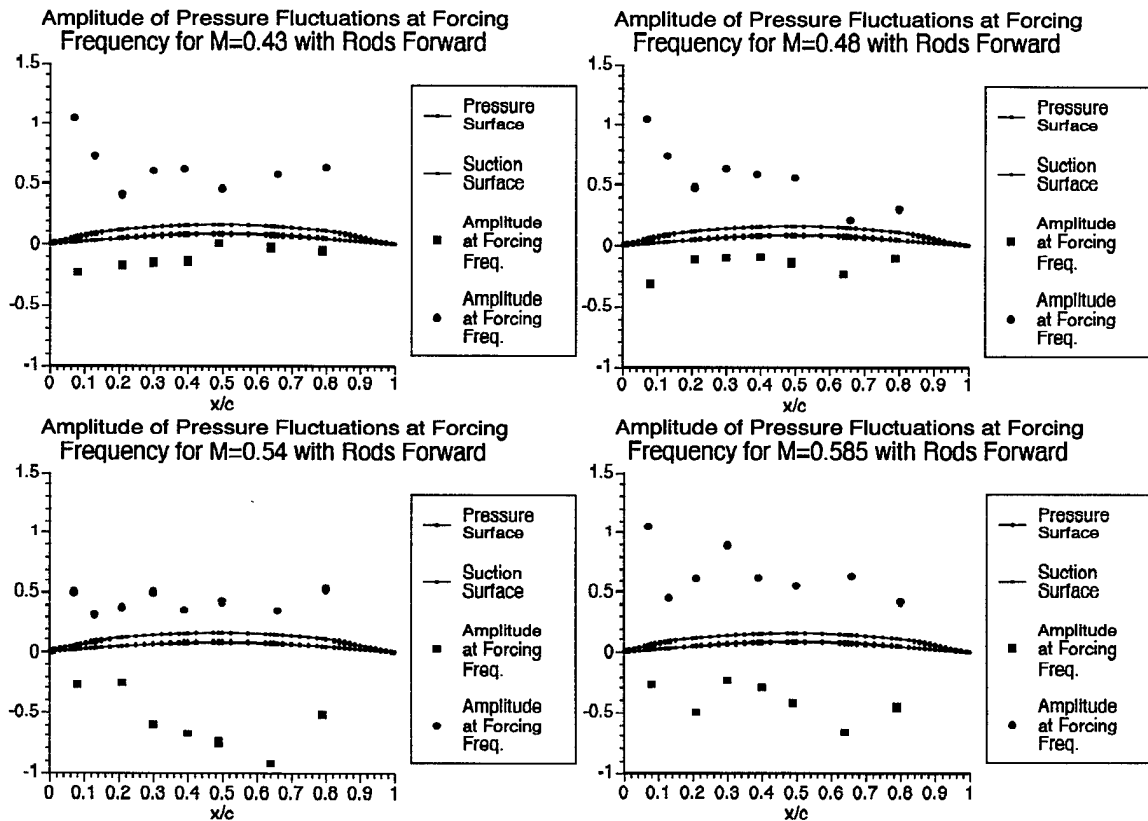


Figure 7.11 Normalized Pressure Amplitude at Primary Forcing Frequency for Increasing Mach Number

surface for the cases examined. The highest Mach number cases again showed the local depressions in unsteady pressure along both surfaces with unsteady pressure of approximately the same magnitude. Although difficult to interpret, the interaction of the potential, the convected, and the associated airfoil interaction with the disturbances appear to cause the mode shapes and strongly varying chordwise amplitudes.

7.6 Concluding Remarks

The forward forcing case is more complex than the rearward forcing cases examine in Chapter 6. The interaction between disturbance source types and the resulting stator aerodynamic adjustments are difficult to decouple since the forcing occurs at the same frequency and the system is effectively coupled due to the compressible subsonic flowfield. Given the complexity of the flow, turbofan manufacturers have tended to widely space the fan rotor and the stators to reduce the aerodynamic potential interactions and allow the rotor wakes to further mix with the mean flow. The increased spacing has reduced unsteady vibration and also reduced the rotor-stator interaction noises from the fan. Unfortunately, dramatically increasing the spacing within a multistage compressor is not feasible in an aircraft engine due to the increased shaft length and system weight. Since the rotors and stators within an aircraft engine remain closely coupled and continue to have failure problems, an improved tailoring of spacing and design flow Mach number could conceivably reduce the unfavorable interaction effects of potential and convected disturbances. Additionally, designers must be aware of the nodal character of the unsteady pressure

signals which could adversely influence the natural bending modes of a stator or blade. Consequently effort must be made to position the unsteady surface pressure nodes away from structural nodes.

CHAPTER EIGHT

ON THE ISSUE OF ACOUSTIC BLOCKAGE

In this chapter, the data for rearward and forward unsteady forcing is examined for evidence of *acoustic blockage*. In order to aid in that examination, the chapter begins with a background section describing what is meant by and how one might recognize *acoustic blockage*.

8.1 Background.

The term *acoustic blockage* was originally coined by Atassi, Fang and Ferrand (Atassi, Fang, and Ferrand, 1994) to identify a proposed physical mechanism for producing large amplifications in unsteady pressure near the maximum Mach number of a near-sonic but fully subsonic flow through a cascade. In earlier research, Atassi, Fang and Patrick noted a sharp rise in the magnitude of the unsteady pressure near the maximum Mach number location on the suction surface of high-Mach but fully-subsonic cascade blades. They conjectured that the physical mechanism was that “ the near-

sonic velocity acts as a barrier preventing the acoustic waves from propagating upstream" (Atassi, Fang, and Patrick, 1993). In a separate paper Atassi noted that unsteady pressures at transonic speeds have been traditionally associated with the unsteady motion of a normal shock ending the supersonic region over the suction side of the vane in an unsteady transonic cascade (Atassi, 1994); yet calculations presented (Atassi, Fang, and Patrick, 1993) gave a similar rise in unsteady pressure near the highest Mach number in a near-transonic, but fully-subsonic cascade, citing the 1993 proposed physical mechanism as the cause of the rise in unsteady surface pressure.

In the 1994 paper (Atassi, Fang, and Ferrand) this proposed mechanism was more fully explored computationally. For a convecting vortical gust, the requirement for *acoustic blockage* was that the flow must have a near sonic Mach number somewhere on the surface of the vanes in the cascade. It was also found that the level of the unsteady pressure due to *acoustic blockage* was strongly reduced as new acoustic modes "cut on." Cut on is the condition that allows the initiation of sound radiation within a duct or passage for a given mode combination (Kurosaka, 1989).

In a concurrent effort Atassi, et al. (1994) modelled a plane, periodic acoustic wave propagating from either the inlet downstream or the exit upstream into a near-transonic converging diverging nozzle. Their plane wave had a reduced frequency, $k_1 = \omega d_i / 2U_\infty$, equal to 0.3, where d_i was the nozzle throat diameter and U_∞ was the inlet velocity. Their results for an inlet Mach number of $M_\infty = 0.64$ are shown in Figures 8.1 and 8.2. Atassi, et al. showed that for a downstream propagating wave, while amplifications did develop at Mach numbers greater than 0.95, the magnitude was far less than that for an upstream propagating wave. In the case of the upstream propagating wave, not only did a large amplification appear, but, significant amplification was present at Mach numbers as low as ≈ 0.62 . Again they conjectured, in their words, this unsteady

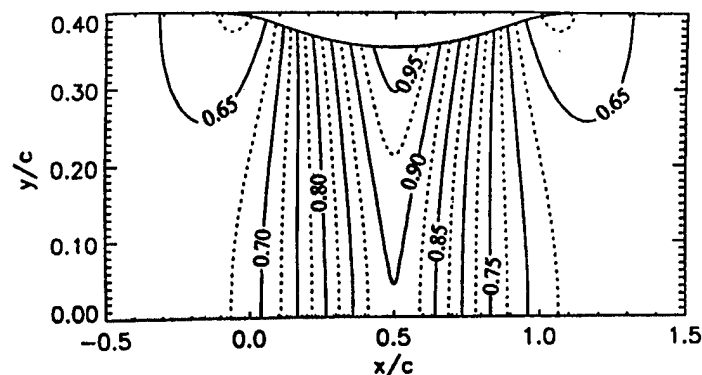


Figure 8.1 Nozzle Geometry and Mean Flow Mach Number Contours, (Atassi, 1994)

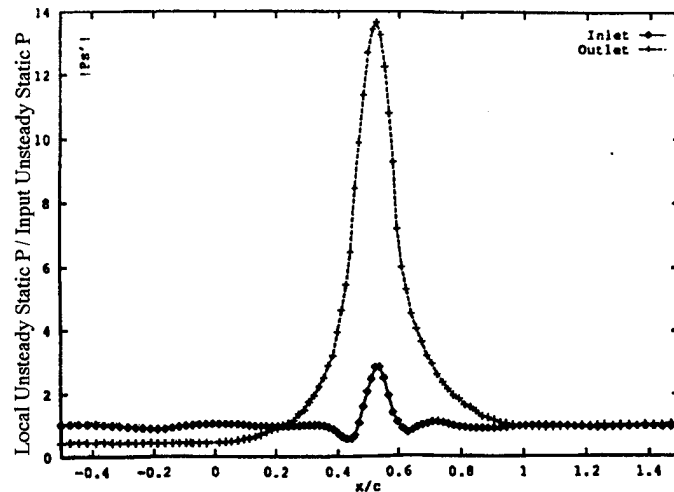


Figure 8.2 Magnitude of Unsteady Pressure for Inlet and Outlet Disturbances for $k = 0.3$, (Atassi, 1994)

“pressure rise is the result of the *acoustic blockage* of the upstream propagating acoustic wave by the near sonic mean flow.”

8.2 Experimental Evidence of Acoustic Blockage in the Present Study.

As discussed in Chapters 5, 6, and 7, the highest Mach numbers in the unsteady (forced) cascade was set by the highest inlet Mach number that still produced unsteady shedding, $M_{inlet} = 0.585$ and $M_{inlet} = 0.50$ for the forward and rearward forcing cases, respectively.

These correspond to the highest inferred Mach numbers on the suction surface of the vanes of 0.81 and 0.73 for the forward and rearward forcing cases, respectively. These inferred Mach numbers

were determined from the surface pressure coefficients using Eq. 5.3. Potential modifications to the cascade to increase these Mach numbers are discussed in Chapter 9. Even though these maximum Mach numbers are not close to sonic, the resulting unsteady pressure data were examined for evidence of *acoustic blockage*.

8.2.1 Forward Forcing Case.

The unsteady pressure response data for the forward forcing cases presented in Chapter 7 was examined for evidence of *acoustic blockage*. Since the signal amplitude for the harmonic frequency was relatively low, and as discussed in Chapter 7, no inference of any particular trends were noted, only the primary-frequency response data were seriously examined; in particular, Figure 7.11 was examined for any indication of acoustic effects. No specific evidence contained in Figure 7.11 would suggest any particular Mach number trend in a build up of unsteady pressure near the maximum Mach number location, near $x/c \approx 0.3$ to 0.4 .

The fact that no evidence of significant acoustic effects is present in the forward forcing cases is not unexpected. First, it is not known whether the reduced frequency ($k \approx 5$) at these Mach

numbers elicits forward travelling acoustic waves from near the trailing edge of the vanes. Further, the strength of such a wave, even if *acoustic blockage* were to amplify it, for a Mach number on the order of ≈ 0.81 , would be much smaller than the potential and convected waves due to the excitation cylinders.

8.2.2 Rearward Forcing Case.

Both the primary-frequency and harmonic unsteady pressure response data were examined for evidence of *acoustic blockage*. The primary-frequency response data shown in Figure 6.10 of Chapter 6, and repeated here as Figure 8.3. Here a trend in the data reveals a unsteady pressure bulge developing at x/c locations between 0.3 and 0.4 with increasing Mach number that is not present in the 0.427 inlet Mach number data. As noted in Chapter 6, this amplification is so great by the 0.5 inlet Mach number case that the signal at $x/c = 0.3$ represents the highest unsteady pressure. Estimating the extent of amplification over what would be present from the 0.427 inlet Mach number case, this could represent an amplification of as much as 4 times that which it might otherwise have been and approximately 1.2 of the signal amplitude at $x/c = 0.8$. Concerning

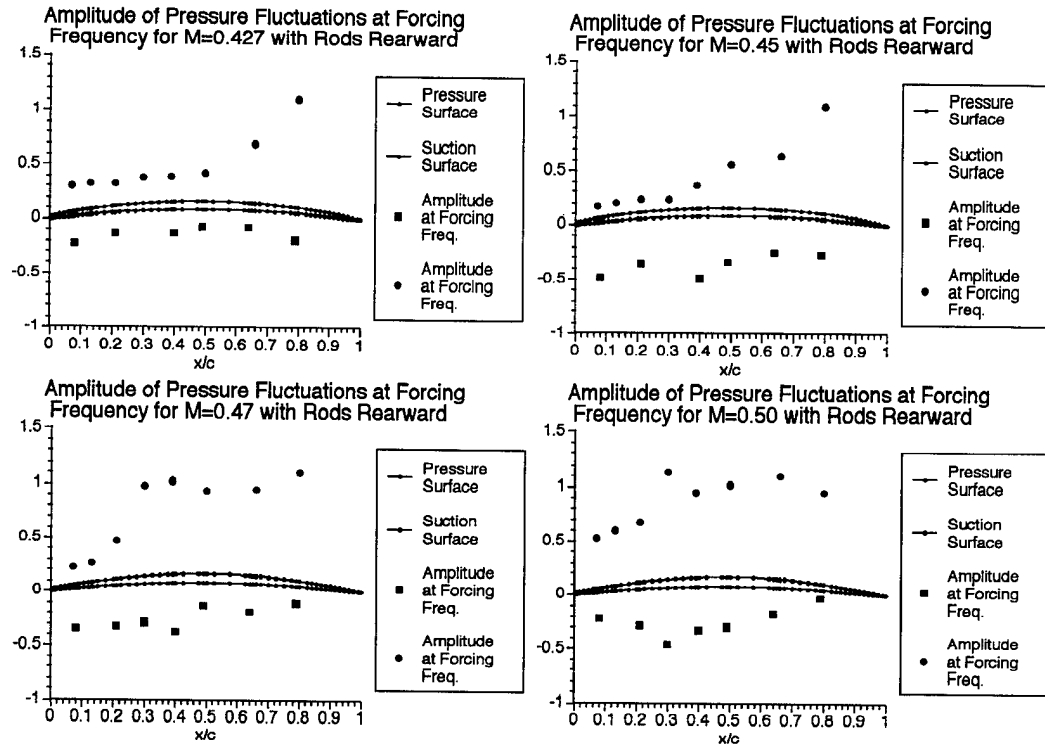


Figure 8.3 Normalized Pressure Amplitude at Primary Forcing Frequency for Increasing Mach Number

the first harmonic, Figure 8.4, shows that there might be some indication of a Mach-number-trend amplification between x/c location 0.3 and 0.4 on the suction side; however, as noted in Chapter 6, these amplitude data are difficult to interpret.

As discussed in Chapter 6, the highest Mach number over the suction surface for the 0.5 inlet Mach number case was inferred to be approximately 0.73 at an x/c location near 0.3 and 0.4. Referring to Figures 8.1 and 8.2, Atassi, et al. saw an amplification of approximately 1.5 at a Mach number of 0.73 ($x/c \approx 0.85$) for the

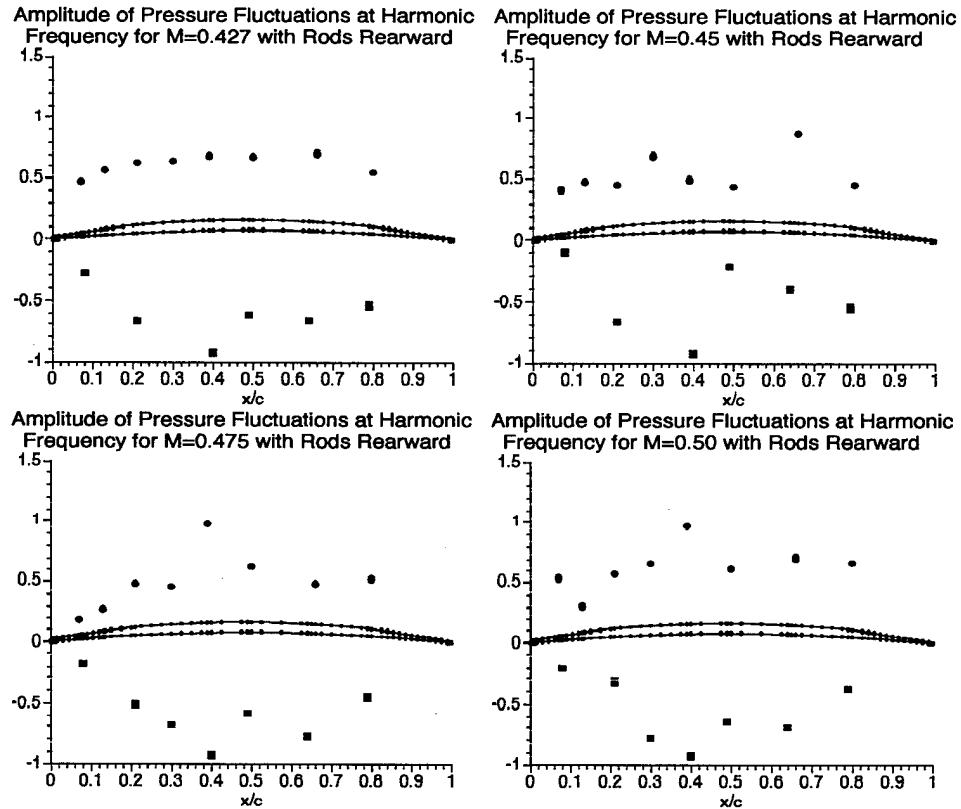


Figure 8.4 Normalized Pressure Amplitude at First Harmonic of Forcing Frequency for Increasing Mach Number

pressure at x/c of 0.3 with increasing Mach number in Figure 8.3 appears unusual and might be consistent with the *acoustic blockage* mechanism and the numerical results of Atassi, et al. for the rearward forced convergent-divergent nozzle, higher experimental passage Mach numbers would be required to interpret the *acoustic blockage* phenomenon. Possible methods to better investigate *acoustic blockage* will be discussed in the next chapter.

CHAPTER NINE

SUMMARY OF CONCLUSIONS AND FURTHER WORK

This dissertation presented the unsteady pressure response from a compressible cascade, with the unsteady forcing produced by von Karman shedding from a row of circular cylinders placed upstream or downstream of the turning vanes. The vanes were production-hardware stator vanes from a Garrett F-109 turbofan engine. The Mach numbers, flow conditions, and unsteady-forcing reduced frequencies used in the cascade experiment were close to actual conditions that the stators would see in an operating F109 engine.

Analysis of these unsteady data has added to the body of knowledge into the nature of unsteady forced response. This chapter will attempt to summarize these and suggest certain implications that appear to logically follow from these insights. Some of these ramifications suggest further work and that too will be briefly discussed. In the future work section, some mention of follow-on F-109 engine work will be made. Finally, a brief list of contributions

of this Dissertation research will be given.

9.1 Major Results and Implications.

9.1.1 Unsteady Pressure Data.

First the data itself must be considered significant. As mentioned in Chapter 1 and in Appendix A, there is a paucity of compressible unsteady cascade data, and these new data add to the available collection. Although a rigorous description of the gust was beyond the scope of the present work, its reduced frequencies and method of creation have been described. On the other hand, great effort was made to describe and analyze the mean flow (time-averaged) conditions into and through the vane row (Chapter 5). Care was taken to carefully condition the trigger signal so that the ensembled pressure response was representative of any single response elicited by the same type gust. Recall that the gust itself was modulated by a lower, essentially-constant frequency (especially at the highest Mach numbers), so that the trigger conditioning captured the peak amplitude during modulation. Each ensembled response (16 signals for each tunnel/forcing condition) was then reduced to a six parameter representation made up of

amplitude, frequency, and phase for a primary (forcing frequency) and harmonic (twice the forcing frequency) two-sine-wave decomposition of the response. The representation makes it easy for any potential user of these data to recreate the response.

9.1.2 Analysis of the Unsteady Response Data

The decomposition of the response data, as described in 9.1.1, made it possible to analyze the data for each of its two component frequencies separately. It, in fact, seems fair to say that no proper analysis of these-type data can be made without performing some type of decomposition. In studying each frequency separately it was possible to attach significance to the amplitude of the response as a function of chordwise position, and, as importantly, the phase relationship as a function of chordwise positions.

9.1.2.1 Forward Forcing.

It is important to point out that without prior experimental research and study of the rearward-forcing data, attaching any significance to the amplitude and phase data for the forward-forcing data would have been nearly impossible. It is, in fact, for this reason

that the chapter on rearward forcing precedes that for the forward forcing in this Dissertation. Having an understanding of the rearward-forcing data, made it possible to extract some significant inference about the nature of the forward forcing gust, including the interaction of the potential and convected disturbances.

Most of the analysis of the response concentrated on the primary response frequency; however, as was the case for the rearward-forced response, the first harmonic frequency in the gust appears to be ascribable to alternate shedding of the vortices (two each cycle) causing a drag fluctuation at two times the primary forcing frequency. As such, it probably represents a cascade flow-axis fluctuation of the velocity. It appears that the complicated phase map (phase vs. chord location) for the forward-forced response in the primary frequency can be partially explained by the forcing gust being made up of two types of superimposed disturbances, both at identical frequency. The first type disturbance, termed here as "potential," is ascribed to the unsteady aerodynamic field generated by the alternating bound circulation on the forcing cylinder, inherent to von Karman shedding. The potential disturbance radiates into the flow at the local acoustic velocity, and so carries

through the vane row at approximately the local flow velocity plus the local speed of sound. The second type gust, termed here the "convected" disturbance, is ascribed to the von Karman vortex street that generates a near sinusoidal velocity fluctuation normal to the mean flow that convects through the vane row at the local velocity. Because of their disparate transport velocities, these two types of disturbances with the same frequency have distinctly different wave lengths. Thus, these two type of disturbances add constructively and destructively in otherwise unexpected ways. The construction/destruction places nodes and maximum unsteady pressure points at locations other than had been previously expected with direct ramifications to unsteady forced response and high-cycle fatigue.

Although this potential and convected nature of the forcing gust in the cascade is due to stationary excitation cylinders, the ramifications toward rotating machines are clear. In a rotating machine, the gusts elicited by a rotor on the stator also contain two components. Each rotor blade has associated with it an aerodynamic potential field fixed in the rotor-blade frame. The field is made to pass by any particular stator vane and its influence propagates at

acoustic speeds. In addition, each rotor blade elicits a vortical wake which subsequently convects toward the stator. Thus, the gust in a rotating machine must also be governed by similar constructive/destructive concepts that govern the forcing gust in the cascade. Similar structural considerations concerning interaction of aerodynamic and structural nodes must also apply.

9.1.2.2 Rearward Forcing.

As in the forward forcing data, proper interpretation of the rearward-forced response was possible only after decomposition into its primary (forcing frequency) and harmonic (twice the forcing frequency) frequency parts. Once decomposed, an interpretation of the phase information demonstrated that the pressure response was due predominantly to potential forcing that propagates upstream into the mean flow at acoustic speed. Further, simple modelling of the disturbance demonstrated why the phase maps were frequency dependent. It also demonstrated the compatible nature of the inferred average Mach numbers to earlier work (Chapter 5) on describing the time-averaged flow environment in the cascade, and the difference in Mach number between the suction and pressure

sides of the vanes.

Analysis of the amplitude of the primary and harmonic parts of the response provided the most instructive insights into the nature of rearward forcing. First, it is clear that unsteady pressure response due to downstream disturbances propagating forward into the vane row are on the same order of magnitude as those due to disturbances generated upstream of the row that propagate convectively and acoustically downstream into the vane row. This has direct ramifications on the problem of stage-to-stage interactions in turbomachinery since nearly all research emphasis has focus on disturbances created upstream of a blade row.

Second, the discontinuity in unsteady pressure up to the 80% chord position implying a possible trailing edge unsteady pressure discontinuity when forced from downstream does not match with the conventional Kutta condition. This finding suggests that the flow physics supports a singularity at the trailing edge in the case of upstream travelling acoustic disturbances, a singularity not supported for a downstream propagating disturbance entering the row from upstream. Again, this finding has direct ramifications toward the stage-to-stage interaction problem.

Third, analysis of the primary frequency, response amplitude data reveals a Mach number trend that is compatible with the hypothesized mechanism of *acoustic blockage*. This compatible evidence has direct ramification on stage-to-stage coupling from downstream disturbance on upstream stages because of the low Mach number applicability to forward travelling waves.

9.2 Suggestions for Future Work.

9.2.1 Further Cascade-Related Work.

Although much has been extracted from the response data of this Dissertation research, it is clear that more work should be done on defining and modelling the unsteady flow field elicited by the excitation cylinders. Such definition would be imperative in order to use the data as bench marks for code developers. Some work would also be useful in how to adapt or modify present numerical methods to incorporate the description of the disturbance as input boundary conditions to existing codes. In this regard, work should be done to either adapt or modify codes to incorporate downstream forcing of the cascades flow fields.

Because of the decreasing disturbance amplitude with Mach

number elicited by the method of producing the cascade disturbance, the full Mach number range possible in the cascade (through transonic) could not be investigated. Because of this, future cascade work should explore means of increasing the Mach number range over which unsteady forcing of the cascade might be achieved. Possible avenues might include (but should not be limited to): a. active flow excitation by piezo-excited trailing-edge regions of a thin guide-vane row up and/or downstream of the present turning vane geometries; b.) replacement of the present guide vanes with thicker specifically-designed turning vanes that cause the flow to achieve transonic speed at significantly lower inlet Mach numbers than for the present-geometry turning vanes; c.) and designing divergent-convergent inlet and outlet sections for the cascade so that the Mach numbers through the excitation-cylinder rows are significantly less than the inlet and outlet Mach numbers for the turning-vane row of the cascade. Suggestion b.) also holds the advantage of providing a larger vane internal volume for inserting pressure transducers and more flexibility in instrumenting locations nearer to the leading and trailing edges of the turning vanes. Such, nearing to trailing-edge locations would facilitate a careful investigation of the proposed

trailing-edge singularity for rearward forcing of the cascade.

Any of the suggested modifications of the cascade would allow for further investigation of *acoustic blockage* in the case of forward forcing; however, any evidence, or lack thereof, for *acoustic blockage* due to forward forcing must accommodate a wider range of gust frequencies. Recall that the present study used only one reduced frequency; therefore, independent of *acoustic blockage* investigations, future cascade work should plan on a range of reduced frequencies. If the present method of forcing is used, this would only require a range of excitation-cylinder diameters be used.

Finally, original thought on the direction of the present Dissertation research had considered the effect of sweep on the forced response. Because of the relationship with the F109 engine, investigating sweep in the cascade should be considered.

9.2.2 Future Planned F109 Engine Work.

The instrumented turning vanes used in this cascade study are scheduled to be installed in the F109 engine at the United States Air Force Academy. The trigger signal, which will be based on blade passing and the associated engine shaft position should be easier to

acquire that the conditional sampling method required for the cascade shedding. Since the stators are installed in a swept position within the engine, comparisons of the two instrumented radial positions should show a differing time response to the disturbances which could reduce overall unsteady forcing of the vane row. These issues and their potential use in the design process will be examined in the follow-on research.

9.3 Contributions of this Dissertation Research.

Finally, this chapter and Dissertation closes with an enumeration of contributions of this work. Some of these contributions are minor, but still seem worth mentioning.

9.3.1 Cascade.

When the work was initially contemplated, the only hardware that existed were the 25, uninstrumented production F109 engine fan stators brought to Notre Dame from the Air Force Academy. An unsteady linear cascade was designed and constructed that incorporated these stator vanes as turning vanes. This design was shown to be successful through the good flow quality demonstrated

for both the unforced and forced conditions over the entire Mach number range of the cascade. The cascade hardware including vane molds will remain at Notre Dame for further research efforts.

9.3.2 Instrumentation.

Instrumenting the relatively-small stator vanes turned out to be no small task. Because of their intended use in the F109 engine, this instrumentation will continue to be a contribution of the present research.

9.3.3 Rearward Forced Studies.

Had it not been for a fortuitous suggestion by Ferrand to force the flow from downstream of the turning vanes, this Dissertation research would have studied only forward forcing of the cascade. Because of the incorporation of this suggestion, to my knowledge, this constitutes the first experimental investigation of downstream-only forcing of a compressible cascade. Schmidt and Okiishi (1977) investigated coupled upstream and downstream forcing in low-Mach-number facilities, but no studies investigated downstream-only forcing, much less at high compressible Mach

numbers.

9.3.4 Decomposition and Interpretation of Gust.

Although others have demonstrated decomposition of the response signal into primary and harmonic frequencies, no other studies have been able to infer clear meaning from the phase maps and amplitudes. This interpretation was only made possible by the fact that the rearward forcing phase map was so unambiguous. Armed with an understanding of the character of the rearward forced response, it was possible to infer the existence of the potential and convected parts, of the forward disturbance, as discussed earlier. As shown by other published presentation of ambiguous phase maps from forward forced experiments, this Dissertation research constitutes the first rational explanation for why these phase maps, not only are complex, but why they cannot be otherwise.

9.3.5 Acoustic Blockage.

As described earlier, this Dissertation research constitutes the first experimental evidence supportive of the supposition of

acoustic blockage. Further, although contained in the results of Atassi, Fang, and Ferrand (1994), this Dissertation research has underscored the importance of this mechanism even at Mach numbers far from transonic.

9.3.6 Possible Trailing Edge Singularity.

Finally, these data for rearward forcing constitute the first experimental evidence of a possible trailing-edge singularity in the case of rearward forcing. This inference along with all the findings regarding rearward forcing make a direct contribution to the problem of stage-to-stage interactions in turbomachines.

APPENDIX A

ENGINE BASED HISTORICAL BACKGROUND

Aeroelasticity has had a rich tradition within the history of manned flight. For instance, Samuel Langley's aerodrome, one of the earliest powered aircraft, had torsionally weak wing tips which probably led to Langley's failure to control his aircraft (Garrick, 1972). During World War I, aerodynamisist Frederick Lanchester investigated an elevator flutter problem on a British bomber which he eliminated by installing a carry-through rod between the separate elevators to increase torsional stiffness (Garrick, 1972). In 1944, the loss of the rudder on the Messerschmitt 163 rocket fighter during a high speed test to Mach 0.94 was shown to be caused by shock induced flutter (Green, 1971). The B-47, the first swept-wing jet bomber, suffered from aileron reversal at high speed (Green, 1964). As speeds continued to increase, the thin wings of aircraft required increased analysis to avoid aeroelastic effects.

While the history of aircraft jet propulsion is less extensive, the common aeroelasticity and vibration problems were seen in

earlier rotating machinery including steam turbines and aircraft turbochargers. While many aircraft aeroelasticity problems involve classical flutter at low angles of attack, the stall flutter phenomenon involving high angles of attack are more typical in turbines and compressors (Hartog, 1985). Another issue in turbomachinery vibrations is the additional number of excitation sources not present in external flows. In 1924, Wilfred Campbell, from the General Electric Company, developed a method to compare excitation sources and component natural frequencies in steam turbines in an attempt to avoid vibration and fatigue difficulties (Campbell, 1924). The Campbell Diagram, with axes of engine speed and frequency, showed potential vibration points as the intersection of excitation sources and component natural frequencies.

Unfortunately unexpected sources, manufacturing variances, and operational deviations still caused problems to occur. For instance, the British ship, Queen Elizabeth 2, had a failure of its 10th stage starboard high pressure (HP) turbine and 9th stage port HP turbine on her maiden voyage. Both turbine rotor failures were caused by resonance from the turbine nozzles (Rao, 1991). Early axial-flow turbochargers, lacking internal cooling passages, often had fatigue

problems caused by lower-pressure cooling air admitted during part of the rotational cycle. Early turbojets suffered similar vibrational problems. Sir Frank Whittle's W2/500 engine, a 1942 design, suffered from compressor resonance fatigue which often lead to catastrophic failure. Unfortunately, in order to eliminate the fatigue problem, the required stiffening of the compressor reduced engine performance by 14 percent (Boyne and Lopez, 1979). The Jumo 004B turbojet used in the Messerschmitt 262, the first production jet fighter, suffered from turbine fatigue cracking while operating at maximum engine speed due to the excitations caused by the combination of six forward combustors and three aft struts. Max Bentele, a Junkers design engineer, eliminated the fatigue problem by increasing the natural frequency of the turbine blades by shortening the blades and reducing the maximum allowable engine speed (Bentele, 1991). While many of the early failures involved turbines, the modern highly loaded transonic fan and compressors have also had numerous failures. For instance, the grounding of the Air Force B-1B bomber fleet in 1991 due to fan failures (Aviation Week, October 7, 1991) and the recent requirement for additional inspections of General Electric CF6 engines following an Egypt Air

Airbus rotor fatigue failure (Associated Press, 25 August 1995).

Many other vibrational issues are discovered during prototype testing but are seldom referenced in the public domain.

Industry Background.

The life span of stationary and rotating compressor and turbine components in turbomachinery is often determined by the fatigue of the individual components in this hostile, unsteady environment. From an operational or commercial standpoint, the fatigue life requirements of components are specified by the operating cycles, either start-stop or idle-full power-idle, or the device operating hours or some combination of these parameters (Vukelich, 1992). The life requirements and the subsequently smaller inspection intervals are required since the majority of the fatigue failures are vibration related and result in crack growth (Rao, 1991). This has important ramifications for air transportation safety and ground-based steam and gas turbine power generation operability. Currently, large aircraft engines are being designed for lives of the range of 20,000 to 40,000 hours, while industrial power generation engines with a less severe operating environment are

designed for 100,000 hours (Wilson, 1984). The F109 fan and compressors have design lives of 18,000 hours (Vukelich, 1992).

With the current level of understanding of unsteady forces within the gas turbine engine, design engineers merely attempt to avoid the occurrence of excitation sources at component bending or torsional mode frequencies. A typical analysis approach for rotating hardware is the Campbell diagram as shown for the Garrett F109 fan in Figure A.1. The slight curvature of the various blade vibration modes with increasing rotational speed is due to Southwell's theorem concerning the at-rest natural frequency and rotational frequency (Hartog, 1985). Due to the complexities of the fan blade shapes, modes are usually found through finite element analysis and verified by holographic techniques using shaker tables. For example, the analyzed and experimentally verified second mode of the F109 fan blade are shown in Figure A.2, with the midspan damper marked in each diagram. The F109 incorporates a fan blade midspan damper for two reasons: to introduce additional bending and torsional restraint which increases the single degree of freedom mode frequencies and to reduce foreign object damage, FOD, susceptibility (Oates, 1989). From an experimental standpoint, the blade midspan

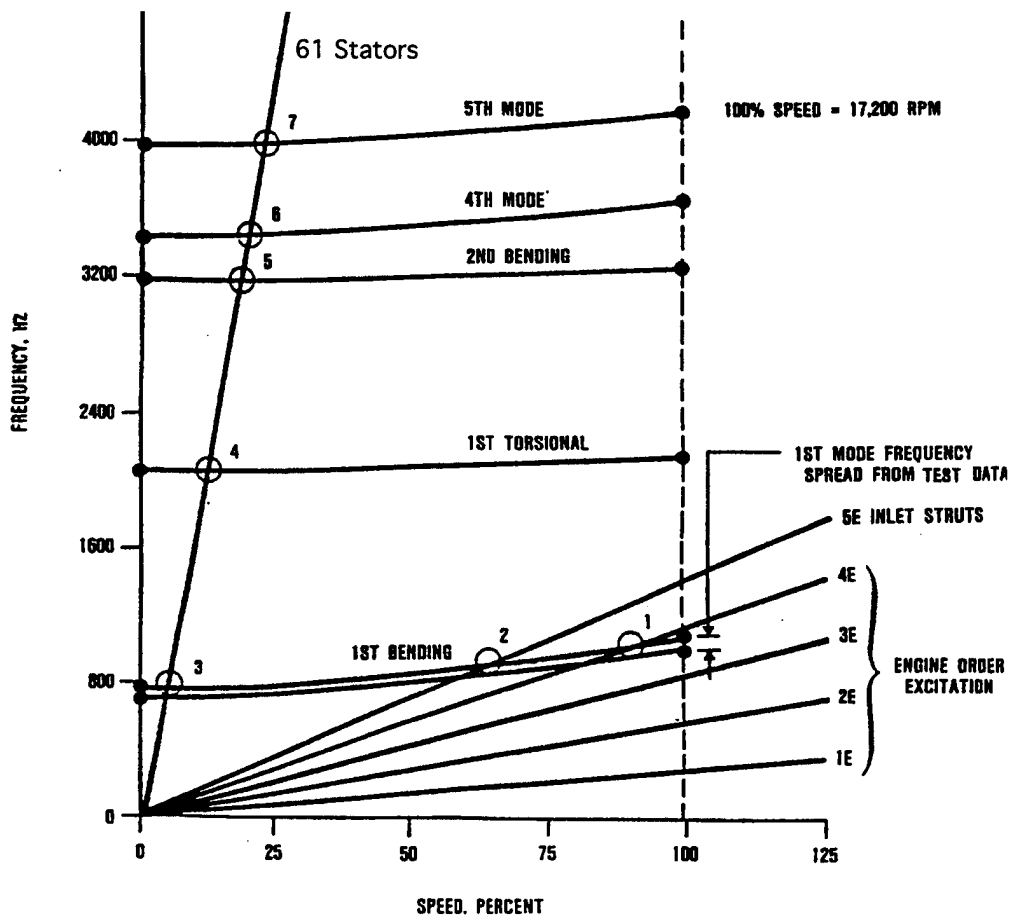


Figure A.1 F109 Fan Blade Campbell Diagram

dampers and their resulting wakes will restrict the downstream stator test region. On the Campbell diagram, potential excitation sources include but are not limited to engine order excitation, inlet distortion, combustor count, support struts and stator assemblies. The higher blade modes are typically a combination of transverse and torsional motion. If an intersection of an excitation source and blade mode on the Campbell diagram occurs within the operating

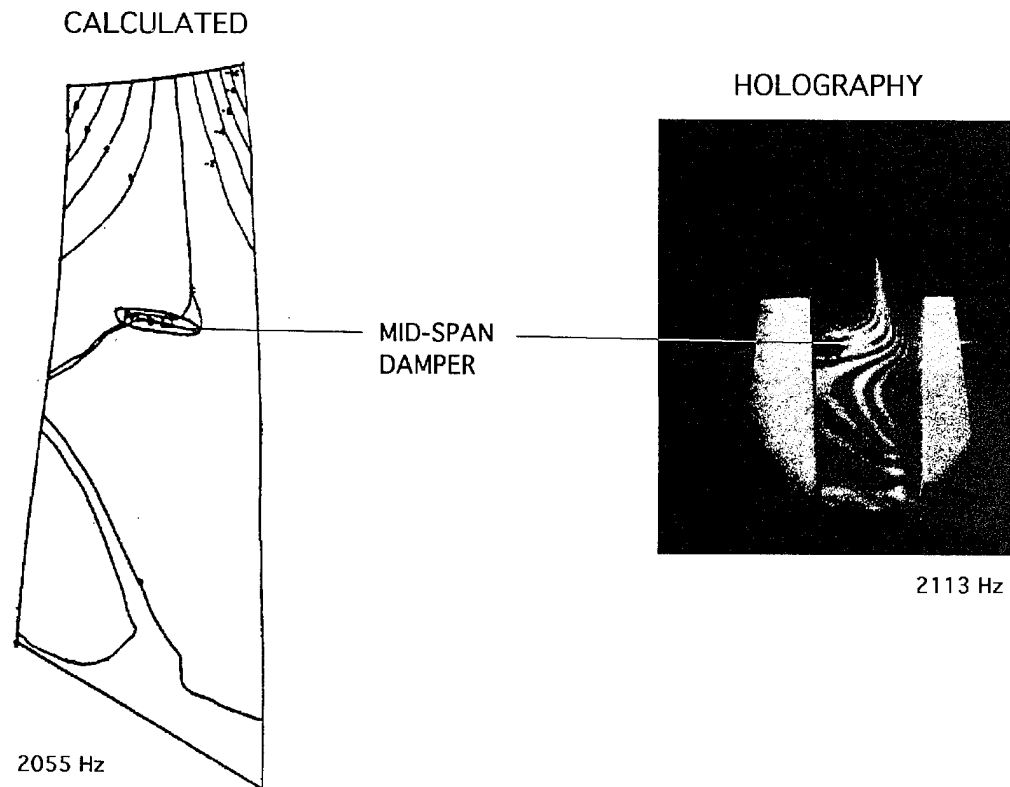


Figure A.2 Second Mode of F109 Fan Blade

range, the source of the excitation or the structure is modified to allow the planned operating point. Since the amplitude of vibration is difficult to predict in the design stage, it is more practical at present to try to avoid potential excitation points. On the Campbell diagram, Figure A.1, the stators provide fan blade excitation at engine speeds below engine idle conditions for the lower blade modes. The higher modes are typically not of major concern due to the expected small displacements and strain levels. Since the fan

must accelerate through the lower potential excitation modes in order to start, the blades are monitored with strain gages during prototype testing to insure low vibration levels occur. If a vibration problem is discovered late in the development process, additional surface rub strips at the hub or at the midspan damper are sometimes used to absorb the transferred energy, for instance, the elimination fan problems on the General Electric F-101 turbofan, otherwise components must be modified and retro-fitted (Aviation Week, October 7, 1991).

Similar analysis techniques are frequently used for stationary hardware but receive less emphasis due to the absence of rotational stresses. Typical sources of excitation for stators are the upstream rotors and their associated wakes, inlet guide vane wakes, inlet distortions, and support struts. Due to the internal and surface modifications necessary to instrument the F109 stators for pressure measurements, no equivalent diagrams are available for the stators. Instead, individual blades are being dynamically tested at equivalent Mach number conditions in the Hessert Center Unsteady Cascade using the same stator positioning technique as on the actual engine with the stators fixed at the tip and pinned at the root.

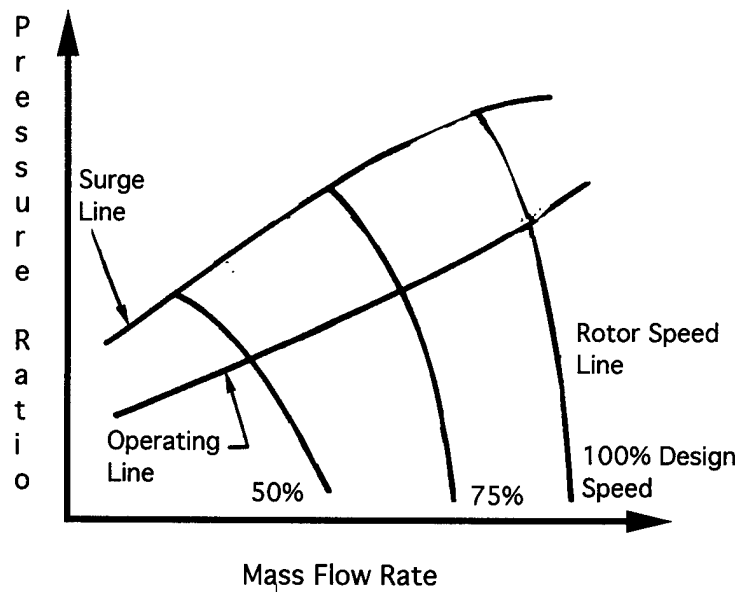


Figure A.3 Generic Compressor Map

operating line occur due to throttle transients or major inlet distortions. Additionally, regions of instability for a given design may further limit the operating envelope of the component. Figure A.4 shows examples of these other constraints superimposed on a typical compressor map (Verdon, 1989). Positive incidence flutter, also known as stall flutter, is the most common type of engine flutter problem (Verdon, 1989). Positive and negative incidence flutter are typically not seen in steady state operation but can occur with certain compressors during throttle transients while the compressor has moved away from the steady throttle operating line.

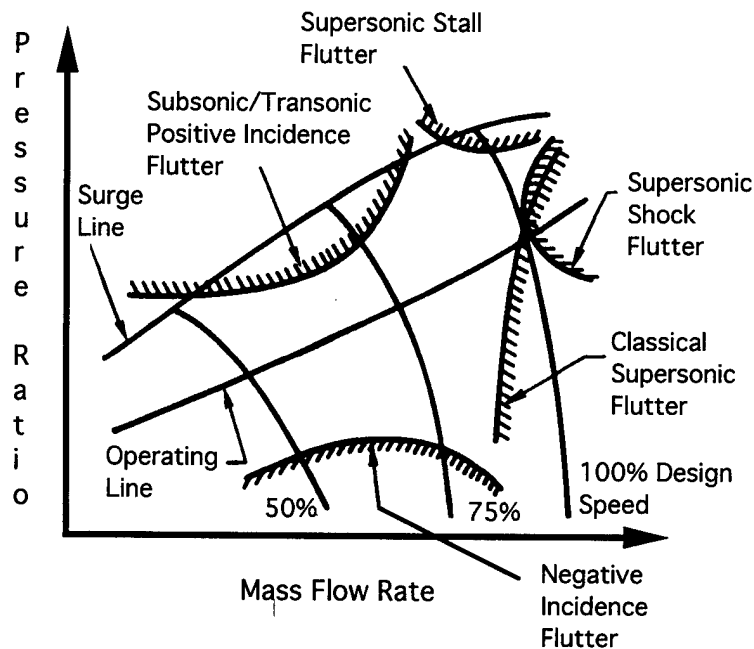


Figure A.4 Generic Compressor Map with Flutter Boundaries

These occurrences are often eliminated by design modification during component prototyping or later avoided by the fuel control system limiting the engine throttling rate. Along the operating line, classical supersonic flutter and supersonic shock flutter are the common problem areas near the maximum speed operating condition. Classical supersonic flutter is the torsional oscillation of the fan blade with a constant phase angle between adjacent blades and caused by supersonic relative flow over the blades. Supersonic shock flutter is somewhat similar but with all blades oscillating at the same frequency and phase angle due to mid-passage shocks.

Since the planned experiment involves steady state operation, the potential flutter cases are limited to near the classical supersonic flutter and supersonic shock flutter regimes. Since the F109 cold-section parts are ENSIP qualified for 18,000 hours, actual fan blade flutter will probably not occur.

A simplified method of viewing flutter is to examine the Pines criteria which states "that (1) *no* flutter exists for the center-of-gravity (c.g.) positions forward of the elastic axis (e.a.) and (2) if the c.g. is aft of the e.a. and if the aerodynamic center (a.c.) is forward of the e.a., flutter is possible only if the frequency ratio ω_h/ω_α is less than some specified amount involving these locations and the radius of gyration" (Oates, 1989). In most aircraft wings, the c.g. at approximately the mid-chord is aft of the e.a. at 25 to 40 percent of chord, while the a.c. at the quarter-chord is forward of the elastic axis. Thus aircraft wing flutter is possible if the frequency criterion is met. For a typical circular arc compressor airfoil, like the F109 stator, the c.g. and e.a. are nearly coincident at the mid-chord. Thus, if the c.g. is slightly forward of the e.a., no flutter is possible, while if slight aft, flutter is frequency dependent. These criteria are provide guidelines during the

modifications inherent in stator instrumentation. Unfortunately, the Pines criteria provide merely rough guidelines and do not consider the additional blade forced response issues. Historically, most large forced response vibrations are avoided through the use of the Campbell diagram previously mentioned and preliminary component testing; however, over the life of the component, the unsteady forces on the blade tend to damage the assembly. This process is collectively termed high cycle fatigue.

Theoretical and Experimental Background.

As aircraft flight speeds increased through the 1920s and 1930s, aircraft wing vibrations and potential control problems forced major research into the area of aeroelasticity and flutter. Considering the theoretical aspects first, Theodorsen examined and proposed a theory to examine the flutter problem in 1935. His technique involved potential flow and the trailing edge Kutta condition (Theodorsen, 1935). Most later analysis techniques use his circulation function, $C(k)$, which was validated independently by Schwarz (Schwarz, 1940). The reduced frequency, k , which is equal to $c\omega/2U_\infty$, where c is the airfoil chord, ω is the oscillation

frequency, and U_∞ is the freestream velocity, is probably the most important parameter in unsteady aerodynamics. While Theodorsen's paper is somewhat difficult to read, Bisplinghoff and Ashley gave a particularly clear presentation of a number of applications of his incompressible theory (Bisplinghoff and Ashley, 1962). At the same time, compressible subsonic flow conditions were established by Possio who solved an integral equation for a distribution of acceleration potential doublets in which a known downwash is represented by an integral of the unknown pressure difference distribution (Oates, 1989). Unfortunately, without a convenient inversion formula for Possio's method, researchers have had to use iterative approximation techniques to find the surface pressures. Further incompressible unsteady flow analysis was based on the early unsteady aerodynamics work of von Karman and Sears. Assuming two-dimensional potential flow with a rectilinear wake, von Karman and Sears represented a thin airfoil as a vortex sheet and examined the influence of the wake on the airfoil (von Karman and Sears, 1938). The cases they examined included an oscillating airfoil and a sharp edge gust entry. Sears extended this analysis for an airfoil traveling through a vertical gust having sinusoidal

variation (Sears, 1941). He showed that the unsteady lift always acts through the quarter chord location. Additionally, the chordwise pressure distribution does not have any phase angle variation and thus no pressure wave propagating along the airfoil. An inherent assumption in this analysis was that the gusts were convected across the airfoil at the freestream velocity. This is frequently termed a "frozen gust" assumption. Kemp and Sears later applied this approach to the interference between moving blade rows (Kemp and Sears, 1953). This technique is actually a single airfoil approach that neglects the influence of neighboring blades on the same row. Kemp and Sears later included the effects of the viscous wake and found that the unsteadiness caused by the viscous wakes is of the same order as the previously examine aerodynamic interference effects (Kemp and Sears, 1955). At approximately the same time, Schlichting added a viscous boundary layer for the first time to the existing steady cascade analysis allowing the calculation of loss coefficients (Schlichting, 1954). Whitehead solved the unsteady flow through an actuator disc composed of blades of small chord compared to the wavelength of the disturbance (Whitehead, 1960).

Following the initial efforts, research in unsteady aerodynamics has continued with a great number of important contributions. In 1958, Meyer examined the effect of wakes on the pressure and velocity distribution for a two-dimensional incompressible flow through a lightly loaded cascade. He showed the presence of strong pressure variations at the intersection of the wake with the downstream airfoil (Meyer, 1958). Lefcort added the influence of finite blade thickness to Meyer's approach and also examined the non-linear wake-distortion effect (Lefcort, 1965). He states that while the wake tended to increase the unsteady lift, the non-linear wake-distortion while the wake was on the airfoil tended to decrease the unsteady lift. In 1968, Horlock added analysis for unsteady velocity variation parallel to the undisturbed flow to the existing base of knowledge of transverse gusts, allowing the calculation of fluctuating lift with applications to fans and compressors (Horlock, 1968). Henderson and Horlock complemented this effort with analysis for small blade spacing compared to the disturbance wavelength (Henderson and Horlock, 1972). Lotz and Raabe added the analysis of non-integer pitch ratios between two relative cascade rows to the numerous studies using a pitch ratio of

unity and also included the influence of neighboring blade wakes (Lotz and Raabe, 1968). Kerrebrock and Mikolajczak examined the effect of upstream wakes as they passed through a row of blades and created a theory that showed the majority of the upstream wake is collected on the pressure surface of the downstream blade (Kerrebrock and Mikolajczak, 1970). Naumann and Yeh further added airfoil camber and blade angle of attack to the existing unsteady analysis (Naumann and Yeh, 1973). This allowed the calculation of unsteady lift of airfoils moving through periodic wakes. Fleeter examined the affects of compressible subsonic flow through a Fourier-transform technique, with the integral equation solved by matrix-inversion (Fleeter, 1973). Adamczyk computationally examined the effect of an airfoil moving through a three-dimensional gust with applications to aircraft-turbulence interactions, turbomachinery, and helicopter rotors (Adamczyk, 1974). His early techniques involving compressible flow required solutions to be expressed in terms of infinite series of Mathieu functions which unfortunately converge very slowly (Oates, 1989). He later formed approximation techniques to eliminate the need for vast computer storage or computational time. Rao later developed

lift and moment equations for cambered airfoils with convecting and non-convecting streamwise gusts (Rao, 1991). Whitehead examined the unsteady incompressible cascade problem using standard vortex sheet techniques and a matrix inversion method (Oates 1989).

Osborne found a compressible solution using Sears' unsteady thin-airfoil theory and match asymptotic expansions (Osborne, 1973). He found a significant decrease in unsteady lift with increasing Mach number until a Mach 0.9 where the results blew-up due to the Prandtl-Glauert transformation. Goldstein and Atassi develop a second-order theory for unsteady incompressible flow for an airfoil subjected to a two-dimensional convected sinusoidal gust (Goldstein and Atassi, 1976). This technique accurately accounts for the distortion of the gust which had been neglected in previous methods. The method used sectionally analytic functions and the method of matched asymptotic expansions to form an analytic solution. It demonstrated the limitations of some of the previous attempts, for instance Horlock or Naumann and Yeh, to include only certain second order effects in the analysis. In 1979, Verdon and Caspar used a somewhat similar approach of an unsteady perturbation about a nonuniform mean flow and found that circular arc airfoil thickness

tended to have a more important effect than airfoil camber on unsteady lift and moment for both bending and torsional oscillations (Verdon and Caspar, 1980). Unfortunately, this analysis was only capable of examining sharp leading-edged airfoils.

Tracing the experimental flutter research to 1938, Bratt and Scruton measured the moment hysteresis in airfoil pitch and the concept of work per cycle in an effort to determine stability derivatives (Bratt and Scruton, 1938). Others worked along similar reasoning using dynamic balances or strain gaged beams (Oates, 1989). By 1957, Rainey's research incorporated miniature pressure transducers which were distributed chordwise to determine the integrated unsteady load distribution on a wings (Rainey, 1957). Walker and Oliver examined the influence of wakes on noise generation and worked to position rows of stationary blades such that the upstream stationary wakes from inlet guide vanes or stators impacted the leading edge of the downstream stationary row to reduce noise levels (Walker and Oliver, 1972). Whitfield, et. al. produced the first three-dimensional mapping of rotor wakes using hot-wire anemometry on a low-speed low-pressure fan without any inlet guide vanes or stators (Whitfield, et al., 1972). Commerford

and Carta examined the unsteady flow on a symmetric airfoil behind a cylinder at high-reduced frequency, $k = 3.9$, at Mach 0.25 and compared the results with the Sears' technique and the computer modelling by Adamczyk (Commerford and Carta, 1974). The wake behind the cylinder produced fluctuations in the flow direction one-third the magnitude of the transverse fluctuations. Their experimental results showed unsteady pressures that were greater than predicted. A phase angle variation along the chord that was not shown in incompressible analysis was also experimentally demonstrated. Fujita and Kovasznay determined the unsteady lift on a symmetrical airfoil in an open jet with an upstream rotating pinwheel used to create oblique wakes (Fujita and Kovasznay, 1974). Unsteady leading-edge flow separations due to the wake were noted at a positive airfoil angle of attack but tended to clear quickly. Evans conducted hot-wire experiments for a rotor only and for a single stage compressor during low-speed operation (Evans, 1975). He found that the phase-resolved periodic velocity fluctuations and random velocity fluctuations were of the same order at the compressor design condition but near the stall condition, random turbulence appeared to be dominant.

In 1977, Gostelow suggested an innovative technique to collect unsteady data in turbomachinery applications using a phase-lock averaging process. His technique incorporated a triggering pulse to start data acquisition at the same phase position on each engine revolution (Gostelow, 1977). Data sets could be ensemble averaged and provide a time-resolved unsteady representation of the pressure distribution on the blade or stator. The additional unsteadiness removed in the ensemble averaging represented signal noise and unsteadiness not due to rotor relative position. Schmidt and Okiishi investigated the unsteadiness in a multistage low-speed compressor using hot-wire and acoustical measurements (Schmidt and Okiishi, 1977). Inlet guide vane wakes had a strong influence on sound pressure level based on their relative position with downstream stators, confirming Walker and Oliver's previous efforts. Additionally, time-averaged and instantaneous velocity vectors were determined for each entrance and exit plane of the three-stage compressor. One limitation of the research rig was, unlike actual engine hardware, all stationary stages had the same blade count. While different from the stationary components, all rotating components also had the same blade count. This simplified layout

can result in unusual sound propagation and vibration issues not present in typical engine hardware. Evans later added the boundary layer profile measurement at three chordwise positions on a stator in a low-speed single-stage compressor and compared these results with his previous cascade boundary layer efforts (Evans, 1978). On the suction surface, the boundary layer was transitional on the forward half of the blade. Furthermore, there was a 180 degree phase shift in velocity fluctuations from the surface to the free stream in this region. Evans found a very poor correlation between unsteady cascade boundary layer growth and that of an actual compressor which showed a strikingly larger growth rate. Fleeter, Jay, and Bennett conducted similar low-speed testing on a single-stage compressor with a pressure ratio of 1.016 and found the Kutta condition was properly satisfied even for high reduced frequency flows (Fleeter, Jay, and Bennett, 1978). Only the first two harmonics were monitored since the higher harmonics have not been the source of vibration problems in turbomachinery. For cases with negative inlet flow incidence angle, the researchers found that the first and second harmonics of the wakes convected at differing velocities on the pressure and suction surfaces. Note that the

computational analysis at that time did not model the differing harmonic velocities. They later made comparison tests of flat plate stators to cambered stators behind the same rotor and compared these results with their transverse gust analysis (Fleeter, Jay, and Bennett, 1980). Compressible comparison calculations were done using the flow Mach number of 0.1 since the incompressible calculations did not match as well.

An organized effort to combine the theoretical and experimental results began through the Air Force Office of Scientific Research (AFOSR) and the Swiss Federal Institute of Technology in which 9 standard configurations involving experimental data were compared with 19 aeroelastic prediction models (Blöcs, 1986). For example, Atassi's technique was model number four. The standardized configurations continue to be benchmark examples for improved computational and analytical models. Atassi and Akai developed a theory for oscillating airfoils in cascade subjected to uniform incompressible flow (Atassi and Akai, 1980). Their solution was different from the previous classical solutions since instead of splitting the solution into circulatory and non-circulatory components, two circulatory components

representing the instantaneous surface and wake solutions were used. Additionally, an analytic solution was determined for the problematic leading edge region of airfoils with finite thickness. Through the use of interblade phase angle for the oscillatory motion, the cascade system could then be accurately reduced to a single airfoil. In addition to unsteady surface pressure, forces and moments, instability and flutter boundaries could be examined.

Other researchers continued their computational and experimental efforts independently of the AFOSR project. For instance, Adachi and Murakami examined the flow through a stage of stators behind a rotating row of cylinders in a low-speed compressor research rig (Adachi and Murakami, 1979). Time-averaged steady and phase-resolved unsteady velocity profiles were determined using an angled hot-wire throughout the stator passage. Experimental results showed wake distortion along the blade surfaces and a large outward radial component in the cylinder wakes. Franke and Henderson characterized the upstream wakes and measured the unsteady stator response of a low-speed compressor rig composed entirely of symmetric airfoils (Franke and Henderson, 1980). Additionally, axial spacing between the rotor and stator was

also varied. The magnitude of the harmonics of the blade passing frequency were noticeably reduced with increased axial spacing. Typical of other experiments, the unsteady surface pressures decreased with chord distance but were larger than the computationally predicted magnitude. Larger differences in phase angle of the unsteady surface pressures between the stator surfaces were noted at increased blade incidence angles. Gallus, Lambertz, and Wallmann also varied the axial distance on their low-speed axial compressor (Gallus, Lambertz, and Wallmann, 1980). Time-averaged flow vectors between the rotor and stator were determined using a stationary five-hole probe, while a rotating three-hole probe was mounted behind the rotor to measure the rotor exit flow. Limited unsteady pressure measurements were taken on both the rotor and stator. Inlet guide vanes were tested and later removed for comparison purposes. The unsteady wakes from the inlet guide vanes provided a measurable source of unsteadiness for the downstream stators. While an expected decrease in unsteady lift was demonstrated for larger rotor/stator axial spacing, the second harmonic of the blade passing frequency was generally quantified to be 20 to 40 percent of the fundamental. In 1982, Dring, Joslyn, and

Hardin conducted extensive experiments on a large scale rotating rig to provide a bench mark for computational efforts with an emphasis on the three-dimensional aspects of flow on the rotor and in the wake (Dring, Joslyn, and Hardin, 1982). In the wake, the maximum radial velocity was 18 percent of the mean flow velocity demonstrating the importance and magnitude of the frequently neglected radial velocities in two dimensional analyses. Zierke and Okiishi conducted a flowfield survey between each row of a low-speed multistage rig using a fast-response total pressure probe (Zierke and Okiishi, 1982). Rotor wakes that had not interacted with stator or inlet guide-vane wakes had higher total pressure values than those that had interacted. The magnitude of periodic unsteadiness behind the first stage stator was much smaller than that behind the first- or second-stage rotor. Carta compared low-speed unsteady cascade data with the theories of Verdon/Caspar and Atassi with excellent results (Carta, 1983). It was found that flat plate analysis only gave general trends and was generally not as useful of a tool. Additionally, the interblade phase angle was found to be the most important parameter determining cascade stability. In 1984, Atassi extended Sears' theory demonstrating the

superposition of airfoil thickness, airfoil camber, and angle of attack in spite of the nonlinear dependence of the unsteady lift on the potential flow. Within the theory, he demonstrated the importance of the transverse wave number, k_2 , which had been neglected in other theories (Atassi, 1984).

Limited unsteady, compressible compressor testing has been conducted at the MIT Blowdown Test Facility and also at the NASA Lewis Research Center. The MIT effort has relied on high-frequency-response probes, while the NASA Lewis team has used laser anemometry (Hathaway, Gertz, et al., 1986). In these studies, the maximum flow unsteadiness on some transonic compressors has been shown at the component maximum efficiency point (Epstein, Gertz, et al., 1987). Additionally, emphasis has been placed on trying to accurately characterize the wake structure shed from a transonic rotor. Buffum and Fleeter conducted experiments in the NASA Lewis Transonic Oscillating Cascade Facility by oscillating a single symmetric airfoil in a cascade and comparing its unsteady surface pressures with the neighboring blades (Buffum and Fleeter, 1990). For this effort, the reduced frequency was 0.39 at Mach 0.65. The goal of the project was to determine oscillating cascade data

for all values of interblade phase angle by using an influence coefficient technique.

The theoretical and experimental research has involved numerous researchers at many international facilities. While neglected here, similar experimental efforts have occurred in turbine research but with increased emphasis on heat transfer related issues. While the theoretical and computational aspects have slowly matured, the vast majority of the experimental results are from incompressible flow conditions which are of limited design value in the current transonic compressors and turbines used in aircraft and ground-based applications. The F109 experiment and the associated cascade work provide much needed compressible subsonic bench marks for computational comparison. Unfortunately, even with the current level of engineering knowledge including the use of Campbell diagrams and finite element modeling of blades and vanes, failures are still occurring quite frequently (Aviation Week & Space Technology, October 7, 1991, and Associated Press Release, 25 August 1995).

APPENDIX B

F109 TURBOFAN ENGINE BACKGROUND

The Garrett F109 turbofan was designed for the Air Force as the engine for the Fairchild Republic T-46, the replacement for the aging Cessna T-37 primary air trainer. Due to the poor aircraft flight characteristics and contractor mismanagement, the aircraft program was canceled, leaving the F109 engine without an aircraft (Aviation Week, March 23, 1987). The F109 has a bypass ratio of 5 to 1, a peak cycle temperature of 1740°R, a sea level thrust of 1,330 pounds and specific fuel consumption 0.396 per hour. The fan has a maximum tip speed of 1,375 ft/sec and a stage pressure ratio of 1.6. In spite of the Fairchild Republic troubles, the Garrett engine was the first engine to successfully pass the Air Force Engine Structural Integrity Program (ENSIP) which required demonstration of fixed life requirements for hot and cold sections of the engine. Additionally, this robust engine was designed for field maintenance allowing the removal of the fan and stator assemblies at the air base engine shop level rather than at a centralized depot. This

feature allows simplified instrumentation of actual engine stator hardware for cascade and engine testing. Individual stators may be changed with only the removal of the fan and fan case.

The F109 was an obvious choice due to the single stage of fan compression including swept stator geometry and a transonic rotor. A single stage would allow flowfield measurements forward and aft of the stage. Additionally, the swept stator geometry would allow intrastage measurements which are possible on low speed rigs but are nearly impossible on most engine geometries. Furthermore, the hollow stators allowed the use of industry-standard pressure transducers. As a first step of the F109 research involving compressible flow, the unsteady cascade experiments conducted at the Hessert Center Unsteady Cascade Facility provide a first step toward quantifying the unsteady forcing functions in turbomachinery.

The long term goal of the F109 stator research effort, a portion of which is reported in this dissertation, is to quantify the unsteady pressure loading on the vanes of a stator in the wakes of the transonic fan upstream of the stator assembly in an operating turbofan engine. The engine research is intended to focus on

compressibility effects and the effect of the existing sweep of the F109 stators, including a comprehensive documentation of the inlet and outlet flow conditions entering and exiting from the stator so that comparisons with computational predictions may be made. A perspective view of an F109, one of which is located in a test cell at the United States Air Force Academy in Colorado, is shown in Figure B.1.

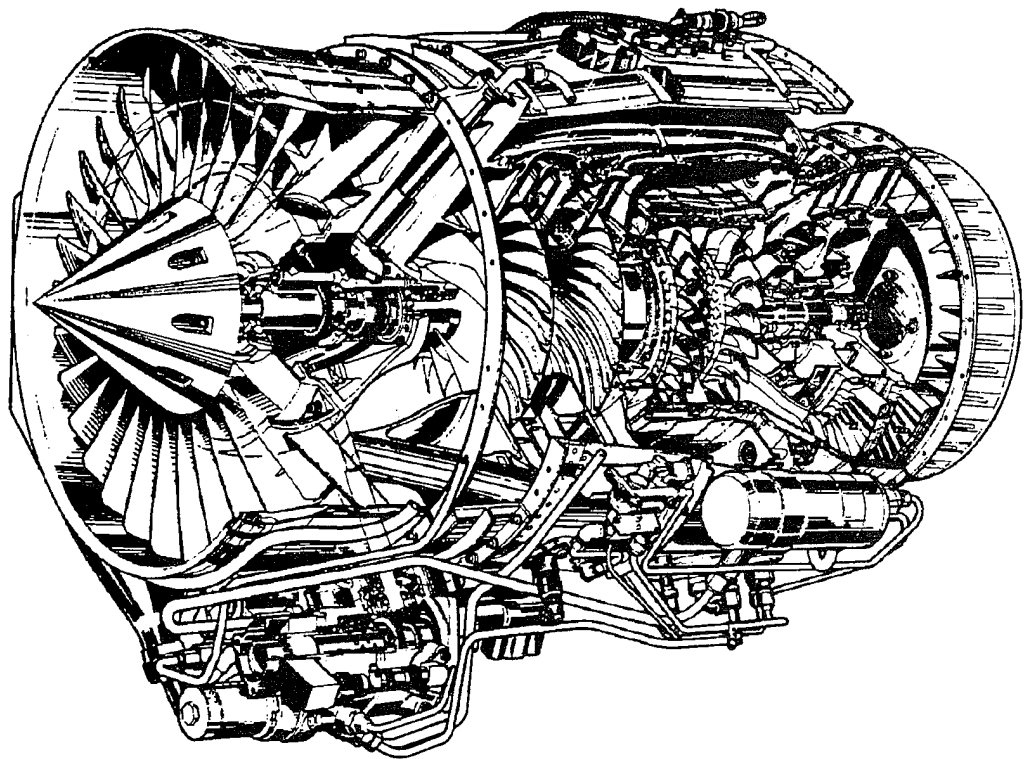


Figure B.1 Garrett F109 Turbofan Engine

As a first step toward performing these engine tests at the Air Force Academy, instrumented stator vanes that will eventually be placed in the engine have been tested in an unsteady, transonic cascade at the Hestert Center for Aerospace Research at the University of Notre Dame. These cascade tests, described in this dissertation, had several objectives, that included testing the structural integrity of the instrumented vanes and verifying that the transducers functioned properly at actual engine-order forcing frequencies and Mach numbers before they were placed in the engine; however, the unsteady cascade tests also represented an opportunity to collect data on compressibility and reduced frequency response of the vanes in the cascade environment.

An F109 is currently installed in Test Cell #3 of the Aeronautics Laboratory at the United States Air Force Academy in Colorado Springs, Colorado. A back-up engine is also in storage at the Academy. Extensive steady state engine cycle parameters, including component operating pressures and temperatures, fuel flow, shaft speeds, and thrust, are available through a Hewlett-Packard HP-3852 data acquisition system. An overhead projection system in the control room allows group viewing of this data

acquisition information. Additionally, engine health monitoring, shaft vibration sensor information, and throttle operating profiles are available through computer downlink from the F109 on-board computer. Engine parameters are stored on computer disk and output through available printers and plotters. The F109 research represents a continuation of this research effort.

APPENDIX C

PRESSURE CAVITY ANALYSIS

Included in this Appendix are the analysis to determine the appropriate pressure chamber characteristics and placement to insure accurate surface pressure measurement on the stator vanes in the cascade and engine. Initial concepts for the unsteady surface pressure measurements included the use of remotely mounted pressure transducers to ease vanes instrumentation difficulties. An associated transfer function would be used to infer the dynamic signal on the vane. The pressure cavity design studies, a portion of which is review here, revealed that the transducer must be nearly surface mounted to provide reasonable system natural frequency and associated magnitude ratio.

C.1 Modeling Pressure Cavity System

The pressure cavity within the stator acts as a second order system. The major dimensions are as shown in Figure C.1 The system can be represented as a pressure driving force, $p_a \pi d^2/4$, a

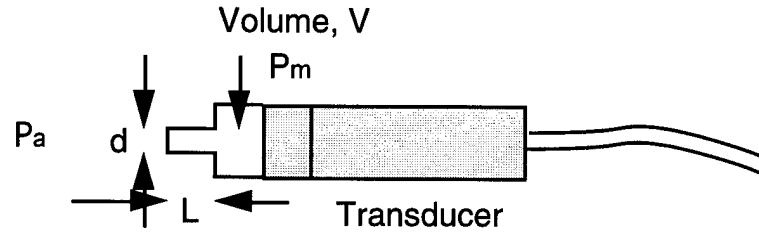


Figure C.1 Pressure Cavity and Pressure Transducer

fluid shear damping force, $8\pi\mu Lx$, and a resulting compression-restoring force, $\pi^2 E_m d^2 x / 16V$. From Newton's second law these can be resolved to:

$$\frac{4L\rho V}{\pi E_m d^2} \ddot{p}_m + \frac{128\mu LV}{\pi E_m d^4} \dot{p}_m + p_m = p_a(t) \quad (C.1)$$

where ρ is the fluid density, μ is the viscosity, E_m is the fluid bulk modulus of elasticity (Figliola and Beasley). After including the effects of the speed of sound, a , the resulting cavity natural frequency, ω_n , and damping ratio, ζ , are respectively:

$$\omega_n = \frac{d\sqrt{\frac{\pi a^2}{LV}}}{2} \quad (C.2)$$

$$\zeta = \frac{32\mu\sqrt{\frac{VL}{\pi}}}{a\rho d^3} \quad (C.3)$$

Equations (C.2) and (C.3) represent the solutions to a dynamic cavity presented by Figliola and Beasley. The Endevco Corporation approach provides slightly different resulting equations for natural frequency and damping ratio:

$$\omega_n = \frac{\sqrt{\frac{3\pi r^2 a^2}{4LV}}}{2\pi} \quad (C.4)$$

$$\zeta = \frac{2\mu \sqrt{\frac{3VL}{\pi}}}{a\pi r^3} \quad (C.5)$$

where r is the radius of the tube. Based on the resulting natural frequency equations, (C.2) and (C.4), the natural frequency could be increased with increased tube diameter to length ratios. Associated with each of the approaches present, a Magnitude ratio comparing the measured pressure with the input pressure. Both approaches were used in estimating the resultant natural frequency and magnitude ratio for various pressure cavity approaches.

C.2 Potential Cavity Designs

The maximum primary frequency present in the F109, based on blade passing frequency, was approximately 8500 hertz. This

frequency formed the basis for the initial designs, considering the resultant system natural frequency and magnitude ratio.

Using a transducer cavity located 3 inches for the vane-surface-pressure measurement location, the natural frequency, ≈ 500 Hz, was well below the 8500 Hz forcing frequency. Consequently, the magnitude ratio was extremely small, ≈ 0.004 , indicating that the input signal would not be sensed at the transducer surface. As a result, external sensing was eliminated from consideration as a viable approach in this application. Sample results for external sensing are shown in Table C.1.

Since the vanes were hollow, there was a potential to use the internal volume as the pressure cavity; however, the resultant natural frequency was still too low, ≈ 1000 Hz, to provide reasonable magnitude ratios for the expected frequencies. The expected measurement pressure was only approximately 3 percent of the input dynamic pressure. These results are presented in Table C.2.

Other designs were attempted; however, the requirement for a high natural frequency to maintain uniform magnitude ratio over the expected frequency ranges led to smaller and smaller tubing length and cavity volumes.

C.3 Final Design

Using a near-surface-mount positioning of the pressure transducer, the natural frequency was estimated to be approximately 45,000 Hz. This was the design final selected for the pressure chamber. The small chamber volume was required to provide the high natural frequency. The magnitude ratio was approximately 1.035. An increased natural frequency would have been preferable; however, this was the smallest size possible. In fact two transducers were lost due to drill bit damage when making the surface tap. Unfortunately, the standard rule of thumb, keeping the measurement frequencies below one-fifth of the system natural frequency was not possible. This was a limitation of the high frequencies required. All cavities were constructed to provide the highest natural frequency possible, at the expense of some of the transducers.

C.4 Sample Calculations

Table C.1 Sample Results for an External Cavity 3 inches from the vane.

External Cavity. The tap and tubing is the capillary								
Pressure	1.63E+03	lb/ft ²	Tap Radius	0.025	in	Tran Frq	150000	Hz
Temp=	519	F	Tap Radius	0.0021	ft	Rule of	30000	Hz
Density=	0.00183	slug/ft ³	Tap Lenth	3	in	Thumb		
Viscosity	3.74E-07	slug/ft s	Tap Length	0.25	ft			
Snd Spd=	1116.62	ft/sec				RPM		
Chamb L	0.25	in	Engine Freq	8495	Hz	16990		
Chamb L	0.02083	ft	Endevco	Method	Figliola	Beasley	Method	Volume
	r	h=	fn =	P / Po	h=	fn=	Mag Ratio	Ratio
Ch Dia in	Radius ID	Damping	Natural Freq		Damping	Natural Freq	M(w)	V/Vtube
0.2	0.00833	0.042	533.148	0.004	0.049	615.6262	0.0053	1.33333
0.4	0.01667	0.084	266.574	0.001	0.097	307.8131	0.0013	5.33333
0.6	0.025	0.126	177.716	0.0004	0.146	205.2087	0.0006	12
0.8	0.03333	0.168	133.287	0.0002	0.194	153.9065	0.0003	21.3333
1	0.04167	0.21	106.63	0.0002	0.243	123.1252	0.0002	33.3333
1.2	0.05	0.252	88.858	0.0001	0.291	102.6044	0.0001	48
1.4	0.05833	0.294	76.164	8E-05	0.34	87.9466	0.0001	65.3333

Table C.2 Sample Results Using Internal Vane Volume as the Cavity.

Using Internal Volume of Blade, Tap is the capillary								
Pressure	1.63E+03	lb/ft ²				Tran Frq	150000	Hz
Temp=	519	F				Rule of	30000	Hz
Density=	0.00183	slug/ft ³	Tap Depth	0.015	in	Thumb		
Viscosity	3.74E-07	slug/ft s	Tap Depth	0.00125	ft	Vol Adj	0.7	
Snd Spd=	1116.62	ft/sec	Chamber A	4.29E-04	ft ²	RPM		
Chamb L	2.5	in	Engine Freq	8495	Hz	16990		
Chamb L	0.20833	ft	Endevco	Method	Figliola	Beasley	Method	Volume
Tap Radius	Tap radius	h=	fn=f(r2/LV	P / Po	h=	fn=	Mag Ratio	Ratio
in	ft	Damping F	Natural Freq		Dampin	Natural Freq	M(w)	V/Vtube
0.01	0.00083	0.1724	917.085	0.01178	0.199	938.478	0.0123	91800
0.015	0.00125	0.0511	1123.2	0.01779	0.059	1407.717	0.0282	40800
0.02	0.00167	0.0216	1296.95	0.02386	0.025	1876.956	0.0513	22950
0.025	0.00208	0.011	1450.04	0.03001	0.013	2346.195	0.0825	14688
0.03	0.0025	0.0064	1588.44	0.03623	0.007	2815.434	0.1233	10200
0.035	0.00292	0.004	1715.71	0.04253	0.005	3284.673	0.1756	7494
0.04	0.00333	0.0027	1834.17	0.0489	0.003	3753.912	0.2424	5738

Table C.3 Sample Result, Final Design, Near Surface Mounted Transducer.

Transducer cavity is the volume, tap is the dynamic capillary								
Pressure	1.63E+03	lb/ft ²	Tap Radius	0.024	in	Tran Frq	150000	Hz
Temp=	519	F	Tap Radius	0.002	ft	Rule of	30000	Hz
Density=	0.00183	slug/ft ³	Tap Length	0.02	in	Thumb		
Viscosity	3.74E-07	slug/ft s	Tap Length	0.0017	ft			
Snd Spd=	1116.62	ft/sec				RPM		
Chamb L	0.05	in	Engine Freq	8495	Hz	16990		
Chamb L	0.00417	ft	Endevco	Method	Figliola	Beasley	Method	Volume
	r	h=	fn =	P / Po	h=	fn=	Mag Ratio	Ratio
Ch Dia in	Radius ID	Damping	Natural Freq		Damping	Natural Freq	M(w)	V/Vtap
0.064	0.00267	6E-04	43802.6	1.0391	6E-04	50578.85	1.029	1.11
in	ft		Hz			Hz		

APPENDIX D

STEADY CASCADE ANALYSIS

As a first approach to the surface pressure analysis of the F109 stator, a flat plate steady cascade study was implemented using a conformal transformation technique. The transformation used by Garrick (Oates, 1988) shows the overall approach of more advanced transformation techniques. The technique assumes a two-dimensional incompressible, inviscid, irrotational flow through a flat-plate cascade. Many advanced techniques for cambered airfoil cascades involve numerous Joukowski transformations followed by conjugate Fourier series. Some advanced techniques require up to three weeks of labor and a keen insight on the proper transformation for reduced blade spacing (Johnsen, 1965). According to Ives, the transformation process has four distinct steps (Ives, 1976). He states "The first of these steps is to remove the effects of slope discontinuities in the airfoil contour and expand regions of rapid flow change (such as the nose region) by analytically mapping the

airfoil, point by point, onto a nearly circular, smooth contour. The second step is a coordinate system translation to place the centroid of the near circle on (or near) the origin. The third step is to obtain a continuous representation of the near-circle contour, and thus of the airfoil by interpolation. The fourth step is to map this nearly circular contour onto a circle." For illustrative purposes, a combined transformation for a flat plate cascade will be used for the present analysis.

D.1 Flat Plate Cascade Analysis.

The simplified Garrick conformal cascade transformation, Equation D.1, represents the cascade with a circle as shown in

$$z = \frac{S}{2\pi} \left(e^{-i\beta} \ln \frac{e^{\psi} + \zeta}{e^{\psi} - \zeta} + e^{i\beta} \ln \frac{e^{\psi} + 1/\zeta}{e^{\psi} - 1/\zeta} \right) \quad (D.1)$$

Figure D1. stator spacing, S , and stagger angle, β , of the transformation are presented in Figure D.2. The transformation parameter, ψ , is related to the actual cascade solidity, $\sigma = c/S$, and must be determined iteratively. The mathematical relationship between solidity and ψ is shown in Equation D.2.

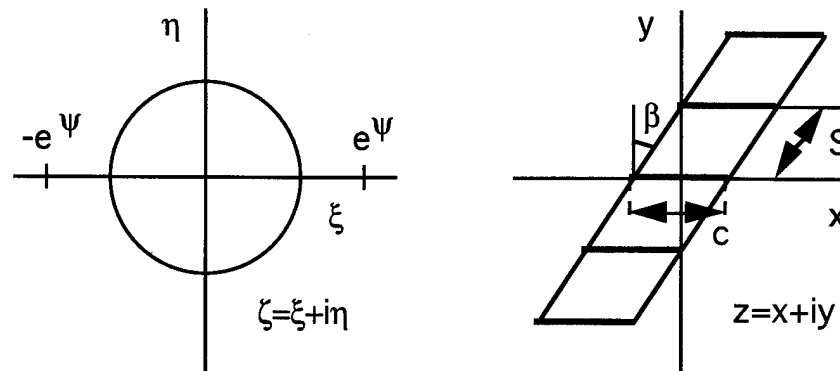


Figure D.1 Cascade Transformation Planes

$$\sigma = \frac{2}{\pi} \left(\cos \beta \ln \frac{\sqrt{\sinh^2 \psi + \cos^2 \beta} + \cos \beta}{\sinh \psi} + \sin \beta \tan^{-1} \frac{\sin \beta}{\sqrt{\sinh^2 \psi + \cos^2 \beta}} \right) \quad (D2)$$

The cascade domain positive and negative infinity positions map as the points e^ψ and $-e^\psi$, respectively. Oates states “. . . that the effect of the transformation has been to bring upstream and downstream infinity in the x plane into the proximity of the circle in the ζ plane. When circulation about the circle exists, the angles of the flow in the proximity of $\zeta = \pm e^\psi$ ($z = \pm \infty$) can be affected. Thus unlike the case for an isolated two-dimensional airfoil, the angle of turning of the fluid can be made other than zero.” In the transformation, the ζ domain can be considered to be an infinite set of Riemann sheets, each of which represents a given strip of the z

domain.

The circulation can be determined by examining the momentum relationships through a two-dimensional, incompressible, inviscid cascade. The continuity equation and the two curved streamlines ensure that the axial flow velocity is constant. The x and y momentum are respectively:

$$F_x = (P_1 - P_2) S \Delta h \quad (D.3)$$

$$F_y = \rho u (v_1 - v_2) S \Delta h \quad (D.4)$$

where Δh is the z direction height. After invoking Bernoulli's equation for incompressible flow to eliminate the pressure terms, the force vector may be expressed only as function of velocity with a magnitude:

$$F = \rho S \Delta h V_{avg} (v_1 - v_2) \quad (D.5)$$

where V_{avg} is the average of V_1 and V_2 as shown in Figure D.2. The resulting circulation around the circuit of one stator blade (Anderson, 1991) is:

$$\Gamma = - \int_c \bar{V} \cdot d\bar{s} = S (v_1 - v_2) \quad (D.6)$$

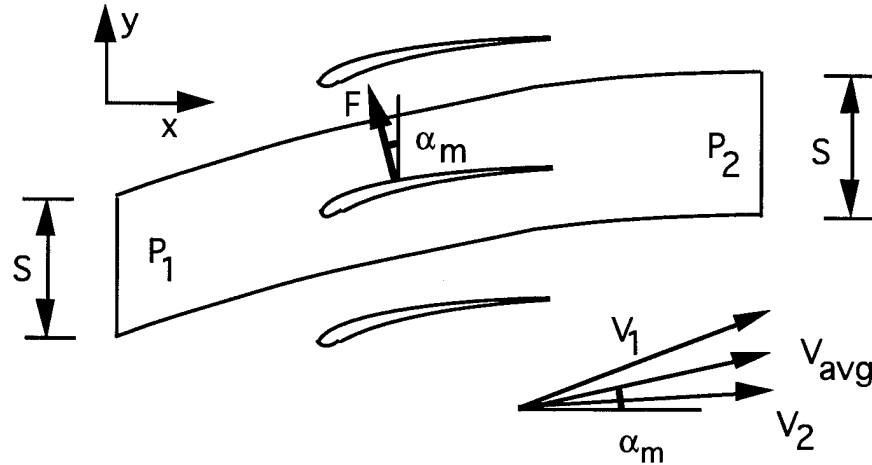


Figure D.2 Momentum Balance

Note that the circulation around a blade is related to the change in tangential velocity. Since the effective change tangential velocity through the cascade is split evenly from inlet to mean and mean to outlet, this change in velocity can be expressed in terms of circulation. More importantly, the far field velocity characteristics on either side of the cascade can be represented with the circulation. Finally, combining Equations D.5 and D.6, the force on an individual blade is:

$$F = \rho \Gamma V_{avg} \Delta h \quad (D.7)$$

just as in the case of an isolated airfoil; however, note that V_{avg} represents the mean velocity based on the inlet and exit velocity, not the incoming freestream velocity.

In order to create the desired inflow and outflow conditions in the physical plane, complex sources were used in the ζ plane. The sources must later be adjusted to satisfy the surface boundary conditions and the Kutta condition at the trailing edge. The resulting sources are:

$$A = V_{\text{avg}} S e^{-i(\alpha + \beta)} - i \frac{\Gamma}{2} \quad @ \quad \zeta = -e\psi \quad (\text{D.8})$$

$$B = -V_{\text{avg}} S e^{-i(\alpha + \beta)} - i \frac{\Gamma}{2} \quad @ \quad \zeta = e\psi \quad (\text{D.9})$$

Using the circle theorem to maintain the proper boundary conditions, two additional sources are included inside the circle. A lengthy complex velocity potential for the ζ plane can then be established, Oates Equation 11.43 (Oates, 1988). Note that the actual circulation, Γ , must still be determined to satisfy the Kutta condition.

On the circular profile of the ζ plane, the Kutta condition implies a continuous pressure at the trailing edge or zero velocity in the circumferential direction at the trailing edge. The resulting circulation, Γ_k , with the Kutta condition is:

$$\Gamma_k = \frac{2 S V_{\text{avg}} \sin \alpha}{\sqrt{\sinh^2 \psi + \cos^2 \beta}} \quad (\text{D.10})$$

The final sequence of equations for the flat plate cascade are shown on the last few pages of this appendix using the Mathcad analysis program. The required input values are the stagger angle, β , solidity, σ , mean flow angle, α , and angular chord position, ϕ . The useful results include relative chord position, x/c ; local velocity ratio, u/V_{avg} ; surface pressure coefficient, C_p ; and cascade flow angles, α_1 and α_2 .

Due to limitations of the flat plate analysis, the exit flow cannot be turned beyond the chord of the stator. Consequently with a high-solidity cascade, the flow analysis shows that the flat-plate-cascade-exit flow is nearly parallel to the chord line. With the Hessert Center cascade stagger angle, solidity, and mean flow angle, the flat plate analysis showed a total turning of 19 degrees while the actual cascade turning was 42.5 degrees. This higher amount of turning due to blade camber matches empirical results for blade exit deviation angles for cascades from Cohen, et al. The cascade geometry and the stator profile coordinates are shown in Appendix E. In the actual engine, the stator turning ranges from 39.8 degrees at the tip to 45.2 degrees at the hub. Even with the turning limitations,

the flat plate analysis provided velocity ratios and pressure coefficients along the chord line as shown on the last few pages of this appendix. These represent the mean flow values around which the unsteady flow would be perturbed. Unfortunately the total turning of the flow does not match the physical case and consequently the stator loading will not match the physical steady loading. More advanced techniques, using a mean-flow-solver, can provide improved surface pressure coefficients but are computationally much more extensive. Given the experimental nature and emphasis on unsteady aerodynamics of this project only simplified computational techniques were examined.

D.2. Sample Flat Plate Calculations for Cascade Geometry.

Solve a cascade conformal mapping equation in Oates (Eqn 11.31) and remaining equations
 C = chord, S = spacing, Sigma = solidity, Beta = stagger angle, Alpha = mean flow angle

$$C \equiv 1.28$$

$$k \equiv 0.80 \quad S \equiv 0.84 \quad \sigma \equiv \frac{C}{S}$$

$$\beta \equiv -0.1588$$

$$\alpha \equiv 0.1702$$

$$\beta \cdot \frac{180}{\pi} = -9.09857 \text{ Deg} \quad \alpha \cdot \frac{180}{\pi} = 9.75174 \text{ Deg}$$

Internal Iterative Procedure finds value of psi (same as a)

Guess psi value: $\psi := 1$ Psi is a parameter related to C/S

Given

$$\left[\cos(\beta) \cdot \ln \left(\frac{\sqrt{\cos(\beta)^2 + \sinh(\psi)^2} + \cos(\beta)}{\sinh(\psi)} \right) + \sin(\beta) \cdot \operatorname{atan} \left[\frac{\sin(\beta)}{\left(\sqrt{\cos(\beta)^2 + \sinh(\psi)^2} \right)} \right] \right] = \sigma \cdot \frac{\pi}{2}$$

$$a := \text{Find}(\psi)$$

The Result is: $a = 0.17984$

Verify the result: $\sigma \cdot \frac{\pi}{2} = 2.39359$

$$\left[\cos(\beta) \cdot \ln \left(\frac{\sqrt{\cos(\beta)^2 + \sinh(a)^2} + \cos(\beta)}{\sinh(a)} \right) + \sin(\beta) \cdot \operatorname{atan} \left[\frac{\sin(\beta)}{\left(\sqrt{\cos(\beta)^2 + \sinh(a)^2} \right)} \right] \right] = 2.39359$$

Redefine "psi" value with "a": $\psi := a$

$$\phi_0 := \operatorname{atan}(\tan(\beta) \cdot \tanh(\psi)) \quad \phi_0 = -0.02849$$

Note that leading edge occurs at $\phi_0 + \pi$ $\phi_{LE} := \phi_0 + \pi$

Set up range of psi values with phi $\phi_k := \phi_0 + k \cdot \frac{\pi}{40}$

$$x_{OC_k} := \frac{1}{(2 \cdot \pi \cdot \sigma)} \cdot \left(\cos(\beta) \cdot \ln \left(\frac{\cosh(\psi) + \cos(\phi_k)}{\cosh(\psi) - \cos(\phi_k)} \right) + 2 \cdot \sin(\beta) \cdot \operatorname{atan} \left(\frac{\sin(\phi_k)}{\sinh(\psi)} \right) \right)$$

$$u_{OV_{inf_k}} := \frac{1}{\sin(\beta) \cdot \cos(\beta)} \cdot \left(\cos(\beta) \cdot \sin(\alpha + \beta) - \sin(\alpha) \cdot \cos(\phi_0) \cdot \frac{\cos\left(\frac{\phi_0 + \phi_k}{2}\right)}{\cos\left(\frac{\phi_0 - \phi_k}{2}\right)} \right)$$

$$\alpha_1 := \text{atan} \left(\sin(\alpha) \cdot \frac{\sqrt{\sinh(\psi)^2 + \cos(\beta)^2} + \cos(\beta)}{\sqrt{\sinh(\psi)^2 + \cos(\beta)^2} \cdot \cos(\alpha) + \sin(\beta) \cdot \sin(\alpha)} \right)$$

$$\alpha_2 := \text{atan} \left(\sin(\alpha) \cdot \frac{\sqrt{\sinh(\psi)^2 + \cos(\beta)^2} - \cos(\beta)}{\sqrt{\sinh(\psi)^2 + \cos(\beta)^2} \cdot \cos(\alpha) - \sin(\beta) \cdot \sin(\alpha)} \right)$$

$$C_{p_k} := 1 - \left(u_{\infty} V_{\infty} \right)^2$$

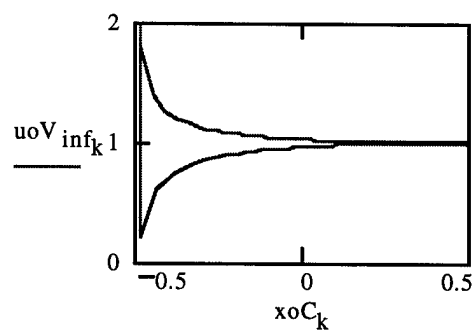
$$\alpha_{1D} := \alpha_1 \cdot \frac{180}{\pi}$$

$$\alpha_{2D} := \alpha_2 \cdot \frac{180}{\pi}$$

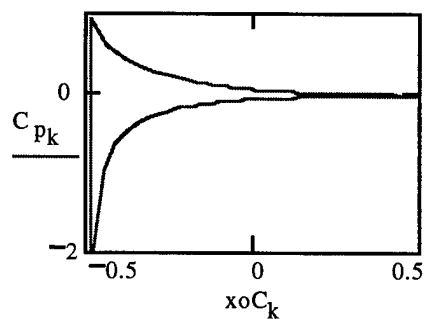
$$\alpha_{1D} = 19.31052 \text{ Deg}$$

$$\alpha_{2D} = 0.1568 \text{ Deg}$$

u over V infinity vs chord position



Pressure Coefficient vs chord position



APPENDIX E

STATOR COORDINATES AND CASCADE GEOMETRY

Table E.1. Stator vane coordinates in terms of half-chord.

$x/(c/2)$	y pressure/(c/2)	y suction/(c/2)
-1.00E+00	0.00E+00	0.00E+00
-9.98E-01	-3.50E-03	1.25E-02
-9.95E-01	-4.50E-03	1.80E-02
-9.93E-01	-5.00E-03	2.30E-02
-9.90E-01	-5.00E-03	2.65E-02
-9.85E-01	-4.00E-03	3.25E-02
-9.80E-01	-2.50E-03	3.80E-02
-9.75E-01	-1.00E-03	4.19E-02
-9.70E-01	6.55E-04	4.50E-02
-9.40E-01	1.03E-02	6.45E-02
-9.10E-01	1.96E-02	8.09E-02
-8.80E-01	2.87E-02	9.67E-02
-8.50E-01	3.74E-02	1.12E-01
-8.20E-01	4.58E-02	1.27E-01
-7.90E-01	5.40E-02	1.41E-01
-7.60E-01	6.18E-02	1.55E-01
-7.30E-01	6.93E-02	1.68E-01
-7.00E-01	7.65E-02	1.80E-01
-6.50E-01	8.79E-02	2.00E-01
-6.00E-01	9.84E-02	2.18E-01
-5.50E-01	1.08E-01	2.35E-01
-5.00E-01	1.17E-01	2.50E-01
-4.50E-01	1.25E-01	2.64E-01
-4.00E-01	1.32E-01	2.76E-01
-3.50E-01	1.38E-01	2.87E-01
-3.00E-01	1.44E-01	2.96E-01
-2.50E-01	1.49E-01	3.04E-01
-1.50E-01	1.55E-01	3.15E-01
-5.00E-02	1.59E-01	3.20E-01
5.00E-02	1.59E-01	3.19E-01
1.50E-01	1.55E-01	3.11E-01
2.50E-01	1.49E-01	2.98E-01
3.00E-01	1.44E-01	2.89E-01
3.50E-01	1.39E-01	2.79E-01
4.00E-01	1.32E-01	2.67E-01

Table E.1. Continued

$x/(c/2)$	y pressure/(c/2)	y suction/(c/2)
4.50E-01	1.25E-01	2.54E-01
5.00E-01	1.17E-01	2.39E-01
5.50E-01	1.09E-01	2.23E-01
6.00E-01	9.90E-02	2.05E-01
6.50E-01	8.85E-02	1.85E-01
6.80E-01	8.18E-02	1.73E-01
7.10E-01	7.48E-02	1.60E-01
7.40E-01	6.75E-02	1.47E-01
7.70E-01	5.99E-02	1.33E-01
8.00E-01	5.20E-02	1.18E-01
8.30E-01	4.38E-02	1.03E-01
8.60E-01	3.53E-02	8.77E-02
8.90E-01	2.65E-02	7.16E-02
9.20E-01	1.74E-02	5.49E-02
9.50E-01	7.99E-03	3.77E-02
9.80E-01	-1.72E-03	2.00E-02
9.90E-01	-8.61E-04	9.98E-03
1.00E+00	0.00E+00	0.00E+00

Table E.2. Cascade Geometry

Spacing, S	0.84 inch
Solidity, σ	1.524
Stagger Angle, β	-9°
Inlet Flow Angle, α_1	21.9°
Flow Turning Angle, ϕ	42.5°
Cascade Angle of Attack, α	9°

APPENDIX F

SURFACE FLOW VISUALIZATION

The flow visualization methods are discussed in Chapter 4, while the results are discussed in Chapter 5.

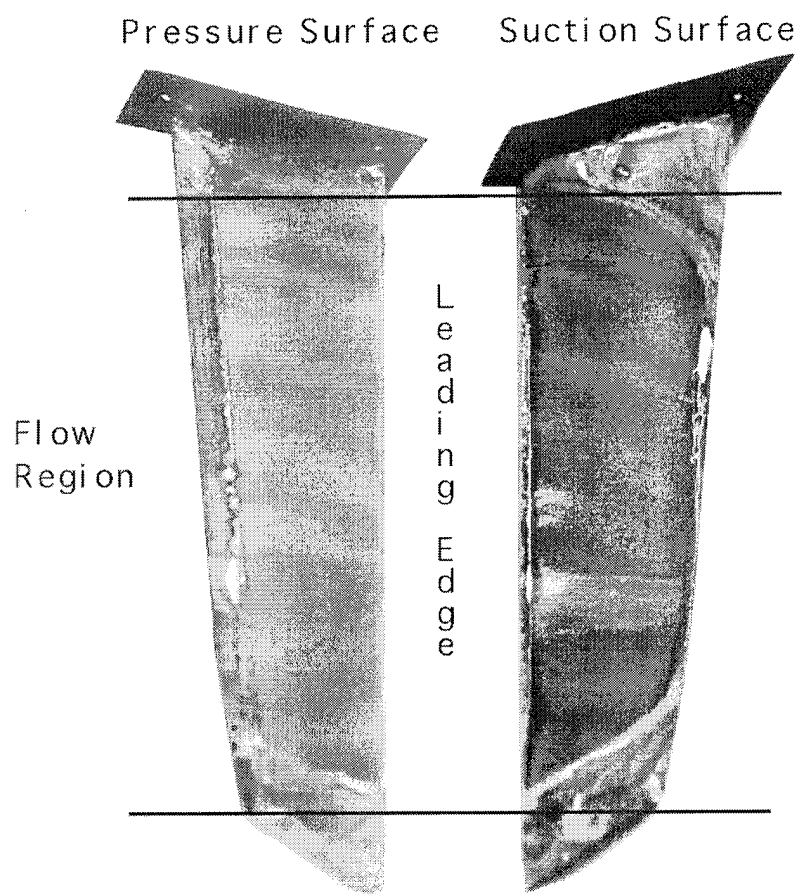


Figure F.1 Clean Tunnel, $M = 0.50$

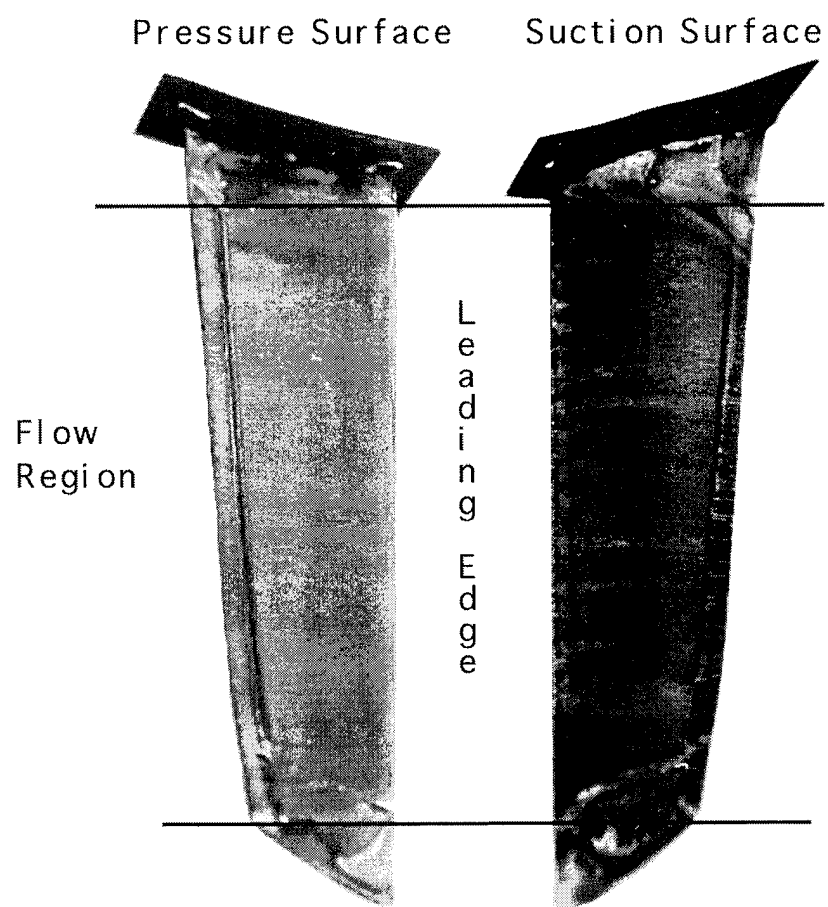


Figure F.2 Rods Forward, $M = 0.43$

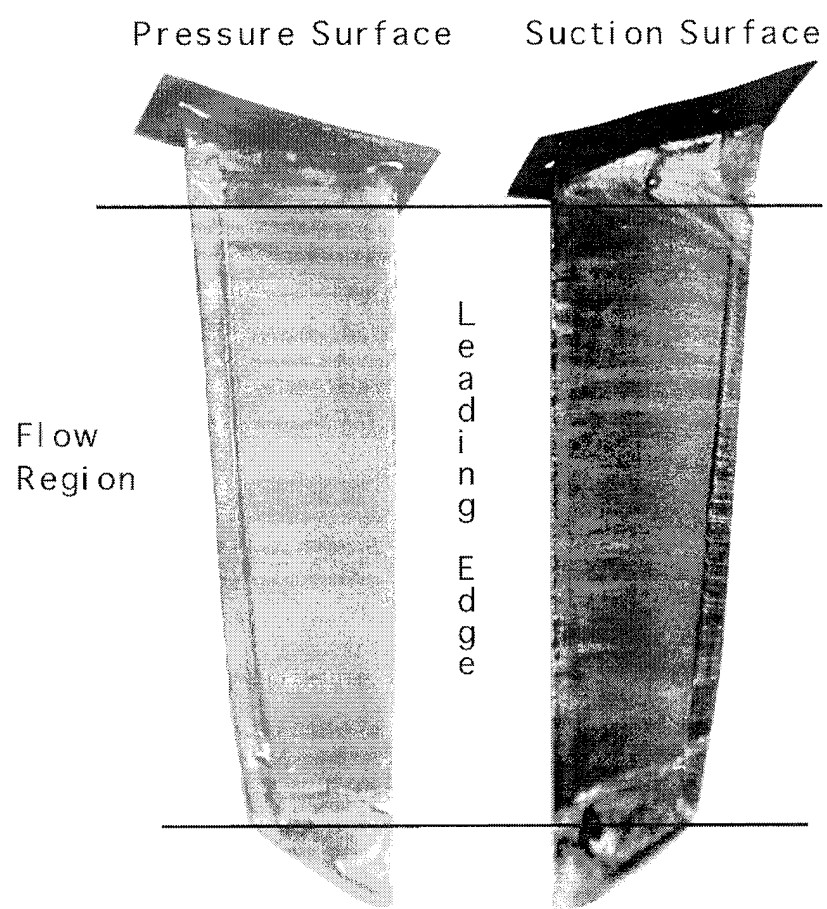


Figure F.3 Rods Forward, $M = 0.58$

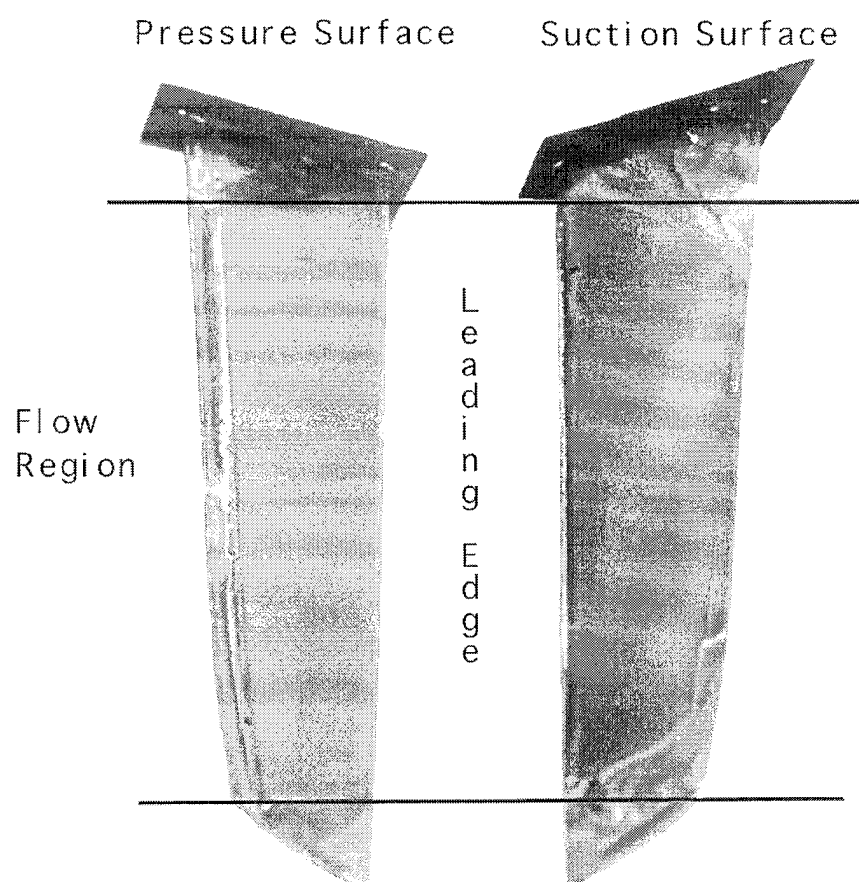


Figure F.4 Rods Rearward, $M = 0.427$

APPENDIX G

REARWARD FORCING DATA

This sections contains rearward forcing data from engine-axis 1 and 2. The important trends are presented in Chapter 6. The engine-axis 2 data will be presented first since it had more consistent stator surface contours from stator to stator, as explained in Chapter 5. The ensembled data are presented first and the phase diagrams follow.

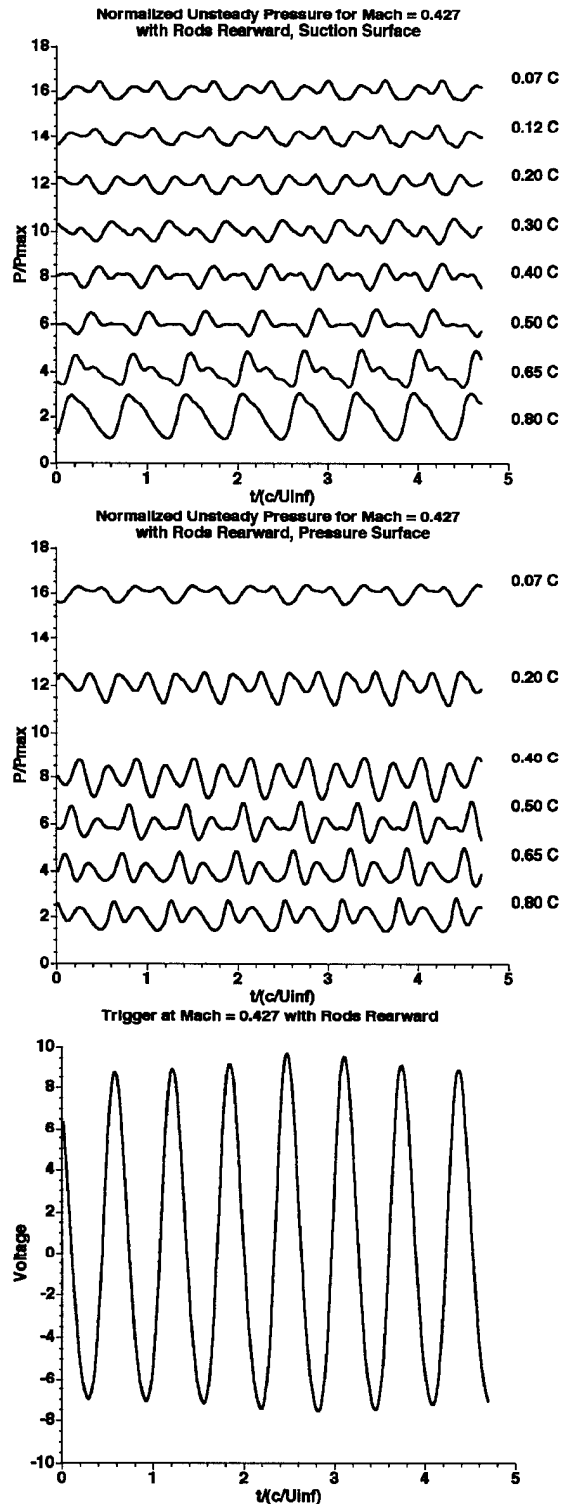


Figure G.1 Engine-Axis-Two Data, $M = 0.427$

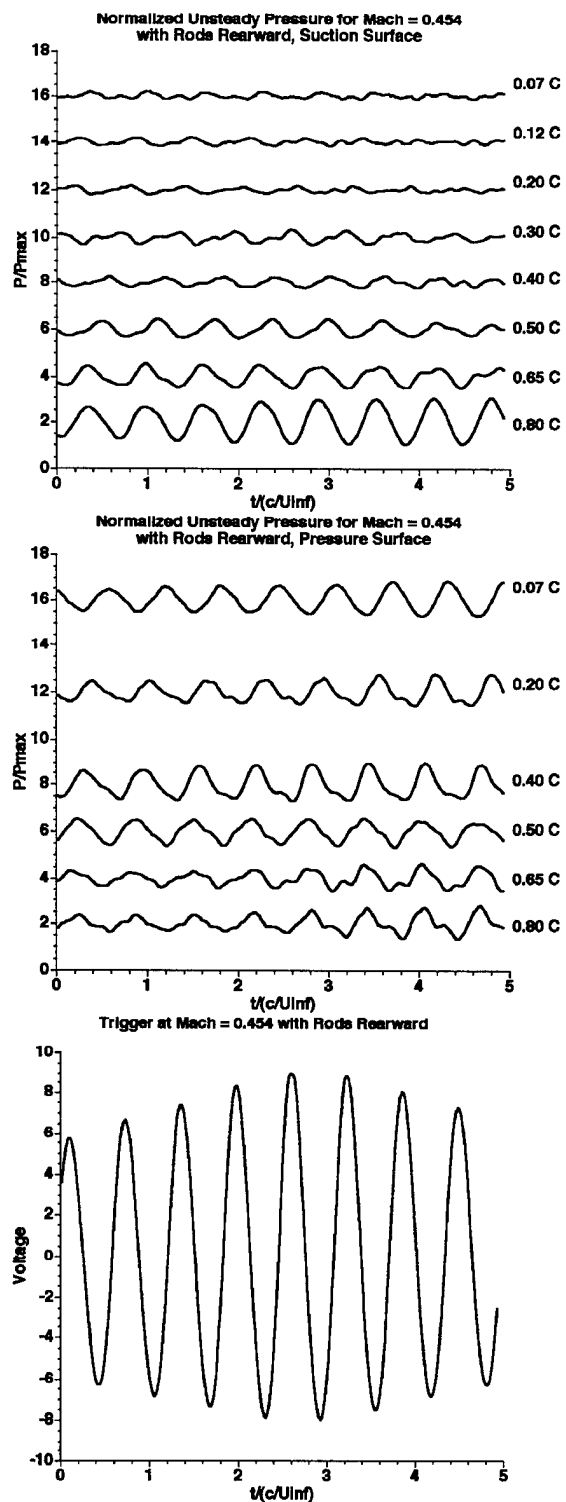


Figure G.2 Engine-Axis-Two Data, $M = 0.454$

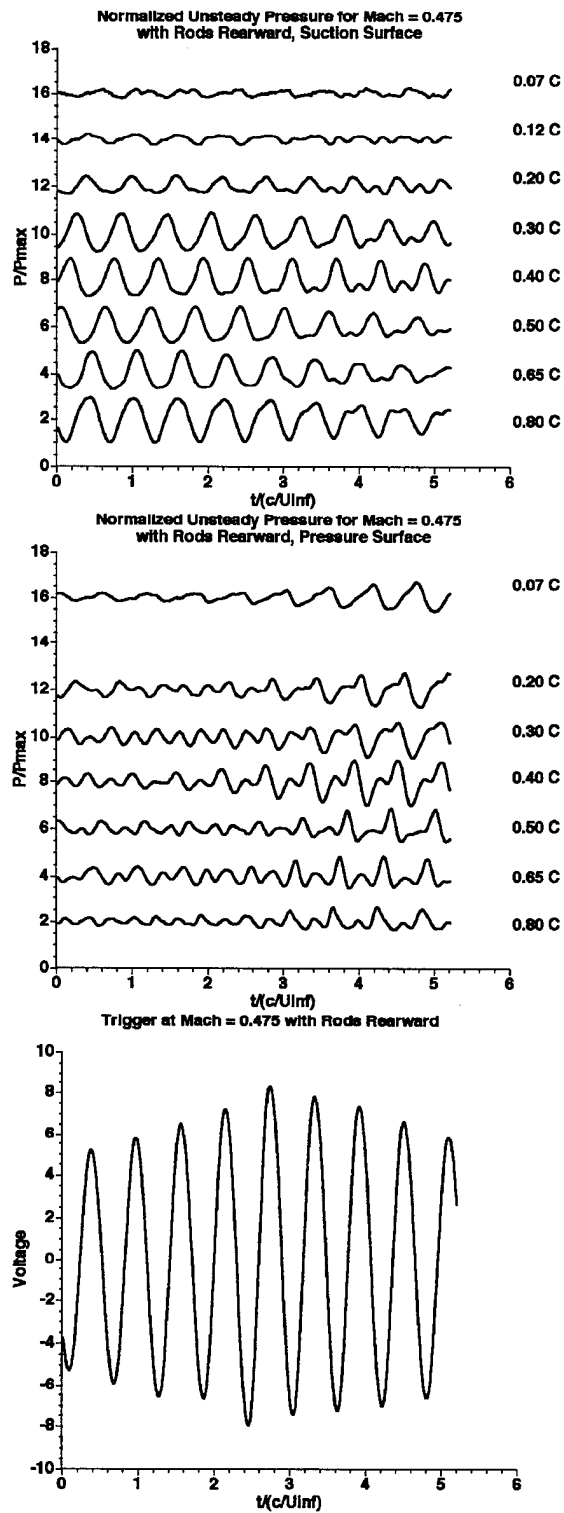


Figure G.3 Engine-Axis-Two Data, $M = 0.475$

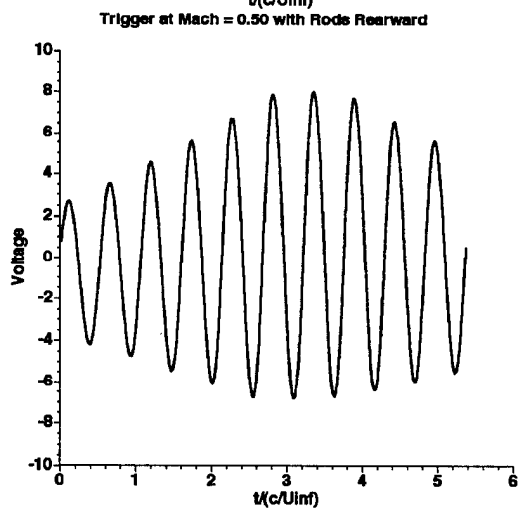
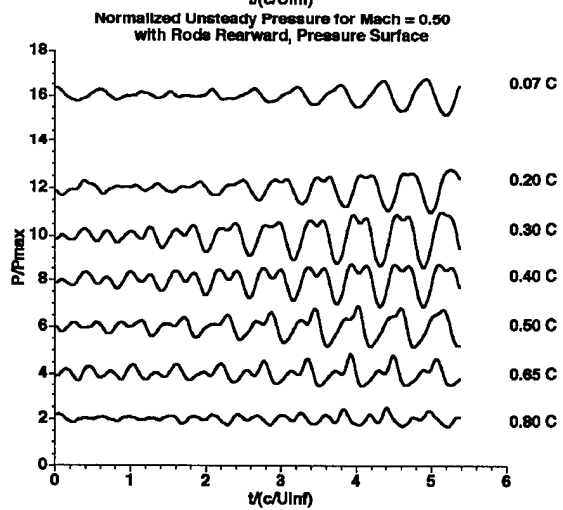
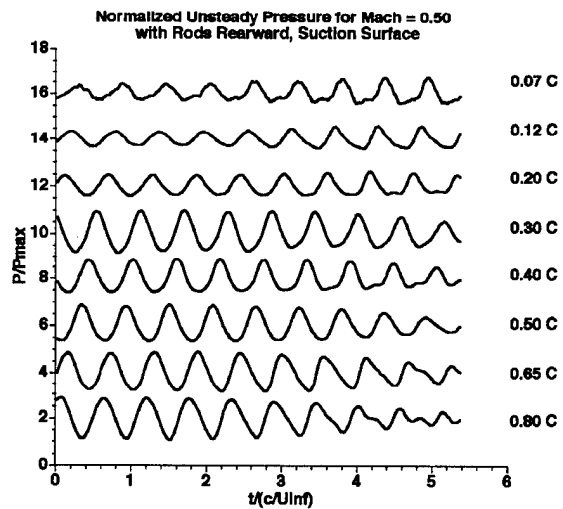


Figure G.4 Engine-Axis-Two Data, $M = 0.50$

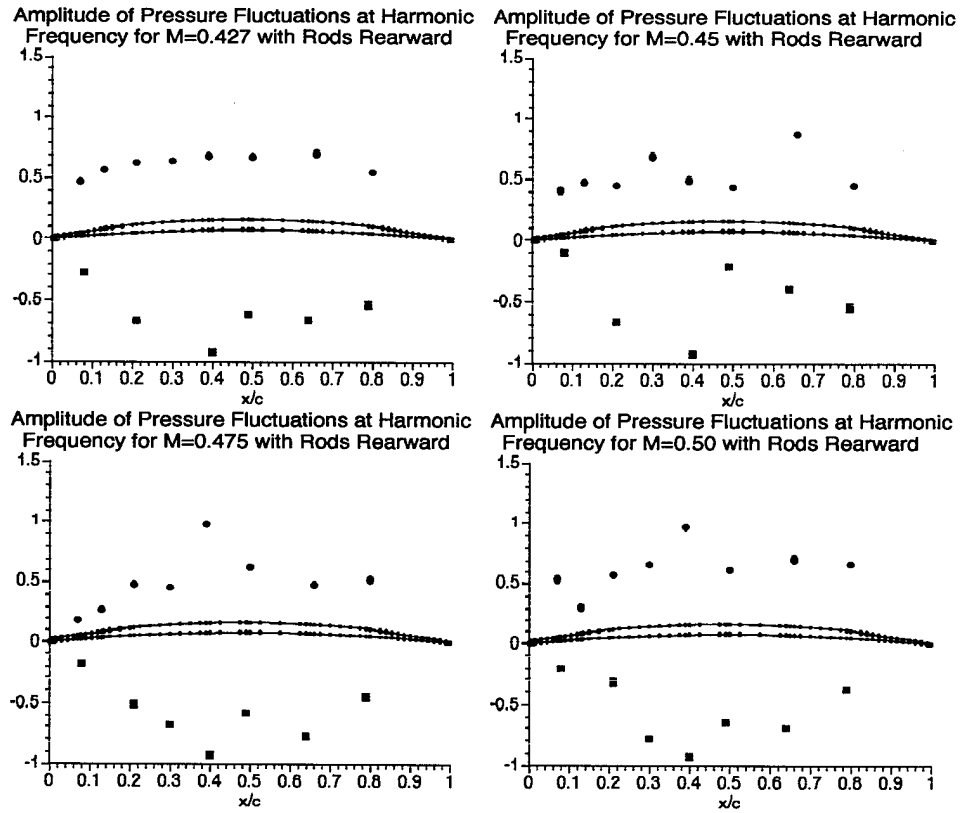


Figure G.5 Harmonic Data Through Mach Number Range

Upstream Travelling Wave for Primary Forcing Frequency of 7676 Hertz and First Harmonic with Mach 0.58 compared with data from Rods Downstream Case with M inlet = 0.45

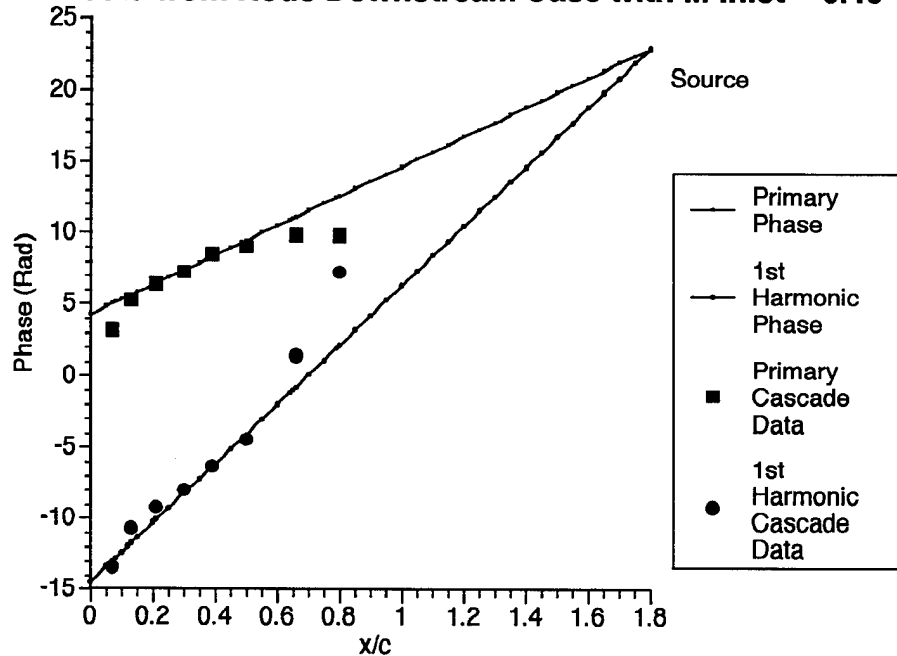


Figure G.6 Suction Surface Phase, $M = 0.45$

Upstream Travelling Wave for Primary Forcing Frequency of 7676 Hertz and First Harmonic with Mach 0.50 compared with data from Rods Downstream Case with M inlet = 0.45

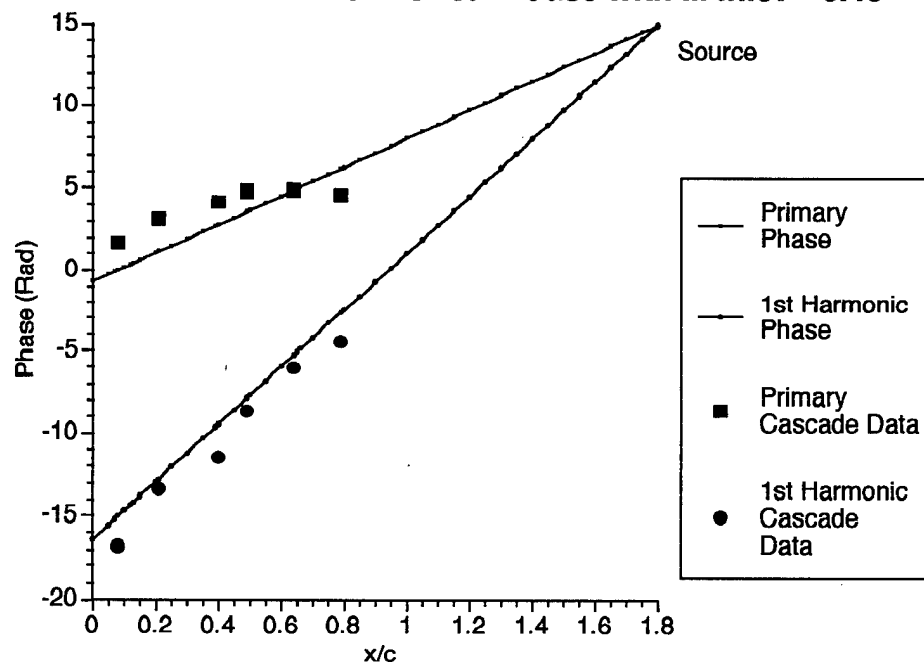


Figure G.7 Pressure Surface Phase, $M = 0.45$

Upstream Travelling Wave for Primary Forcing Frequency of 8694 Hertz and First Harmonic with Mach 0.66 compared with data from Rods Downstream Case with $M_{inlet} = 0.475$

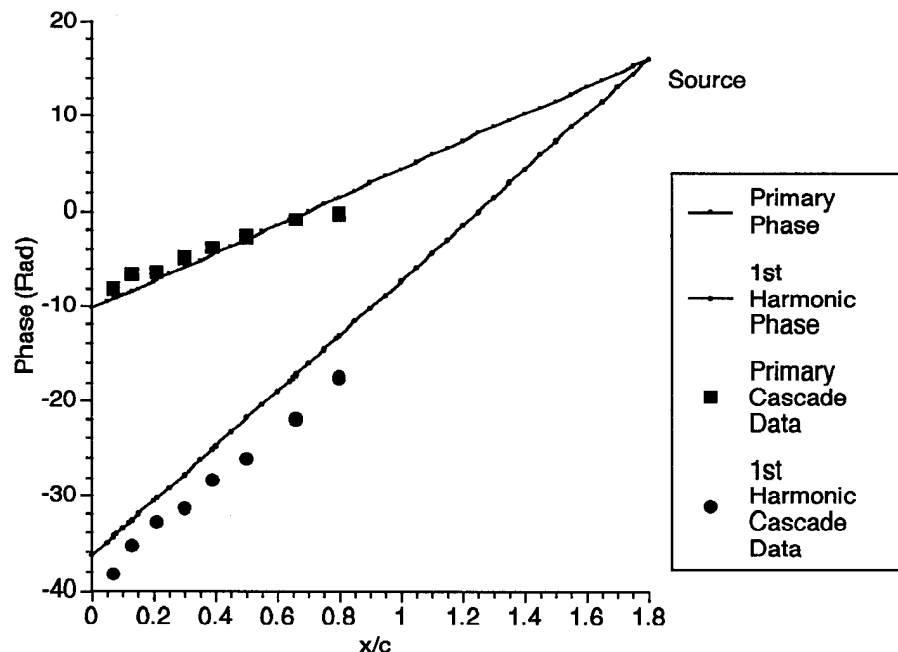


Figure G.8 Suction Surface Phase, $M = 0.475$

Upstream Travelling Wave for Primary Forcing Frequency of 8694 Hertz and First Harmonic with Mach 0.60 compared with data from Rods Downstream Case with $M_{inlet} = 0.475$

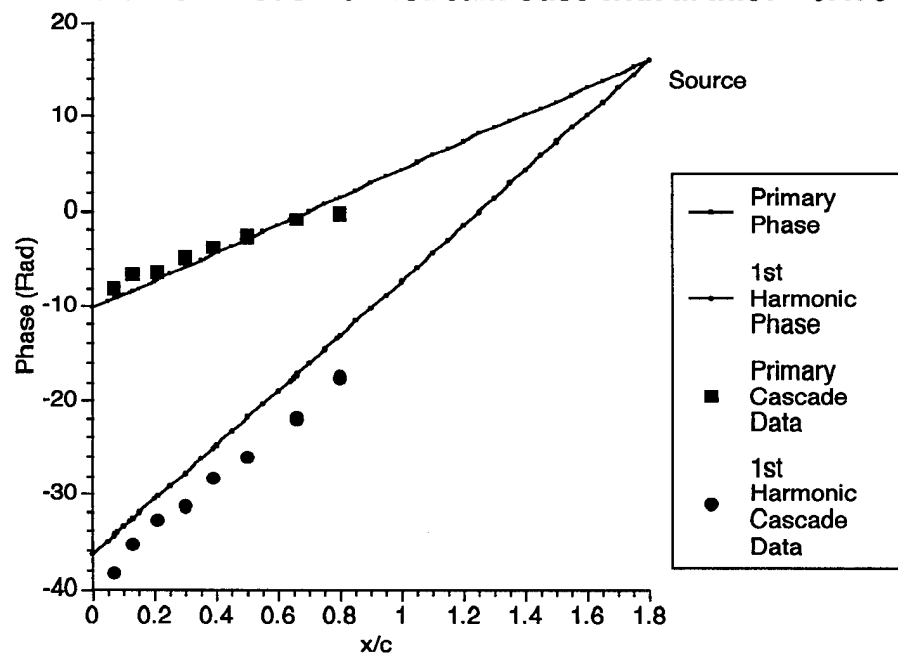


Figure G.9 Pressure Surface Phase, $M = 0.475$

Upstream Travelling Wave for Primary Forcing Frequency of 9117 Hertz and First Harmonic with Mach 0.71 compared with data from Rods Downstream Case with $M_{inlet} = 0.50$

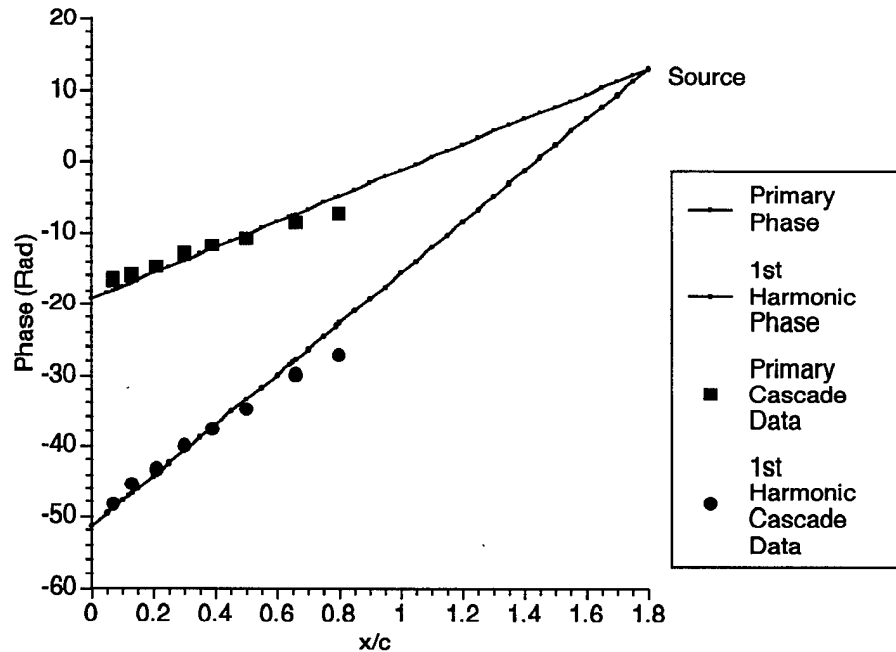


Figure G.10 Suction Surface Phase, $M = 0.50$
Upstream Travelling Wave for Primary Forcing Frequency of 9117 Hertz and First Harmonic with Mach 0.66 compared with data from Rods Downstream Case with $M_{inlet} = 0.50$

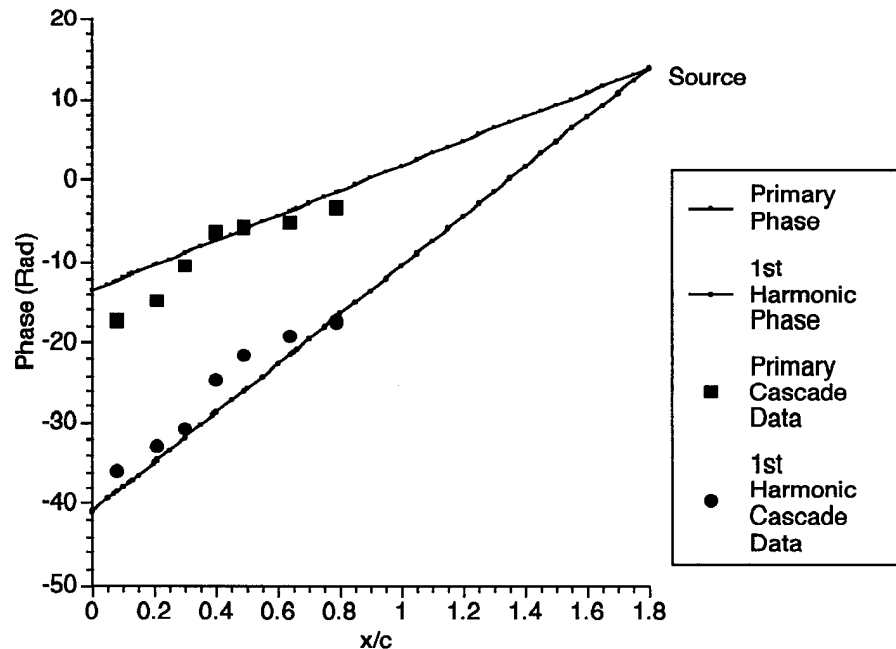


Figure G.11 Pressure Surface Phase, $M = 0.50$

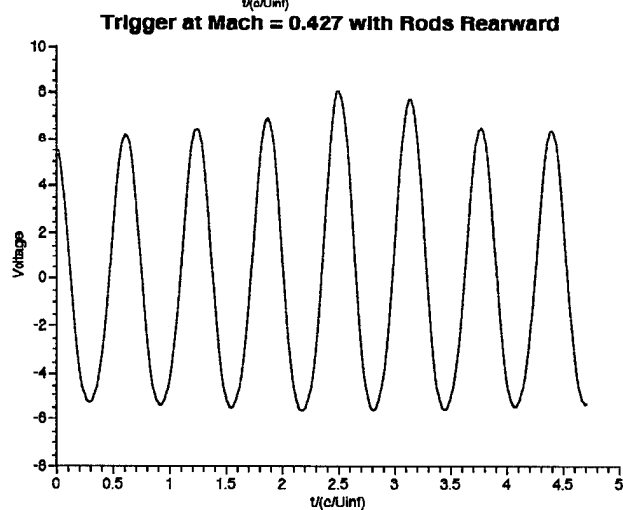
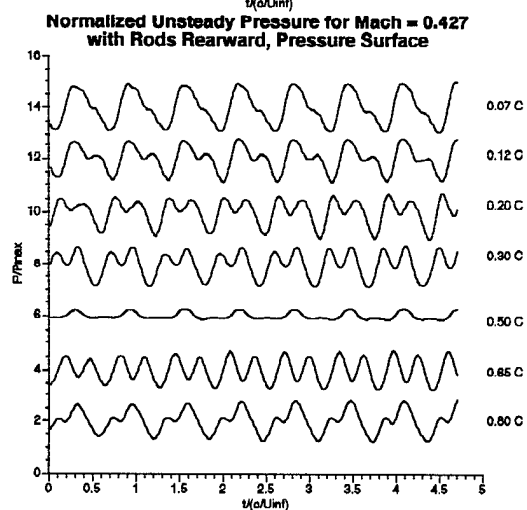
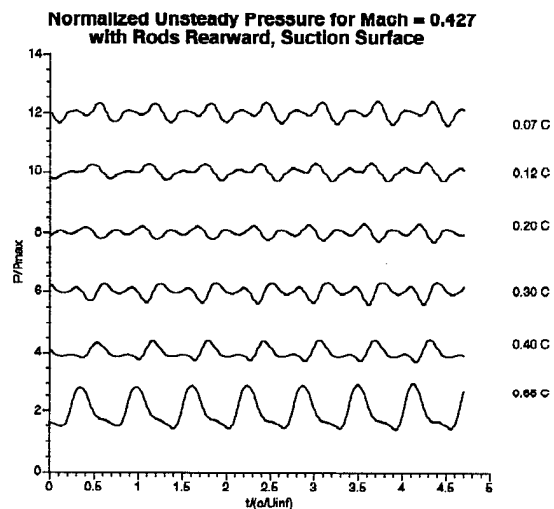


Figure G.12 Engine-Axis-One Data, $M = 0.427$

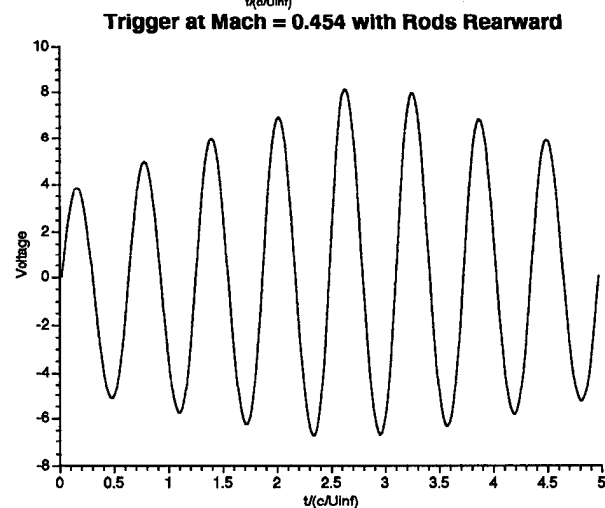
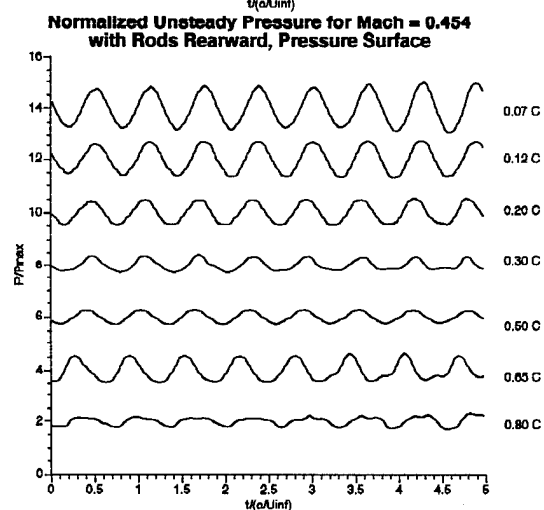
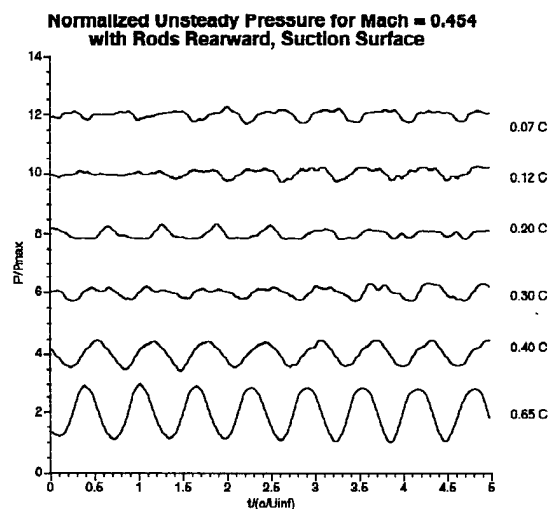


Figure G.13 Engine-Axis-One Data, $M = 0.454$

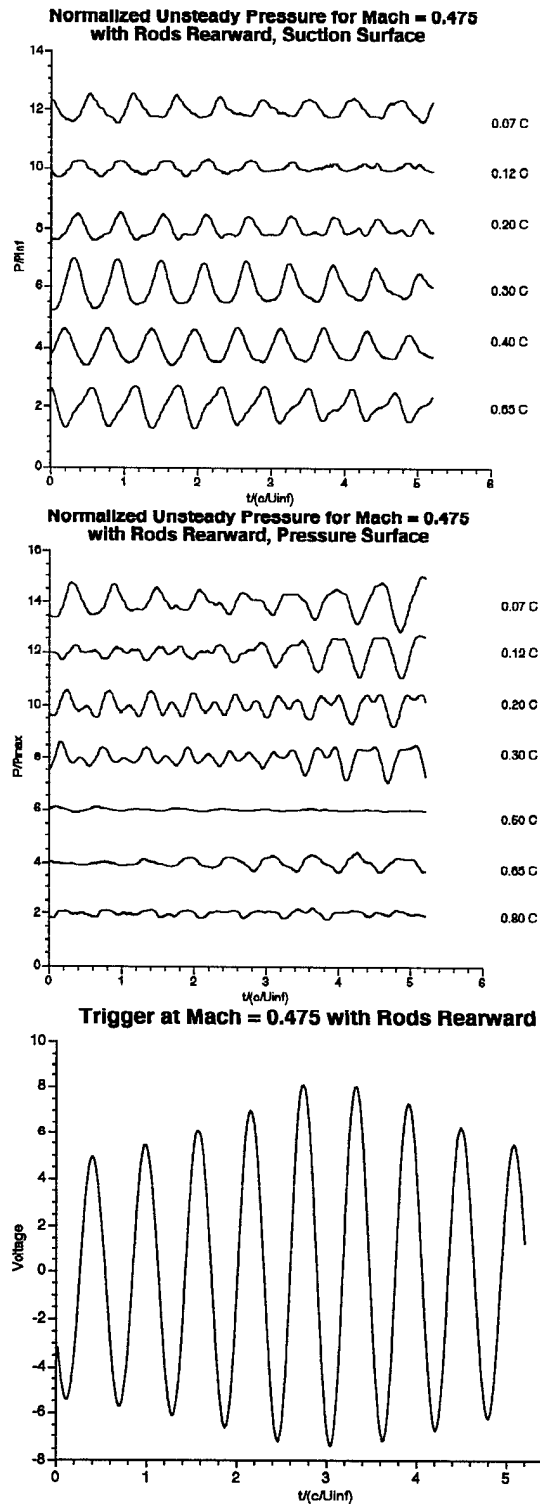


Figure G.14 Engine-Axis-One Data, $M = 0.475$

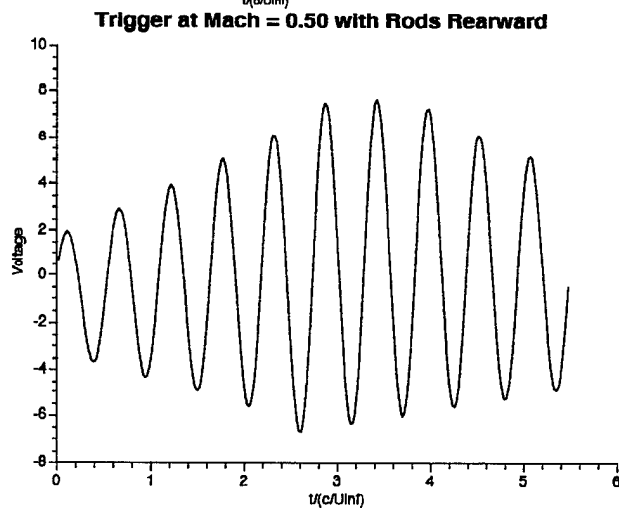
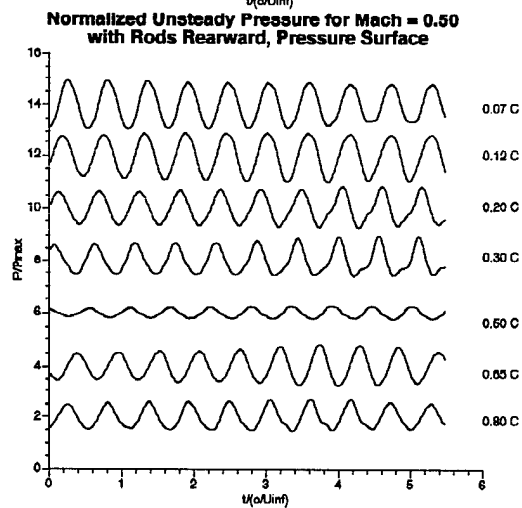
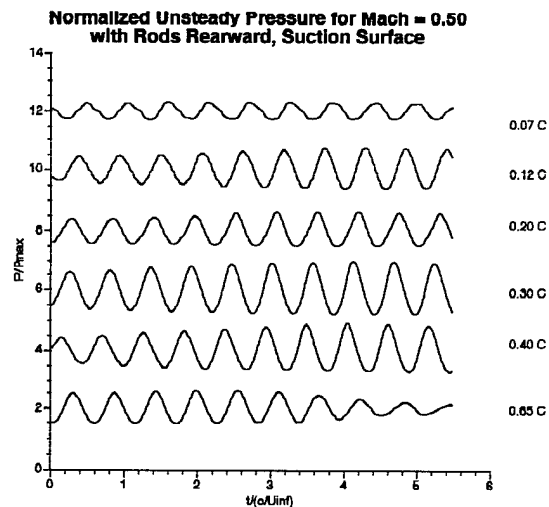


Figure G.15 Engine-Axis-One Data, $M = 0.50$

APPENDIX H

FORWARD FORCING DATA

This sections contains forward forcing data from engine-axis 1 and 2. The important trends are presented in Chapter 8. The engine-axis 2 data will be presented first since it had more consistent stator surface contours from stator to stator, as explained in Chapter 5. The ensembles of the transducers are presented.

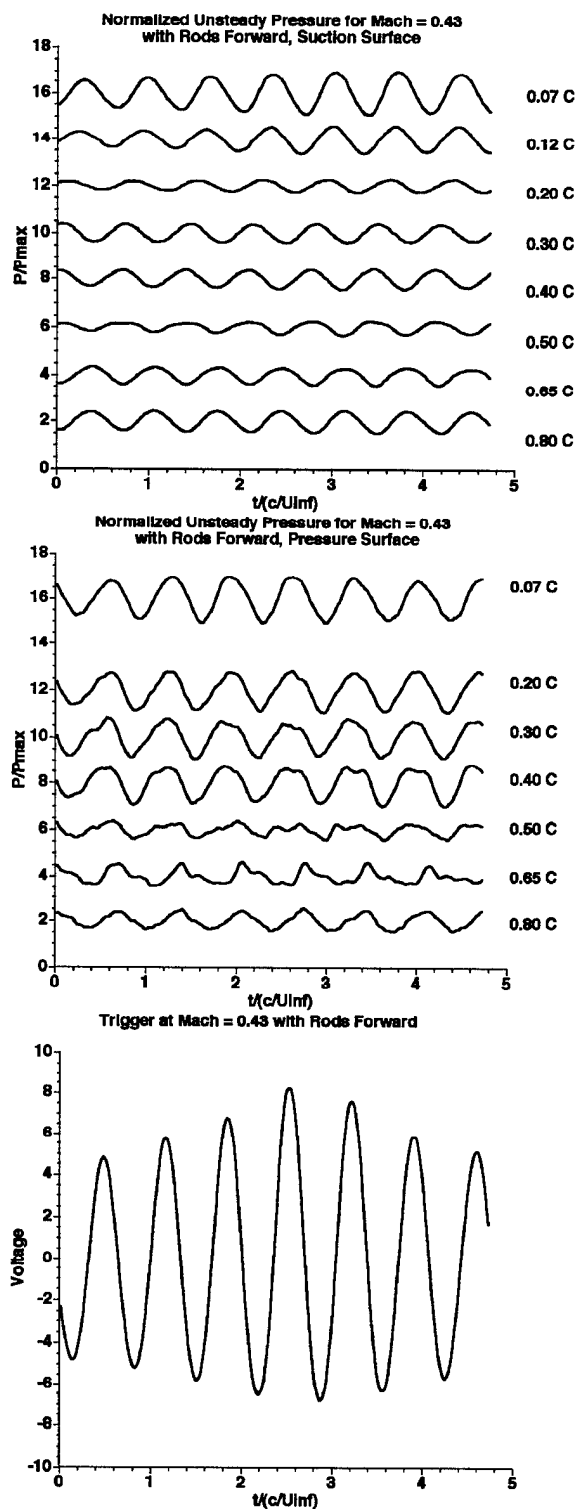


Figure H.1 Engine-Axis-Two Data, $M = 0.43$

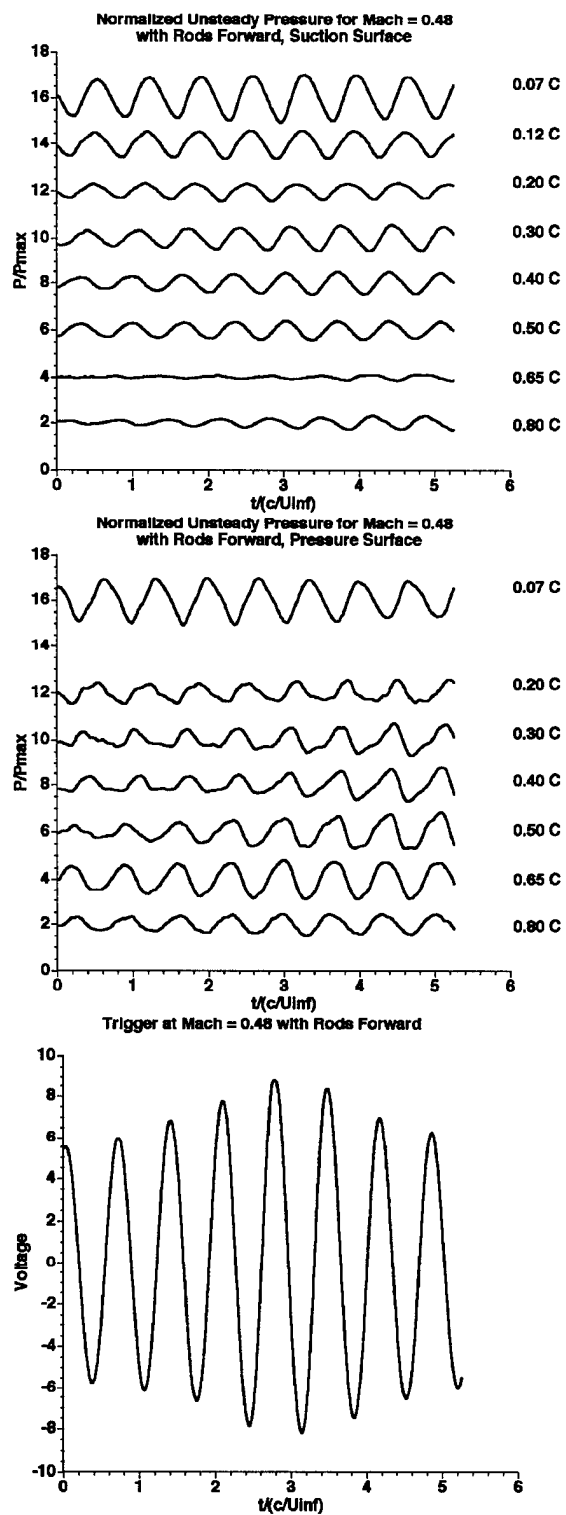


Figure H.2 Engine-Axis-Two Data, $M = 0.48$

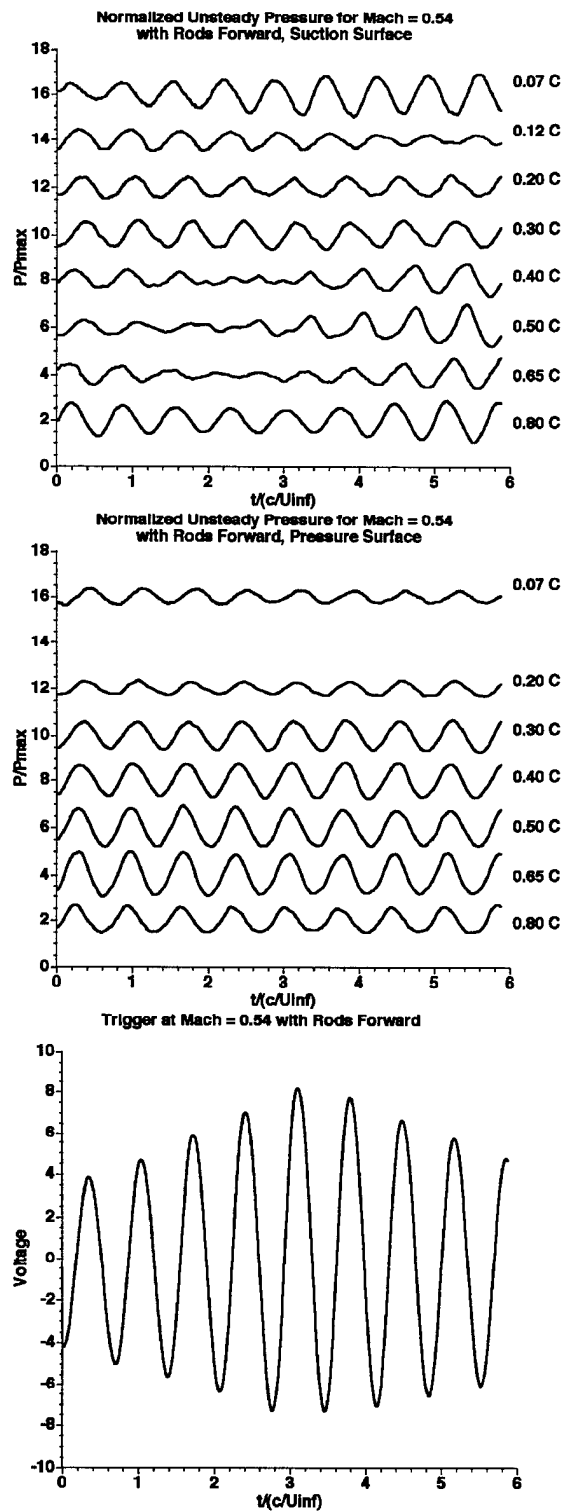


Figure H.3 Engine-Axis-Two Data, $M = 0.54$

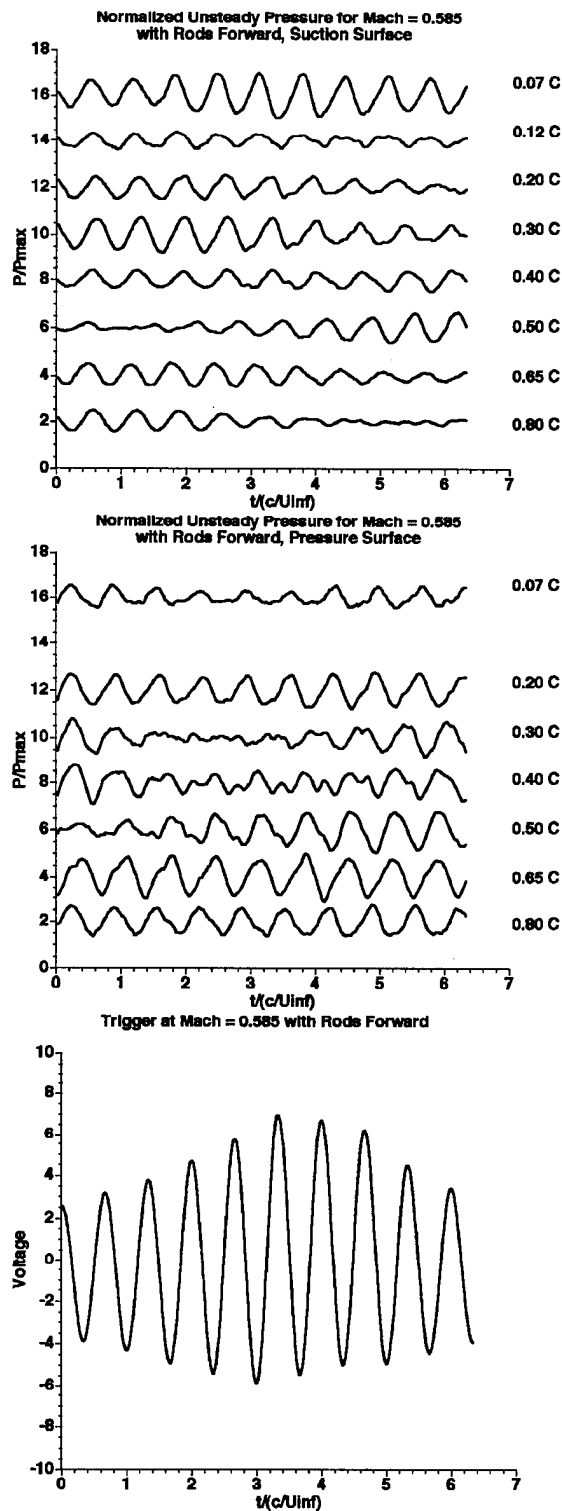


Figure H.4 Engine-Axis-Two Data, $M = 0.585$

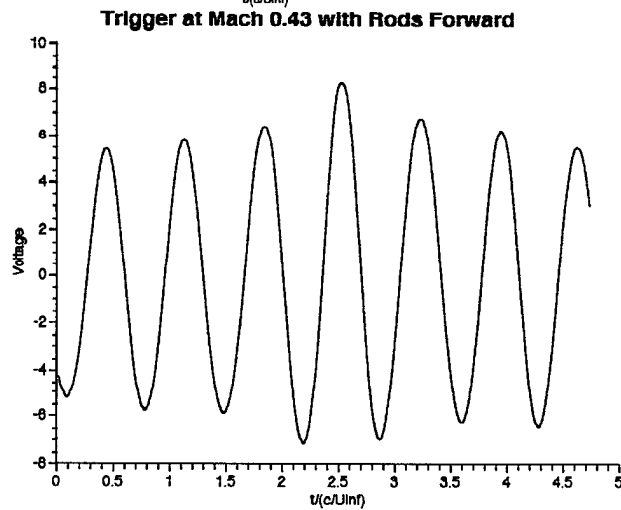
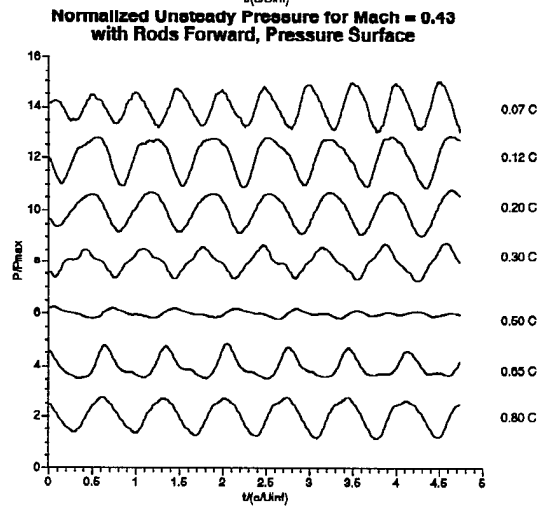
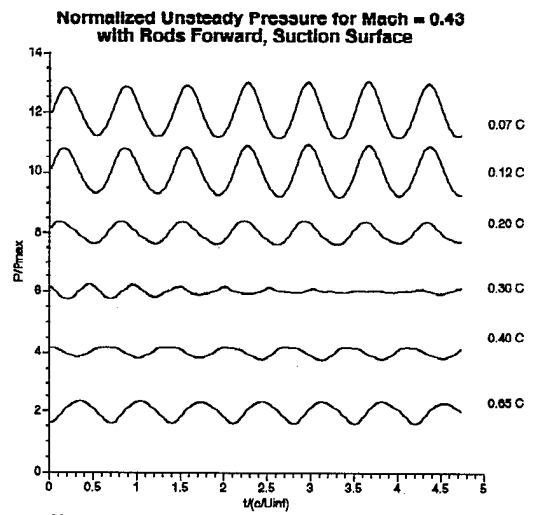


Figure H.5 Engine-Axis-One Data, $M = 0.43$

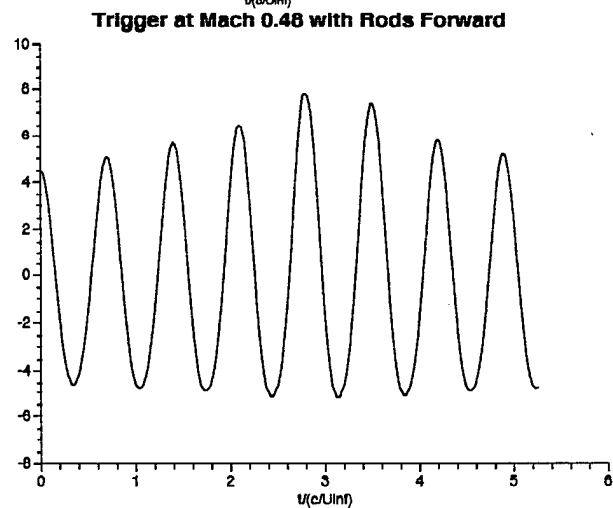
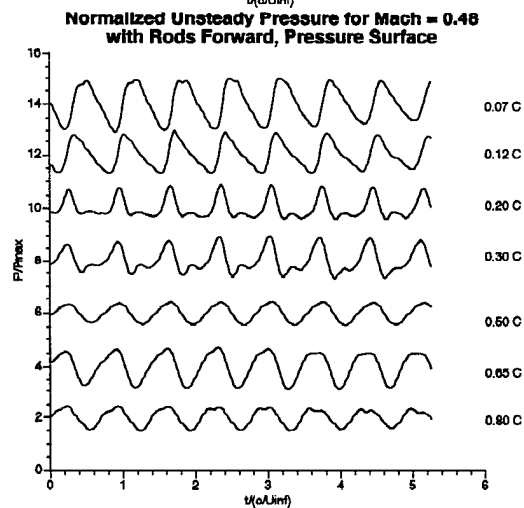
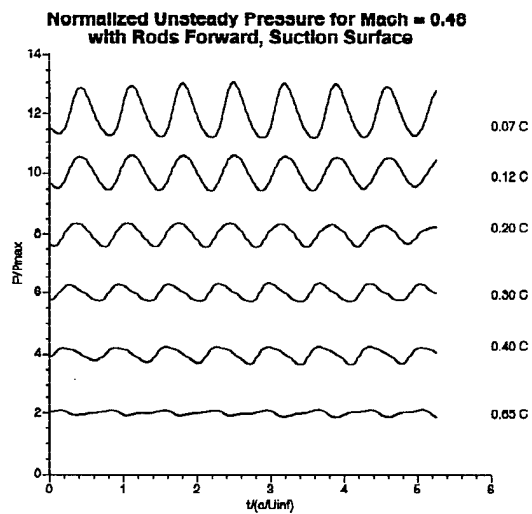


Figure H.6 Engine-Axis-One Data, $M = 0.48$

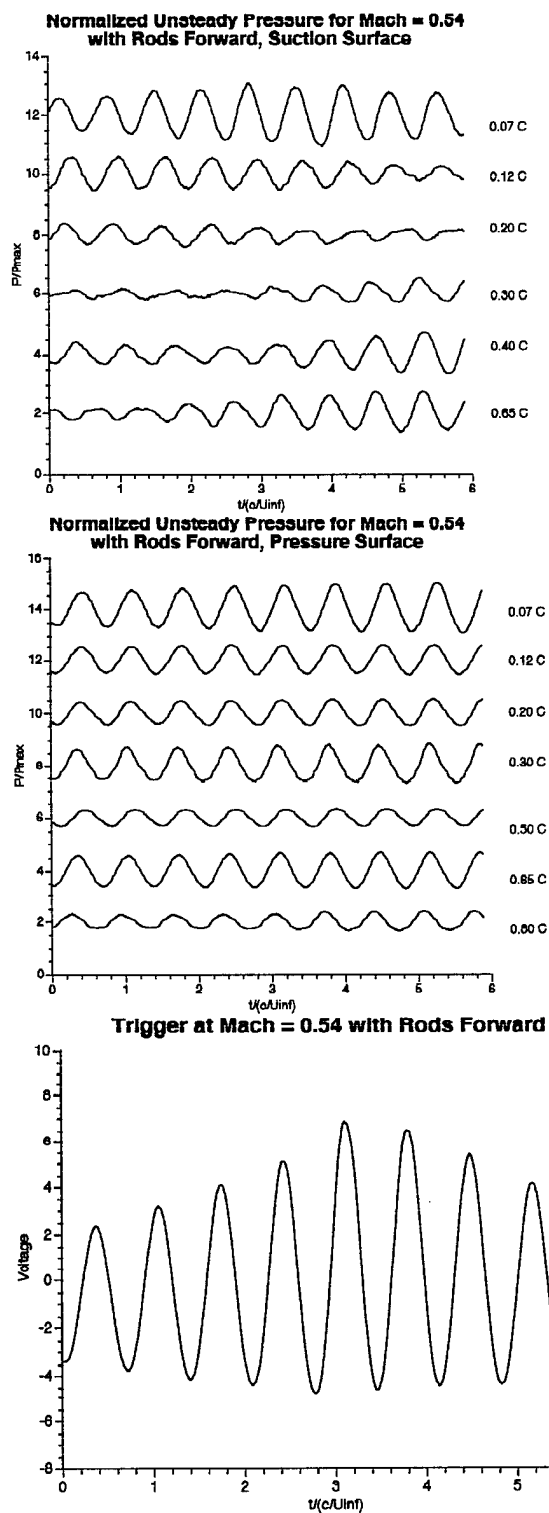


Figure H.7 Engine-Axis-One Data, $M = 0.54$

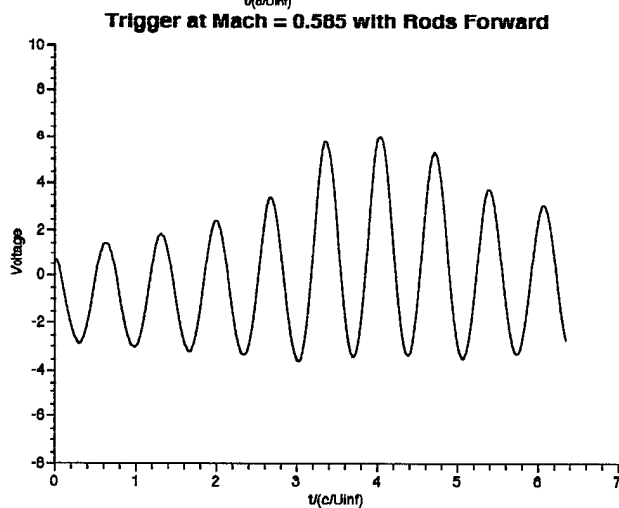
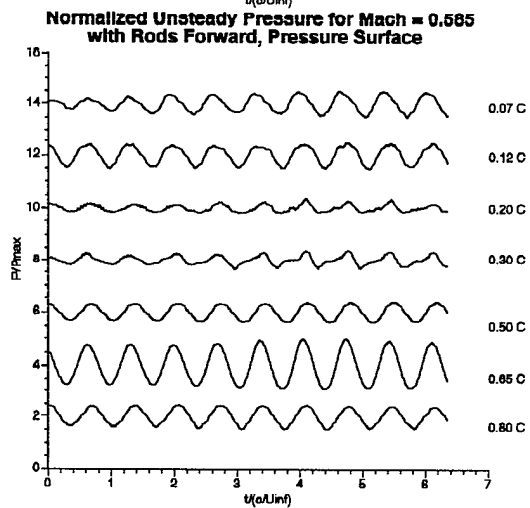
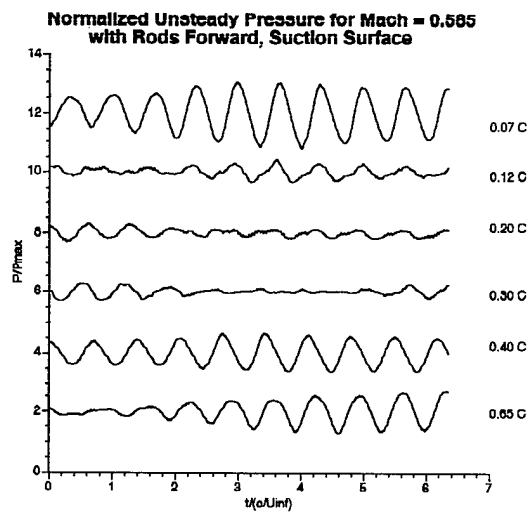


Figure H.8 Engine-Axis-One Data, $M = 0.585$

APPENDIX I

CASCADE DUCT ANALYSIS

An analysis of the cutoff frequency for the cascade system based on the wave equation, Eq (I.1), was conducted. The regions examined include the cascade inlet, individual cascade passage, and cascade exit. Following the analysis for transverse modes, an analysis for compressible, axial, acoustic modes is included.

I.1 Duct Model.

Each duct was modelled as shown in Figure I.1, where h is the local height and d is the local channel depth.

$$\frac{1}{a_{\infty}^2} \frac{\partial^2 P'}{\partial t^2} = \frac{\partial^2 P'}{\partial x^2} + \frac{\partial^2 P'}{\partial y^2} + \frac{\partial^2 P'}{\partial z^2} \quad (I.1)$$

Given the wave equation, Eq. (I.1) and the boundary conditions of the normal velocity component equalling zero at the wall, the equation may be solved using the separation of variables technique by assuming as solution of the form:

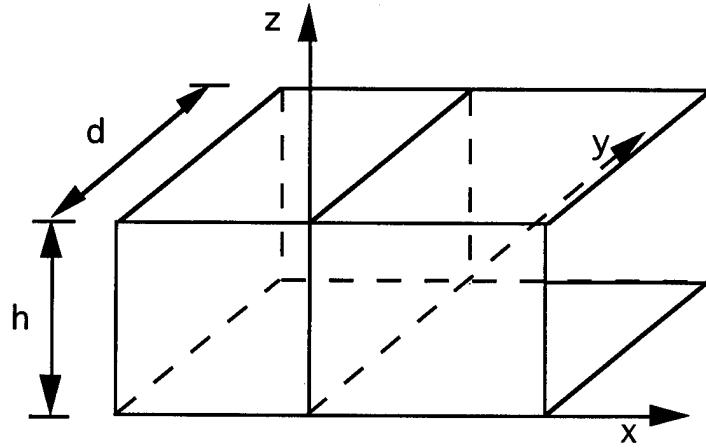


Figure I.1 Duct Coordinates

$$P'(x,y,z,t) = \tilde{P}(x,y,z)e^{-i\omega t} = X(x)Y(y)Z(z)e^{-i\omega t} \quad (1.2)$$

Using the wall boundary conditions, the y and z direction component solutions have the form:

$$Y(y) = \cos\left(\frac{n\pi y}{d}\right) \quad (1.3)$$

$$Z(z) = \cos\left(\frac{m\pi z}{h}\right) \quad (1.4)$$

where n and m are the integer mode numbers in the y and z directions, respectively. The duct axial component, $X(x)$, has the form:

$$X(x) = e^{\pm i x \sqrt{\left(\frac{\omega}{a_\infty}\right)^2 - \left(\frac{n\pi}{d}\right)^2 - \left(\frac{m\pi}{h}\right)^2}} \quad (1.5)$$

The character axial direction term determines whether the unsteady

pressure with transmit within the duct or decay with distance.

If the pressure disturbance at the initial position, $x = 0$, can be represented in the form:

$$P'(x=0,y,z,t) = f(y,z)e^{-i\omega t} \quad (1.6)$$

then the final for the unsteady pressure solution would be:

$$P'(x,y,z,t) = \sum_{n=0}^{\infty} \sum_{m=0}^{\infty} \frac{4}{dh} \left(\int_0^d \int_0^h f(y,z) \cos\left(\frac{n\pi y}{d}\right) \cos\left(\frac{m\pi z}{h}\right) dydz \right) * e^{ix\sqrt{\left(\frac{\omega}{a_{\infty}}\right)^2 - \left(\frac{n\pi}{d}\right)^2 - \left(\frac{m\pi}{h}\right)^2} - i\omega t} \quad (1.7)$$

The last two terms under the radical are often combined and often defined as the “transverse component,” K_{mn} as shown:

$$K_{mn} = \sqrt{\left(\frac{n\pi}{d}\right)^2 + \left(\frac{m\pi}{h}\right)^2} \quad (1.8)$$

The magnitude of this transverse component compared with the other term under the radical of Eq. (1.7) determines the “cut-off” frequency of the given m and n mode. The various situations are:

$$\frac{\omega}{a_{\infty}} > K_{mn} \quad \text{Wave propagates} \quad (1.9)$$

$$\frac{\omega}{a_{\infty}} = K_{mn} \quad \text{Cut-off Condition} \quad (1.10)$$

$$\frac{\omega}{a_{\infty}} < K_{mn} \quad \text{Wave decays exponentially} \quad (1.11)$$

In the cascade inlet and cascade outlet, with 5 disturbances sources spaced across the row in the y direction. Thus, the y-axis mode number, n , would be five or integer multiples. Within the cascade row, the y-axis mode number, n , would be one or integer multiples.

1.2 Model Results.

At the lowest testing frequencies, the unsteady pressure decays in both the cascade entrance or exit and also within the vane passages since the magnitude of the transverse components is less than ω/a_{∞} in all cases. However, within the vane passage at twice the forcing frequency, the calculated ω/a_{∞} would double causing certain conditions where the harmonic would propagate. This trend was confirmed in Chapter 6 at the lowest Mach number, $M = 0.427$.

At the highest testing frequencies, the wave always decays in amplitude in the cascade inlet and exit. There are cases where the wave can propagate within the vane passage for the primary and the harmonic. However, in the actual experiments at the highest Mach

number with the cylinders placed forward of the cascade row, the sound level coming out of the inlet had decreased. This was probably due to the increased effective distance the unsteady pressure had to travel.

I.3 Sample Calculations for Duct Mode.

Table I.1 Sample Results at 6700 Hz, Lowest Primary Testing Frequency

Within the Cascade Passage		h mode	d mode	
	Freq	m	n	K mn
if $\omega/a > K$ mn wave propagates	6700 Hertz	0	1	47.124
if $\omega/a = K$ mn cutoff freq	Spd of Sound	1	1	48.057
if $\omega/a < K$ mn exponential decay	1100 ft/sec	2	1	50.754
	d, depth	3	1	54.955
full width = 4.0	0.80 in	4	1	60.348
one blade passage= 0.8	h, height	5	1	66.643
	4 in	0	2	94.248
		1	2	94.718
	ω/c	2	2	96.114
	38.27	3	2	98.398
		4	2	101.51
		5	2	105.37
Cascade Inlet or Outlet		h mode	d mode	
	Freq	m	n	K mn
if $\omega/a > K$ mn wave propagates	6700 Hertz	0	5	235.62
if $\omega/a = K$ mn cutoff freq	Spd of Sound	1	5	235.81
if $\omega/a < K$ mn exponential decay	1100 ft/sec	2	5	236.37
	d, depth	3	5	237.31
full width = 4.0	4.00 in	4	5	238.62
one blade passage= 0.8	h, height	5	5	240.29
	4 in	0	10	471.24
		1	10	471.33
	ω/c	2	10	471.62
	38.27	3	10	472.09
		4	10	472.74
		5	10	473.59

Table I.2 Sample Results at 9200 Hz, Highest Primary Testing Frequency

Within the Cascade Passage		h mode	d mode	
	Freq	m	n	K mn
if $\omega/a > K$ mn wave propagates	9200 Hertz	0	1	47.124
if $\omega/a = K$ mn cutoff freq	Spd of Sound	1	1	48.057
if $\omega/a < K$ mn exponential decay	1100 ft/sec	2	1	50.754
	d, depth	3	1	54.955
full width = 4.0	0.80 in	4	1	60.348
one blade passage= 0.8	h, height	5	1	66.643
	4 in	0	2	94.248
		1	2	94.718
	ω/c	2	2	96.114
	52.55	3	2	98.398
		4	2	101.51
		5	2	105.37
Cascade Inlet or Outlet		h mode	d mode	
	Freq	m	n	K mn
if $\omega/a > K$ mn wave propagates	9200 Hertz	0	5	235.62
if $\omega/a = K$ mn cutoff freq	Spd of Sound	1	5	235.81
if $\omega/a < K$ mn exponential decay	1100 ft/sec	2	5	236.37
	d, depth	3	5	237.31
full width = 4.0	4.00 in	4	5	238.62
one blade passage= 0.8	h, height	5	5	240.29
	4 in	0	10	471.24
		1	10	471.33
	ω/c	2	10	471.62
	52.55	3	10	472.09
		4	10	472.74
		5	10	473.59

I.4 Acoustic Mode Calculations.

The follow section is based on the methods developed by Fang and Atassi for determination of the acoustic character of ducts in compressible flow (Fang and Atassi, 1993). It represents the next logical step following the previously discussed classical

transverse-mode analysis. The convective wave equation, shown in Eq. I.12, has solutions of the form shown in Eq. I.13.

$$\frac{1}{a_0^2} \frac{D_0^2 p'}{Dt^2} - \nabla^2 p' = 0 \quad (I.12)$$

$$p' = \sum_{n=-\infty}^{\infty} c_{n+} p'_{n+} + \sum_{n=-\infty}^{\infty} c_{n-} p'_{n-} \quad (I.13)$$

where the coefficients $c_{n\pm}$ are complex constants and $p'_{n\pm}$ has the form shown in Eqs. (I.14) and (I.15).

$$p'_{n\pm} = e^{i[(a_{n\pm}y_1 + b_{n\pm}y_2 + k_3x_3) - k_1t]} \quad \text{for upstream} \quad (I.14)$$

$$p'_{n\pm} = e^{i[(a_{n\pm}y_1' + b_{n\pm}y_2' + k_3x_3) - k_1t]} \quad \text{for downstream} \quad (I.15)$$

After substituting Eqs. (I.14) and (I.15) into Eq. (I.12) and the quasi-periodicity condition $p'(x+s,t) = p'(x,t)e^{i\sigma}$, results in a system of equations involving $a_{n\pm}$ and $b_{n\pm}$.

$$M^2(a_{n\pm} - k'_1)^2 + a_{n\pm}^2 + b_{n\pm}^2 + k_3^2 = 0 \quad (I.16)$$

$$b_{n\pm} - \frac{2n\pi + \sigma - a_{n\pm}s^*}{\tilde{s}} = 0 \quad (I.17)$$

where $k'_1 = k_1/U_0$ and s^* and s are the components of the spacing vector \tilde{s} parallel and perpendicular, respectively, to the mean flow

for the upstream or downstream condition. The solution of Eqs. (I.16) and (I.17) for $a_{n\pm}$ is

$$a_{n\pm} = \frac{-k'_1 M^2 \tilde{s}^2 + (2n\pi + \sigma)s^* \pm d_n \tilde{s}}{d^{\dagger 2}} \quad (I.18)$$

where

$$d_n = \sqrt{\beta^2 (\kappa^2 d^{\dagger 2} - \Gamma_n^2)} \quad (I.19)$$

$$\kappa = \sqrt{\frac{k'_1 M^2}{\beta^4} - \frac{k_3^2}{\beta^2}} \quad (I.20)$$

$$\Gamma_n = 2n\pi + \sigma + \frac{s^* k'_1 M^2}{\beta^2} \quad (I.21)$$

$$d^{\dagger} = \sqrt{s^{*2} + \beta^2 \tilde{s}^2} \quad (I.22)$$

$$\beta = \sqrt{1 - M^2} \quad (I.23)$$

It should be noted that the terms of $a_{n\pm}$ are all real except for a possible imaginary component of d_n . The transition between d_n including an imaginary component and having only real represents the cut-on condition for a given acoustic mode. Table I.3 shows the possible modes for the forward and rearward forcing cases. It should be noted that over the range of Mach numbers tested, the possible acoustic modes are similar for forward and rearward forcing of the

vane row.

Table I.3 Possible Acoustic Modes for Tested Limits of Forward and Rearward Cases

	Rods Forward $M_\infty = 0.43$	Rods Forward $M_\infty = 0.585$	Rods Rearward $M_\infty = 0.427$	Rods Rearward $M_\infty = 0.50$
Primary $k_1 = 5.0$	$n = 0$	$n = 0$	$n = 0$	$n = 0$
1st Harmonic $k_1 = 10.0$	$n = 0$	$n = -1$ $n = 0$ $n = 1$	$n = 0$	$n = -1$ $n = 0$ $n = 1$

APPENDIX J

UNCERTAINTY ANALYSIS

An uncertainty analysis was conducted on the pressure measurement portion of the Notre Dame Cascade Facility. The uncertainty approach explained in the Theory and Design for Mechanical Measurements, by Figliola and Beasley, was used throughout this analysis. The measurement equipment for the cascade is shown in Figures J.1. The entire analysis, using the Mathcad analysis program, is contained in the back of this appendix. A nominal Kulite pressure transducer, serial number 4485-1-31, acted as an example for this analysis since a total of thirty-two transducers were used in the full experiment. All analysis was conducted to a 95 percent confidence level. Most of the uncertainties were due to propagating bias errors moving from one piece of equipment to the next.

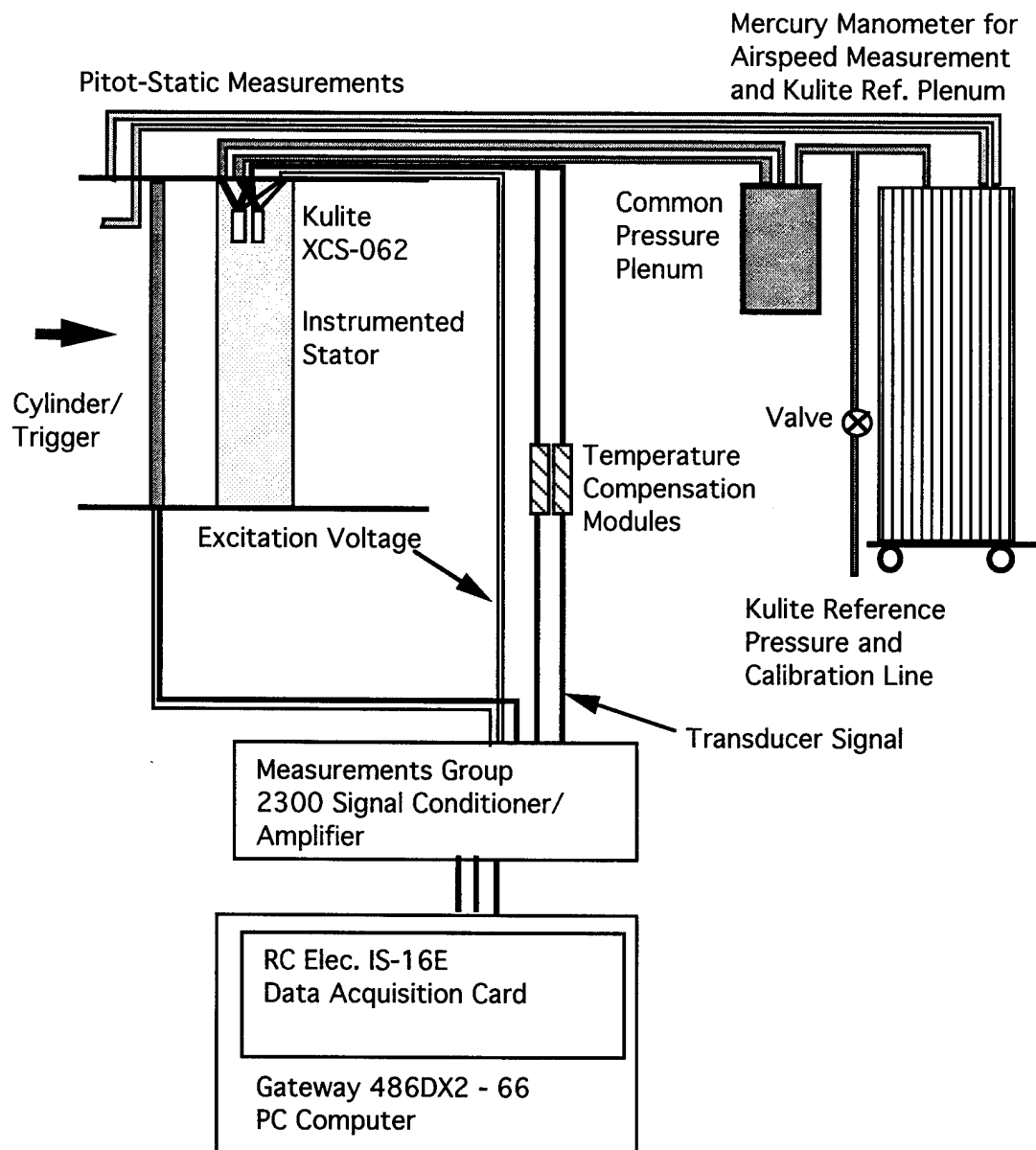


Figure J.1. Experimental Equipment Schematic

J.1 Analysis Discussion.

All analysis steps followed the logical data acquisition process from device to device. Previous uncertainties were considered bias errors in the next device.

The analysis for the cascade testing started with the Fortin wall barometer used for atmospheric pressure measurement. The correction for brass thermal expansion was also included in the measurement. The largest potential source of error, found by comparing the sensitivity multiplied by elemental error source, was the value of the density of mercury. For instance, there were two values for the mercury density in Engineering Thermodynamics, by Reynolds and Perkins, thus the difference between the values was considered to be the potential bias. Any gravitational errors were neglected. The total uncertainty for the barometer was 0.17 percent of the atmospheric pressure.

The mercury manometer bank was used as the calibration standard for the high speed in-draft wind tunnels. The interpolation error contributed the largest portion of the uncertainty since the scale was only in tenths of an inch. Again, any gravitational errors were neglected. The error at a typical manometer height of 5 inches

was 1.01 percent of the pressure reading.

The Vishay 2300, by Measurement Group, has an excitation voltage output, in addition to signal amplification and conditioning capabilities. The Vishay peak-to-peak ripple was the largest contributor to the uncertainty of the excitation voltage. The total uncertainty represented 0.017 percent of the excitation voltage. This had little influence in the following Kulite pressure transducer analysis.

The Kulite transducers used in the cascade experiments were ultraminiature XCS-062 differential pressure gages with a five pound per square inch range. The transducers have a temperature compensated range of 70°F to 170°F; however, the cascade tunnel has an operating temperature of approximately 45°F at Mach 0.50. The lack of proper temperature compensation for cascade testing caused the largest single transducer uncertainty, otherwise the cumulative uncertainty would have been 0.51 percent. The second largest bias source was the non-linearity of the transducer. In fact, this inherent weakness was disguised in the Kulite technical specifications since the non-linearity was stated as a combined hysteresis and non-linearity value error. The total uncertainty at the

transducer stage including the power supply was 1.10 percent.

The signal conditioning/amplification stage of the Vishay 2300 had gain accuracy as the largest internal uncertainty contributor. However, even this was small compared to the propagating bias error. The total uncertainty of the pressure was nearly unchanged at 1.10 percent.

With the RC-Electronics high speed Data Acquisition Card as the next component in the process, the largest source of card bias was the reading accuracy which was 0.18 percent of the input voltage. The total uncertainty of the data acquisition system was 1.10 percent of the output voltage.

The calibration technique for the transducers involved fifteen different mercury manometer readings that varied from seven inches of positive transducer reference pressure to seven inches of negative reference pressure. Half the calibration points were approached with increasing pressure while the others were approached with decreasing pressure through one pressure cycle. At each given pressure, 512 data points were read. The readings at each point were viewed graphically to insure a normal distribution and were reduced to a mean and a standard deviation. The precision

based on twice the worst standard deviation (0.00309 Volts) was an order magnitude less than the estimated bias error of the data acquisition system (0.0693 Volts). *The propagating bias increased the final differential pressure uncertainty to 1.51 percent for cascade testing.* However, if the pressure was expressed as an absolute pressure even including any barometer bias, the uncertainty percentage decreased to 0.39 percent, which concealed the actual uncertainty for the pressure measurement.

For the dynamic signal, phase lock averaging using the trigger, as described in Chapter 4, was required to construct a nominal blade. The number of data ensembles was important to achieve a final consistent wave structure over the data window. Given the conditional sampling requirement caused by the varying trigger amplitude, discussed in Chapter 4, a final ensemble size of 400 sets was established based on the sample ensemble size results and the hard-drive data storage capabilities. Example results are shown in Figure J.2.

Figure J.3 shows two sine wave representation for the 0.07 c position with rearward forcing, a worst case in terms of disturbance magnitude and possible phase variation from the trigger.

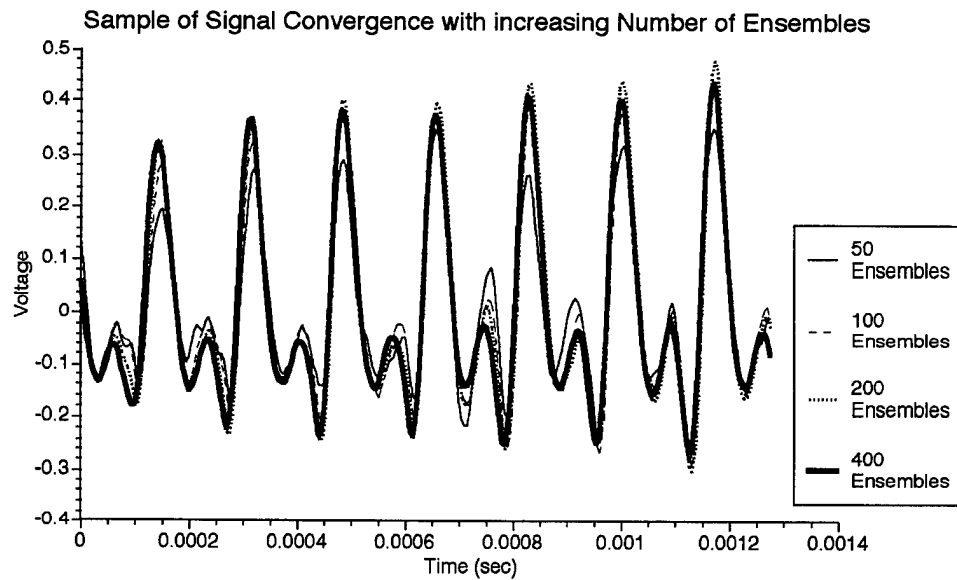


Figure J.2 Ensemble Size Comparison

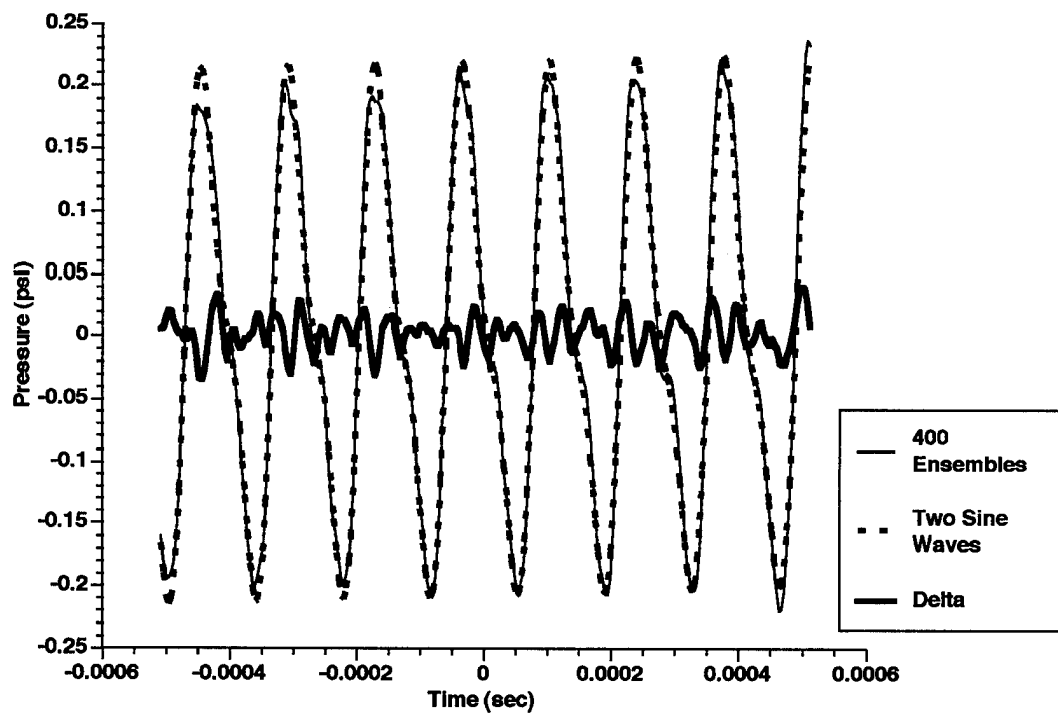


Figure J.3 Ensemble and 2 Sine Wave Representation with Associated Error

The rms error for a given chordwise position is listed in the tables of Chapters 6 and 7.

BAROMETER UNCERTAINTY

All Parameters Assumed as Bias Errors due to Single Measurements

MEASURED Room Temperature (deg C)

$$\text{Temp} \equiv 20.0$$

MEASURED Barometer Value (in Hg)

$$\text{Baro} \equiv 28.62 \text{ in}$$

Barometer Resolution (in)

$$\text{Baro}_{\text{res}} \equiv 0.01$$

Accuracy Assumed (in)

$$\text{Baro}_{\text{acc}} \equiv 0.005$$

Uncertainty of Barometer (ft)

$$B_{\text{Baro}} \equiv \sqrt{\left(\frac{\text{Baro}_{\text{res}}}{2 \cdot 12}\right)^2 + \left(\frac{\text{Baro}_{\text{acc}}}{12}\right)^2}$$

Thermometer Resolution (deg)

$$\text{Therm}_{\text{res}} \equiv 1.0$$

Accuracy Assumed (deg)

$$\text{Therm}_{\text{acc}} \equiv 0.5$$

Uncertainty of Thermometer (deg C)

$$B_{\text{Therm}} \equiv \sqrt{\left(\frac{\text{Therm}_{\text{res}}}{2}\right)^2 + (\text{Therm}_{\text{acc}})^2}$$

Brass Thermal Expansion Correction (percentage)

$$\text{Brass} := 1.621939 \cdot 10^{-2} \cdot \text{Temp} + 1.204424 \cdot 10^{-3} \quad (\text{With } R2 = 0.9999998)$$

CALCULATED Atmospheric Pressure (in Hg)

$$\text{Hg}_{\text{in}} := \text{Baro} \cdot \left(1 - \frac{\text{Brass}}{100}\right)$$

$$\text{Hg}_{\text{in}} = 28.527 \text{ in}$$

Reynolds and Perkins, Engineering Thermodynamics, pg 598, definitions of pressure

$$1 \text{ in Hg} = 0.489771 \text{ lb/in}^2$$

$$\text{Den}_1 := 26.304 \text{ slug/ft}^3$$

Reynolds and Perkins pg 663 at 20 deg C (68 deg F)

$$1 \text{ in Hg} = 0.490573 \text{ lb/in}^2$$

$$\text{Den}_2 := 26.348 \text{ slug/ft}^3$$

Assume Wrong Value Used (slug/ft3)

Worst Case Analysis

$$\text{Den}_{\text{acc}} := \text{Den}_2 - \text{Den}_1$$

$$B_{\text{Den}} := \text{Den}_{\text{acc}}$$

RESULTANT ATMOSPHERIC PRESSURE (lb/ft2)

$$P_{\text{atm}} := \frac{\text{Den}_2 \cdot 32.174 \cdot \text{Hg}_{\text{in}}}{12}$$

$$P_{\text{atm}} = 2.015 \cdot 10^3 \text{ lb/ft}^2$$

Determine Sensitivity

$$dPdDen := \frac{Baro}{12} \cdot \left(1 - \frac{Brass}{100}\right) \cdot 32.174$$

$$dPdBaro := \frac{Den\ 2}{12} \cdot \left(1 - \frac{Brass}{100}\right) \cdot 32.174$$

$$dPdTherm := Den\ 2 \cdot \frac{Baro}{12} \cdot \left(\frac{-1.621939 \cdot 10^{-2}}{100}\right) \cdot 32.174$$

Determine Sensitivity *Elemental Uncertainty

$$B_{Den} \cdot dPdDen = 3.365$$

$$B_{Baro} \cdot dPdBaro = 0.041$$

$$B_{Therm} \cdot dPdTherm = -0.232$$

Determine Uncertainty of Barometer Pressure Reading

$$U_{Patm} := \sqrt{(B_{Den} \cdot dPdDen)^2 + (B_{Baro} \cdot dPdBaro)^2 + (B_{Therm} \cdot dPdTherm)^2}$$

$$U_{Patm} = 3.374 \text{ lb/ft}^2 \text{ (95\%)}$$

$$\text{Percentage: } \frac{U_{Patm}}{P_{atm}} \cdot 100 = 0.167 \quad \%$$

ATMOSPHERIC PRESSURE

$$P_{atm} = 2.015 \cdot 10^3 \quad +/- \quad U_{Patm} = 3.374 \text{ lb/ft}^2 \text{ (95\%)}$$

NOTRE DAME CALIBRATION STANDARD UNCERTAINTY FOR HIGH SPEED TUNNELS

All Parameters Assumed as Bias Errors due to Single Measurements.

All Notre Dame calibrations conducted using Mercury Manometer Bank.

Most Calibrations traverse -7 inch to 7 inches mercury on the reference side of the Transducers.

Manometer Resolution (in)	Interpolation Error	Example Manometer Height
$\text{Manom}_{\text{res}} \equiv 0.1$	$B_{\text{int}} := \frac{\text{Manom}_{\text{res}}}{2 \cdot 12} \text{ ft}$	$h := 5 \text{ in}$

Reynolds and Perkins, Engineering Thermodynamics, pg 598, definitions of pressure

$$1 \text{ in Hg} = 0.489771 \text{ lb/in}^2 \quad \text{Den}_1 := 26.304 \text{ slug/ft}^3$$

Reynolds and Perkins pg 663 at 20 deg C (68 deg F)

$$1 \text{ in Hg} = 0.490573 \text{ lb/in}^2 \quad \text{Den}_2 := 26.348 \text{ slug/ft}^3$$

$$\text{Den}_{\text{acc}} := \text{Den}_2 - \text{Den}_1 \quad \text{Worst Case Analysis}$$

$$B_{\text{Den}} := \text{Den}_{\text{acc}} \quad \text{Assume Wrong Value Used (slug/ft}^3\text{)}$$

$$P = \text{Den} \cdot g \cdot h$$

Determine Sensitivity

Determine Sensitivity *Elemental Uncertainty

$$dP_{d\text{Den}} := \frac{h}{12} \cdot 32.174$$

$$B_{\text{Den}} \cdot dP_{d\text{Den}} = 0.59 \text{ lb/ft}^2$$

$$dP_{dh} := \text{Den}_2 \cdot 32.174$$

$$B_{\text{int}} \cdot dP_{dh} = 3.532 \text{ lb/ft}^2$$

Determine Uncertainty of Manometer Pressure Reading

$$P := \text{Den}_2 \cdot 32.174 \cdot \frac{h}{12}$$

$$B_{14} := \sqrt{(B_{\text{Den}} \cdot dP_{d\text{Den}})^2 + (B_{\text{int}} \cdot dP_{dh})^2}$$

$$B_{14} = 3.581 \text{ lb/ft}^2 \text{ (95\%)}$$

$$U_{14} := B_{14}$$

$$\text{Percentage: } \frac{B_{14}}{P} \cdot 100 = 1.014 \%$$

Differential Pressure Value

$$P = 353.217 \quad +/\text{-} \quad U_{14} = 3.581 \text{ lb/ft}^2 \text{ (95\%)}$$

Uncertainty Analysis for VISHAY #2300 Excitation Voltage

Maximum Voltage (Volts)	$V_{\max} := 15$
Voltage Regulation (%)	$V_{\text{reg}} := 0.01$
Ripple and Noise (rms V) (peak to peak,V)	$V_{\text{rms}} := 100 \cdot 10^{-6}$ $V_{\text{pp}} := 0.002$
Excitation Voltage (Volts)	$V_E := 15.00$
Resolution of Voltage (Volts)	$V_{\text{res}} := 0.001$
Interpolation Error (Volts)	$V_{\text{int}} := \frac{V_{\text{res}}}{2}$

All known error sources are bias errors due to lack of precision information.

Sensor Transducer Stage B2 for Power Supply (PS):

$$B_{2\text{PS}} := \sqrt{\left(V_E \cdot \frac{V_{\text{reg}}}{100}\right)^2 + V_{\text{rms}}^2 + V_{\text{pp}}^2 + V_{\text{int}}^2}$$

$$B_{2\text{PS}} = 0.0026 \text{ Volts (95\%)}$$

$$V_E \cdot \frac{V_{\text{reg}}}{100} = 0.0015$$

$$V_{\text{rms}} = 1 \cdot 10^{-4}$$

$$V_{\text{pp}} = 0.002$$

$$V_{\text{int}} = 5 \cdot 10^{-4}$$

Uncertainty of Power Supply Voltage:

$$U_{\text{PS}} := B_{2\text{PS}} \quad U_{\text{PS}} = 0.0026$$

$$\text{Percentage: } \frac{U_{\text{PS}}}{V_E} \cdot 100 = 0.017 \quad \%$$

EXCITATION VOLTAGE:

$$V_E = 15 \text{ Volts } \pm U_{\text{PS}} = 0.0026 \text{ Volts (95\%)}$$

Kulite Pressure Transducer (XCS-062) Uncertainty Analysis

From Specifications Sheet:	Assume Output Voltage	$V_o := 0.09 \text{ V}$
Full Scale Output (Nominal, V)		$FSO := 0.150$
Hysteresis (% Typical)		$Hyst := 0.1$
Combined Hysteresis and Non-Linearity (% Typical)		$HystNonLin := 0.5$
Repeatability (% Typical)		$Repeat := 0.1$
Thermal Zero Shift (% Full Scale/100 deg)		$TherZero := 2.0$
Thermal Sensitivity Shift (% / 100 deg)		$TherSen := 2.0$

$$\text{Calculate Non-Linearity } NonLin := \sqrt{HystNonLin^2 - Hyst^2}$$

$$NonLin = 0.4899$$

Calculate effect of power supply uncertainty (Power supply)

$$V_E := 15.00 \text{ Volts}, U_{PS} := 0.0026 \text{ Volts},$$

Sensitivity := 0.025067 V/psid from Kulite #31 test sheet

$$\text{ResistanceTerm} := \frac{\text{Sensitivity}}{V_E}$$

Resistance Term from Eqn 6.24 Figliola and Beasley.

$$\text{ResistanceTerm} = 0.0017$$

Sensitivity: $dVdVE := \text{ResistanceTerm}$

$$dVdVE \cdot \frac{U_{PS}}{V_E} = 2.8966 \cdot 10^{-7}$$

Sensor Transducer Stage

$$B_{22} := \sqrt{Hyst^2 + NonLin^2 + Repeat^2 + (dVdVE \cdot V_E)^2}$$

$$B_{22} = 0.5105 \quad \% \quad B_{22V} := \frac{B_{22}}{100} \cdot V_o$$

In actual engine application, transducer thermally compensated over range from 70 to 170 deg F. In cascade application, at Mach=0.50,

$$T_{\text{static}} := 45 \text{ deg F}$$

Environmental Effects

$$B_{\text{TherZero}} := \frac{\text{TherZero} \cdot \text{FSO}}{100} \cdot \left(\frac{70.0 - T_{\text{static}}}{100} \right) \quad \text{V}$$

$$B_{\text{ThermSen}} := \frac{\text{TherSen}}{100} \cdot \left(\frac{70.0 - T_{\text{static}}}{100} \right)$$

$$B_{\text{TherZero}} = 7.5 \cdot 10^{-4} \text{ V}$$

$$B_{\text{ThermSen}} = 0.005$$

$$B_{27} := \sqrt{B_{\text{TherZero}}^2 + (B_{\text{ThermSen}} \cdot V_o)^2}$$

$$B_{27} = 8.7464 \cdot 10^{-4} \quad \text{V}$$

Cascade Application

$$B_{2C} := \sqrt{B_{22V}^2 + B_{27}^2}$$

$$B_{2C} = 9.8798 \cdot 10^{-4} \text{ V}$$

Uncertainty for Cascade

$$U_{KC} := B_{2C}$$

$$U_{KC} = 9.8798 \cdot 10^{-4} \text{ V (95\%)}$$

Percentages:

$$\frac{U_{KC}}{V_o} \cdot 100 = 1.0978 \quad \%$$

Output Voltage for Cascade

$$V_o = 0.09 \quad \pm U_{KC} = 9.8798 \cdot 10^{-4} \text{ V (95\%)}$$

Uncertainty of data acquisition process (from transducer to Vishay 2300
signal conditioner/amplifier to RC Electronics IS-16E Card for Engine Testing.
VISHAY #2300 SIGNAL CONDITIONER/AMPLIFIER

$$\text{Input Drift (V/deg C)} \quad \text{InpDrift} := 1 \cdot 10^{-6}$$

$$\text{Assume} \quad \text{DeltaT} := 1 \quad \text{Deg C}$$

$$\text{Signal to Noise Ratio (dB)} \quad \text{SNR} := 102$$

$$\text{Gain Accuracy (\%)} \quad \text{GainAcc} := 0.5 \quad \text{Gain Used} \quad \text{Gain} := 70$$

$$\text{Offset Accuracy (V)} \quad \text{OffsetAcc} := 2 \cdot 10^{-6} \quad \text{Offset Used} \quad \text{Offset} := 0.0$$

Assume Kulite Pressure Transducer

$$V_{in} := 0.09 \quad \text{+/-} \quad U_{KC} := 9.8798 \cdot 10^{-4} \text{ Volts}$$

VISHAY Signal Conditioning/Amplifier Stage Bias Error.
Note $V_{out} = (V_{in} + \text{Offset}) \cdot \text{Gain}$

Determine Sensitivities:

$$dV_{out}dV_{in} := \text{Gain} \quad dV_{out}dV_{in} \cdot U_{KC} = 0.0692 \quad \text{V}$$

$$dV_{out}d\text{Offset} := \text{Gain} \quad dV_{out}d\text{Offset} \cdot \text{OffsetAcc} = 1.4 \cdot 10^{-4} \text{ V}$$

$$dV_{out}d\text{Gain} := V_{in} + \text{Offset}$$

$$dV_{out}d\text{Gain} \cdot \frac{\text{GainAcc}}{100} = 4.5 \cdot 10^{-4} \quad \text{V}$$

$$V_{\text{Noise}} := \frac{V_{in}}{10^{\left(\frac{\text{SNR}}{20}\right)}}$$

$$V_{\text{Noise}} = 7.149 \cdot 10^{-7} \quad \text{V}$$

$$B_{23} := \sqrt{(dV_{out}dV_{in} \cdot U_{KC})^2 + \left(dV_{out}d\text{Offset} \cdot \frac{\text{OffsetAcc}}{100}\right)^2 + \left(dV_{out}d\text{Gain} \cdot \frac{\text{GainAcc}}{100}\right)^2 + V_{\text{Noise}}^2}$$

Environmental Effects:

$$B_{27} := \sqrt{(\text{InpDrift} \cdot \text{DeltaT})^2}$$

$$V_{out} := V_{in} \cdot \text{Gain}$$

$$B_{23} = 0.0692 \quad \text{V}$$

VISHAY Uncertainty:

$$B_{27} = 1 \cdot 10^{-6} \quad \text{V}$$

$$B_{2Vis} := \sqrt{B_{23}^2 + B_{27}^2}$$

$$U_{Vis} := B_{2Vis}$$

VOLTAGE OUT OF VISHAY

$$V_{out} = 6.3 \quad \text{+/-} \quad U_{Vis} = 0.0692 \quad \text{V (95\%)}$$

$$\text{Percentage:} \quad \frac{U_{Vis}}{V_{out}} \cdot 100 = 1.0978 \quad \%$$

RC-ELECTRONICS IS-16E, DATA ACQUISITION CARD

Assume card in +/- $V_{\text{Mode}} := 2.5$

Resolution (bits) $\text{Res} := 12$

$$\text{Res } V := \frac{2 \cdot V_{\text{Mode}}}{2^{\text{Res}}} \quad \text{Res } V = 0.0012 \quad V$$

Accuracy (%Reading) $\text{Acc} := 0.05$

Linearity (+/- Bit) $\text{Lin} := 1$

$$B_{\text{Acc}} := V_{\text{out}} \cdot \frac{\text{Acc}}{100} + \text{Res } V$$

Quantization Error (Volts)

$$B_{\text{Quant}} := \frac{\text{Res } V}{2} \quad B_{\text{Lin}} := \text{Res } V$$

$$B_{24} := \sqrt{B_{\text{Acc}}^2 + B_{\text{Lin}}^2 + B_{\text{Quant}}^2 + U_{\text{Vis}}^2}$$

$$B_{\text{Acc}} = 0.0044 \quad V$$

$$B_{\text{Lin}} = 0.0012 \quad V$$

$$B_{\text{Quant}} = 6.1035 \cdot 10^{-4} \quad V$$

RC ELEC. CARD VOLTAGE OUT AND UNCERTAINTY

$$U_{\text{RC}} := B_{24}$$

$$\text{Percentage} \quad \frac{U_{\text{RC}}}{V_{\text{out}}} \cdot 100 = 1.1002 \quad \%$$

$$V_{\text{out}} = 6.3 \quad \pm U_{\text{RC}} = 0.0693 \quad \text{Volts (95\%)}$$

Uncertainty of Calibration Curve for Transducer #31 of Stator #11

Fifteen manometer heights were tested with 512 data points per height. The resulting curve fit is $P(V)=0.3958 \cdot V - 0.00144$, $R^2=0.99995$. The mean of the fifteen separate height standard deviations was 0.002855. The largest standard deviation was 0.003089.

Curve Fit parameters:

Standard error of slope (Bias)

$$m := 0.3958 \quad \text{lb/in}^2\text{V}$$

$$SE_m := 0.000809 \quad \text{lb/in}^2\text{V}$$

$$b := -0.00144 \quad \text{lb/in}^2$$

Standard error of Y intercept (Bias)

$$SE_b := 0.004334 \quad \text{lb/in}^2$$

Error of Calib. Standard

Worst Case Std Dev

$$B_{14} := 3.581 \quad \text{lb/ft}^2$$

$$\text{StdDev} := 0.003089 \quad \text{V}$$

$$B_{14} := \frac{B_{14}}{144} \quad \text{lb/in}^2$$

$$\text{FROM RC Elec CardCarV}_{\text{out}} := 6.3 \quad \text{V} \quad U_{PC} := 0.0693 \quad \text{V (95\%)}$$

Determine Sensitivities: $P=m \cdot V_{\text{out}}+b$

Determine Sensitivity*Elemental Error

$$dP_{dm} := V_{\text{out}}$$

$$dP_{dm} \cdot SE_m = 0.005 \quad \text{lb/in}^2$$

$$dP_{dV_{\text{out}}} := m$$

$$dP_{dV_{\text{out}}} \cdot U_{PC} = 0.027 \quad \text{lb/in}^2$$

$$dP_{db} := 1$$

$$dP_{db} \cdot SE_b = 0.004 \quad \text{lb/in}^2$$

Calibration Curve Fit Errors

$$B_{32} := \sqrt{(dP_{dm} \cdot SE_m)^2 + (dP_{dV_{\text{out}}} \cdot U_{PC})^2 + (dP_{db} \cdot SE_b)^2}$$

$$P_{32} := \text{StdDev} \cdot m$$

$$B_{14} = 0.025 \quad \text{lb/in}^2$$

$$B_{32} = 0.028 \quad \text{lb/in}^2$$

$$P_{32} = 0.001 \quad \text{lb/in}^2$$

Determine Overall Uncertainty

$$U_{\text{Press}} := \sqrt{(B_{14})^2 + B_{32}^2 + (2 \cdot P_{32})^2}$$

$$U_{\text{Press}} = 0.038 \quad \text{lb/in}^2 \text{ (95\%)}$$

DETERMINE PRESSURE DIFFERENCE VALUE for Transducer #31

$$\text{Press}_{31} := m \cdot V_{\text{out}} + b$$

$$\text{Press}_{31} = 2.492 \quad +/- \quad U_{\text{Press}} = 0.038 \quad \text{lb/in}^2 \quad (95\%) \text{ below Atmospheric Pressure}$$

Percentage:

$$\frac{U_{\text{Press}}}{\text{Press}_{31}} \cdot 100 = 1.513 \quad \%$$

From Barometer Uncertainty

$$P_{\text{atm}} := 2.015 \cdot 10^3 \quad +/- \quad U_{\text{Patm}} := 3.374 \quad \text{lb/ft}^2 \quad (95\%)$$

$$P_{\text{atm}} := \frac{P_{\text{atm}}}{144} \quad U_{\text{Patm}} := \frac{U_{\text{Patm}}}{144}$$

$$P_{\text{atm}} = 13.993 \quad \text{lb/in}^2$$

$$U_{\text{Patm}} = 0.023 \quad \text{lb/in}^2$$

DETERMINE ABSOLUTE PRESSURE on Transducer #31

$$P_{\text{abs}} := P_{\text{atm}} - \text{Press}_{31} \quad U_{\text{abs}} := \sqrt{U_{\text{Press}}^2 + U_{\text{Patm}}^2}$$

$$P_{\text{abs}} = 11.501 \quad +/- \quad U_{\text{abs}} = 0.044 \quad \text{lb/in}^2 \quad (95\%)$$

Percentage:

$$\frac{U_{\text{abs}}}{P_{\text{abs}}} \cdot 100 = 0.386 \quad \%$$

REFERENCES

- Adachi, T., and Murakami, Y., "Three Dimensional Velocity Distribution Between Stator Blades and Unsteady Force on a Blade due to Passing Wakes," Japan Society of Mechanical Engineers, August, 1979, pp. 1074-1082.
- Adamczyk, J.J., "Passage of a Swept Airfoil through an Oblique Gust," Journal of Aircraft, May, 1974, pp. 281-287.
- Anderson, J.D., Jr., Fundamentals of Aerodynamics, McGraw-Hill, New York, 1991.
- Atassi, H.M., personal communication, University of Notre Dame, 22 June, 1995.
- Atassi, H.M., "The Sears Problems for a Lifting Airfoil Revisited - New Results," Journal of Fluid Mechanics, Vol. 141, 1984, pp. 109-122.
- Atassi, H.M., "Unsteady Aerodynamics of Vortical Flows: Early and Recent Developments," Aerodynamics and Aeroacoustics, Editor K.Y. Fung, World Scientific, Chapter 4, pp. 119-169, 1994.
- Atassi, H.M., and Akai, T.J., "Aerodynamic and Aeroelastic Characteristics of Oscillating Loaded Cascades at Low Mach Number, Part I: Pressure Distribution, Forces, and Moments," Journal of Engineering for Power, Vol. 102, No. 2, 1980, pp. 344-351.
- Atassi, H.M., and Akai, T.J., "Aerodynamic and Aeroelastic Characteristics of Oscillating Loaded Cascades at Low Mach Number, Part II: Stability and Flutter Boundaries," Journal of Engineering for Power, Vol. 102, No. 2, 1980, pp. 352-356.
- Atassi, H.M., Fang, J., and Ferrand, P., "A Study of the Unsteady

- Pressure of a Cascade Near Transonic Flow Condition," ASME Paper 94-GT-476, International Gas Turbine and Aerospace Congress and Exposition, The Hague, Netherlands, 1994.
- Atassi, H.M., Fang, J., and Patrick, S., "Direct Calculation of Sound Radiated From Bodies in Nonuniform Flows," *Journal of Fluids Engineering*, Vol. 115, 1993, pp. 573-579.
- Batill, S.M., and Nebres, J.V., "Application of Digital Filtering Techniques to Unsteady Pressure Measurements," AIAA-91-0061, 29th Aerospace Sciences Meeting, Reno, Nevada, 1991.
- Bentele, M., Engine Revolutions: The Autobiography of Max Bentele, Society of Automotive Engineers, Warrendale, PA, 1991.
- Bisplinghoff, R.L., and Ashley, H., Principles of Aeroelasticity, John Wiley and Sons, New York, 1962.
- Blöcs, A., and Fransson, T.H., "Aeroelasticity in Turbomachines: Comparison of Theoretical and Experimental Cascade Results," Lausanne Institute of Technology, Switzerland, Communication du laboratoire de Thermique Appliquee No. 13, 1986.
- Boyne, W.J., and Lopez, D.S., The Jet Age: Forty Years of Jet Aviation, Smithsonian Institution Press, Washington City, 1979.
- Bratt, J.B., and Scruton, C., "Measurements of Pitching Moment Derivatives for an Aerofoil Oscillating About the Half-Chord Axis," British Aeronautical Research Council, London, R&M 1921, November, 1938.
- Buffum, D.H., and Fleeter, S., "Oscillating Cascade Aerodynamics by an Experimental Influence Coefficient Technique," *Journal of Propulsion*, Vol. 6, No. 5, 1990, pp. 612-620.
- Campbell, W., "Protection of Steam Turbine Disc Wheels from Axial Vibration," ASME Paper 1920, May 1924.
- Carta, F.O., "Unsteady Aerodynamics and Gapwise Periodicity of

- Oscillating Cascaded Airfoils," Journal of Engineering for Power, July, 1983, pp. 565-574.
- Cohen, H., Rogers, G.F.C., and Saravanamuttoo, H.I.H., Gas Turbine Theory, Longman Scientific & Technical, Singapore, 1987.
- Commerford, G.L., and Carta, F.O., "Unsteady Aerodynamic Response of a Two-Dimensional Airfoil at High Reduced Frequency," AIAA Journal, January, 1974, pp. 43-48.
- Davis, E.L., "The Measurement of Unsteady Pressures in Wind Tunnels," AGARD Report 169, London, March, 1958.
- Dring, R.P., Joslyn, H.D., and Hardin, L.W., "An Investigation of Axial Compressor Rotor Aerodynamics," Journal of Engineering for Power, January, 1982, pp. 84-96.
- Epstein, A.H., Gertz, J.B., Owen, P.R., and Giles, M.B., "Vortex Shedding in High-Speed Compressor Blade Wakes," Journal of Propulsion, Vol. 4, No. 3, 1987, pp. 236-244.
- Evans, R.L., "Boundary-Layer Development on an Axial-Flow Compressor Stator Blade," Journal for Engineering for Power, April, 1978, pp. 287-293.
- Evans, R.L., "Turbulence and Unsteadiness Measurements Downstream of a Moving Blade Row," Journal of Engineering for Power, January, 1975, pp. 131-139.
- Fabian, M.K., and Jumper, E.J., "Unsteady Pressure Distributions around Compressor Vanes in an Unsteady, Transonic Cascade," AIAA-95-0302, 33rd Aerospace Sciences Meeting, Reno, Nevada, 1995.
- Fang, J., and Atassi, H.M., "Compressible Flows with Vortical Disturbances Around a Cascade of Loaded Airfoils," Unsteady Aerodynamics, Aeroacoustics, and Aeroelasticity of Turbomachines and Propellers, Springer-Verlag, New York, 1993.

Figliola, R.S., and Beasley, D.E., Theory and Design for Mechanical Measurements, John Wiley and Sons, New York, 1991.

Fleeter, S., "Fluctuating Lift and Moment Coefficients for Cascaded Airfoils in a Nonuniform Compressible Flow," *Journal of Aircraft*, Vol. 10, No. 2., 1973, pp. 93-98.

Fleeter, S., Jay, R.L., Bennett, W.A., "Rotor Wake Generated Unsteady Aerodynamic Response of a Compressor Stator," *Journal of Engineering for Power*, October, 1978, pp. 664-675.

Fleeter, S., Jay, R.L., Bennett, W.A., "The Time-Variant Aerodynamic Response of a Stator Row Including the Effects of Airfoil Camber," *Journal of Engineering for Power*, April, 1980, pp. 334-343.

Franke, G.F., and Henderson, R.E., "Unsteady Stator Response to Upstream Rotor Wakes," *Journal of Aircraft*, July, 1980, pp. 500-507.

Fujita, H., and Kovasznay, L.S., "Unsteady Lift and Radiated Sound from a Wake Cutting Airfoil," *AIAA Journal*, Vol. 12, No. 9, 1974, pp. 1216-1221.

Fung, Y.C., An Introduction to the Theory of Aeroelasticity, Dover Publications, 1993, p. 66.

Gallus, H.E., Lambertz, J., and Wallmann, T., "Blade-Row interaction in an Axial Flow Subsonic Compressor Stage, *Journal of Engineering for Power*," January, 1980, pp. 169-177.

Garrick, I.E., "On the Plane Potential Flow past a Lattice of Arbitrary Aerofoils," *NACA Rep. 788*, 1944.

Garrick, I.E., "Perspectives in Aeroelasticity," Aeroelasticity in Turbomachines, Detroit Diesel Allison, 1972, pp. 1-75.

"GE to Test Production Design of B-1B Fan Blade Dampers," *Aviation*

- Week & Space Technology, McGraw-Hill, October 7, 1991, p. 17.
- Glegg, S.A.L., personal communication, University of Notre Dame, November 8, 1995.
- Goldstein, M.E., and Atassi, H., "A Complete Second-Order Theory for the Unsteady Flow about an Airfoil due to a Periodic Gust," *Journal of Fluid Mechanics*, Vol. 74, Part 5, 1976, pp. 741-765.
- Goldstein, S., Modern Developments in Fluid Dynamics, Oxford Press, Oxford, England, 1943.
- Gostelow, J.P., "A New Approach to the Experimental Study of Turbomachinery Flow Phenomena," *Journal of Engineering for Power*, January 1977, pp. 97-105.
- Gostelow, J.P., Cascade Aerodynamics, Pergamon Press, Oxford, England, 1984.
- Green, W., Rocket Fighter, Random House, New York, 1971.
- Green, W., The World's Fighting Planes, Doubleday, Garden City, New York, 1964.
- Hartog, J.P.D., Mechanical Vibrations, Dover, 1985, p. 270.
- Hathaway, M.D., Gertz, J.B, Epstein, A.H., and Strazisar, A.J., "Rotor Wake Characteristics of a Transonic Axial-Flow Fan," *AIAA Journal*, Vol. 24, No. 11, 1986, pp. 1802-1810.
- Hawthorne, W.R., Aerodynamic of Turbine and Compressors, Princeton University Press, Princeton, New Jersey, 1964.
- Heiser, W., personal communication, U.S. Air Force Academy, January, 1992.
- Henderson, R.E., and Horlock, J.H., "An Approximate Analysis of the Unsteady Lift on Airfoils in Cascade," *Journal of Engineering for Power*, October, 1972, pp. 233-240.

- Horlock, J.H., "Fluctuating Lift Forces on Aerofoils Moving Through Transverse and Chordwise Gusts," *Journal of Basic Engineering*, December, pp. 494-500, 1968.
- Ives, D.C., "A Modern Look at Conformal Mapping Including Multiply Connected Regions," *AIAA Journal*, Vol. 14, no. 8, pp. 1006-1011, 1976.
- "Jet Engine Inspections Urged," Associated Press Release, 25 August 1995.
- Johnsen, I.A., and Bullock, R.O., Aerodynamic Design of Axial-Flow Compressors, NASA SP-36, Washington, D.C., 1965.
- Kemp, N.H., and Sears, W.R., "Aerodynamic Interference Between Moving Blade Rows," *Journal of the Aeronautical Sciences*, Vol. 20, No. 9, 1953, pp. 585-612.
- Kemp, N.H., and Sears, W.R., "The Unsteady Forces Due to Viscous Wakes in Turbomachines," *Journal of the Aeronautical Sciences*, July, 1955, pp. 478-483.
- Kerrebrock, J.L., and Mikolajczak, A.A., "Intra-Stator Transport of Rotor Wakes and Its Effect on Compressor Performance," *Journal of Engineering for Power*, October, 1970, pp. 359-368.
- "Kulite Miniature IS Silicon Diaphragm Pressure Transducer Catalog," Bulletin KS-1000E, Leonia, New Jersey, 1992.
- Kurosaka, M., "AA 526 Aircraft Engine Noise," Course Notes, Lesson #8, University of Washington, October, 1989.
- Lefcort, M.D., "An Investigation into Unsteady Blade Forces in Turbomachines," *Journal of Engineering for Power*, October, 1965, pp. 345-354.
- Lotz, M., and Raabe, J., "Blade Oscillations in One-Stage Axial Turbomachinery," *Journal of Basic Engineering*, December,

1968, pp. 485-493.

Lykins, C., and Watson K., "IHPTET: Technology Teams in Action," Aero-Propulsion and Power Directorate, Wright-Patterson AFB, Ohio, 1993.

Manwaring, S.R., and Wisler, D.C., "Unsteady Aerodynamics and Gust Response in Compressors and Turbines," ASME Paper 92-GT-422.

Meyer, R.X., "The Effect of Wakes on the Transient Pressure and Velocity Distributions in Turbomachines," Transactions of the American Society of Mechanical Engineers, October, 1958, pp. 1544-1552.

Naumann, H., and Yeh, H., "Lift and Pressure Fluctuations of a Cambered Airfoil under Periodic Gusts and Applications in Turbomachinery," Journal of Engineering for Power, January, pp. 1-10, 1973.

Oates, G.C., Aerothermodynamics of Gas Turbine and Rocket Propulsion: Revised and Enlarged, AIAA Educational Series, Washington D.C., 1988.

Oates, G.C., Aircraft Propulsion Systems Technology and Design, AIAA Educational Series, Washington D.C., 1989.

O'Connor, L., "Taming Vibrations in Turbines," Mechanical Engineering, April, 1993, pp. 49-52.

Osborne, C., "Compressible Unsteady Interactions between Blade Rows," AIAA Journal, Vol. 11, No. 3, pp. 340-346, 1973.

Press, W.H., Teukolsky, S.A., Vetterling, W.T., Flannery, B.P., Numerical Recipes in Fortran: The Art of Scientific Computing, Cambridge University Press, Cambridge, UK, 1986.

Rainey, A.G., "Measurement of Aerodynamic Forces for Various Mean Angles of Attack on an Airfoil Oscillating in Pitch and on Two

Finite-Span wings Oscillating in Bending with Emphasis on Damping in Stall," NACA Report 1305, 1957.

Rao, J.S., Turbomachine Blade Vibration, John Wiley and Sons, New Delhi, India, 1991.

Reynolds, W.C., and Perkins, H.C., Engineering Thermodynamics, McGraw-Hill, New York, 1977.

Schlichting, H., "Problems and Results of Investigations on Cascade Flow," Journal of the Aeronautical Sciences, March, 1954, pp. 163-178.

Schlichting, H., Boundary Layer Theory, McGraw-Hill, New York, 1955.

Schmidt, D.P., and Okiishi, T.H., "Multistage Axial-Flow Turbomachine Wake Production, Transport, and Interaction," AIAA Journal, Vol. 15, No. 8, 1977, pp. 1138-1145.

Schwarz, L., "Berechnung der Druckverteilung einer Harmonisch sich Verformenden Tragfläche in ebener Strömung," Luftfahrt-Forschung, Vol 17, 1940, p. 379.

Sears, W.R., "Some Aspects of Non-Stationary Airfoil Theory and Its Practical Application," Journal of the Aeronautical Sciences, Vol. 8, No. 3, pp. 43-47, 1941.

"T-46 Termination Will Force Closure of Fairchild Facility on Long Island," Aviation Week & Space Technology, McGraw-Hill, March 23, 1987, p. 27.

Theodorsen, T., "General Theory of Aerodynamic Instability and the Mechanism of Flutter," NACA Report 496, 1935.

Verdon, J.M., and Caspar, J.R., "Subsonic Flow Past an Oscillating Cascade with Finite Mean Flow Deflection," AIAA Journal, Vol. 18, No. 5, 1980, pp. 540-548.

Verdon, J.M., "Unsteady Aerodynamics for Turbomachinery

Aeroelastic Applications," Unsteady Transonic Aerodynamics, AIAA Progress in Astronautics and Aeronautics, Vol. 120, 1989. pp. 287-347.

von Karman, T., and Sears, W.R., "Airfoil Theory for Non-Uniform Motion," Journal of the Aeronautical Sciences, Vol. 5, No. 10, pp. 6-17, 1938.

Vukelich, S., "US Air Force Structural Integrity Program," University of Tennessee Space Institute, Tullahoma, Tennessee, June, 1992.

Walker, G.J., and Oliver, A.R., "The Effect of Interaction Between Wakes from Blade Rows in an Axial Flow Compressor on the Noise Generated by Blade Interaction," Journal of Engineering for Power, October, 1972, pp. 241-248.

Whitehead, D.S., "Force and Moment Coefficients for Vibrating Aerofoils in Cascade," British Aeronautical Research Council, London, R&M 3254, 1960.

Whitfield, C.E., Kelly, J.C., Barry, B., "A Three-Dimensional Analysis of Rotor Wakes," Aeronautical Quarterly, November, 1972, pp. 285-300.

Wilson, D.G., The Design of High-Efficiency Turbomachinery and Gas Turbines, MIT Press, Cambridge, Massachusetts, 1984.

Zierke, W.C., and Okiishi, T.H., "Measurement and Analysis of Total-Pressure Unsteadiness Data from an Axial-Flow Stage," Journal of Engineering for Power, April, 1982, pp. 479-488.